UNIVERSITY OF BIRMINGHAM

Heat-induced alterations of dental tissues

By

Michael Sandholzer

A thesis submitted to
The University of Birmingham
for the degree of
DOCTOR OF PHILOSOPHY

School of Dentistry
The University of Birmingham
March 2014

DEDICATED TO MY FAMILY

Synopsis

In forensic investigations involving severely burned human remains, dental analysis stands alone as other means of identification are often destroyed. It is therefore important to perform lab-based research to characterise any tissue changes providing relevant information that can facilitate these investigations. The aim of the present work was to investigate the influence of duration of heat exposure and heating regimes regarding the macroscopic, compositional, structural and crystalline alterations of dental tissues.

A range of experiments were carried out using a total of 215 freshly extracted human teeth, exposed to temperatures of 400 to 1000°C. Shrinkage and shape preservation was analysed using X-ray micro-computed tomography (micro-CT), whilst crystalline alterations were evaluated with synchrotron-based X-ray scattering experiments. The alterations of organic constituents were assessed using thermogravimetry (TGA) and Fourier-transformed infrared spectroscopy (FTIR). Moreover, calibrated digital photographs were used to document and analyse colour alterations.

Although dentinal shrinkage was already found at 400°C, tooth morphology was well preserved even at 1000°C. Surface colour alterations were linked to the gradual degradation of organic components, and were also highly dependent upon the duration of heat exposure and the heating regime. The crystalline alterations were less influenced by these factors, providing relevant reference values for cremation temperature estimations.

The combination of novel analytical approaches enabled the documentation and quantification of heat-induced alterations of dental tissues, providing an improved understanding of the influences of heating regimes on the macroscopic, compositional, structural and crystalline alterations. The results of the present work can be used in the forensic identification process and allow an improved estimation of the cremation temperature range based on human dental remains.

Acknowledgments

Foremost, I want to thank my supervisors Professors Gabriel Landini, Damien Walmsley and Phil Lumley for giving me the opportunity to pursue this Ph.D. They challenged me to reach higher, work harder and go further than I dreamed possible. I am also much obliged to Prof. Alexander Korsunsky and his Ph.D. students Alexander, Nikos and Tan at the University of Oxford for the fruitful collaboration. Although soon earning the nickname 'Trouble', thanks to the lab technicians Gay, Michelle and Sue for their support to realise some of my experiments. Thanks to all the other collaborators, funding bodies, advisors and academics worldwide that believed in me and enabled some incredible opportunities.

To spend time up in the air and travel the world was definitely the most encouraging momentum during this Ph.D. During the last three years, I was able to attend numerous national and international conferences, expand my knowledge, meet up with old friends and connect with many new people. I will never forget the great time I had in the postgraduate office and the local pubs. From day one all made me feel welcome and accepted my Austrian Manners (pun intended). A special thanks to Eisha for introducing me to crisp sandwiches and Twitter, Helen for the amazing cakes and travel companionship, Jonathan for the help with the image analysis and his indefinite clumsiness, Krunal for the daily baguette walk and the tech talk, and Owen for pointing out auntie Julie in Colmore Bar and dragging me to all the noisy gigs. The years abroad told me to be truly grateful for those close friends that continue conversations after a long period where the last one ended, and most importantly never question the friendship. Thanks for being there for me: Alexander, Christina, David, Jasmin, Kathy and Sarah. I also want to thank all friends and colleagues not mentioned by name that encouraged and motivated me over the years in one way or the other.

Zuletzt möchte ich meinen Eltern Günther und Christine, sowie meinen Schwestern Margareta und Lucia für die kontinuierliche Unterstützung und den emotionalen Rückhalt danken. Dank euch konnte ich meine Ziele bestmöglich verfolgen – ohne jegliche Sorgen. Diese Arbeit ist euch gewidmet.

Table of contents

List of figures

Unless stated otherwise, all figures result from my own work.

List of tables

Unless stated otherwise, all tables result from my own work.

List of abbreviations

1-D	one-dimensional
2-D	two-dimensional
3-D	three-dimensional
ABFO	American Board of Forensic Odontologists
ANOVA	Analysis of variance
ATR-FTIR	Attenuated reflectance Fourier-transformed infrared spectroscopy
AVI	Audio Video Interleave (video file format)
CBCT	Cone beam computed tomography
CCD	Charge-coupled device
CI	Crystallinity index
CIE	Commission internationale de l'éclairage
CT	Computed tomography
DLS	Diamond Light Source
DNA	Deoxyribonucleic acid
DSLR	Digital single-lens reflex camera
DVI	Disaster victim identification
EDS	Energy dispersive X-ray spectroscopy
FTIR	Fourier-transformed infrared spectroscopy
HAp	Hydroxyapatite
HPLC	High-performance liquid chromatography
IR	Infrared
JPG	Joint Photographic Expert Group (image file format)
LSD	Least significant difference
LUT	Lookup table
Micro-CT	X-ray micro-computed tomography
MS	Mass-spectrometry
NIST	National Institute of Standards and Technology
NRRD	Nearly Raw Raster Data (image file format)

PBS	Phosphate buffered saline
PMMA	Poly-methylmetacrylate
ROI	Region of interest
RT	Room temperature
SAXS	Small-angle X-ray scattering
SD	Standard deviation
SE	Secondary electron
SEM	Scanning electron microscopy
TCP	Tribasic calcium phosphate
TEM	Transmission electron microscopy
TGA	Thermogravimetric analysis
WAXS	Wide-angle X-ray scattering
XRD	X-ray diffraction
XRF	X-ray fluorescence

Declaration

I hereby declare that this thesis is my own work and effort. Where other sources of information have been used, they have been acknowledged. The X-ray scattering data analysis, reported in chapters 2.9 and 6 was conducted by Mrs. Tan Sui as part of an ongoing collaboration between the School of Dentistry (University of Birmingham) and the Department of Engineering (University of Oxford), investigating thermal and mechanical alterations of dental tissues.

Reprints of the following seven peer-reviewed publications resulting from work conducted during the Ph.D. scholarship are included in the Appendix (Chapter 11.2), with written permission of Elsevier, Wiley-Blackwell and Royal Society Publishing.

Sandholzer MA, Walmsley AD, Lumley PJ, Landini G. *Radiologic evaluation of heat-induced shrinkage and shape preservation of human teeth using micro-CT.* Journal of Forensic Radiology and Imaging 2013; 1(3) 107-111, DOI 10.1016/j.jofri.2013.05.003.

Sandholzer MA, Sui T, Korsunsky A, Walmsley AD, Lumley PJ, Landini G. *X-ray scattering evaluation of ultrastructural changes of human dental tissue with thermal treatment*. Journal of Forensic Sciences 2014; 59(3) 769-774, DOI 10.1111/1556-4029.12400.

Sui T, **Sandholzer MA**, Le Bourhis E, Baimpas N, Landini G, Korsunsky AM. *Structure-mechanical function relations at nano-scale in heat-affected human dental tissue.* Journal of the Mechanical Behavior of Biomedical Materials 2014, 32 113-124, DOI 10.1016/j.jmbbm.2013.12.014.

Sui T, **Sandholzer MA**, Lunt AJG, Baimpas N, Smith A, Landini G, Korsunsky AM. *In-situ X-ray scattering evaluation of heat-induced ultrastructural changes in dental tissues and synthetic hydroxyapatite* Journal Royal Society Interface 2014, 11(95), 20130928, DOI 10.1098/rsif.2013.0928

Sui T, Lunt A, Baimpas N, **Sandholzer MA**, Hu J, Dolbnya IP, Landini G, Korsunsky AM. *Hierarchical modelling of in situ elastic deformation of human enamel based on photoelastic and diffraction analysis of stresses and strains.* Acta Biomaterialia 2014,10(1) 343-354, DOI 10.1016/j.actbio.2013.09.043.

Sui T, **Sandholzer MA**, Baimpas N, Dolbnya IP, Walmsley AD, Lumley PJ, Landini G, Korsunsky AM. *Multi-scale modelling and diffraction-based characterization of elastic behaviour of human dentine.* Acta Biomaterialia 2013; 9(8) 7937-7947, DOI 10.1016/j.actbio.2013.04.020**.**

Sui T, **Sandholzer MA**, Baimpas N, Dolbnya IP, Landini G, Korsunsky AM. *Hierarchical modelling of elastic behaviour of human enamel based on synchrotron diffraction characterization*. Journal of Structural Biology 2013; 184(2) 136-146, DOI 10.1016/j.jsb.2013.09.023.

Dissemination of research

The work conducted during the Ph.D. scholarship resulted in 7 peer-reviewed publications, 7 invited talks and academic lectures, and 15 conference presentations (7 delivered as presenter).

Invited talks and academic lectures

· Royal Society of Chemistry (Teesside Section), Middlesbrough – June 2013
· Midlands SEM User Meeting, Birmingham – June 2013
· Faculty of Life Sciences, University of Vienna – April 2013
· Institute of Physics, University of Vienna – April 2013
· British Association of Forensic Odontology, Brighton – November 2012
· British Association of Forensic Odontology, York– November 2011
· Royal Society of Medicine (Clinical Forensic and Legal Medicine Section), London – October 2011

Conference presentations (as presenter)*

2014
Sui T, **Sandholzer MA**, Baimpas N, Lunt AJG, Dolbnya IP, Hu J, Walmsley AD, Lumley PJ, Landini G, Korsunsky AM. *Hierachical modelling and X-ray analysis of human dentine and enamel.* International Multi Conference of Engineers and Computer Scientists, Hong Kong (China).

2013
Sui T, **Sandholzer MA**, Le Bourhis E, Baimpas N, Landini G, Korsunsky AM. *Nano-scale thermo-mechanical structure-property relationships in human dental tissues studied by nano-indentation and synchrotron X-ray scattering.* 15th International Conference on Biomedical Engineering, Singapore (Singapore) published in: The 15th International Conference on Biomedical Engineering, IFMBE Proceedings 43, 251-54.

Sandholzer MA*, Sui T, Korsunksy AM, Walmsley AD, Lumley PJ, Landini G. *Structural and functional characterisation of dental nanostructures.* British Society for Oral and Dental Research Meeting, Bath (UK).

Tomson PL, **Sandholzer MA**, Lumley PJ, Sui T, Korsunksy AM, Smith AJ, Cooper PR. *Dissolution products from MTA release novel growth factors from dentine.* British Society for Oral and Dental Research Meeting, Bath (UK).

Sandholzer MA*, Walmsley AD, Lumley PJ, Landini G. *Heat-induced shrinkage and shape preservation of teeth: A radiologic evaluation.*. International Organization for Forensic Odonto-Stomatology Congress, Florence (Italy) published in: Journal of Forensic Odontostomatology 2013; 31(1) Suppl 1:40-1.

Sandholzer MA*, Sui T, Lunt AJG, Korsunksy AM, Walmsley AD, Lumley PJ, Landini G, *Ultrastructural changes of biological apatite with in situ thermal treatment.* UK Society for Biomaterials Conference, Birmingham (UK) published in: UK Society for Biomaterials 13th Annual Conference Abstract Book, ISBN 978-09559548-4-9.

Sui T, **Sandholzer MA**, Baimpas N, Dolbnya IP, Landini G, Korsunsky AM. *Multi-scale modelling and X-ray diffraction characterization of elastic behaviour of human dental tissue*. 7th International Conference on Materials for Advanced Technologies, Singapore (Singapore).

Sui T, **Sandholzer MA**, Landini G, Korsunsky AM. *Multi-scale modelling and diffraction-based characterization of elastic behaviour of human enamel.* 13th International Conference on Fracture, Bejing (China) published in: Proceedings of the 13th International Conference on Fracture, Beijing.

Sui T, **Sandholzer MA**, Baimpas N, Landini G, Walmsley AD, Lumley PJ, Korsunsky AM. *Ultrastructural changes in burnt dental tissue revealed by synchrotron X-ray scattering.* International Multi Conference of Engineers and Computer Scientists, Hong Kong (China) published in: Lecture Notes in Engineering and Computer Science (2), 775-779.

2012

Sandholzer MA*, Sui T, Korsunksy AM, Teschler-Nicola M, Landini G. *Ultra-structural evaluation of cremated teeth using small and wide-angle x-ray scattering (SAXS/WAXS).* 19th European Meeting of the Paleopathology Association, Lille (France).

Sui T, **Sandholzer MA**, Landini G, Korsunsky AM. *In situ SAXS evaluation of ultrastructural changes of human dental tissues with thermal treatment.* 14th CMA Conference on Materials Science and Engineering, Didcot (UK).

Sandholzer MA*, Walmsley AD, Lumley PJ, Landini G. *Heat-induced alterations of dental tissues: Implications for the identification of fire victims.* SkyScan User Meeting, Brussels (Belgium) published in: Micro-CT User Meeting Abstract Book, ISBN 978-90816781-0-0.

Robinson JP, Claridge E, Cooper PR, Grover LM, **Sandholzer MA**, Walmsley AD. *3D Slicer: A Free, Open Source Tool for 3D Image Registration.* SkyScan User Meeting, Brussels (Belgium) published in: Micro-CT User Meeting Abstract Book, ISBN 978-90816781-0-0.

2011

Sandholzer MA*, Baron K, Walmsley AD, Lumley PJ, Landini G. *Investigation on heat-induced alterations of skeletal hard tissue microstructure using x-ray microtomography.* 8th International Symposium Advances in Legal Medicine, Frankfurt (Germany) published in: Rechtsmedizin 2011(21):341–432.

Sandholzer MA*, Teschler-Nicola M, Walmsley AD, Lumley PJ, Landini G. *High-resolution micro-CT imaging as a novel tool in the analysis of cremated bones and teeth: A comparison of experimental results with Bronze Age human remains.* 13th Annual BABAO Conference, Edinburgh (UK).

Chapter 1 – Introduction

1.1. Structure and composition of teeth

The normal deciduous and permanent human dentition comprises of 20 and 32 teeth respectively, subdivided into anterior (incisors, canines) and posterior (premolars, molars) teeth. Although similar in tissue structure and composition, the size, morphology as well as the number of roots varies depending on the tooth type (Hillson, 1996).

Human teeth can be divided into the crown, which is normally exposed to the oral cavity, and the roots, which after eruption, are anchored to the alveolar bone of the jaws by means of the periodontal ligament (Higgins and Austin, 2013). The crown portion is covered by enamel, the hardest material in the human body. Enamel consists of approximately 96% inorganic material by weight (around 90% by volume), while the remaining 4% are made up by organic components and water (Boyde, 1989). The primary component of the inorganic phase in teeth is a calcium-deficient form of hydroxyapatite [$Ca_5(PO_4)_3(OH)$] with substitutions of chemical groups, often referred to as biological apatite or bioapatite (Elliott, 1994). The microstructure of enamel is formed of densely aligned enamel rods (6-8µm in diameter), with a keyhole-like section, allowing only very small particles to permeate through (Higgins and Austin, 2013, Meckel et al., 1965). In contrast to the enamel microstructure, the arrangement of the underlying crystalline structure is still part of ongoing investigations (Al-Jawad et al., 2012, Raue et al., 2012).

The root portion of a tooth is composed of dentine and is covered by cementum, which anchors it by means of the periodontal ligament to the alveolus of the tooth socket. Dentine consists of approximately 70% inorganic material, 20% organic material and 10% water by weight. The volume ratio of dentine equals approximately 47% inorganic material, 32% organic material and 21% water (Frank and Nalbandian, 1989). Similar to enamel, the inorganic phase is formed by biological apatite crystals, which are arranged in a collagen matrix. Dentinal tubules, 1 to 3µm in diameter, span across the entire dentine. The dentinal tubules are occupied by fluid and cellular processes of odontoblasts, the cells responsible for dentine deposition.

The odontoblasts are located in the pulp cavity, a richly vascularised and innervated connective tissue that also contains many other cell types, including fibroblasts, plasma cells, nerve fibres, immunocompetent cells, and undifferentiated mensenchymal stem cells (Higgins and Austin, 2013).

The unique structure, composition and location within the body make teeth extremely durable, even if the body is decomposed, exposed to trauma or high temperatures (Adams, 2003b). Tooth development and alveolar eruption are frequently used to estimate the age of individuals. Furthermore, over the course of a lifetime distinctive treatments and dental wear take place, influencing the appearance of the dentition, which becomes an individual physical feature frequently used in the determination of human identity in forensic contexts (AlQahtani et al., 2010).

1.2. The role of the dentition in the determination of human identity

1.2.1. Methods of human identification

The identification process of deceased individuals can be a major challenge, especially in mass fatality incidents. Positive identification is important for various reasons and can be achieved by forensic techniques such as fingerprints, deoxyribonucleic acid (DNA) and dental analysis. Besides the need to reconstruct the circumstances of an accident, crime or natural disaster the positive identification is of importance for criminal prosecutions and legal reasons such as inheritance, insurance or contractual obligations (Anderson et al., 2007, Cordner et al., 2011, Pretty and Sweet, 2001). Moreover, identification of the deceased is important for relatives going through the process of grieving, enabling closure in knowing that a loved one has been found (Berman et al., 2013). According to Pretty et al. (2013) between 2000 and 2010 over 500,000 people died in mass fatality incidents worldwide, caused intentionally (e.g. 9/11 in New York, 7/7 London terrorist attacks), natural causes (e.g. the 2004 and 2011 tsunamis in South-East Asia, Victorian bushfires in Australia) or accidental technical failures (e.g. Air France flight 447 in 2009) (Berman et al., 2013, Pretty et al., 2013, Senn and Weems, 2013).

In general, distinctions are made between ‘open’ and ‘closed’ disasters. An open disaster is referred as a ‘*major catastrophic event resulting in the deaths of a number of unknown individuals for whom no*

prior records or descriptive data are available' (Interpol, 2009). The actual number of victims is initially unknown; examples include the Kaprun cable car accident in 2000 (Meyer, 2003), the 2004 Boxing Day tsunami in South-East Asia (Schuller-Gotzburg and Suchanek, 2007) or the 1987 Kings Cross Underground fire in London (Brough, 1991). In contrast, a closed disaster is defined as '*a major catastrophic event resulting in the deaths of number of individuals belonging to a fixed, identifiable group (e.g. aircraft crash with passenger list)*' (Interpol, 2009). A combination of an open and closed disaster can occur when airplanes crash into residential areas, as in the case of the Concorde crash in 2000 (Air France flight 4590) or the Lockerbie bombing in 1988 (Pan Am flight 103) (Laborier et al., 2004, Moody and Busuttil, 1994).

According to the 2009 Interpol Disaster Victim Identification Guide, the primary and most reliable means of victim identification are fingerprints, DNA and dental analysis. Secondary means of identification include personal descriptions, medical findings/evidence (e.g. implanted surgical devices or surgical/traumatic scars) and clothing (Interpol, 2009). However, personal description and visual identification can lead to false positive or false negative identifications (Sweet, 2010). Nonetheless, circumstantial evidence of an event (e.g. body found in the missing persons' car), individual jewellery or tattoos can help during the identification process (Cordner et al., 2011, Dolinak and Matshes, 2005).

Fingerprints are unique soft tissue features and do not change throughout life, nonetheless skin destructions affecting the papillary layer might alter their appearance (Interpol, 2013). The identification by means of fingerprints requires *antemortem* records, often found in national and international fingerprint databases (Senn and Weems, 2013). In cases involving charred, fragmented or decomposed remains, fingerprint identification is often restricted or impossible (Adams, 2003b, Berman et al., 2013).

The genetic information encoded in the DNA is assumed to be unique for every person, with the exemption of identical twins. Investigators use primary DNA sources, such as blood or tissue samples (i.e. pap-smear tests, tooth remnants or hair roots), but also DNA collected from secondary DNA

sources like clothing, toothbrushes or combs, can be used to produce an individuals' record (Berman et al., 2013, Interpol, 2009, Sweet et al., 1999). Comparative DNA analysis can be performed in cases involving charred, fragmented or severely decomposed remains, to facilitate the identification of individual body parts (Interpol, 2009, Williams et al., 2004).

1.2.2. Odontological identification of human remains

Identification using dental records is an efficient, reliable, rapid and economical procedure, often used in combination with other means of identification (Schuller-Gotzburg and Suchanek, 2007, Senn and Weems, 2013, Sweet, 2010).

The uniqueness of dental features has been known since Roman times, so that even single teeth could be used for identification if containing sufficient unique features (Lipton et al., 2013, Sweet, 2010). If only three possibilities (unrestored, filled, or missing) would be considered per tooth of the adult dentition, the number of combinations would equal 3^{32}, or about 1.85×10^{15} (Clement, 1998). When besides the two possibilities of unrestored or missing teeth, all possible combinations of filled surfaces (mesial, occlusal, distal, facial, and/or lingual) are taken into account, there would be 33^{32}, or about 3.91×10^{48} possible combinations (Adams, 2003a). However, those statistical values are hypothetical, as they assume random occurrence and equal probability, whilst decay and treatment of teeth do not occur randomly. For example dental records of young people often show similar treatment patterns such as single-surface fillings of the first permanent molars (Clement, 1998). Adams (2003a, 2003b) included the frequency of occurrence of dental treatments in a large population sample and reported that even with a limited number of dental treatments a rare dental patterns can occur, comparable to that of the variability of mitochondrial DNA observed in humans.

1.2.3. Comparative dental identification

The odontological identification of human remains is a comparative process, by matching *antemortem* dental records and *postmortem* findings of the individual size, shape and acquired characteristics of the dentition (Clement, 1998, Sweet, 2010). Dental records used to correlate *antemortem* and *postmortem* findings can be obtained from written clinical notes, dental charts, dental radiographs, plaster casts, clinical computed tomography (CT) scans or photographs (Berman et al., 2013).

The processes involved in comparative dental identification in routine cases and mass fatality incidents are the same. Circumstances, personal belongings (e.g. passport, ID card, driving licence) or missing persons databases allow presumptive or tentative identification and are commonly followed by requests of dental records from the individuals' dentist (Pretty, 2007).

Antemortem records are most often available for patients from developed countries that regularly receive dental assessment, although the quality of such can play an important role in the comparison process. The dentist should provide all original dental records available, as duplicates might miss critical markers and notations (Sweet, 2010). The *postmortem* records normally consist of photographs, radiographs and dental charts (Pretty and Sweet, 2001, Wood and Kogon, 2010).

Depending on the preservation of the body, the American Board of Forensic Odontologists (ABFO) recommends to additionally take dental impressions (if applicable) and resection of the jaws (Berman et al., 2013). The resection of the jaws allows replicating angles found in *antemortem* radiographs. In general, the *postmortem* examination and comparative dental identification is performed by two forensic odontologists, each performing the dental examination with subsequent discussion on any unclear issues (Clement, 1998). In cases involving multiple fatalities, the dental team would normally use computer assisted dental identification systems, such as WinID3 or DAVID, to cut down the number of possible identification case. These software packages allow the entry of *antemortem* and *postmortem* records combined with an automatic comparison and internal ranking system of possible matches (Al-Amad et al., 2007).

In general, individuals with multiple dental restorations or rare features are easier to identify than those with little or no dental treatment (Pretty and Sweet, 2001). With increasing trends in oral health, growing numbers of patients have a low incidence of caries and consequently lack restorations which can make the identification process more difficult (Bernstein, 1998, Sweet, 2000).

Even in identification cases of children and adolescents, where none or only very little treatments and restorations are present, dental records should be collected and can still be of great value (Schuller-Gotzburg and Suchanek, 2007). During orthodontic treatments, dental casts are created that can give important information on the number and positions of teeth as well as on the morphology of the crown (Johansen and Bowers, 2012). One major influence on the identification process can be the long duration between the last *antemortem* visit to the dentist, additional dental treatment between two records or dental wear over time, requiring the judgement of a trained forensic odontologists to establish identification (Clement, 1998, Sweet, 2010). Nonetheless, even with incomplete dental records (e.g. missing written records or radiographs), forensic odontologists are commonly able to establish positive identifications as long as there are no unexplainable discrepancies (Table 1.1). For example, a missing tooth noted in *antemortem* records, but present *postmortem* can also be used to exclude a person (Pretty, 2007, Pretty and Sweet, 2001).

To enable a professional judgement of dental evidence, continuous professional training is necessary. Over the course of the last decade, especially following the 2004 Boxing Day tsunami in South-East Asia, international collaborations between forensic odontologists were established and national/international standards and guidelines were developed (Interpol, 2009, Lain et al., 2011, Schuller-Gotzburg and Suchanek, 2007, Senn and Weems, 2013, Sweet, 2010). The presence of country-specific dental treatments, various dental abbreviation/notation systems and notes in foreign languages also resulted in the creation of specialised national disaster victim identification (DVI) teams (Clement, 1998). Generally, guidelines for the dental identification such as the ‘Manual of Forensic Odontology’ are updated and adapted regularly and form the basis for the training of forensic odontologists (Herschaft et al., 2006, Senn and Weems, 2013).

Table 1.1 Four conclusions reached when reporting a dental identification (Berman et al., 2013)

Positive identification	The *antemortem* and *postmortem* data match in sufficient detail, with no unexplainable discrepancies, to establish that they are from the same individual
Possible identification	The *antemortem* and *postmortem* data have consistent features but because of the quality of either the *postmortem* remains or the *antemortem* evidence, it is not possible to establish identity positively
Insufficient evidence	The available information is insufficient to form the basis for a conclusion
Exclusion	The *antemortem* and *postmortem* data are clearly inconsistent

1.2.4. The role of imaging in dental identification

In 1897, a fire during a society charity event in Paris killed 126 people, and as the thermal damage made visual identification impossible, dentists assisted in fire victim identification using dental records (Botha, 1986). In 1943 the first use of dental radiography in a forensic identification case was recorded. Since then, X-ray imaging played a vital role in the identification process due to the accurate recording of dental features and anatomical landmarks (Andersen et al., 1995, Bernstein, 1998, Lipton et al., 2013, Pretty et al., 2013). Knight (1984) noted that *'dental radiography is probably the most important forensic use of radiography, measured in numbers of cases'*. Currently, most commonly bitewing, peri-apical and panorama radiographs are used for dental identification (Beck, 2011, Pallagatti et al., 2011). Yet one of the main disadvantages of standard radiographs is projection geometry causing distortion and magnification of the image (Berketa et al., 2010). In general, the use of digital radiography and computer-based archives changed the process of comparative dental identification, allowing the enhancement of radiographs and robust backup of *antemortem* and *postmortem* data (Pretty et al., 2013).

Since the mid-1970s computer-aided identification systems are used to facilitate comparisons (Al-Amad et al., 2007). Automated computer-assisted comparison of dental radiographic features has been tested extensively but they are strongly dependent on the radiographs' quality (Jain and Chen, 2004, Lin et al., 2012, Nomir and Abdel-Mottaleb, 2007). Recent comparative approaches successfully used three-dimensional (3-D) dental biometrics for comparative dental matching (Zhong et al., in press).

In the last decade, CT imaging became of increasing importance in forensic radiography (Bassed and Hill, 2011, Silva et al., 2011, Thali et al., 2003). The CT approach provides non-invasive high-resolution images that enable to create 3-D models of the human body. Besides virtual autopsies (Baglivo et al., 2013), CT imaging has been effectively used for the identification of victims of the 2009 Victorian bushfires (Bassed et al., 2011, Bassed and Hill, 2011). Thali et al. (2006) and Jackowski et al. (2006a) noted that clinical CT scans provide appropriated records for dental identification, enabling the rapid creation of *postmortem* documentation of the dental structures.

More recently, cone-beam CT (CBCT, a high-resolution CT for craniofacial structures) has been used for dental age estimation (Maret et al., 2011). In contrast to conventional radiography, CT technology also allows the differentiation of filling materials (composite, amalgam, ceramic, temporary fillings) based on their radiopacity (Jackowski et al., 2006b). However, the precise determination of the dental restoration material, i.e. composition, is not possible at the current stage of research (Bassed and Hill, 2011). With a growing numbers of patients lacking dental restorations, other features, like the crown and root morphology need to be considered in *antemortem-postmortem* comparisons (Bernstein, 1998, Savio et al., 2006, Sweet, 2000). Current clinical CTs and CBCTs have a spatial resolution of approximately 1mm and 0.1mm respectively, allowing the visualisation of the dental morphology and structures. Although the resolution and quality of clinical CTs and CBCTs constantly evolve, when X-rays interfere with metal-containing restorations streak artefacts occur, reducing the image quality (Jackowski et al., 2006b, Thali et al., 2006). Beck (2011) noted that conventional intra-oral radiographs are likely to remain the cornerstone of dental identification until significant improvement of metal artefact reduction algorithms for the various CT systems are made. Such algorithms have since been developed, and need to be integrated into the software of future imaging systems (Tohnak et al., 2011).

1.3. Odontological identification of fire victims

Burned dental remains are frequently found after natural disasters, airplane crashes or house fires, as a result of either direct contact with open flames or the exposure to high temperatures (Bush and Bush, 2011, Lain et al., 2011, Savio et al., 2006). Especially in cases of prolonged fires with temperatures above 700°C, dental analysis stands alone as other materials used as primary (fingerprints and DNA) or secondary (e.g. clothing) means of identification are often destroyed (Fairgrieve, 2008, Hill et al., 2011a, 2011b).

Andersen et al. (1995) classified six grades of fire injuries to teeth and jaws: (0) no injury, (1) injury to anterior teeth, (2) injury to anterior and posterior teeth (unilaterally), (3) injury to anterior and posterior teeth (bilaterally), (4) fragments of jaw bone including teeth and/or roots, and (5) no dental

remains. In their review of 292 single fire cases, the authors stated that 25% of the cases led to severe damage of the dentition (grade 2-5). Bohnert et al. (1998) listed the effects of fire on the skull more specifically, based on observations of cremations carried out at 670° to 810°C. After 8 to 10 minutes, the facial soft tissue is charred and only sparse soft tissue remains visible; after 20 minutes prominent parts of the facial skull are destroyed. Similar observations were reported by other experimental crematoria-based studies (Fairgrieve, 2008, Günther and Schmidt, 1953).

Posterior teeth tend to be better preserved than anterior teeth due to their size and the heat protection, offered by the tongue, layers of skin, mucosa, muscle and adipose tissue and are therefore more likely to be used in the odontological identification process (Berketa, 2013). During the cremation process in modern crematoria, for the first 10 to 24 minutes, the soft tissue protection keeps the temperature inside the oral cavity as low as 87°C, depending on the nutritional state of the body, age, temperature and time of exposure (Schweitzer and Eichenhofer, 1980). Lain et al. (2011) and Bush and Bush (2011) reported, that teeth shrink and are often removed from their anatomical position as an effect of extensive heat exposure. Posterior teeth with multiple roots tend to remain in the alveolar bone sockets, whilst single-rooted are mostly found isolated (Günther and Schmidt, 1953).

Currently, comparative dental identification is the most reliable and frequently applied identification method in cases involving high temperature exposure (Bernstein, 1998, Jablonski and Shum, 1989, Lain et al., 2011, Savio et al., 2006). The positive identification and investigation of severely burned human remains requires careful examination, forensic experience and excellent skills in comparative dental anatomy (Lain et al., 2011). Since the thermal stress or the surrounding environment (e.g. destroyed airplane, collapsed building) can lead to extreme fragmentation of the skeletal remains, investigators are often confronted with isolated teeth or fragments thereof (Hill et al., 2011b, Lain et al., 2011). The dental remains should be photographed *in situ* and examined by a forensic odontologist, before the body is moved. Great care is necessary to ensure a proper recovery to eventually facilitate dental identification.

The use of clearly labelled padded containers is recommended after fixing the remains with clear acrylic spray paint, hair spray or cyanoacrylate (Griffiths and Bellamy, 1993, Hill et al., 2011b, Mincer et al., 1990, Schmidt, 2008).

Griffiths and Bellamy (1993) suggested that multiple radiographs should be taken to replicate possible *antemortem* records. Whilst Bush and Bush (2011) noted that standard radiographs of isolated burned dental remains (without structural relationship of the jaws) only provide little information for comparative dental radiography, Hill et al. (2011b) emphasised that crucial evidence can still be obtained from burned dental remains and a number of significant radiographic details are conserved. Future investigations of fire victims are likely to involve CT imaging, as it allows the examination without interference of the body and digital storage of information for later evaluation (Woisetschlager et al., 2011).

The identification rate of fire victims in mass disasters can be highly successful. As early as 1949, 72 of the 119 victims of a fire on board of a steamship could be identified using dental radiographs (Bernstein, 1998). All 155 victims of the Kaprun cable car fire were identified within 19 days, and 112 of the 113 victims of the Concorde disaster were identified by dental means (Laborier et al., 2004, Meyer, 2003). In contrast, after the 1984 Victorian bushfires only 64% of the 22 victims could be identified by dental means, as the access, presence or quality of patient records was limited (Bastiaan, 1984).

1.3.1. Dental restorative materials as an aid in fire victim identification

In general, skeletal hard tissue can endure temperatures of up to 1600°C, with dental remains often being the only remnants (Clement, 1998, Holden et al., 1995). Besides dental remains, other medical or dental artefacts (e.g. orthopaedic/prosthetic devices) can give additional information to provide positive victim identification (Bonavilla et al., 2008, Matoso et al., 2013, Warren, 2008).

Metal implants and restorations can resist mechanical and thermal influences, and can aid in the identification process (Berketa et al., 2011, Berketa et al., 2010, Berman et al., 2013).

The melting points of common dental restorative materials are given in Table 1.2, emphasising the importance of dental restorative materials as an aid in identification cases involving temperatures above 1000°C.

Merlati et al. (2002, 2004) observed that dental prostheses and dental restorations are able to resist even higher temperatures than theoretically predicted and that the composition of fragments can be identified using scanning electron microscopy (SEM). The composition and properties of metal alloys of prosthetic work can also be used to determine the country of origin (Marella and Rossi, 1999). Depending on their composition, dental braces used for orthodontic treatments can survive 700 to 980°C, making them also potentially useful for identification of adolescent individuals (Campobasso et al., 2007). Additionally, marking of dentures and prostheses could facilitate and support the matching process, however the prevalence of denture marking is generally low (Andersen et al., 1995, Murray et al., 2007, Taylor et al., 2002). Besides metal-based materials, root canal filling materials can survive prolonged heat exposure and may be used in the identification process (Campobasso et al., 2007, Hill et al., 2011b). Although the high temperatures lead to altered colour and appearance of the dental restorative materials, they are able to resist temperatures of up to 1200°C (Brandao et al., 2007, Moreno et al., 2009, Patidar et al., 2010).

To classify and determine the composition of composite resins and root canal fillings mainly energy dispersive X-ray spectroscopy (EDS) and X-ray fluorescence (XRF) have been used (Bonavilla et al., 2008, Bush et al., 2006, Bush and Bush, 2010, 2011).

Aside from invasive analytical techniques, heat-induced alterations in dental materials have been analysed with X-ray imaging, reporting the specific behaviour of filling materials and metal implants including their changes in morphology and radiological appearance (Berketa et al., 2011, Rossouw et al., 1999, Woisetschlager et al., 2011).

Table 1.2 Melting points of dental restorative materials [adapted from Berketa et al. (2010), Berman et al. (2013), Norrlander (1995), and Purves (1975)]

Dental restorative material	Melting point
Gold crown alloys	870-1090°C
Base metal alloys	1275-1500°C
Porcelain/metal alloys	1150-1260°C
Porcelain low fusing	760-980°C
Porcelain medium fusing	1090-1300°C
Porcelain high fusing	1300-1400°C
Chrome/cobalt alloy	1370-1570°C
Titanium implant	> 1600°C
Silver amalgam	Hg in silver amalgam begins to vaporise at 100°C. Metals of the silver alloy (Ag, Cu, Zn and Sn) melt over a wide range from 230-980°C.
Composite restorations	Organic materials evaporate at relatively low temperatures; inorganic components withstand temperatures well over 1090°C.
Acrylic resins	Melting at 110°C, incineration >540°C

1.4. Experimental approaches for the analysis of burned dental remains

When providing relevant information to support the identification process, it is essential to characterise and comprehend any material and dental tissue changes that take place in high-temperature conditions.

Burned dental remains found at crime scenes or as part of archaeological excavations might have been exposed to a wide range of temperatures. Whilst the average temperature of a wooden campfire is in the range of 400 to 700°C, house fires can reach around 700 to 900°C (Fairgrieve, 2008, Norrlander, 1995, Shipman et al., 1984). The temperatures of burning motor vehicles range between 800 and 1100°C, especially when involving petrol (Berketa et al., 2011, Merlati et al., 2002). Crematoria operate between 900 and 1000°C, whilst natural fire storms were recorded to reach up to 2000°C (Bastiaan, 1984, Hill et al., 2011b, Norrlander, 1995). The presence of combustible material and oxygen availability determines the durations and peak temperatures of fires (Fairgrieve, 2008). Many fires have been reported to smoulder for days or even weeks after the event. Examples include the Victorian bushfires and the World Trade Centre after the 9/11 attacks (Berketa et al., 2011, Hill et al., 2011b, Walker et al., 2008). The lab-based experimental approaches generally do not take the fire behaviour into account, as the fire is often divided into multiple phases and can increase by 400 to 800°C within 5 minutes in house fires and ritual cremations (Dent et al., 1995, Dodwell, 2012, Shipman et al., 1984).

McKinley (2000) and Symes et al. (2008) showed that there is also a great variation in peak temperatures in different parts of the body depending on the placement of the body, topography of the surrounding environment and presence of fire accelerants.

Mayne-Correira (1997) highlighted that the inconsistency in terminology and lab-based experimentation with a variety of skeletal materials has produced disparate conclusions regarding the analysis of burned human remains. This is also reflected by an evaluation of lab-based heating regimes used to model thermal stress in human teeth and dental materials (Table 1.3). A constant

exposure to a temperature should be comparable to the sudden thermal shock generated by fires or explosions, whilst an incremental temperature increase approach should model the slower increase in temperature due to the presence of soft tissues (Bohnert et al., 1998, Muller et al., 1998). Most research on dental tissues has been based on laboratory-based heating regimes that can be grouped into these two ‘subtypes’. These are either constant exposure at a certain temperature for a fixed duration or an incremental temperature increase to a specific target temperature. Moreover, there are also differences regarding the cooling regime used, with the majority of publications stating the immediate removal of the specimens from the heating device, or allowing cooling down overnight. Nonetheless, the influence of the different heating and cooling regimes on the macroscopic, compositional, structural and crystalline alterations of dental tissues has yet not been investigated.

Table 1.3 Comparison of 17 lab-based heating protocols for human teeth and dental restorative materials. Types of cooling (Type 1: removed from heating device and cooled in air to room temperature (RT); Type 2: left overnight to cool down)

	Study subject	Temperature increase	Temperature range	Time of exposure	Type of cooling
Beach et al. (2008)	32 sound teeth (permanent dentition)	N/A	204°C to 593°C	30/60min	N/A
Bonavilla et al. (2008)	16 teeth (endodontically treated)	N/A	900°C	30min	N/A
Burns (1987)	46 samples (mandibles, permanent dentition)	N/A	500°C, 950°C	90min	Type 1
Bush and Bush (2010)	2 mandibles, 2 maxillae	N/A	1010°C	150min	Type 2
Bush et al. (2006)	5 teeth (10 composite resins)	N/A	900°C	30min	N/A
Fereira et al. (2008)	30 sound teeth (permanent dentition)	18.8°C/min	1150°C	60 min (RT-1150°C)	Type 1
Fereira Paz et al. (2010)	140 sound teeth (permanent dentition)	18.8°C/min	250°C to 1150°C	28.5 min (13.5min to 250°C, maintained 15min) to 77.2 min (62.2 min to 1150°C, maintained 15min)	Type 1
Karkhanis and Franklin (2009)	90 human teeth (deciduous dentition)	N/A	100°C to 1100°C	30min	Type 1
Merlati et al. (2002)	18 teeth (12 treated, 6 control) 24 crowns/bridges (18 fixed, 6 removable)	30°C/min	200°C to 1100°C	6.6 min (RT-200°C) to 36.6 min (RT-1100°C)	Type 1
Merlati et al. (2004)	100 teeth (75 with restorative fillings, 25 control)	30°C/min	200°C to 1100°C	6.6 min (RT-200°C) to 36.6 min (RT-1100°C)	Type 1
Moreno et al. (2009)	200 human teeth (150 with restorative fillings, 50 control)	10°C/min	200°C to 1200°C	N/A	Type 1
Muller et al. (1998)	58 sound teeth (permanent dentition)	N/A	150°C to 1150°C	60min	Type 1
Myers et al. (1999)	66 sound teeth (permanent dentition)	N/A	300°C to 750°C	30/60/90min	Type 1
Patidar et al. (2010)	72 teeth (60 restorative fillings, 12 control) 2 mandibles	N/A	400°C to 1150°C	5/15/30min	N/A
Rossouw et al. (1999)	28 samples (4 different restorative fillings)	N/A	260°C to 500°C	5/15/30min	N/A
Savio et al. (2006)	90 teeth (60 endodontically treated, 30 control)	30°C/min	200°C to 1200°C	6.6 min (RT-200°C) to 36.6 min (RT-1100°C)	Type 1
Woisetschlager et al. (2011)	122 molars (with 10 different restorative materials)	N/A	200°C to 1100°C	4.0 min (RT-200°C) to 208.2 min (RT-1100°C)	Type 1

1.5. Heat-induced alterations of skeletal hard tissue

Extensive research has been carried out on the effects of high temperatures on animal and human bone, with the general assumption that heat-induced alterations of teeth were similar (Mayne-Correira, 1997, McKinley, 2000, Thompson, 2004, Ubelaker, 2009).

Mayne-Correira (1997) and Thompson (2004) categorized four transformation stages during the cremation process of bone, and reported the major heat-induced alterations and corresponding temperature ranges (Table 1.4). During the dehydration stage, water in the bone tissue is lost due to the breaking of hydroxyl (OH^-) bonds and also fracture patterns occur. During the decomposition stage organic components are lost, leading to further weight loss as well as colour changes. Moreover, this stage was associated with more brittle bone. During the inversion and fusion stages, the bone crystalline structure changes lead to shrinkage. The temperature ranges in Table 1.4 result from lab-based studies of bone, yet dental tissues are likely to react differently due to their morphological, structural and compositional characteristics. Therefore, the present work aims to investigate and clarify these differences.

Table 1.4 Four stages of heat-induced transformations in bone reported by Mayne-Correira (1997) and Thompson (2004)

Stage of transformation	Evidence	Temperature range (Mayne-Correira 1997)	Temperature range (Thompson 2004)
Dehydration	Fracture patterns; weight loss	100 to 600°C	100 to 600°C
Decomposition	Colour change; weight loss; reduction in mechanical strength; changes in porosity	500 to 600°C	300 to 800°C
Inversion	Increase in crystal size	700 to 1100°C	500 to 1100°C
Fusion	Increase in mechanical strength; reduction in dimensions; increase in crystal size; changes in porosity	1000°C +	700°C +

1.5.1. Macroscopic alterations of burned dental remains

1.5.1.1. Morphology

In bone, heat-induced warping and deformation can occur at high temperatures, yet these morphological changes have not been described for human teeth (Gonçalves et al., 2011, Karkhanis and Franklin, 2009, Shipman et al., 1984, Thompson, 2005).

The crown tends to separate from the root and shatter at elevated temperatures, referred to as 'popping off' due to the characteristic sound frequently encountered during experimental studies (Purves, 1975). This phenomenon has been described in crematoria as well as lab-based experiments, at various temperatures. Muller et al. (1998) and Beach et al. (2008) indicated that the crown becomes extremely friable and likely to shatter after heating teeth for 30 to 60 minutes at around 450°C, whilst Merlati et al. (2002) reported the shattering of the enamel at 800°C when heating up the teeth slowly.

The separation of the crown and shattering of the enamel has been explained by the different thermal properties and shrinkage rates of dentine and enamel (Figure 1.1). This leads to heat-induced stress along the dentine-enamel junction followed by the 'popping off' of the enamel (Brown et al., 1970, Hughes and White, 2009, Lin et al., 2010a, Lin et al., 2010b). Besides the different thermal properties of dentine and enamel, the boiling and steaming of water in the dentinal tubules has been considered to be responsible for the 'popping off' phenomenon as well (Botha, 1986).

In contrast to the crown, the morphology of the root portion has been reported to not change extensively (Endris and Berrsche, 1985). Superficial and internal cracks in the dentine start to appear around 600°C, resulting in increased fragility (Muller et al., 1998). The increase of cracks at higher temperatures has been shown in histological sections, dental radiographs and micro-computed tomography (micro-CT) models (Fereira et al., 2008, Fereira et al., 2010, Sandholzer et al., 2014, Savio et al., 2006).

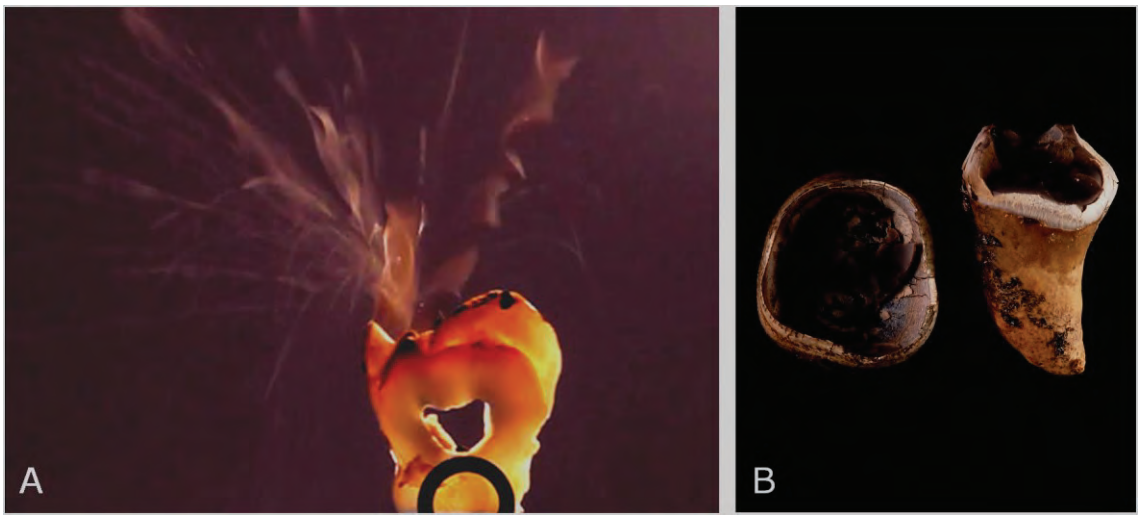

Figure 1.1 Heat-induced failure of dentine-enamel junction

(A) Shattering of enamel at 450°C visualised in a tooth section heated over a Bunsen burner flame

(B) Separation of complete crown from the root section after constant exposure for 30min at 500°C.

Scanning electron microscopy has been previously used to investigate the differences of heat- and trauma-induced cracks, indicating that it is not possible to compile traumatic and heat-induced fractures in dental tissues (Campbell and Fairgrieve, 2011). These cracks can be explained by the dehydration and loss of organic matrix in the dentine, making the dentine more fragile. Hughes and White (2009) indicate that cracks are likely to be caused by the intertubular tensile stress, but also a spontaneous evaporation of water or rapid cooling could be responsible. Moreover, SEM studies found that the dentinal tubules diameter is reduced as a consequence of high temperatures (Harsanyi, 1975, Karkhanis and Franklin, 2009, Muller et al., 1998), whilst Shipman et al. (1984) found an enlargement of tubules; a discrepancy that could be explained by the biological variation of tubule diameters, as well as the number and location of SEM measurements. The typical keyhole-shaped section of enamel prisms can still be identified in fragments of enamel that were heated at 1000°C, allowing the microscopic identification as enamel (Yamamoto et al., 1990).

Generally, the knowledge on the preservation of distinct morphological features of the dentition such as root curvature and pulp chamber morphology are important for fire victim identification, especially in the absence of dental restorations or implants (Sweet, 2010). Most studies dealing with heat-induced alterations of dental tissues reported none or only minimal morphological alterations for temperatures up to 1100°C (Beach et al., 2008, Endris and Berrsche, 1985, Merlati et al., 2002). The melting of teeth into atypical, globular formations has been reported between 1300 and 1600°C (Clement, 1998, Harsanyi, 1975).

1.5.1.2. Surface colour

The main macroscopic feature of burned dental remains is the gradual change in surface colour (Figure 1.2). Temperature-dependent shifts from the roots' natural pale yellow colour to black, brown, greyish-blue, chalky-white and finally white-pink have been reported (Fairgrieve, 2008, Karkhanis and Franklin, 2009, Moreno et al., 2009). The surface colour changes in enamel are more subtle from natural pale yellow colour to pale brown, light grey and white (Karkhanis and Franklin, 2009).

Figure 1.2 Heat-induced surface colour alterations of teeth

Progressive, temperature-dependent shift from the roots' natural pale yellow colour to black/dark brown (400°C), brown (500-600°C), greyish-blue (700°C), light grey (800°C), chalky-white (900°C) and white/pink (1000°C).

This figure is reprinted from Sandholzer et al. 'Radiologic evaluation of heat-induced shrinkage and shape preservation of human teeth using micro-CT' Journal of Forensic Radiology and Imaging 2013; 1(3), p.107-111, with permission from Elsevier.

The surface colour changes of burned teeth have been previously associated with the loss of organic content (Endris and Berrsche, 1985, Merlati et al., 2002, Moreno et al., 2009). Moreover, the combustion of chemical groups in the mineral phase and defects in the crystal lattice of biological apatite can lead to alterations of the surface colour (Berzina-Cimdina and Borodajenko, 2012). In general, colour changes help to deduce a temperature range to which skeletal remains have been exposed, but were found to be influenced by temperature, duration, oxygen availability and other external factors (Herrmann, 1972, Shipman et al., 1984, Walker et al., 2008).

Besides a simple description of colours (Muller et al., 1998), various researchers used the 'Munsell Soil colour chart' or similar colour catalogues for the description of the root and enamel surface colour, giving some limited selection of the colour variation that is present in heat-affected teeth (Beach et al., 2008, Endris and Berrsche, 1985, Karkhanis and Franklin, 2009, Shipman et al., 1984). In general, the description and determination of colours is highly subjective and also dependent on various external factors, including the positioning of the observer or the illuminant (i.e. the light source). Besides these aforementioned descriptive studies, flatbed scanners, digitalised photographs and spectrophotometry have been used to document colour alterations of skeletal tissue (Beach et al., 2008, Fereira et al., 2008, Walker et al., 2008). Quantitative colorimetric measurements would be favourable to document colour alterations, however most of those previous approaches lacked appropriate standardisation or system calibration.

Nonetheless, subjective descriptions of colours and inconsistency in experimental approaches have resulted in highly disparate conclusions regarding colour alterations. Besides the duration of heat exposure, the heating/cooling regime and presence of soft tissue might influence the colour alterations of teeth, but this has not yet been investigated.

1.5.1.3. Shrinkage

In addition to surface colour changes, shrinkage is another aspect that has to be taken into account when analysing burned dental remains. Heat-induced dimensional changes in animal and human bone have been previously described, however very limited data is available on the heat-induced dimensional changes of human teeth. The amount of bone shrinkage studied in laboratory and field experiments, is reported to be in the range of 0.5 to 27% (Buikstra and Swegle, 1989, Großkopf, 2004, Thompson, 2005, Ubelaker, 2009). Most of these studies evaluated shrinkage using calliper measurements, with the shrinkage rate reported either as linear/two-dimensional (2-D) or volumetric/three-dimensional (3-D) shrinkage, leading to this high variability of reported results. Moreover, the experimental conditions as well as structural and mineral composition of the skeletal material are the likely key variables determining the rate of shrinkage.

As early as 1875, heat-induced shrinkage of craniofacial structures has been mentioned in the literature (von Hofmann, 1875). The experimental studies that followed were mainly descriptive, reporting that teeth shrink considerably and are often found to be removed from their anatomical position (Norrlander, 1995). In general, the rate of shrinkage of teeth has been assumed to be similar to that in bone (Shipman et al., 1984).

A linear shrinkage of 1.4 to 2% was described for dentine when dried in nitrogen atmosphere at 60 to 100°C (van der Graaf and Ten Bosch, 1993). The linear shrinkage of dentine was reported to be 6% after an experimental cremation, however no details about the experimental conditions were presented (Dijkstra, 1938). Kindler was the first to specifically investigate the shrinkage of teeth over a larger range of temperature, reporting a grading system of minimal, minor and definite shrinkage (Kindler 1978, cited by Großkopf 2004). An estimate of 20 to 25% heat-induced shrinkage of teeth was reported by Maples and Browning (1995). Nevertheless, quantitative data on the heat-induced shrinkage of human teeth has not yet been reported and would add relevant information for comparative dental radiography of isolated teeth and fragments.

1.5.2. Destruction of organic components

Investigations on the effects of high temperatures on teeth also provide important information on the preservation of organic components, such as the collagen matrix and DNA. The organic constituents contribute to approximately 20% of the tooth weight, chemically predominately consisting of collagen type 1, CO_3^{2-}, NH, CH_3-CH_2, C=O, and C-H functional groups (Elliott, 1994, Reyes-Gasga et al., 2008).

Fourier-transformed infrared spectroscopy (FTIR) can provide information on the thermal alterations and destruction of organic constituents. This technique is based on the measurements of vibrations of molecule bonds as an infrared (IR) beam is interfering with the sample. Each molecule bond shows characteristic peaks or bands of absorbance at particular wavelengths within the IR spectrum that can be compared with databases of known substances. For studies on heat-affected skeletal tissue, the mid-IR region (4000 to 400 cm^{-1} wavelength) is normally used. This region contains the main peaks/bands for phosphates (PO_4^{3-}) of the mineral phase, as well as carbonates (CO_3^{2-}) and other components of the organic phase (Hollund et al., 2013, Thompson et al., 2009). Carbonates can be used to track the loss of organic material during the heating process, as the peaks/bands decrease at elevated temperatures. Whilst compositional alterations in burned animal and human bone have been previously investigated using FTIR (Hollund et al., 2013, Mkukuma et al., 2004, Thompson et al., 2009), there is only limited FTIR data available for heat-induced alterations up to 600°C in human dental tissues (Reyes-Gasga et al., 2008). Additional FTIR studies, including real-time approaches, could be used to further understand the heat-induced destruction of organic components.

Collagen is thought to have similar thermal properties as DNA, and has previously been used to investigate DNA preservation at elevated temperatures (Mayne-Correira, 1997, Walker et al., 2008). Whilst soft, non-mineralised collagen melts and forms gelatine when heated to 60°C, mineralised collagen remains more or less unchanged at these low temperatures (Holden et al., 1995). Histological sections of heat-affected bone showed some collagen structures were still present at 500°C, with

collagen fibres starting to denature and alter their appearance at 100°C (Fernandez Castillo et al., 2013a, Fernandez Castillo et al., 2013b).

Several studies have been conducted on the extraction of DNA from heat-affected teeth, reporting disparate results. Duffy et al. (1991) isolated dental pulp cells from dental remains, stating that teeth exposed for 1h at 100°C could not be used for sex determination anymore. Exposing teeth for 2min to a Bunsen burner flame (no temperature details reported) also led to the complete loss of high- and low-molecular-weight DNA in teeth (Schwartz et al., 1991). With improvements in DNA analysis, and the introduction of the polymerase chain reaction (PCR) amplification, pulpal DNA was successfully extracted from isolated animal teeth that had been exposed at 525°C for 15min (Rees and Cox, 2010). Although DNA preservation strongly depends on soft tissue protection, duration and temperature of the fire, modern techniques generally enable sex determination for remains exposed up to 300 to 400°C (Barker et al., 2008, Williams et al., 2004). Von Wurmb-Schwark et al. (2005) do not recommend post-cremation genetic analysis of modern cremations, as no DNA is preserved. Da Silva et al. (2012) recently confirmed this recommendation, as extraction of genomic dental DNA using PCR was not possible at any of the periods (10, 30 and 60 min) and temperatures (600, 800 and 1000°C) analysed.

1.5.3. Crystalline alterations

Whilst organic material denatures at elevated temperatures, mineral structures are generally well preserved. By using high-magnification SEM or transmission electron microscopy (TEM) morphological changes of the hydroxyapatite (HAp) crystals can be visualised (Reiche et al., 2002). Shipman et al. (1984) categorised the changes in HAp morphology in dentine and enamel, indicating a trend of increasing crystallite size and more smooth appearance at elevated temperatures. Similar trends were also reported for heat-affected bone (Holden et al., 1995).

Unaltered bone tissue shows a low crystallinity with small HAp crystals and high lattice strain, whilst heat-affected tissue shows an increase in HAp crystal size and lower lattice strains. The crystallinity index (CI) is a ratio of two intensity peaks of HAp, and gives information about the mean changes in crystal size and microscopic structural order of tissue (Hollund et al., 2013, Reiche et al., 2002, Squires et al., 2011, Thompson et al., 2013, Thompson et al., 2011). The CI can be quantified by FTIR, X-ray diffraction/scattering (XRD or wide angle X-ray scattering, WAXS) and Raman spectroscopy, and is frequently reported in literature. However, the CI does not characterise individual crystalline features (e.g. size, morphology) and may fail to describe adequately the complexity and heterogeneity of heat-induced processes (Hollund et al., 2013, Piga et al., 2008, Piga et al., 2009, Rogers et al., 2010).

Wide angle X-ray scattering analysis is capable of showing distinct differences in crystallite size, enabling reliable cremation temperature estimations (Hollund et al., 2013, Piga et al., 2008, Shipman et al., 1984). Most of the research to date has focused on the heat-induced compositional and structural alterations of bone tissue (Beckett et al., 2011, Hiller et al., 2003), with only very limited data about the changes in dental tissues (Piga et al., 2009). The XRD analysis of heat-affected human bone and teeth showed that HAp derived from bone and teeth react differently to heat, implicating that those tissues have to be separately investigated when a precise temperature estimation is desired (Piga et al., 2009).

Small angle X-ray scattering (SAXS) can provide additional information about the mean crystallite thickness, degree of alignment and shape of crystallites (Hiller and Wess, 2006). Lab-based SAXS was successfully used to characterise the heat-induced alterations of crystallite size in archaeological and experimentally altered bone (Etok et al., 2007, Hiller and Wess, 2006). However, there is no SAXS data available for heat-affected dental tissues. Further analytical approaches, combining X-ray scattering techniques could be used to investigate the heat-induced alterations of dentine and enamel, in order to develop a structural reference for heat-affected dental tissues.

1.6. Aim and objectives

The overall aim of the present work was to investigate the influence of duration of heat exposure and heating regimes regarding the macroscopic, compositional, structural and crystalline alterations of dental tissues. This aim was addressed by means of the following objectives:

- Investigation of heat-induced destruction of organic structures using high-precision measurements of weight loss (analytical scale, TGA) and compositional alterations (FTIR); including a real-time FTIR approach (Chapter 3)
- Analysis of colour alterations using quantitative colorimetric measurements (Chapter 4)
- Quantification of heat-induced structural alterations using conventional radiography and micro-CT imaging to characterize morphological preservation, shrinkage and fracture formation (Chapter 5)
- Analysis of heat-induced crystalline alterations of dentine and enamel using synchrotron-based X-ray scattering (SAXS/WAXS) analysis; including real-time approaches (Chapter 6).

Chapter 2 – Materials and Methods

2.1. Sample preparation

The sample material consisted of 215 freshly extracted premolars (n=90) and molars (n=125) that were disinfected in 15mM sodium azide solution and washed under running water for 5 to 6 hours and then mechanically cleaned to eliminate soft tissue residues. Teeth that showed signs of damage (e.g. broken roots, visible cracks in enamel), endodontic treatments, restorations or caries were excluded from the study. Before experimentation, the samples were stored in a freezer at -20°C for up to 4 weeks. The teeth were taken out of the freezer 2 to 3 hours before the heating experiments and kept in phosphate buffered saline (PBS) solution according to Jameson et al. (1993). Upon examination with X-ray micro-computed tomography (Chapter 2.5.2) no cracks within the dental tissues were observed previous to the experiments. Details such as age and sex of the patients from which the teeth were obtained remained anonymous as part of confidentiality regulations as required by the ethical approval from the National Research Ethics Committee (NHS-REC reference 09.H0405.33/ Consortium R&D No. 1465).

The FTIR, TGA and X-ray scattering experiments required bucco-lingual cross-sections and cubic samples. Therefore 1 to 3mm cross-sections were cut using an Isomet low speed diamond saw (Buehler Ltd., Lake Bluff, Illinois, USA). Subsequently, a Phoenix Beta variable speed grinding/polishing machine (Buehler Ltd., Lake Bluff, Illinois, USA) was used with a series of grinding papers (P800 to P2400) to further polish the samples. A digital calliper (0.03mm precision) was used to assess the dimensions of the specimens during the sample preparation.

To investigate the thermal alterations of the organic dental components using TGA, cubic dentine samples (3×3×3mm) were placed in a rotating 10% formic acid bath for 14 days to eliminate the mineral content.

2.2. Photography and video imaging

To document the sample preparation, experimental conditions and surface colour alterations, digital photographs were taken with a Nikon D40 digital single-lens reflex (DSLR) camera (Nikon, Tokyo, Japan), with a range of lenses (Nikkor AF-S DX 18-55mm 1:3.5-5.6; Nikkor 50mm 1:1.4; Sigma 105mm 1:2.8 DG Macro). The pictures were taken with a neutral colour setting in sRGB colour space and saved by the camera in RAW (uncompressed) and JPG (1:4 compressed). For photographs of the sample preparation and experimental setup the focus, shutter speed and aperture were adjusted depending on the light situation. For the documentation of the surface colour alterations, the DSLR was mounted on a camera stand and uniform lighting was created using two 50W spiral photo lamps (Tabletop Lighting Kit, Smick Trading, UK). The samples were placed on a glass plate elevated 5cm from a piece of green or black felt background. To reduce reflections of the glass surface, a Hoya circular filter (Tokina Co., Ltd., Japan) was used. An elongated exposure time (1/10s) and low aperture (f 16) ensured that the background appeared uniform and facilitated the subsequent image analysis (Section 2.8.1). For colour and size calibration of the images, a Gretag Macbeth Color Checker Chart (X-Rite Inc., Grand Rapids, USA) as well as a metric tape were used. The heat-induced failure of the dentine-enamel junction was filmed at 24 frames per second with a Nikon P7000 digital camera (Nikon, Tokyo, Japan) in AVI video mode.

2.3. Scanning electron microscopy (SEM)

Changes in the dental microstructure were analysed with scanning electron microscopy (SEM). The samples were coated with a gold layer using an Emitech 550X sputter coater (Emitech Limited, Ashford, UK) to make the sample conductive for electrons and prevent charging. A JEOL JSM-5800LV (JEOL Ltd., Tokyo, Japan) operated in high-vacuum mode at 20kV accelerating voltage and a Zeiss MA10 (Carl Zeiss AG, Munich, Germany) operated in high-vacuum mode at 10kV accelerating voltage were used with variable working distances. The resulting images were captured on the secondary electron (SE) detector and had at a range of magnifications (40 to 5000×).

2.4. Thermal treatment

2.4.1. Laboratory furnace

The laboratory furnace was used for experiments designated to evaluate the influence of duration of heat exposure and heating regimes on shrinkage, morphology, weight loss and surface colour alterations, using a total of 172 posterior teeth (81 premolars, 91 molars; Table 2.1). Teeth were put in individual crucibles and placed in an ashing furnace (Carbolite AAF 11/3, Sheffield, United Kingdom). The cooling phase was documented using the internal temperature probe of the furnace and an infrared thermometer (Ebro TFI 650, Ebro Electronic GmbH, Ingolstadt, Germany) obtained thanks to an American Board of Forensic Odontologists (ABFO) research grant. All specimens of the experiments that involved the laboratory furnace were weighed before and after the thermal treatment with a high-precision analytical scale (Ohaus TS400D, Pine Brook, USA). To determine the overall dental weight loss, all fragments of dentine and enamel were collected from the crucible and included in the weight measurements.

Fifty six teeth (28 premolars, 28 molars) were subdivided into seven temperature groups for 30min constant exposure (400 to 1000°C, in steps of 100°C). The teeth were removed from the furnace after the desired duration and left to cool down to room temperature (RT) (cooling from 900°C to RT in 40min). To investigate the influence of other heating regimens, this study focused on the three temperature groups of 400°C, average temperature of a campfire (Shipman et al., 1984), 700°C, average temperature of house fires (Fairgrieve, 2008), and 900°C, average temperature in modern crematoria (Norrlander, 1995). Six additional groups (n=48, 24 premolars, 24 molars) for incremental increase (samples removed as the desired temperature was reached) and cooling down overnight (30min constant exposure and cooling overnight) at 400, 700 and 900°C were tested. The mean temperature increase of the furnace was 20.75°C/min for the incremental increase group, resulting in a total heat exposure time of 9.5, 25.5 and 42.5min for 400, 700 and 900°C respectively.

The influence of duration of heat exposure on the surface colour, nine additional duration groups (n=63, 28 premolars, 35 molars; 5, 15 and 45min constant exposure at 400 to 1000°C in steps of 100°C) were studied. Additionally, ten teeth (5 premolars, 5 molars) were exposed for 30min at 900°C to assess the shape alterations at high temperatures using digital radiographs. The influence of soft tissue on surface colour alterations was investigated by placing nine teeth (4 premolars, 5 molars) into individual 25g pieces of fresh chicken breast (30min constant exposure at 400, 700 and 900°C).

For the FTIR experiment (Section 2.5.1), a total of 40 cubic samples (36 experimental, 4 control) of dentine and enamel (2×2×2mm) were prepared from nine freshly extracted molars. Two cubes each were exposed for 30min to constant temperatures between 100 and 1000°C, in steps of 50°C. The first (*ex situ*) X-ray scattering experiment (see section 2.6.1) involved 14 tooth sections (3×1×0.5mm; 12 experimental, 2 control) from four posterior teeth (2 premolars, 2 molars). Twelve tooth sections were subdivided into six temperature groups for 30min constant exposure at 400 to 900°C, in steps of 100°C. After the heat exposure, all teeth and tooth sections were stored in padded containers as suggested by Hill et al. (2011b). The fragile nature of heat-affected teeth required careful handling and examination to reduce the risk of further fragmentation. Yet, to prevent interference with the colour analysis, the teeth were not fixated with a cyanoacrylate adhesive or poly-methylmetacrylate (PMMA) as proposed in literature (Fereira et al., 2008, Griffiths and Bellamy, 1993, Hill et al., 2011b).

2.4.2. Direct heating of tooth cross-sections

The heat-induced ‘popping off’ of the enamel (as described in 1.5.1.1) was investigated using video imaging. In order to document this phenomenon, three 1mm thick bucco-lingual cross-sections from three teeth (1 premolar, 2 molars) were used. The cross-sections were fixed using a small clamp 15cm above the opening of a Bunsen burner. The flame was adjusted to a blue colour (~600°C) and measured with a Type K thermocouple probe before placing the Bunsen burner underneath the cross-section. An infrared thermometer (Ebro TFI 650, Ebro Electronic GmbH, Ingolstadt, Germany) was used to continuously measure the tooth surface temperature during the heat exposure.

Table 2.1 Overview of heating experiments involving laboratory furnace.Types of cooling (Type 1: removed from heating device and cooled in air to room temperature (RT); Type 2: left overnight to cool down to RT)

	Study subject	Temperature increase	Temperature range	Time of exposure	Type of cooling
Constant exposure	56 teeth (28 premolars, 28 molars)	N/A	400 to 1000°C	30min	Type 1
Incremental exposure	24 teeth (12 premolars, 12 molars)	20.75°C/min	400, 700, 900°C	9.5min (RT to 400°C), 25.5min (RT to 700°C) and 42.5min (RT to 900°C)	Type 1
Cooling overnight	24teeth (12 premolars, 12 molars)	N/A	400, 700 , 900°C	30min	Type 2
Assessment of influence of duration on colour	63 teeth (28 premolars, 35 molars)	N/A	400 to 1000°C	5, 15, 45min	Type 1
Assessment of shape alterations	10 teeth (5 premolars, 5 molars)	N/A	900°C	30min	Type 1
Assessment of influence of soft tissue	9 teeth (4 premolars, 5 molars)	N/A	400, 700 , 900°C	30min	Type 1
FTIR experiment	40 cubic samples (9 molars)	N/A	400 to 1000°C	30min	Type 1
X-ray scattering experiment	14 sections (2premolars, 2molars)	N/A	400 to 900°C	30min	Type 1

2.4.2. Synchrotron furnace setup

Three 1mm bucco-lingual cross-sections derived from three freshly extracted molars were heated in a custom-built tube furnace as proposed by Dent et al. (1995) to evaluate the crystalline alterations in real time using X-ray scattering. The ceramic sample chamber was heated by a system of heating wires and two X-ray transmittant windows allowed the transmission of the X-ray beam. The temperature was remotely controlled and an internal thermocouple provided the sample chamber temperature. The experimental setup only allowed the simulation of incremental increase so, in order to study the influence of the heating rate, the tooth cross-sections were heated at rates of 6, 12 and 24°C/min. The heating process was stopped at 880 to 900°C and the cross-sections were removed after cooling down to room temperature.

2.4.3. Thermogravimetry (TGA)

The influence of different heating regimes on the weight-loss over time was evaluated by thermogravimetric analysis (TGA) on twenty cubic samples derived from five molars. The TGA experiment was performed at the Department of Chemistry, University of Warwick, using a Mettler Toledo DSC-1 Star (Mettler Toledo Ltd., Leicester, UK). Sixteen dentine samples (3×3×3mm; eight normal, eight demineralised) and four enamel samples (2×2×2mm) were prepared as described in Section 2.1. For each heating rate five cubic samples (two dentine, two demineralised dentine, and one enamel) were analysed. To match the laboratory furnace incremental increase setup, the cubic samples were heated at a rate of 20.75°C/min up to 900°C, whilst the three other groups were matched with the heating regime of the synchrotron furnace setup at rates of 6, 12 and 24°C/min up to 900°C. By calculating the first derivative of the weight loss curve ($\Delta_{Mass}/\Delta_{Temperature}$) changes in the rate of weight loss were investigated. Five additional dentine cubes were prepared to analyse percentage of absorbed water. The freshly cut cubes were weighed in using the analytical scale and subsequently dried using a series of increasing alcohol concentrations (70, 95, 99 and 100% ethanol for 30min each) and kept overnight in a oven at 60°C (SI 20H, Stuart Scientific, UK) before a second weighing.

2.4.4. Fourier-transformed infrared spectroscopy (FTIR) heating stage

For the real-time analysis of the combustion of organic components, measurements were conducted on three 10-15µm thin sections of three molars using a FTIR600 heating stage (Figure 2.1, kindly loaned for one week by Linkam Scientific Instruments Ltd, Guildford, UK). The heating rate of 12°C/min was matched with the TGA and synchrotron furnace setup. Due to equipment restrictions (water circulator pump was not provided as part of loan), the sections could only be heated to 400°C, and were removed as soon as 400°C was reached and subsequently cooled down to room temperature.

2.5. X-ray imaging

2.5.1. Digital radiographs

Digital radiographs were taken to document structural and dimensional changes of teeth in 2-D using a customized Kodak 2100 intra-oral X-ray system setup (Carestream Health Inc., Rochester, NY, USA) using 60kV voltage, 4µA current and 0.1s exposure time. The setup allowed a fixed object-detector distance, minimizing geometric enlargement. Size calibration was performed using two grade 200 high-precision aluminium bearing balls (diameter: 1mm±5µm and 5mm±5µm; CCR Products, West Hartford, USA).

2.5.2. X-ray micro-computed tomography (Micro-CT)

Micro-CT was used to investigate the structural and dimensional alterations of teeth in 3-D, as well as to produce high-resolution planning models for the X-ray scattering experiments. All scans were carried out with a SkyScan 1172 (Bruker SkyScan, Kontich, Belgium). A flat field correction was taken on the day prior to scanning using the SkyScan control software to correct for variations in the pixel sensitivity of the CCD detector. Teeth were scanned at 13.5µm camera pixel resolution using 80kV voltage, 100µA current and a 0.5mm Aluminium filter, resulting in 480 projection images. Tooth sections were scanned at 0.5 to 2.9µm camera pixel resolution using 40 to 80kV voltage, 100 to 120µA current and a 0.5mm Aluminium filter, depending on the specimen size and thickness. Subsequent reconstruction of the projection images and analysis are described in Section 2.7.2.

2.6. Fourier-transformed infrared spectroscopy (FTIR)

2.6.1. Attenuated Reflective Fourier-transformed infrared spectroscopy (ATR-FTIR)

FTIR measurements were used to provide information on heat-induced compositional changes of dental tissue. The analysis was performed on a Nicolet 6700 FTIR machine (Thermo Scientific Instruments Corp., Madison, USA). For the ATR-FTIR experiment, cubic samples were mechanically crushed and sieved using a 105µm sieve to provide a homogenous grain size. The powdered samples were analysed using the Smart Miracle ATR attachment (Figure 2.1A; PIKE Technologies, Madison, USA) and Omnic 8 software suite (Thermo Scientific Instruments Corp., Madison, USA). Three individual measurements per temperature group were performed. Each resulting spectrum represented the average of 32 scans within the mid-IR spectrum (range: 4000 to 400 cm^{-1}) at a resolution of 0.482 cm^{-1}.

2.6.2. Real-time Fourier-transformed infrared spectroscopy

A FTIR600 heating stage (Figure 2.1B) was fitted into the Nicolet 6700 FTIR machine allowing real-time measurements of the compositional changes in transmission mode. The cross-sections were mounted in a sample chamber and KBr windows were fitted to optimise the transmission of the IR-beam. The Linksys32 control software (Linkam Scientific Instruments Ltd, Guildford, UK) was used to remotely adjust the heating rate. The real-time function of the Omnic 8 software suite was used for continuous measurements of five individual values. These values included the carbonate (CO_3^{2-}) group peaks at 1415, 1460 and 1546cm^{-1}, the organic tissue and water peak at 1640cm^{-1} as well as the overall 'organic' region between 1415 and 1650cm^{-1} (Thompson et al., 2013). A total of 1,002 measurements were recorded for each value and sample during the heating from room temperature to 400°C.

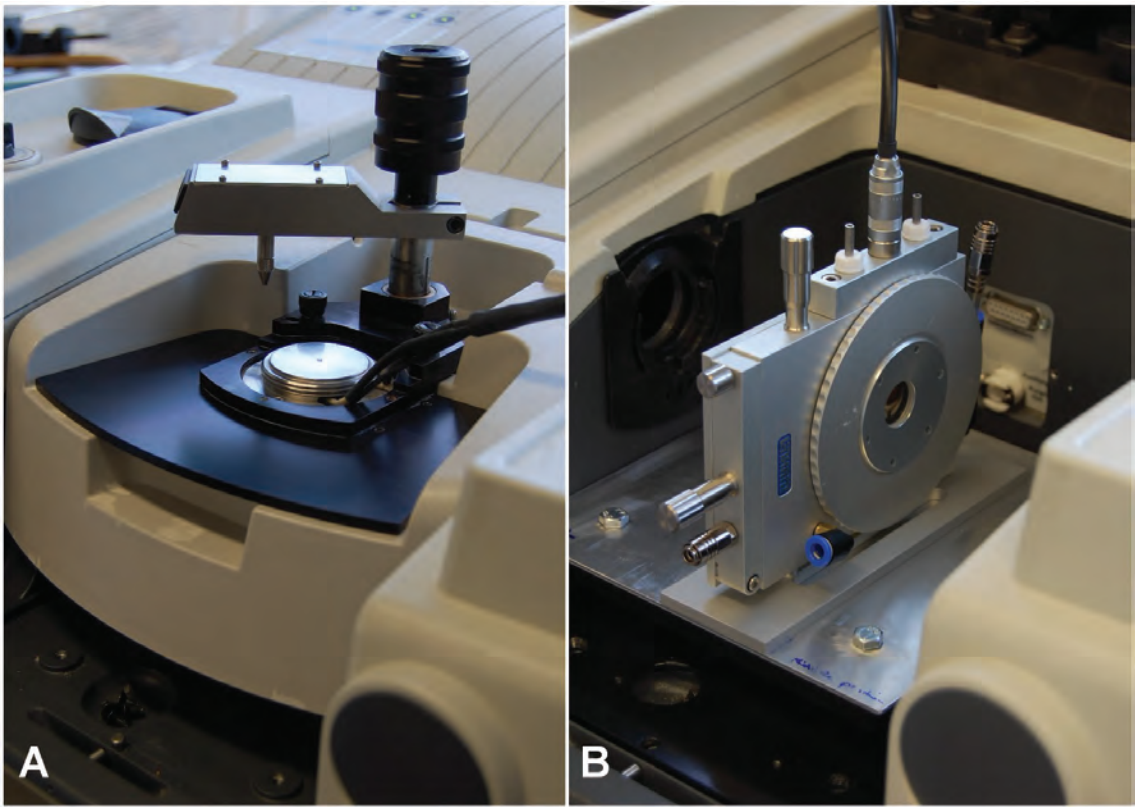

Figure 2.1 Fourier-transformed infrared spectroscopy (FTIR) setup

(A) ATR-FTIR setup with diamond crystal window and pressure arm for powdered samples

(B) Heating stage setup (FTIR600, Linkam Scientific Instruments Ltd, Guildford, UK) allowing real-time FTIR measurements in transmission mode.

2.7. Synchrotron X-ray scattering

2.7.1. X-ray scattering data acquisition

The electron density of a material causes an incident X-ray beam to be scattered in certain angles. The wide-angle X-ray scattering (WAXS) patterns typically appear as separated rings with various width and intensity levels. The rings contain information related to the material structure (e.g. HAp crystallites and organic components in dental tissue; Figure 2.2.). Additionally, the small-angle X-ray scattering (SAXS) patterns contain information on size, shape and alignment of a crystalline material. Traditional lab-based X-ray scattering methods (e.g. XRD) analyse powdered samples, providing averaged results of the entire sample. To investigate local characteristics of dental nanostructures, synchrotron-based X-ray scattering experiments were conducted.

The *ex situ* synchrotron X-ray scattering experiment was carried out on the I22 SAXS beamline at the Diamond Light Source (DLS) facility (Oxford Harwell Campus, Didcot, UK) and used sections that were previously burned in the laboratory furnace (Section 2.4.1). A monochromatic 18keV X-ray beam focused to a beam size of 14.5×19μm was used to analyse the samples. The sample-detector distance was 1,040mm, enabling the entire SAXS and a partial WAXS pattern to be captured on a 2-D Pilatus 2M detector (Dectris Ltd., Baden, Switzerland). A small tungsten structure (beamstop) was positioned in front of the detector to prevent the incident X-ray beam from directly hitting the detector. Two longitudinal line scans with 14 measurements each were collected in transmission mode from fixed locations within all samples (scan step 100μm). Additionally, transverse line scans with six measurements each were performed for selected samples exposed at 400, 600 and 800°C. In order to further document spatial variation of the measurements, 0.6×0.6mm region of interests (ROIs) of all samples including the dentine-enamel junction were mapped, resulting in a 15×15 grid of 225 scattering patterns (scan step 40μm).

The real-time synchrotron X-ray scattering experiment was also performed on the I22 SAXS beamline at the DLS facility and used the synchrotron furnace setup described in Section 2.4.2.

A monochromatic 18keV X-ray beam was used to illuminate the samples with a focused beam of 65×120μm. The specific furnace design allowed the incident X-rays to be transmitted directly through the tooth sample. The SAXS patterns were collected in enamel and dentine at four fixed locations within the specimens. A Pilatus 2M detector (Dectris Ltd., Baden, Switzerland) was positioned at a distance of 2,892mm for the SAXS measurements. A lightly compacted disk of National Institute of Standards and Technology (NIST) silicon powder was used for the WAXS data calibration, and a disk of silver behenate ($AgC_{22}H_{43}O_2$) powder was used for the SAXS data calibration.

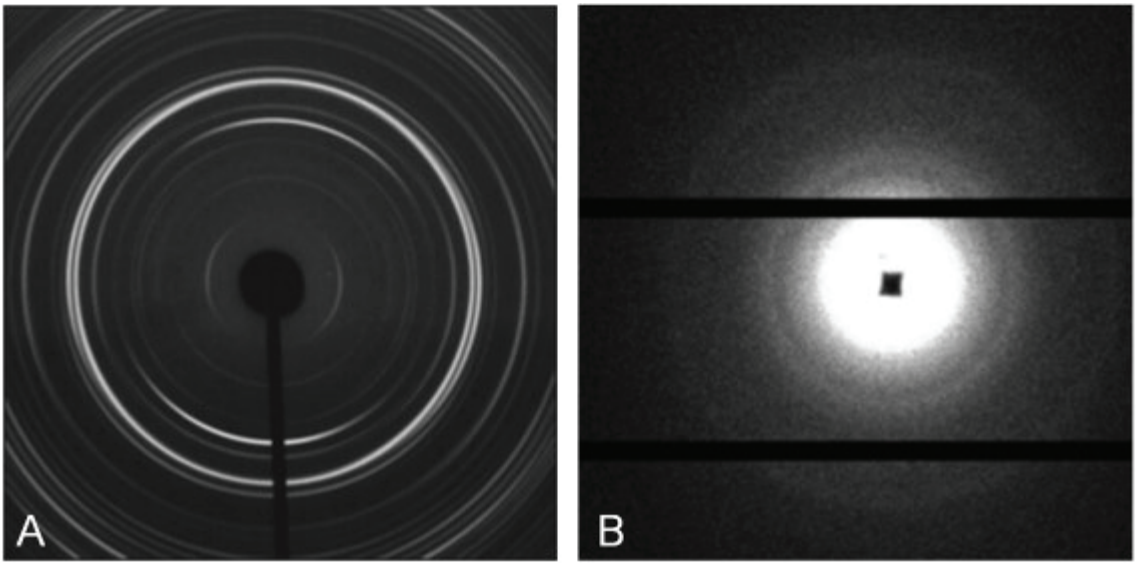

Figure 2.2 Representative small and wide-angle X-ray scattering (SAXS/WAXS) patterns

(A) Representative WAXS pattern of enamel. Separated rings with various width and intensity levels indicating the underlying crystalline structure. The dark region in the centre is the beamstop

(B) Representative SAXS pattern of enamel. The black lines are the borders of the individual sections of the detector, and the dark spot in the centre is the beamstop.

2.8. Image processing and analysis

2.8.1. Photographic colour analysis

For colour calibration of the digital photographs, a Gretag Macbeth Color Checker Chart was used. Image processing and analysis was done in Fiji (Schindelin et al., 2012) using ImageJ versions 1.45f to 1.48c (Rasband, 1997-2013). Image calibration was performed using the 'Chart White Balance' plugin (van der Haeghen and Naeyaert, 2006). A macro was recorded in Fiji to produce a mask, creating a uniform black background and facilitate the colour analysis (Figure 2.3, and Appendix 11.1). A selection of 6,000 pixels was cropped from each tooth of the different test groups, which was equal to a root surface area of 23.6mm^2. As the computing time to compare all colours of all temperature groups was not justifiable, a colour reduction was performed. Wu's colour reduction algorithm implemented into the '3D Color Inspector' plugin (Barthel, 2007) was used to reduce the colour information of the previously calibrated digital photographs.

To evaluate the effects of reducing the number of colours, the colour entropy was calculated. Entropy is a measure of uncertainty in the distribution of values within a defined space and is reported in units called 'bits'. Hence, colour entropy indicates how dispersedly/compactly distributed the colours of the individual selections are within the three-dimensional RGB colour space (Sun et al., 2006). Entropy is defined as the $-\sum p_i * \log_2(p_i)$, where p_i is the probability of occurrence of a colour (i.e. counts for each colour divided by the total number of pixels in an image), and $\log_2$ is the logarithm in base 2. An image that contains just a single colour has the minimum entropy value of 0, whilst an image containing equal proportions of each of the 16'777'216 colours of the RGB colour space has the maximum entropy value of 24. For this study, the entropy of each cropped region containing 6,000 pixels was calculated using an ImageJ macro written by G. Landini (see Appendix 11.1).

Additional colour calculations were performed to evaluate the differences in surface colour alterations between the individual experimental groups. In general, colours can be reported as spectra or numerical values in colour spaces, with RGB and CIE L*a*b* being the most frequently used

numerical quantification systems. The RGB colour model indicates that red (R), green (G) and blue (B) light is added together to produce a wide range of colours.

In order to determine colour changes and differences between two samples more precisely, the Commission Internationale de L'éclairage (CIE) developed the ΔE (delta-E 1976) equation, which is based on an alternative colour space called CIE L*a*b*. This colour space describes colour based on the mixture of three metrics: L* is the lightness (white L=100, black L=0), a* indicates the colour contents in a green (negative) and red (positive) axis, and b* values indicates the colour contents in a blue (negative) and yellow (positive) axis. The ΔE 1976 equation between two colours $L^*_1a^*_1b^*_1$ and $L^*_2a^*_2b^*_2$ is defined as the Euclidean distance $\sqrt{[(L^*_2-L^*_1)^2 + (a^*_2-a^*_1)^2 + (b^*_2-b^*_1)^2]}$. This enables the comparison of colours by giving a single value proportional to the difference between two colours (Lindbloom, 2009). ΔE values above 1 to 2.3 have been reported to be the just noticeable colour differences distinguishable by normal human vision (Lindbloom, 2009, Mahny et al., 1994, van der Haeghen and Naeyaert, 2006). Nonetheless, the ΔE value does not provide information on the colours themselves.

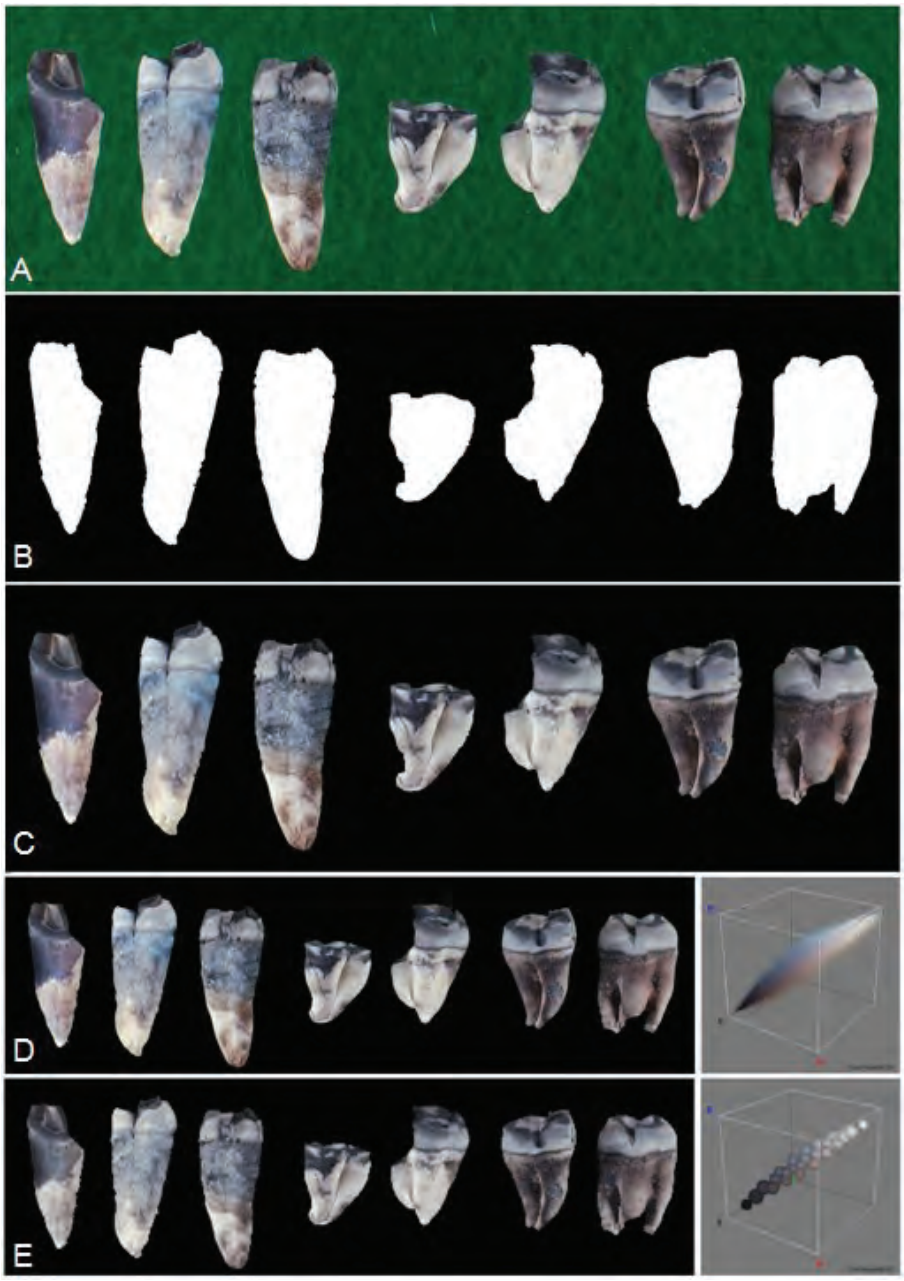

Figure 2.3 Quantitative colorimetric analysis of surface colour alterations

(A) Colour-calibrated image with original green felt background

(B) Creation of uniform black background using Fiji macro

(C) Background added to colour-calibrated image

(D) Colour-calibrated image and corresponding colours in RGB colour space

(E) Photograph after Wu-Chant colour reduction and corresponding colours in RGB colour space.

2.8.2. X-ray micro-computed tomography (Micro-CT) data analysis

The micro-CT projection images were reconstructed using the SkyScan NRECON software suite (Bruker SkyScan, Kontich, Belgium) with a uniform attenuation coefficient to produce cross-sectional images of the dental samples. Subsequently, 3-D models were rendered using the Fiji '3D viewer' plugin (Schmid et al., 2010).

To investigate the dentinal shrinkage, the cross-sectional images were converted into NRRD stack files in Fiji and a 3-D fast rigid registration of pre- and post-scans was performed using 3D Slicer version 3.6.4 (Fedorov et al., 2012) as described by Robinson et al. (2012). The pre- and post-scan image stacks were loaded back into Fiji and after a manual determination of the region of interest (ROI) the registered image stacks were cropped using the 'Slice Remover' tool. To prevent a false-positive influence of broken coronal dentine on dentinal shrinkage the analysed ROI was limited to non-fragmented dentine parts, with a minimum of 400 slices (equal to 5.4mm) included in the analysis. Subsequently, the image stacks were binarised using the same thresholding values. The resulting pre- and post-volume values were exported to SPSS version 19 (IBM SPSS Inc., Armonk, USA) for further statistical analysis.

2.9. X-ray scattering data analysis

The analysis of the X-ray scattering (SAXS/WAXS) data was conducted by Mrs. Tan Sui as part of an ongoing collaborative project between the School of Dentistry (University of Birmingham) and the Department of Engineering (University of Oxford) (Sandholzer et al., 2014, in press, Sui et al., 2014a, Sui et al., 2013a, Sui et al., 2013b, Sui et al., 2014b).

2.9.1. Small-angle X-ray scatting (SAXS)

Small-angle X-ray scatting (SAXS) patterns provide information about the mean crystallite thickness, degree of alignment and particle shape. For an initial quantitative analysis 2-D diffraction images were converted into one-dimensional (1-D) intensity profiles and pre-processed using the Fit2D software

package (Hammersley, 1997). The mean crystallite thickness (*T*) was determined using established methods (Fratzl et al., 1992). Frequently, *T* is used as the definition of the mean crystallite thickness without any assumption of the particle shape (Hiller et al., 2003).

The crystallite shape in dental tissue is usually considered to be needle- or platelet-like (Marten et al., 2010). For the special case of needle or platelet shaped particles *T* can be interpreted as an average measurement of the smallest dimension of crystallite (i.e. mean crystallite thickness). By taking further factors (e.g. the mineral volume fraction) into account, the actual thickness of the crystallite can be calculated based on the mean thickness results (Glatter and Kratky, 1982, Tesch et al., 2001).

The crystallite orientation, referred to as the degree of alignment (ρ) is used to describe the percentage of aligned particles in a sample. The crystalline degree of alignment was determined as explained and illustrated in Sui et al. (2013b). The value for the crystalline degree of alignment ranges from 0 to 1, with ρ=0 indicating no predominant orientation and ρ=1 corresponding to perfect alignment of all crystallites (Rinnerthaler et al., 1999, Tesch et al., 2001).

As outlined by Sui et al. (2013b) the crystallite shape can be directly obtained from the logarithmic format of the SAXS profile plot. If the absolute value of the slope of this plot is close to 1, the particle has a needle-like shape, whilst if it is close to 2, the shape is platelet-like. Values above 2 correspond to a more complex (polydisperse) crystal morphology (Hiller and Wess, 2006).

2.9.2. Wide-angle X-ray scatting (WAXS)

The analysis of WAXS patterns establishes the relationship between the spacing of atomic planes in crystallites and the scattering angle at which these planes produce intense reflections (Hiller and Wess, 2006). Each intensity peak corresponds to a certain group of lattice planes within a certain crystallographic phase of the mineral. Therefore, diffraction pattern analysis can be used to identify and quantify the crystallographic phases and structure parameters (i.e. characteristic arrangement of atoms). A strong and distinct ring obtained from HAp is that of the (002) lattice plane, which contains information on the orientation of the principal axis (Deymier-Black et al., 2010).

The dimensions of the crystallites cause diffraction peak broadening that can be used to deduce the particle size, by calculating the full width at half maximum (FWHM) variation ratio (Shipman et al., 1984).

2.10. Statistical analysis

The statistical analysis was performed with SPSS versions 19 and 20 (IBM Co., Armonk, USA) and in R v.3.0.2 (R Core Team, 2013). First, the measurements of weight loss and shrinkage as well as SAXS/WAXS results were tested for normality using Shapiro-Wilk tests. Subsequently, the computed differences of the weight loss, shrinkage and mean crystallite thickness were statistically analysed with one-way analysis of variance (ANOVA) and post-hoc Least Significant Difference (LSD) tests. A two-tailed independent sample t-test was used to evaluate the statistical difference in dentinal shrinkage and weight loss between premolars and molars. Probability levels of $p<0.05$ (95% confidence interval) were considered statistically significant. The Pearson's correlation coefficient was calculated to show the strength of the relationship between colour entropy and number of colours.

Hierarchical tree diagrams (dendrograms) based on the complete linkage (maximum) clustering method were chosen to visualise trends in surface colour alterations. The colours grouped into the earliest four to five clusters were used to evaluate whether particular colour groups could be related to specific temperature regions.

Chapter 3 – Results: Heat-induced weight loss and compositional changes

High-precision analytical scale measurements and thermogravimetric analysis (TGA) were used to evaluate the influence of duration of heat exposure and heating regimes on the weight loss of dental tissues. Additionally, the destruction of organic components and lattice carbonates was documented with attenuated total reflectance (ATR) and real-time Fourier-transformed infrared spectroscopy (FTIR).

3.1. Weight loss of teeth

3.1.1. Analytical scale measurements

High-precision analytical scale measurements were made to provide information on the weight loss of teeth. The enamel was fully preserved and attached in all 400°C groups and partially separated from the coronal dentine or fragmented between 500 and 600°C. Complete separation and fragmentation of the enamel was found in all teeth heated at and above 700°C (Figure 3.1). To determine the overall weight loss, all fragments of dentine and enamel were collected from the crucibles and included in the measurements. A two-tailed independent sample t-test found no significant difference between the weight loss of premolars and molars ($p=0.841$). Burned soft tissue remains that were still present in the crucibles made it difficult to determine the accurate rate of weight loss for the samples of the soft tissue protection group.

3.1.2. Influence of duration of heat exposure and heating regimes on weight loss

The influence of duration was analysed by exposing teeth for 5, 15, 30 and 45min at 400°C to 1000°C. Additionally, the influence of heating regimes (incremental increase as well as cooling overnight) was tested for three temperatures (400, 700 and 900°C). To compare the weight loss of the individual groups, a one-way ANOVA with a post-hoc least significant difference (LSD) test was performed to identify significant differences in weight loss. The results of the mean weight loss and the significance levels of mean weight loss differences are presented in Tables 3.1 and 3.2.

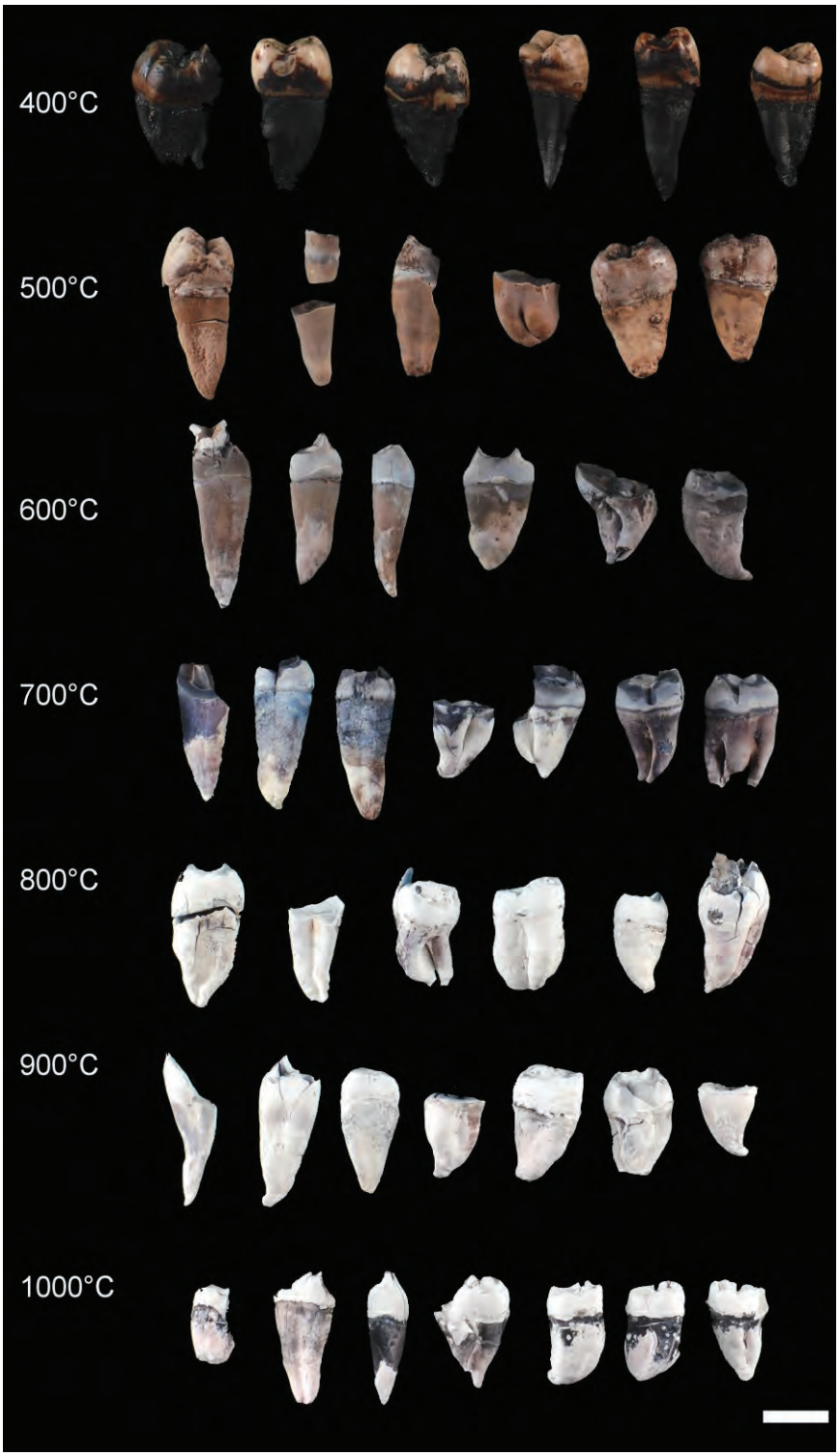

Figure 3.1 Fragmentation of enamel after 30min constant exposure at high temperatures

Preservation and attachment of enamel visible at 400°C, whilst fragmentation occurred between 500 and 600°C. Complete separation and fragmentation of enamel at and above 700°C. Scale bar = 10mm.

Table 3.1 Mean weight loss of teeth after exposure to elevated temperatures of 400 to 1000°C (n=179)**.** Values given as percentage weight loss ± 1 SD (standard deviation).

Temperature	**INC**	**5min CON**	**15min CON**	**30min CON**	**45min CON**	**ON**
400°C	7.8 ± 0.5	11.4 ± 0.8	18.5 ± 1.5	16.1 ± 1.5	20.2 ± 0.8	18.0 ± 0.7
500°C	-	16.0 ± 3.6	21.0 ± 2.4	20.0 ± 1.2	27.2 ± 2.1	-
600°C	-	30.2 ± 0.9	26.6 ± 4.1	25.6 ± 3.6	32.0 ± 2.8	-
700°C	20.1 ± 1.9	28.9 ± 3.9	30.5 ± 4.0	27.1 ± 2.6	29.6 ± 2.9	29.3 ± 3.1
800°C	-	27.7 ± 1.5	30.6 ± 1.9	30.0 ± 1.6	33.9 ± 3.9	-
900°C	27.1 ± 3.9	29.4 ± 3.3	34.0 ± 3.6	30.8 ± 3.4	33.5 ± 3.1	32.3 ± 2.0
1000°C	-	34.0 ± 1.4	34.1 ± 2.4	32.9 ± 1.5	33.6 ± 1.9	-

INC Incremental increase, removed from furnace when temperature was reached
CON Constant exposure for specified duration, removed from furnace when duration was reached
ON Constant exposure for 30min, removed from furnace after cooling overnight.

Table 3.2 Significance levels of mean weight loss differences. Statistical significance was evaluated using an ANOVA with post-hoc LSD test, 95% confidence interval (no significant difference shown in grey; $p<0.05$ indicated in blue).

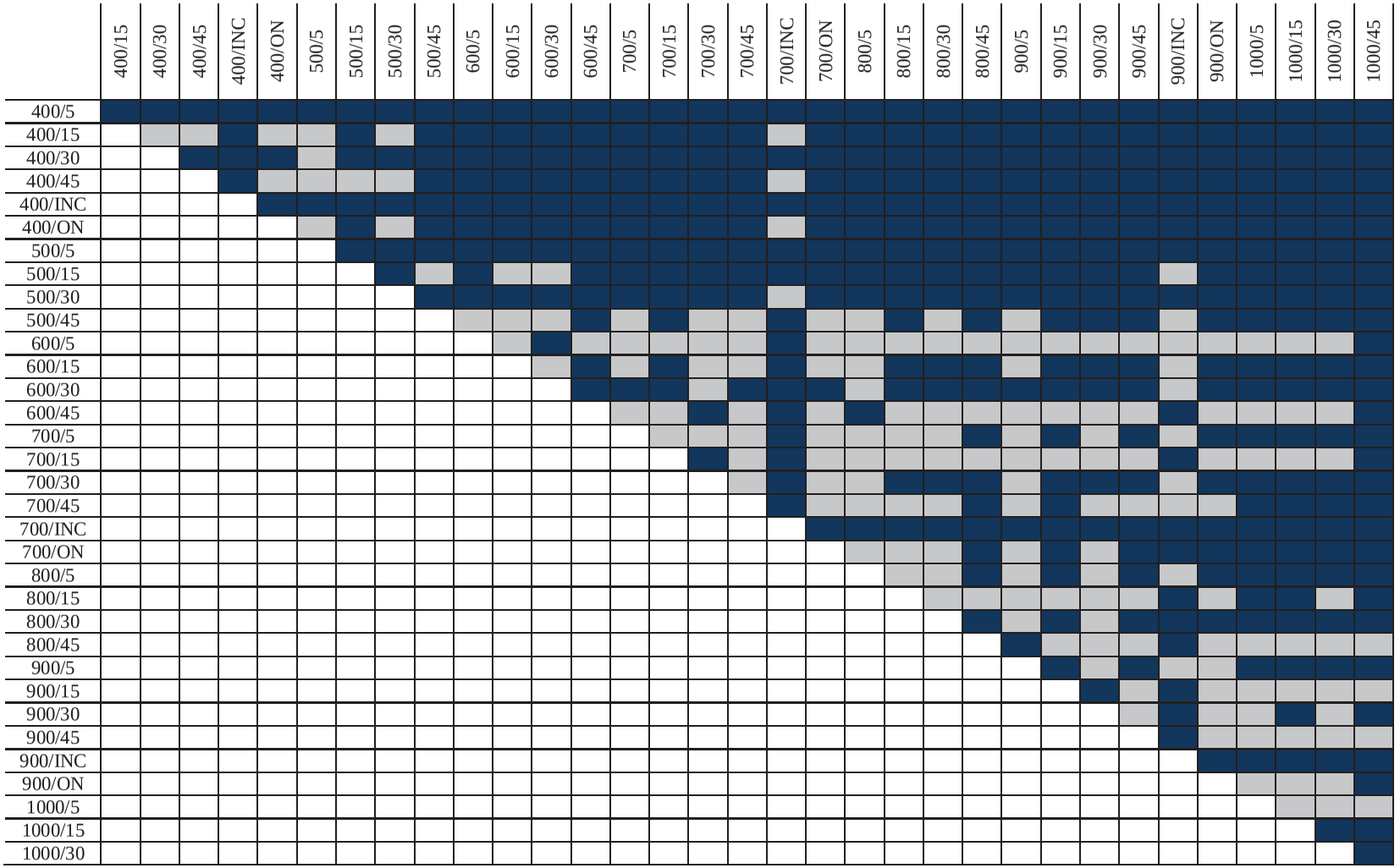

Influence of duration of heat exposure

The statistical analysis of the various duration groups revealed trends in the amount of weight loss. Whilst the duration of temperature exposure played a role in temperature groups at or below 600°C, the weight loss was less variable in the groups exposed to ≥700°C. A maximum average weight loss of 33.9% was recorded for the group exposed constantly to 800°C for 45min. There was no statistical difference in weight loss between the 15 and 45min constant exposure groups for all tested temperature groups, apart from the 600°C groups ($p=0.009$; Table 3.2). When teeth were exposed for only 5min, they showed a similar weight loss ($p>0.05$) to the subordinate 45min groups, with exception of the 900°C 5min/800°C 45min pairing ($p=0.021$).

Influence of heating regimes

The 400 and 700°C incremental increase groups did significantly differ from all constant exposure groups of the same temperature. Whilst the 400°C incremental increase group did not overlap with any other tested temperature group, teeth of the 700°C incremental increase group lost a similar amount of weight as the 500°C 30min constant exposure group ($p=0.929$). The weight loss of the 900°C incremental group was similar to the 600°C 15min constant exposure group ($p=0.973$), and significantly differed from all other 900°C constant exposure groups apart from the 5min constant exposure group ($p=0.079$).

Cooling overnight after 30min constant exposure primarily affected the weight loss in the 400°C group, and was comparable to the 500°C 30min constant exposure test group ($p=0.913$). The 700 and 900°C overnight cooling groups were similar to the constant exposure groups of the same temperature, and only differed significantly from the respective incremental increase groups ($p<0.0005$).

3.1.2. Thermogravimetric (TGA) measurements

Following the analytical scale measurements, further investigations using time- and temperature-resolved thermogravimetric analysis (TGA) were made. Twenty freshly cut cubic samples of dentine (n=8), enamel (n=4) and demineralised dentine (n=8) were subdivided into four heating rate groups (6, 12, 20.75 and 24°C/min) to determine temperature regions of increased rates of weight loss and study the influence of various heating regimes on the weight loss over time. The TGA equipment could only simulate incremental temperature increase, with 20.75°C/min increase equalling the heating rate used in the laboratory furnace experiments. The 6, 12 and 24°C/min groups mimicked the temperature increase that was used in the real-time FTIR and synchrotron X-ray scattering experiments (Chapters 3.2.2 and 6.4).

The weight loss of the enamel samples was relatively uniform in all tested heating rate groups, ranging from 4.0 to 4.2%. For dentine, the average weight loss after heating from room temperature (RT) to 900°C ranged between 31.6 and 33.5%, depending on the heating regime. To determine the water content of the dentine samples, five dentine cubes that were dried using a row of increasing alcohol concentrations and kept at 60°C overnight, showing an average weight loss of 7.0%. The demineralised samples lost 97.9 to 100.0% of their weight, indicating that the fastest increase rate (24°C/min) did not destroy all organic components (Figure 3.2 and Table 3.3).

In order to identify temperature ranges leading to substantial weight loss, the first derivative of the TGA curve ($\Delta_{Mass}/\Delta_{Temperature}$) was calculated. In dentine, distinct peaks were observed in the regions of 125 to 175°C and 330 to 360°C. A shift of those peaks was observed, depending on the heating rate (Figure 3.2A). For demineralised dentine, peaks were found in the regions of 170 to 180°C, 315 to 330°C and 590 to 640°C, again related to the chosen temperature increase (Figure 3.2B).

Table 3.3 Mean percentage weight loss at rates of 6, 12, 20.75 and 24°C/min for dentine (n=2), enamel (n=1) and demineralised dentine (n=2) heated from RT to 900°C.

	Weight loss %		
Temperature increase	**Enamel**	**Dentine**	**Demineralised**
6°C/min	4.0	33.5 ± 1.7	100.0 ± 0.1
12°C/min	4.1	31.9 ± 3.1	99.7 ± 0.2
20.75°C/min	4.1	33.1 ± 0.3	99.5 ± 0.2
24°C/min	4.2	31.6 ± 0.8	97.9 ± 1.3

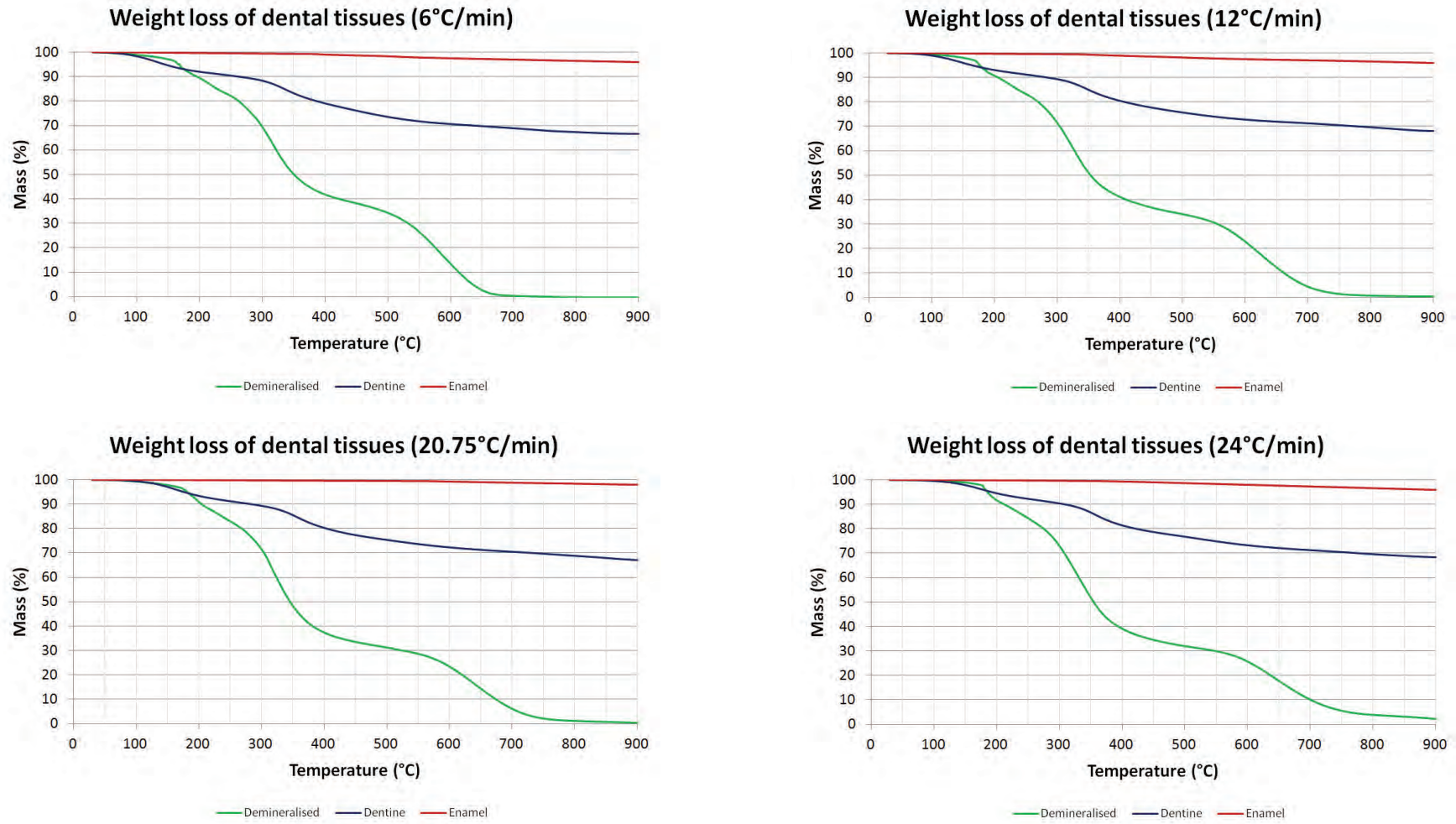

Figure 3.2 Thermogravimetric plots showing the average weight loss at rates of 6, 12, 20.75 and 24°C/min for dentine, enamel and demineralised dentine heated from RT to 900°C.

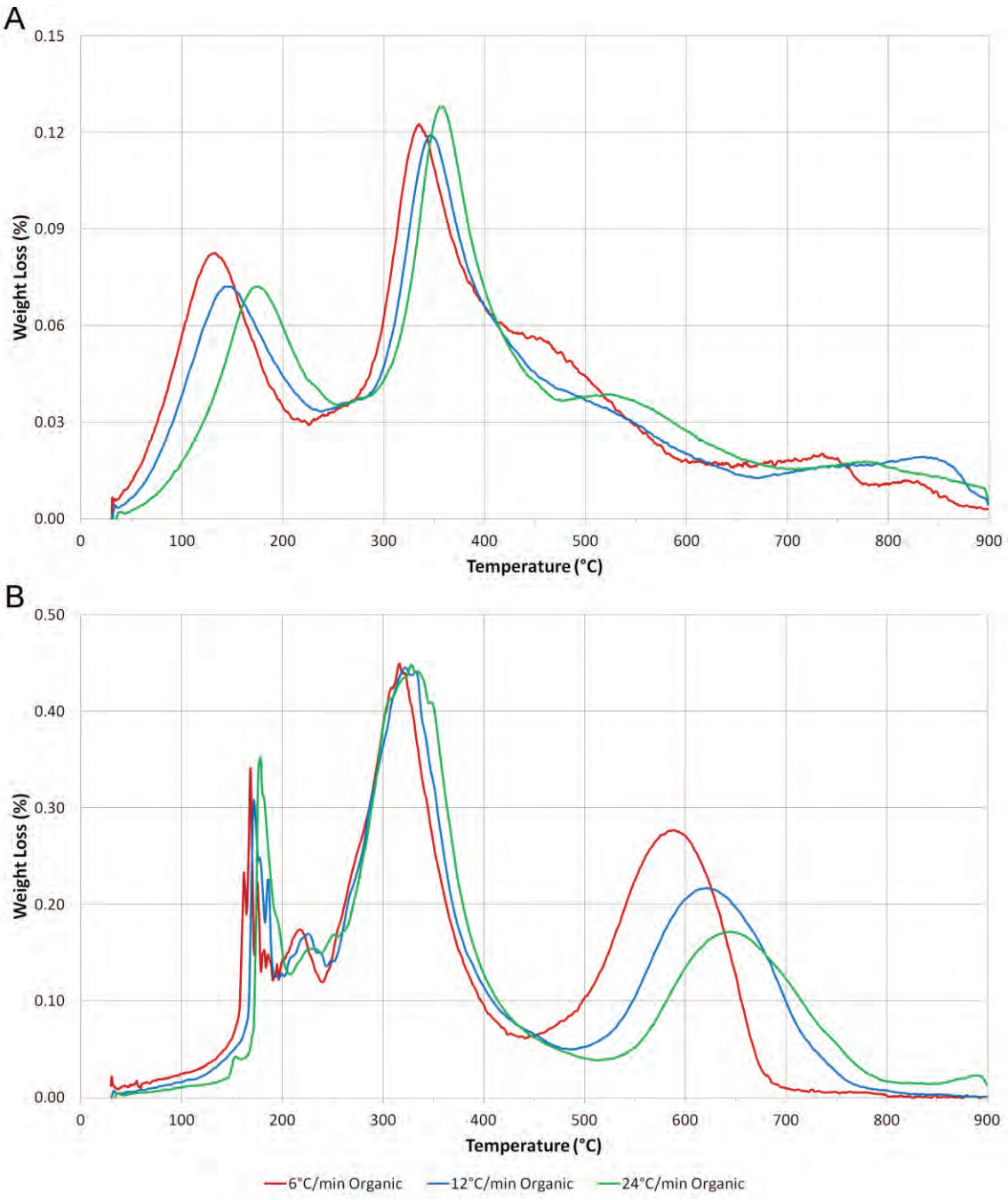

Figure 3.3 First derivative of TGA curves indicating regions of increased weight loss at heating rates of 6, 12 and 24°C/min for **(A)** dentine and **(B)** demineralised dentine heated from RT to 900°C.

3.2. Compositional alterations of teeth

To further understand the compositional alterations, an attenuated total reflectance (ATR-) FTIR analysis was performed. Additionally, a real-time FTIR heating setup was used to investigate the time- and temperature-resolved loss of organic components and lattice carbonates during the heating process.

3.2.1. Attenuated Reflective Fourier-transformed infrared spectroscopy (ATR-FTIR) analysis

At room temperature dentine and enamel showed compositional differences, with organic components and lattice carbonates more predominant in dentine (Figure 3.4). The peaks between 1400 and 1540cm^{-1} are associated with lattice carbonate (CO_3^{2-}) substitutions of the phosphate (PO_4^{3-}) or hydroxyl (OH^-) groups in hydroxyapatite. The peaks between 1540 and 1650cm^{-1} are associated with chemical structures (amides) present in collagen and other proteins (Hollund et al., 2013, Mkukuma et al., 2004). The height of the inorganic phosphate peak at 1030cm^{-1} appeared as not being influenced by the heating process. With increasing temperature, the peaks in the 1400-1650cm^{-1} region began to decrease in dentine around 250°C, with a clear loss seen at 400°C. At elevated temperatures, the peaks of organic structures and apatite substitutions reduced further. Whilst the predominant loss of the collagen-related peak (1640cm^{-1}) was already seen at 700°C, a flat spectrum in the entire 1400 to 1650cm^{-1} region at 900°C indicated the principal loss of organic structures and lattice carbonates in dentine (Figure 3.5).

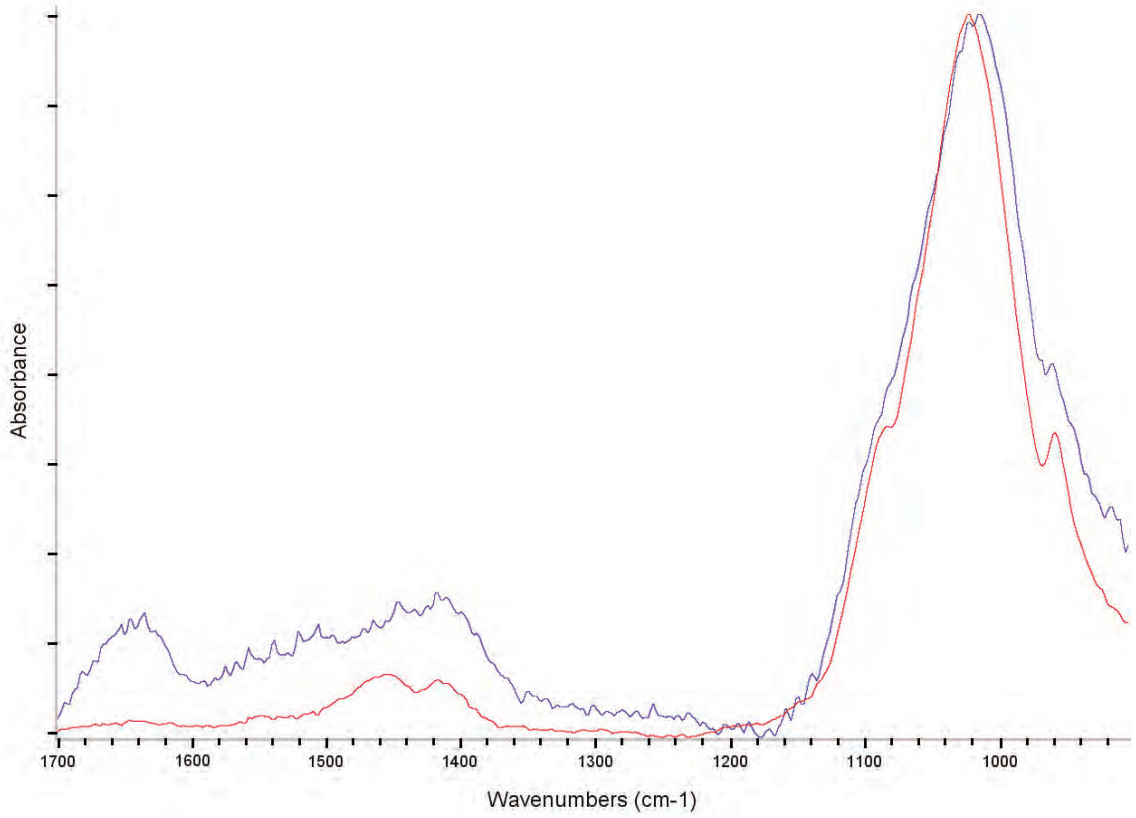

Figure 3.4 FTIR spectra of dentine (blue) and enamel (red) at room temperature.

The phosphate peak at 1030cm^{-1} is linked to the mineral components of dental tissues. Peaks between 1400 and 1540cm^{-1} are associated with lattice carbonates, peaks between 1540 and 1650cm^{-1} are related to chemical structures (amides) present in collagen and other proteins. In contrast to dentine, enamel showed no peaks in the collagen/protein related region (1540 to 1650cm^{-1}).

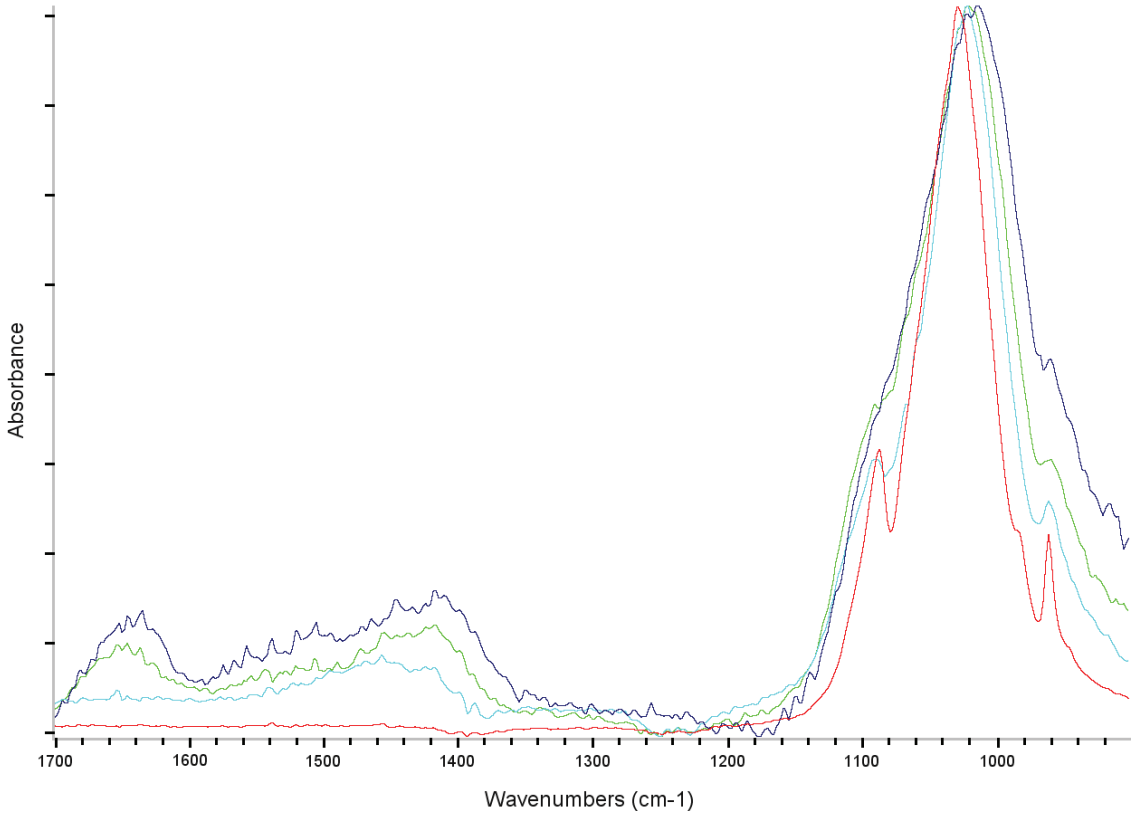

Figure 3.5 Changes of FTIR spectrum of dentine after 30min constant exposure to 400, 700 and 900°C compared to room temperature. Compared to RT (dark blue) the organic component peaks (1400-1650cm^{-1}) reduce between 400 (green) and 700°C (cyan). At 900°C (red) a flat line indicates the principal loss of the organic components in dentine. The height of the inorganic phosphate peak (1030cm^{-1}) was not influenced by the heating process.

3.2.2. Real-time Fourier-transformed infrared spectroscopy measurements

The real-time FTIR heating equipment could only simulate incremental temperature increase up to 400°C. A 12°C/min temperature increase was selected to match the heating rates used in the TGA and real-time synchrotron X-ray scattering experiments (Chapters 3.1.2 and 6.4).

The real-time FTIR measurements were used to further analyse the heat-induced destruction of the organic components and lattice carbonates in dentine. The peaks at 1415, 1460, 1546 and 1640cm^{-1} as well as the overall area between 1415 and 1650cm^{-1} were analysed (Figure 3.5). The area between 1415 and 1650cm^{-1} diminished by 35% after the dentine cross sections were heated from RT to 400°C. The two analysed peaks associated with amide groups from collagen (1546 and 1640cm^{-1}) lost 63 to 67% of their intensity (i.e. peak height), already starting at around 60°C. The two group peaks at 1415 and 1460cm^{-1} associated with lattice carbonates were less affected (12 to 22% decrease of peak height), with the 1415cm^{-1} peak showing no changes up to 280°C.

Moreover, a temperature dependent discolouration of the tooth cross-section was observed during the real-time FTIR experiment. The natural colour of dentine changed to dark yellow/light brown between 255 and 270°C, altering to a darker brown around 290 to 300°C and finally becoming black around 340°C.

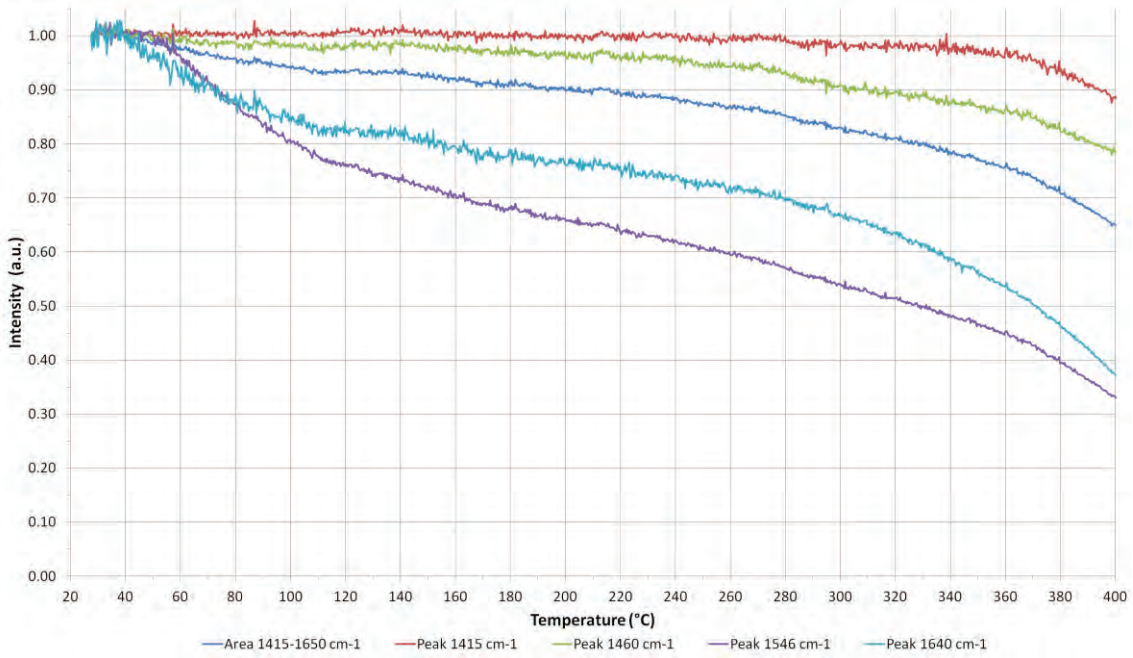

Figure 3.6 Real-time FTIR measurements of the heat-induced destruction of organic components and lattice carbonates in dentine heated from RT to 400°C. Peaks associated with lattice carbonates (1415 and 1460cm^{-1}) were less affected by elevated temperatures than peaks associated with amide groups from collagen (1546 and 1640cm^{-1}).

Chapter 4 – Results: Heat-induced surface colour alterations

As presented in the previous chapter, the duration of heat exposure and the heating regimes (constant exposure, incremental increase, cooling overnight) influenced the weight loss and composition of dental tissues. The destruction of organic material has previously been associated with the alterations of surface colour, which is one of the main macroscopic feature of burned dental remains (Endris and Berrsche, 1985, Shipman et al., 1984). Therefore, the influence of both, duration of heat exposure and heating regimes on the surface colour changes was assessed by computational image analysis on calibrated digital photographs.

4.1. Influence of duration of heat exposure on surface colour

The influence of four heating duration subgroups (5, 15, 30 and 45min) were tested for each of the seven temperatures investigated (n=84; 400 to 1000°C, Figure 4.1). As the enamel was frequently fragmented at elevated temperatures, the colorimetric analysis was limited to the root surface. A progressive shift of the root surface colour from a natural pale yellow at room temperature to predominantly dark yellow/black (400°C), brown (500 to 600°C), greyish-blue (700°C), light grey (800°C), chalky-white (900°C) and patches of white, black and pink (1000°C) was observed.

The 500°C 5min group visually appeared similar to the 400°C 15 to 45min exposure groups, as did the colours found for teeth of the 500°C 45min and the 600°C 5min group. Generally, with prolonged exposure times, the colour difference between the duration groups was less apparent upon visual examination.

Figure 4.1 Example of root surface colour alterations after exposure to various temperatures (A-G: 400 to 1000°C). Groups: 5min (upper left), 15min (upper right), 30min (lower left) and 45min (lower right). Scale bar = 5mm.

In addition to subjective visual examination, a quantitative approach was used to investigate the surface colour alterations. Areas of interest of 6,000 pixels (60×100px, equalling to a root surface area of 23.6mm^2) were cropped from the calibrated digital photographs. These regions featured between 247 and 4,878 colours, adding up to a total of 99,631 colours for all 84 selections (Figure 4.2).

The colour entropies of the individual selections are shown in Figure 4.3A, indicating how dispersedly/compactly distributed the colours of the individual selections are within the 3-D RGB colour space. The Pearson's correlation coefficient was calculated to assess the strength of the relationship between colour entropy and number of colours present in the area of interest. As expected, there was a positive correlation between the colour entropy and the number of colours ($r=0.780$, $n=84$, $p=0.0001$). A plot of the colour entropy values of the individual duration groups (Figure 4.3B) showed that the lowest colour entropy occurred in the 400°C 15, 30 and 45min and 500°C 5min groups. A strong decline in colour entropy was seen for the 400°C groups, indicating more homogeneous colour alterations after prolonged exposure (15 to 45min). The low colour entropy in the 500, 600 and 700°C 5min compared with the related 15, 30 and 45min groups showed that colour changes were more heterogeneous with prolonged exposures. In contrast, the 800, 900 and 1000°C 5min groups had a higher entropy compared to the 15, 30 and 45min groups, indicating that the colour appearance was more homogeneous with prolonged exposures. Overall, colour entropy fluctuated less with prolonged exposures, pointing towards less variable and more comparable colour appearance.

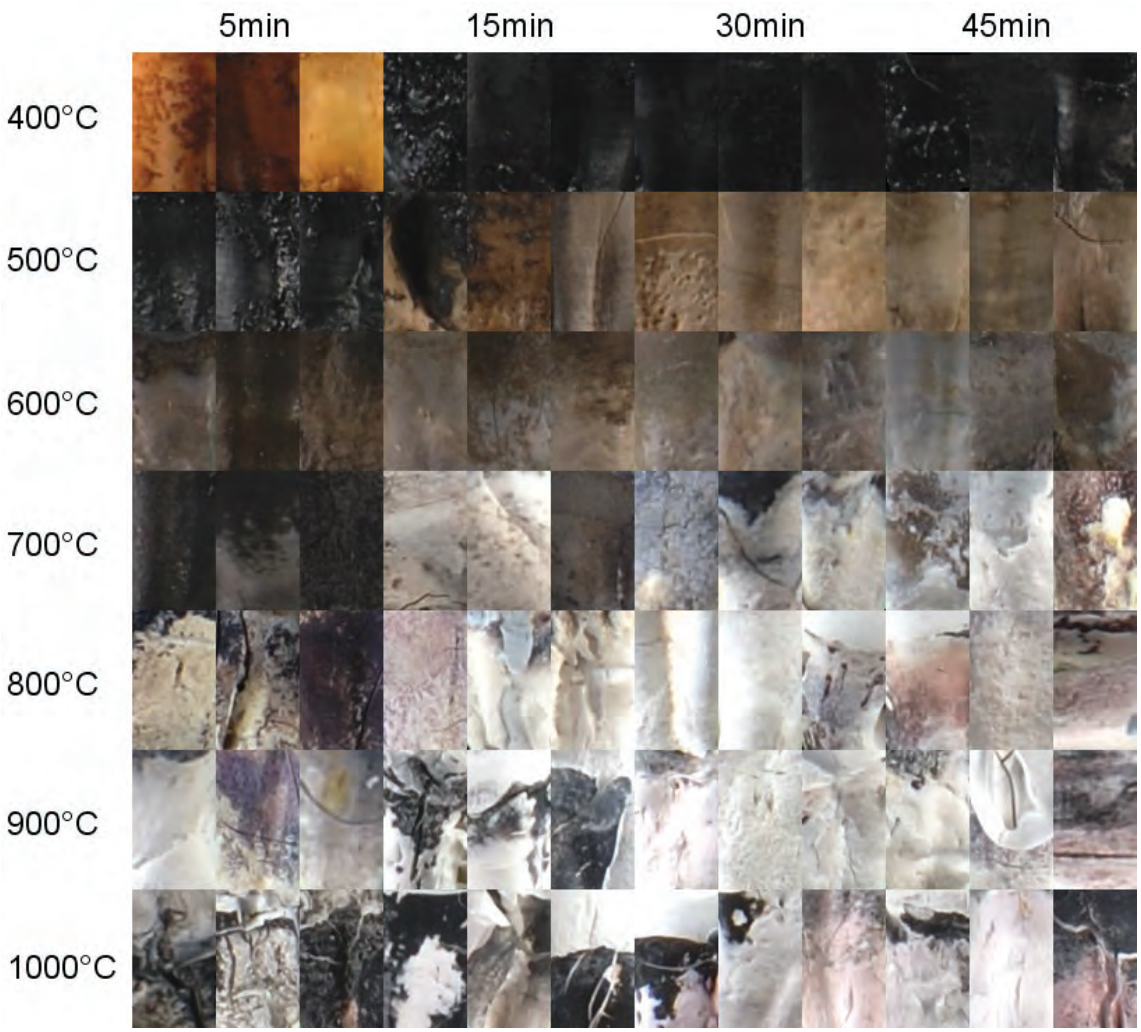

Figure 4.2 Root surface colour alterations after exposure to elevated temperatures (400 to 1000°C). Each row represents one temperature group, and column triplets indicate the individual selections of the different duration groups (5, 15, 30 and 45min constant exposure). The individual regions equal a root surface area of 23.6mm^2.

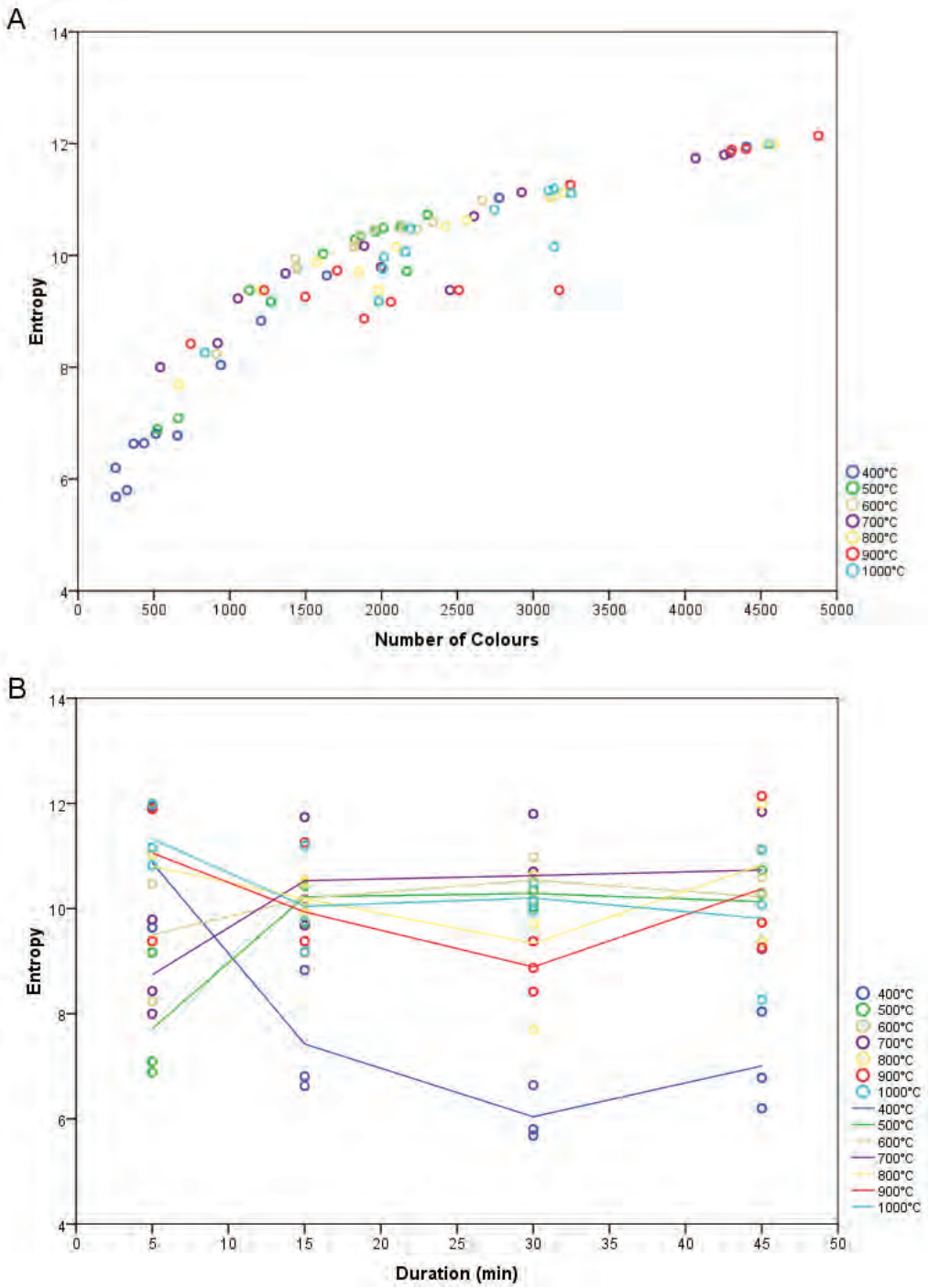

Figure 4.3 Colour entropy of root surface colours after exposure to elevated temperatures

(A) Colour entropy according to temperature exposure. Each point represents the measurement of an individual tooth

(B) Colour entropy plotted by duration of heat exposure. The circles indicate the individual data points, and the lines indicate the group means.

4.1.1. Colour reduction process

To reduce the colour information for each duration group (triplet of tiles) down to a palette of the most representative colours, the Wu-Quant colour reduction algorithm implemented in the '3D Color Inspector' plugin was used (Barthel, 2007). To preserve less predominant colours (e.g. blue tinges in the 700°C 30min group), the selections were reduced down to only 16 colours. A reduction to less than 16 colours resulted in colour palettes that did not represent the colour diversity present in the various temperature groups (Figures 4.4 and 4.5).

With each of the 28 duration groups reduced to 16 colours, a total of 434 colours were identified, with 14 colours (3%) overlapping between groups. Ten (62.5%) of those overlapping colours were from the 15 to 45min 400 and 500°C 5min groups, the other six (37.5%) were from the 900 and 1000°C groups. Due to the reduced number of colours, lower colour entropy values were computed. However, the reduction to 16 colours showed similar entropy trends to the original images (Figure 4.6). Colour palettes representing the individual duration and temperature groups, after the application of the Wu-Chant colour reduction algorithm are shown in Figure 4.7.

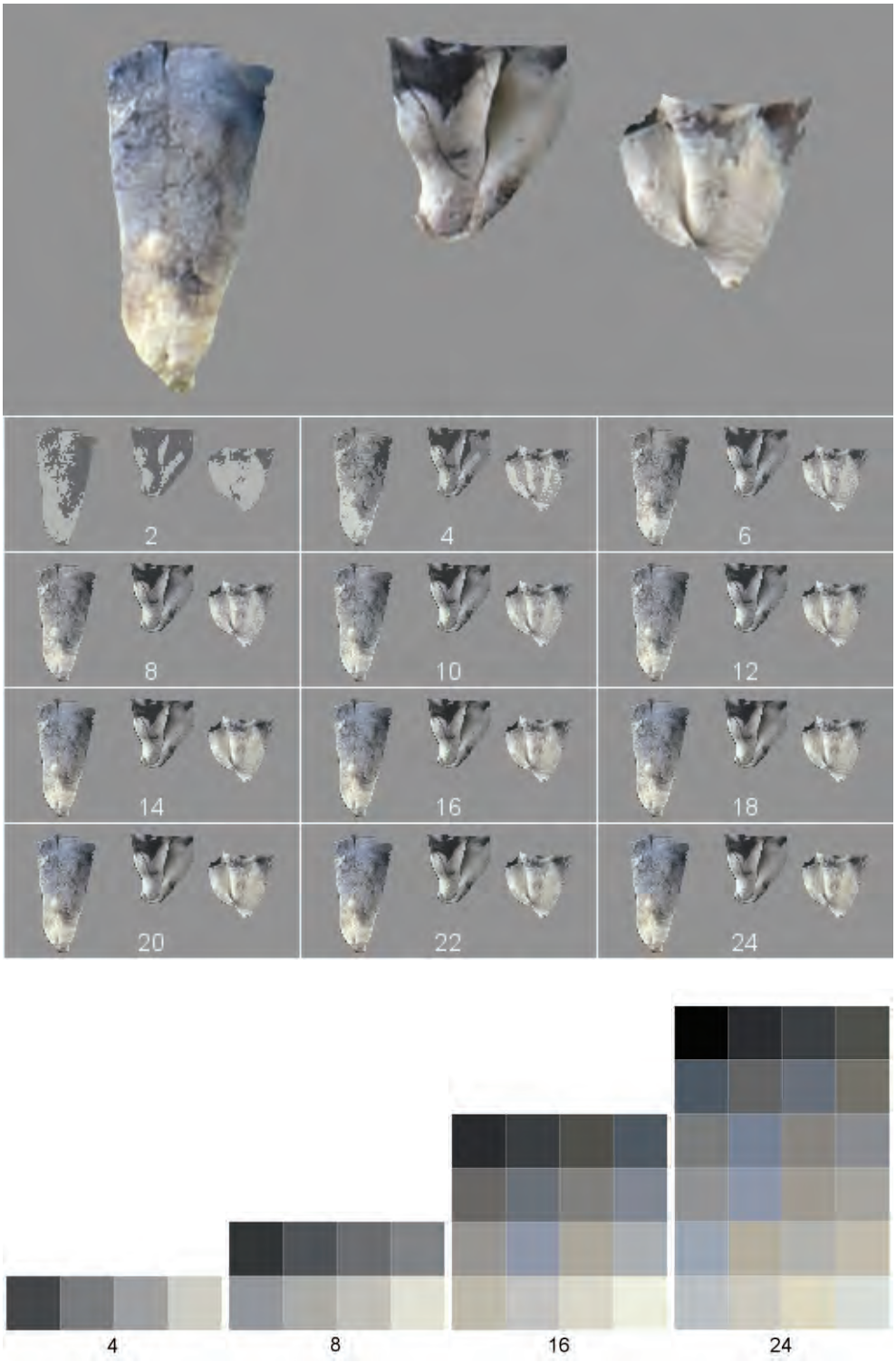

Figure 4.4 Results of the Wu-Chant colour reduction algorithm. Original image (21,148 colours) reduced to two to 24 colours with corresponding palettes. A minimum of 16 colours was found to still represent the colour diversity of the individual test groups.

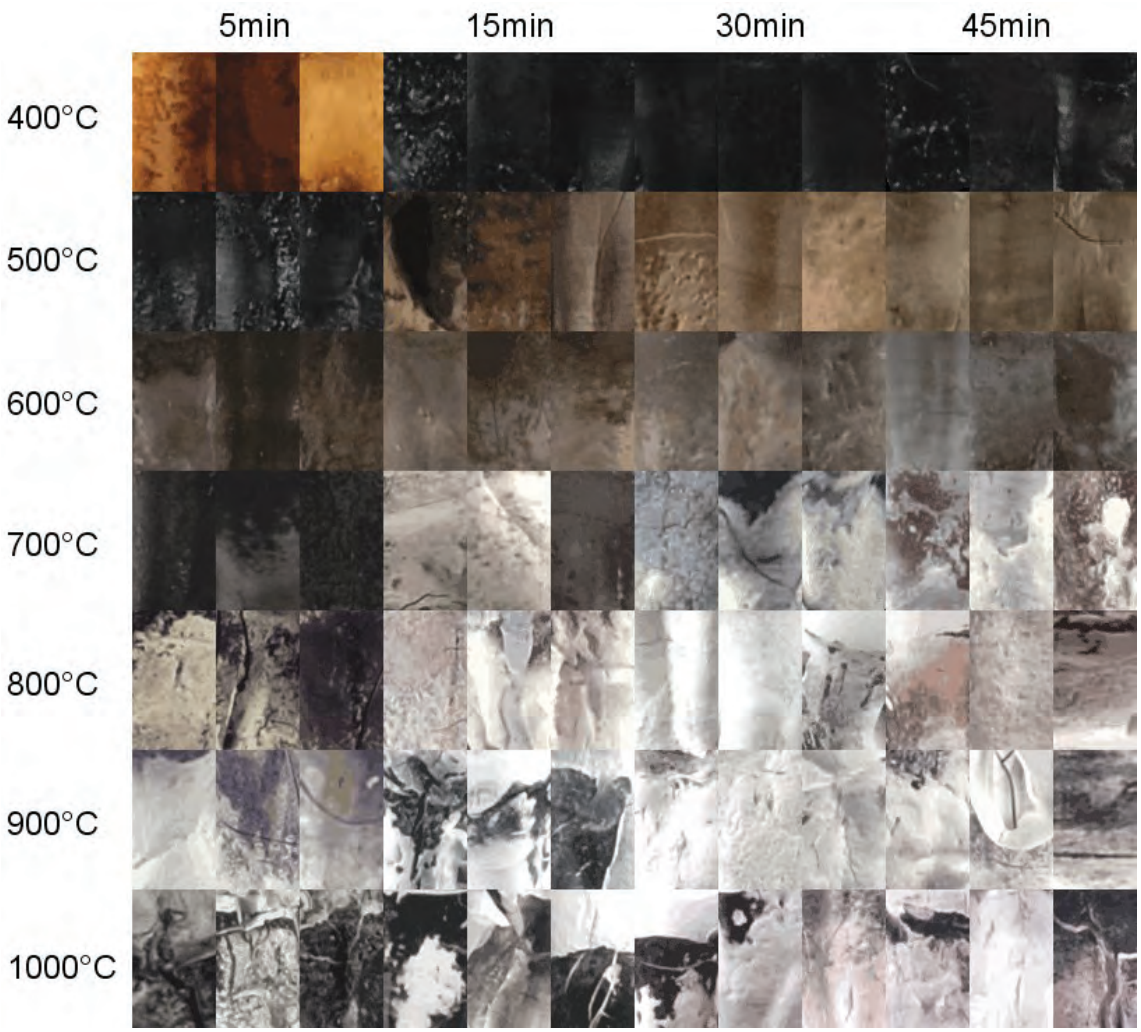

Figure 4.5 Root surface selections after applying the Wu-Chant colour reduction algorithm (down to 16 colours) after 5, 15, 30 and 45min constant exposure to high temperatures (400 to 1000°C). Each row represents one temperature group.

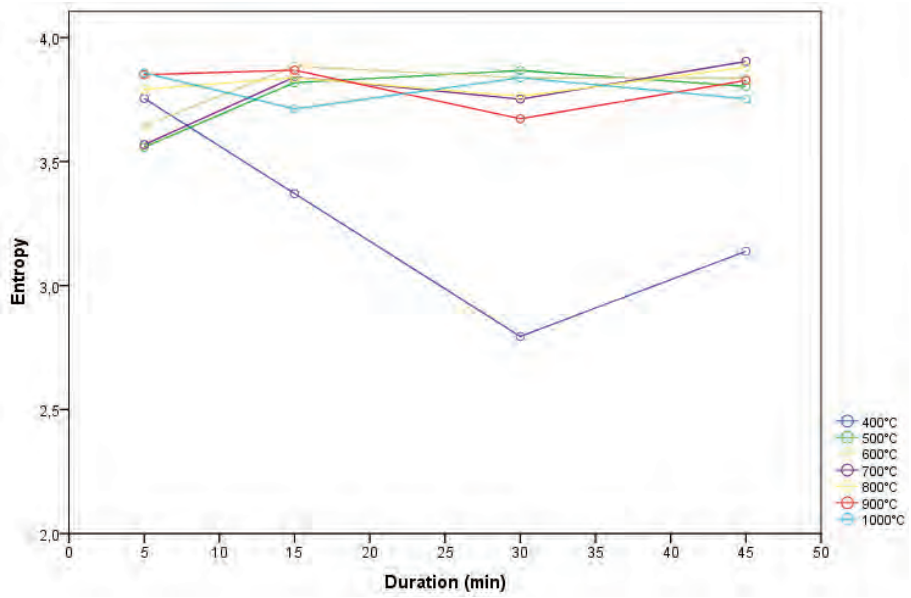

Figure 4.6 Colour entropy of root surface colours after exposure to elevated temperatures plotted against the duration following the application of the Wu-Chant colour reduction algorithm (16 colours). The circles indicate the individual entropy values of the individual duration group triplets, connected by an interpolation line.

.

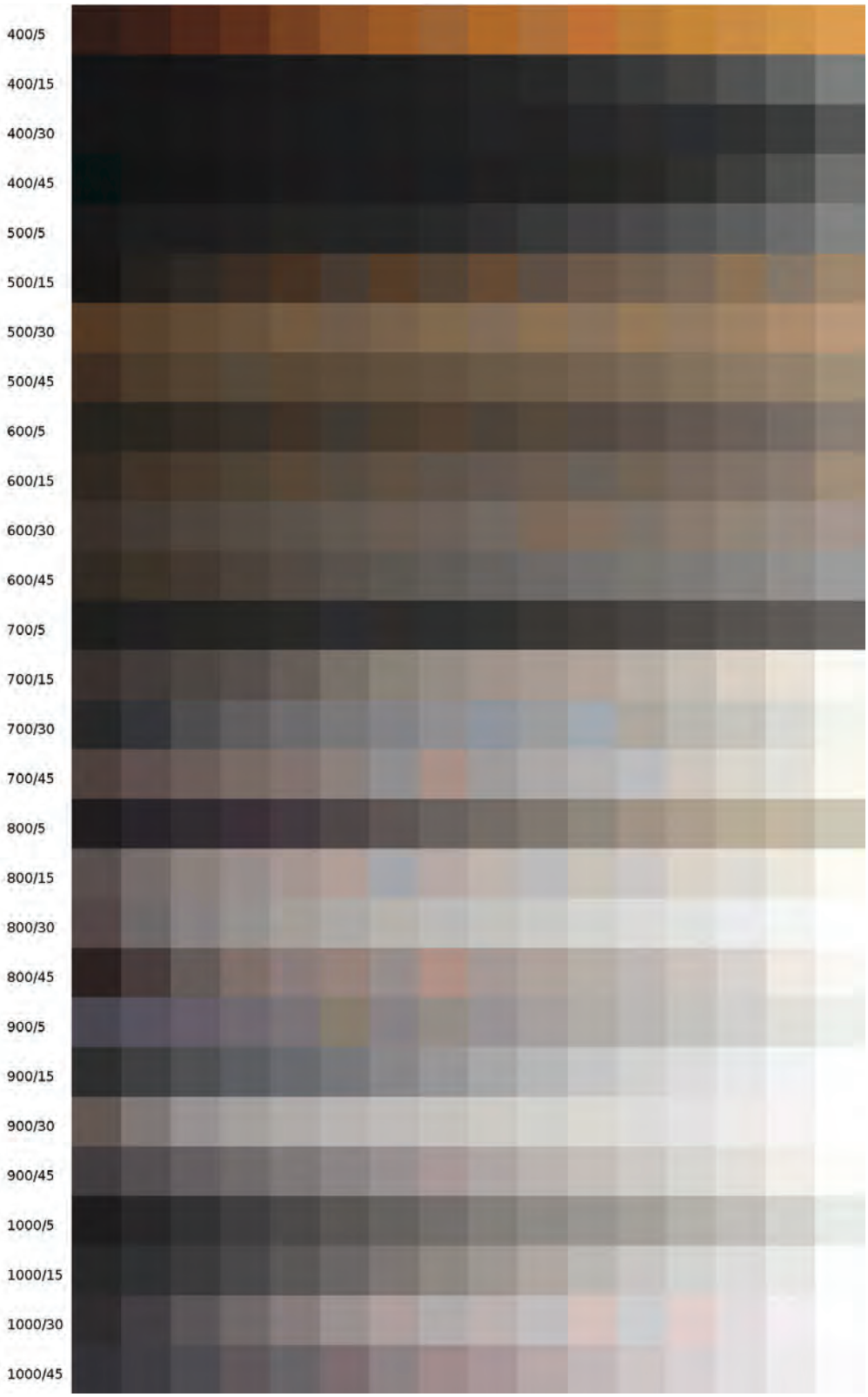

Figure 4.7 Palettes of root surface colour alterations after the application of the Wu-Chant colour reduction algorithm. Each row represents 16 colours of an individual duration group.

4.1.2. Hierarchical cluster analysis of colour alterations

Hierarchical tree diagrams were computed to visualise trends in surface colour alterations and to evaluate whether certain colours could be related to specific temperature regions. The distribution of colours of the individual duration and temperature groups within the L*a*b* colour space are given in Figure 4.8. A calculation of the Euclidean distances between each of the 448 colours provided the ΔE for all possible 100,128 pairings. The ΔE was found to range between 0 (no colour difference) and 99.6 (highly different colours; Figure 4.9), with a mean ΔE of 31.6 ± 20.1. Only 174 pairings had a ΔE of <1 (0.2%) and 1,026 pairings of <2.3 (1.0%), indicating that the vast majority of the colours provided in the reduced colour palettes are distinguishable as distinct colours by normal human vision (Lindbloom, 2009, Mahny et al., 1994, van der Haeghen and Naeyaert, 2006). Nonetheless, many colours within a group and between groups might appear similar.

Since the ΔE values do not provide information on the actual surface colours, a hierarchical cluster analysis of L*a*b* values was performed and visualised using dendrograms to investigate the potential usefulness of colour palettes for *a posteriori* determination of temperature ranges.

To investigate how related the colours might be, the branches of the dendrograms were ‘cut’ at a clustering distance that would provide the first five main clusters, containing between 11 and 175 colours (Figure 4.10). The earliest cluster of the dendrogram (Cluster 1) showed the highest level of dissimilarity and only contained eleven colours (2.5% of all colours), all of them belonging to the 400°C 5min group (Figure 4.11). Cluster 2 consisted of 86 colours (19.2%), with all of them associated with temperatures of 700°C or higher (Figure 4.12). The third cluster (Cluster 3, Figure 4.13) included 146 colours (32.6%) derived from 25 of the 28 duration groups (89%). Cluster 4 incorporated 29 colours (6.5%), mainly made up of colours from the 400°C 15 to 45min and 500°C 5min groups (86%; Figure 4.14). The fifth cluster (Cluster 5) consisted of 175 colours (39.1%) derived from all duration groups (Figure 4.15).

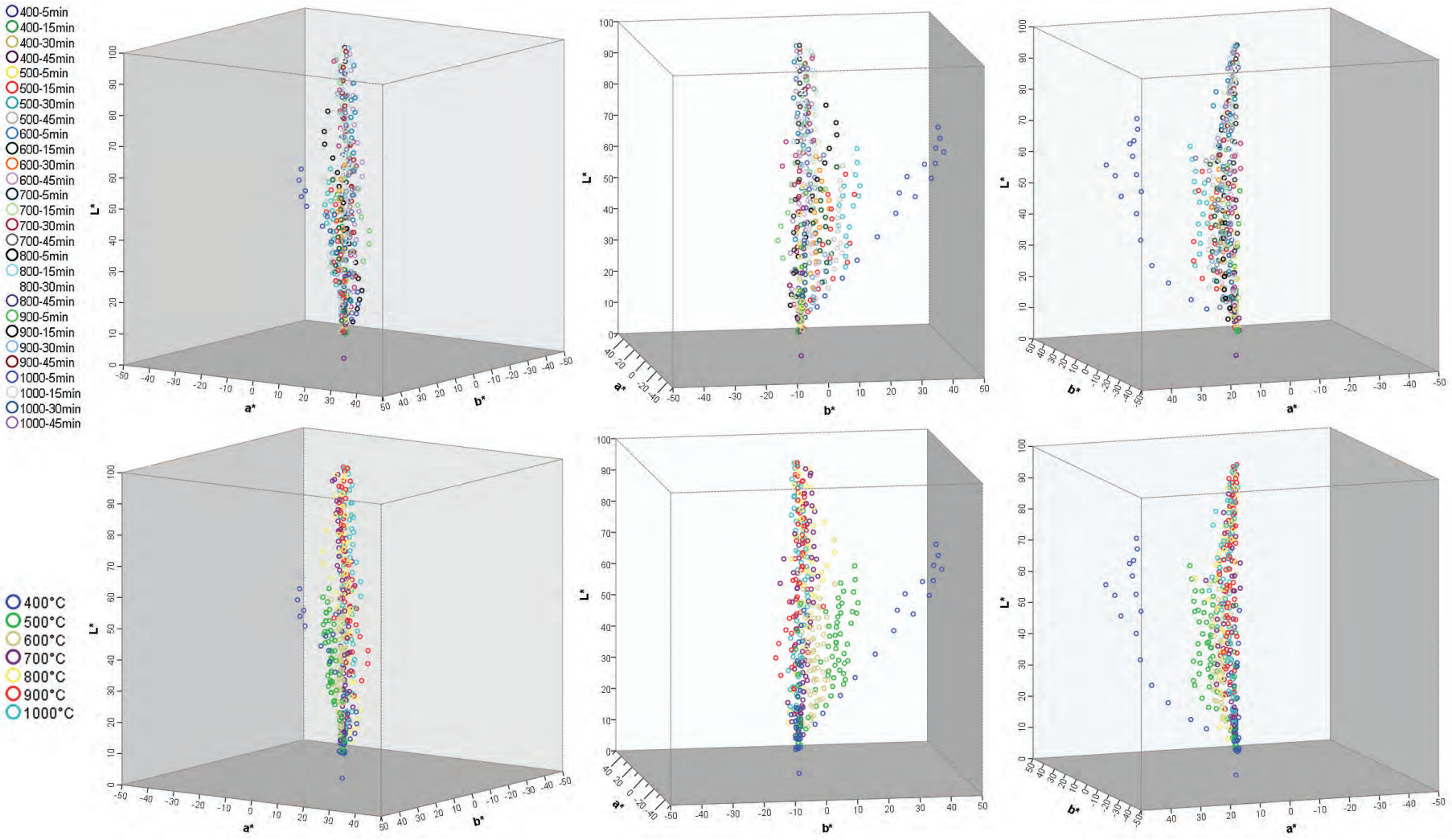

Figure 4.8 Colour distribution of the individual duration groups (top) and temperature groups (bottom) within the L*a*b* colour space.

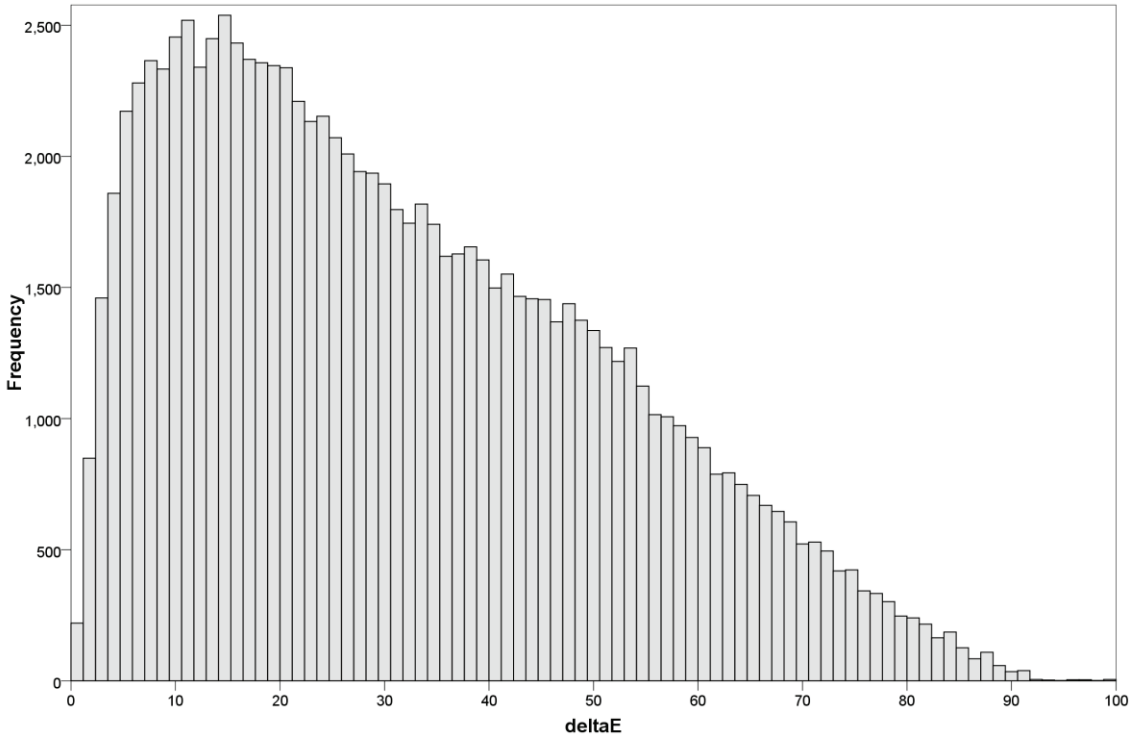

Figure 4.9 ΔE value distribution between each of the 448 colours (100,128 pairings)

The ΔE ranged between 0 (no colour difference) and 99.6 (highly different colours). The mean ΔE was 31.6 ± 20.1, with only 174 pairings having a ΔE of <1 (0.2%) and 1,026 pairings of <2.3 (1.0%), indicating that the vast majority of the colours provided in the reduced colour palettes could be differentiated by the normal human vision.

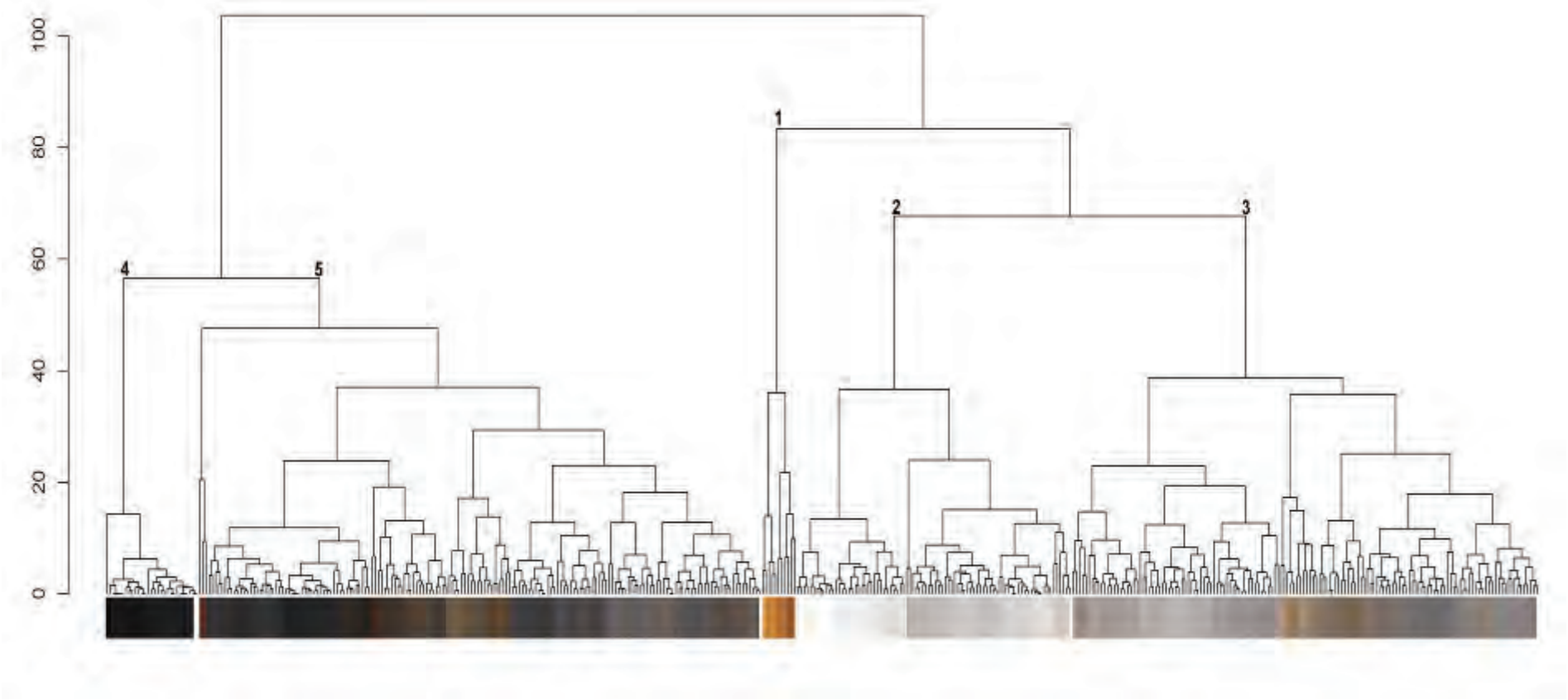

Figure 4.10 Hierarchical cluster analysis of root surface L*a*b*colours after 5, 15, 30 and 45min constant exposure to elevated temperatures (400 to 1000°C). The branches of the dendrogram were 'cut' at a distance of 50 to provide five main clusters, containing between eleven and 175 colours within a ΔE range of 50 or less.

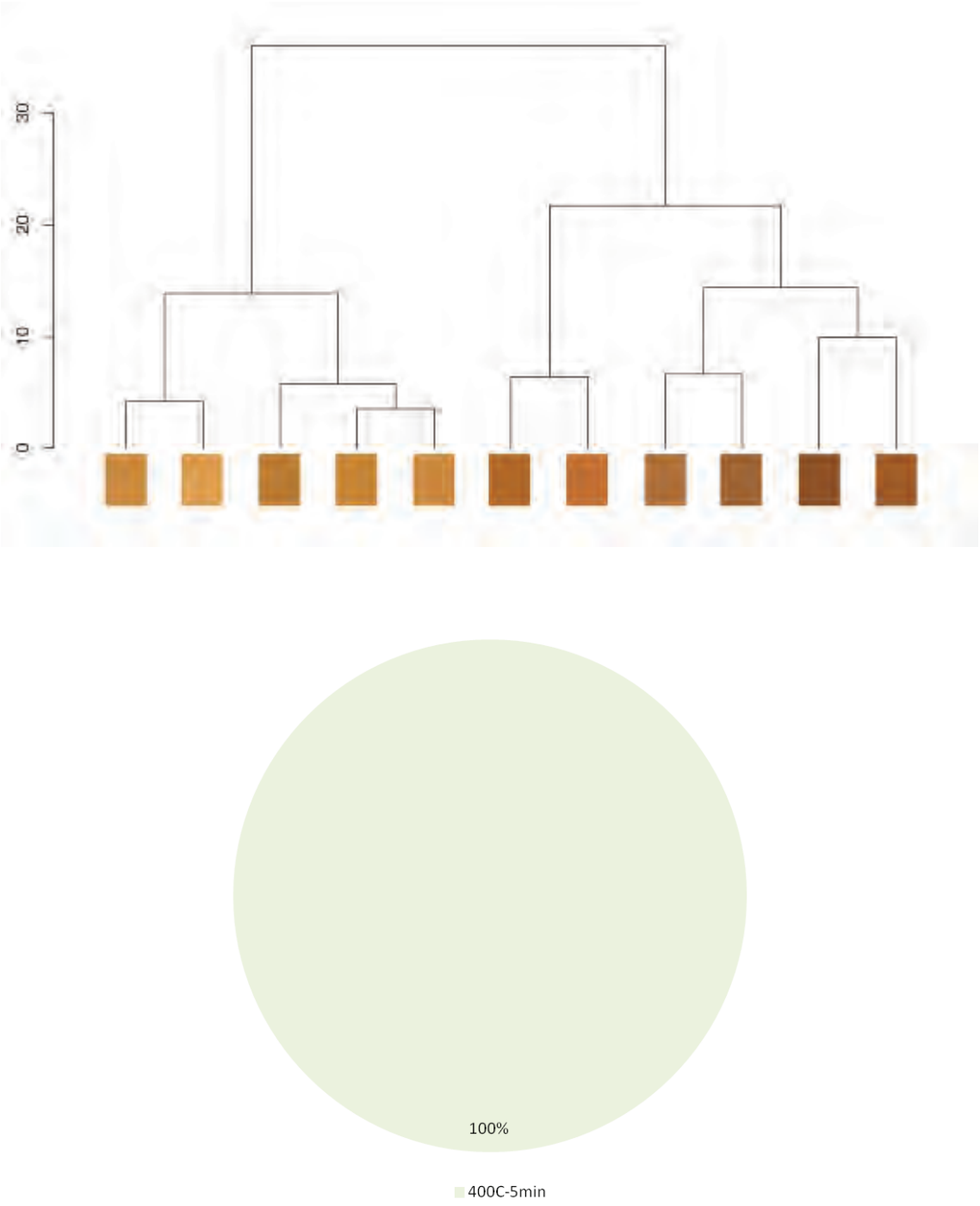

Figure 4.11 First cluster of root surface colour alterations. Dendrogram representing colours of Cluster 1 (n=11, 2.5% of all colours) and corresponding chart indicating that all colours of the cluster belong to the 400°C 5min group.

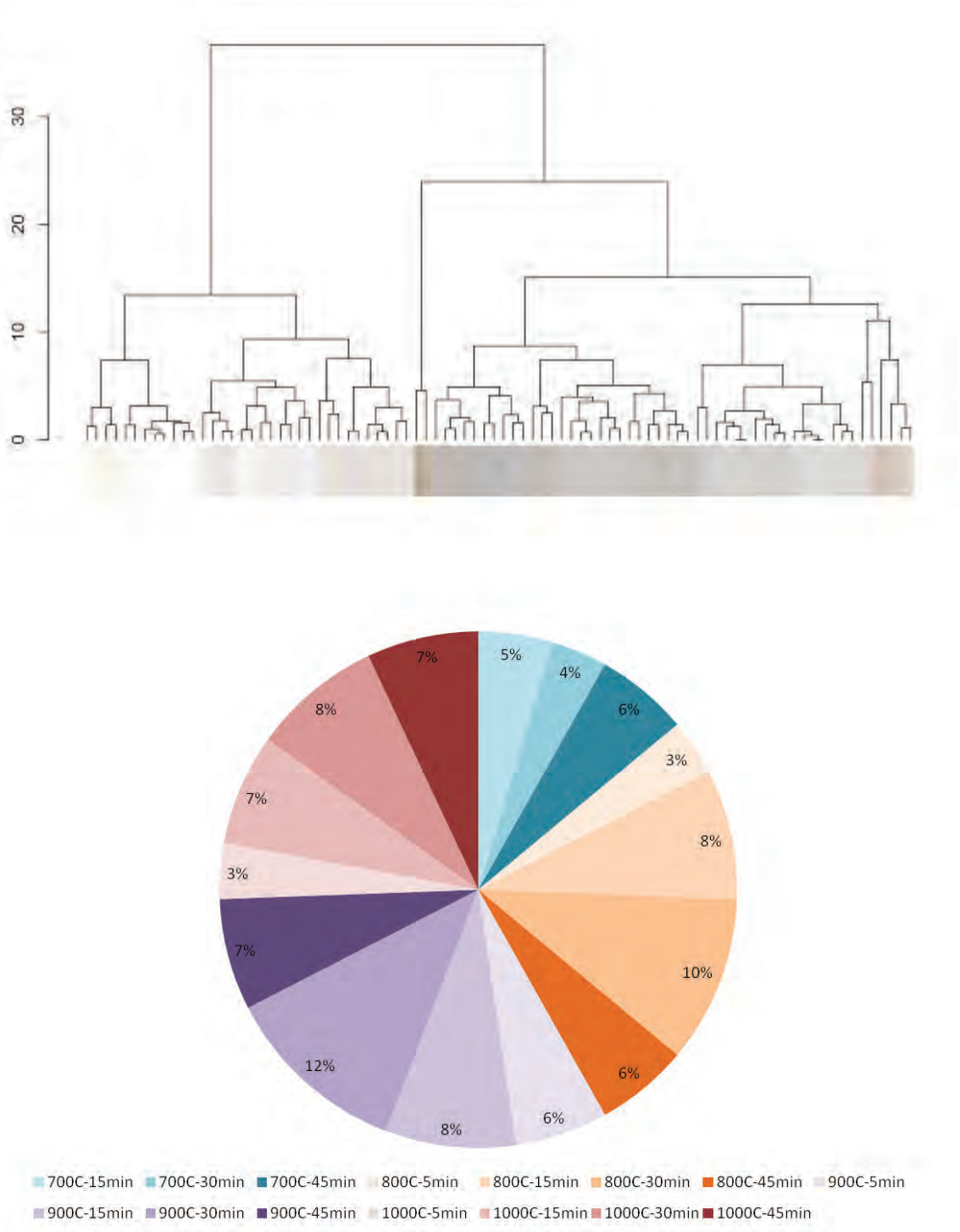

Figure 4.12 Second cluster of root surface colour alterations. Dendrogram representing colours of Cluster 2 (n=86, 19.2% of all colours) and corresponding chart indicating that colours of the cluster are associated with temperatures of 700°C or higher.

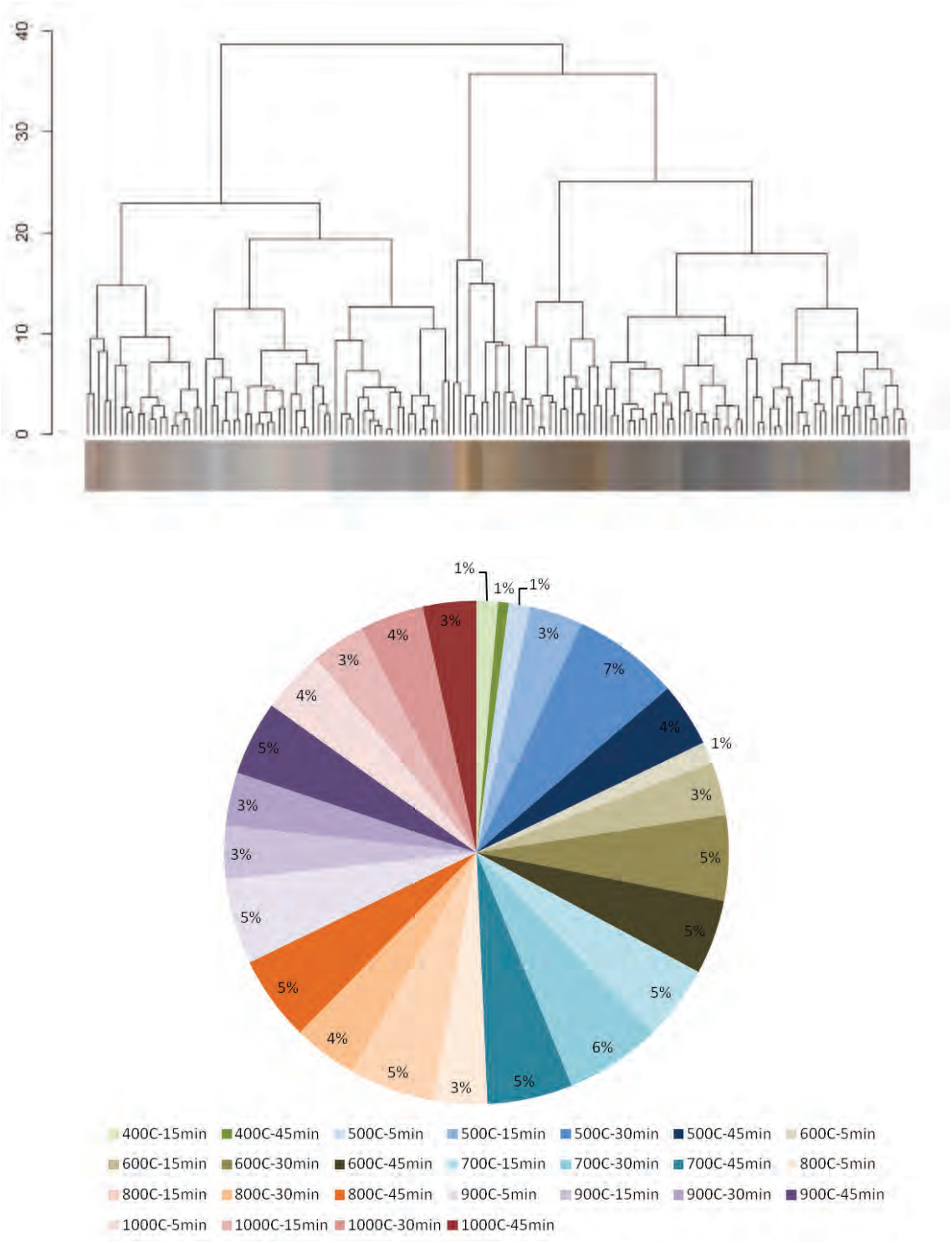

Figure 4.13 Third cluster of root surface colour alterations. Dendrogram representing colours of Cluster 3 (n=146, 32.6% of all colours) and corresponding chart showing that colours of the cluster are derived from 25 of the 28 duration groups.

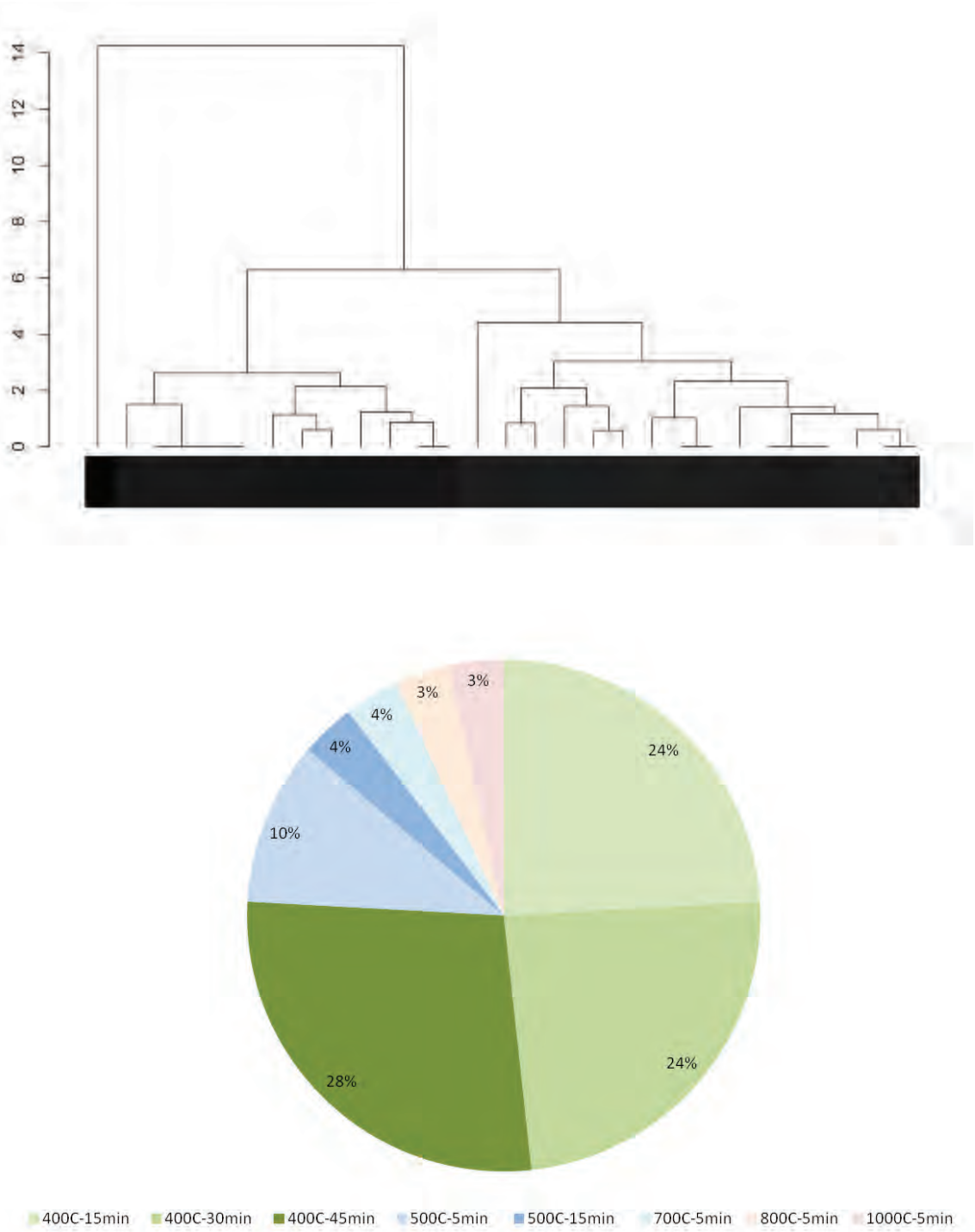

Figure 4.14 Fourth cluster of root surface colour alterations. Dendrogram representing colours of Cluster 4 (n=29, 6.5% of all colours) and corresponding chart presenting that this cluster is mainly made up of colours from the 400°C 15 to 45min and 500°C 5min groups.

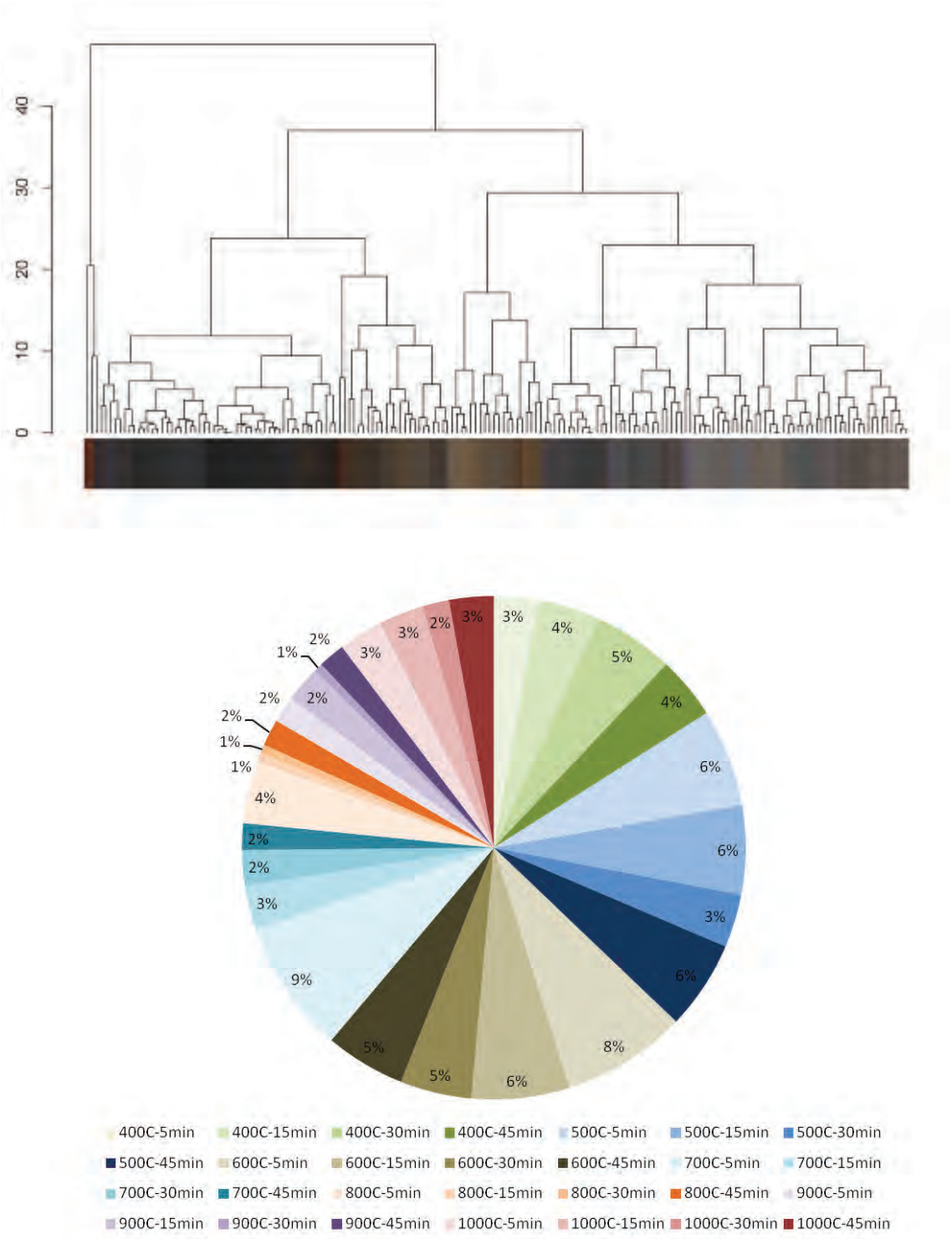

Figure 4.15 Fifth cluster of root surface colour alterations. Dendrogram representing colours of Cluster 5 (n=175, 39.1% of all colours) and corresponding chart showing that colours of the cluster are derived from all tested duration groups.

4.2. Influence of the heating regimes and soft tissue protection on surface colour

The influence of heating regimes and soft tissue protection on the roots' surface colour was tested using 36 posterior teeth (400, 700 and 900°C; Figure 4.16).

The 400°C incremental increase group visually appeared similar to the 400°C 5min constant exposure group, whilst teeth of the overnight cooling and soft tissue protection groups visually acquired similar surface colours as teeth with 15 to 45min constant exposure at 400°C or 5min at 500°C. In the 700°C groups, the heating regimes and soft tissue protection showed the biggest influence, with a variety of colours found in these groups. With exposure to higher temperatures (900°C) however, the visual colour difference between the individual groups was less apparent.

Similarly to the previous colour analysis, selections of 6,000 pixels (23.6mm^2 root surface area) were cropped from each tooth (n=36; Figure 4.17). The cropped regions had between 250 and 3,512 colours, adding up to a total of 47,064 colours for all 36 selections. Out of these 47,064 colours, 21,503 colours (45.7%) belonged to the 700°C groups. A colour reduction to 16 colours was performed by using the Wu-Quant colour reduction algorithm for the individual test groups (triplet of tiles; Figure 4.17). A total of 191 colours were found after the colour reduction, with one colour (0.5%) of the 900°C groups overlapping.

In the subsequent hierarchical cluster analysis, the branches of the dendrogram were 'cut' at a distance of 50 to provide four main clusters, containing between 15 and 85 colours (Figure 4.18 and 4.19). The first cluster contained 15 colours (7.8% of all colours), with 87% belonging to the 400°C incremental group. The second cluster included 85 colours (44.3% of all colours), mainly associated with the 700 and 900°C groups (89%). The third cluster consisted of 32 colours (16.7% of all colours) derived from all treatment groups. The fourth cluster incorporated 60 colours (31.2% of all colours), mainly made up of colours from the 400°C and 700°C groups.

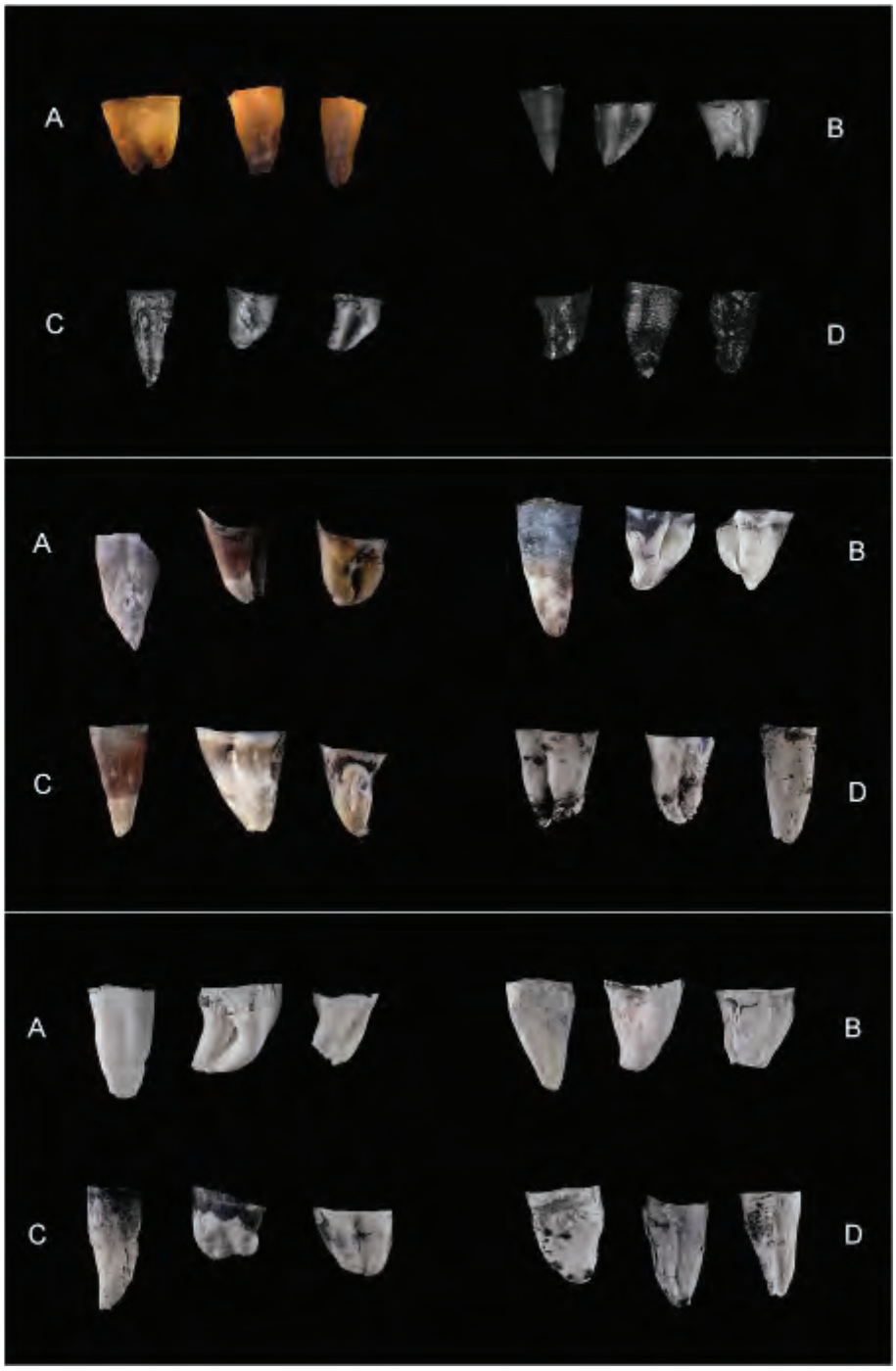

Figure 4.16 Differences in colour alterations of human teeth at 400, 700 and 900ºC using various heating regimes. **(A)** Incremental increase **(B)** 30min constant exposure **(C)** 30min constant exposure with overnight cooling and **(D)** 30min constant exposure with soft tissue protection.

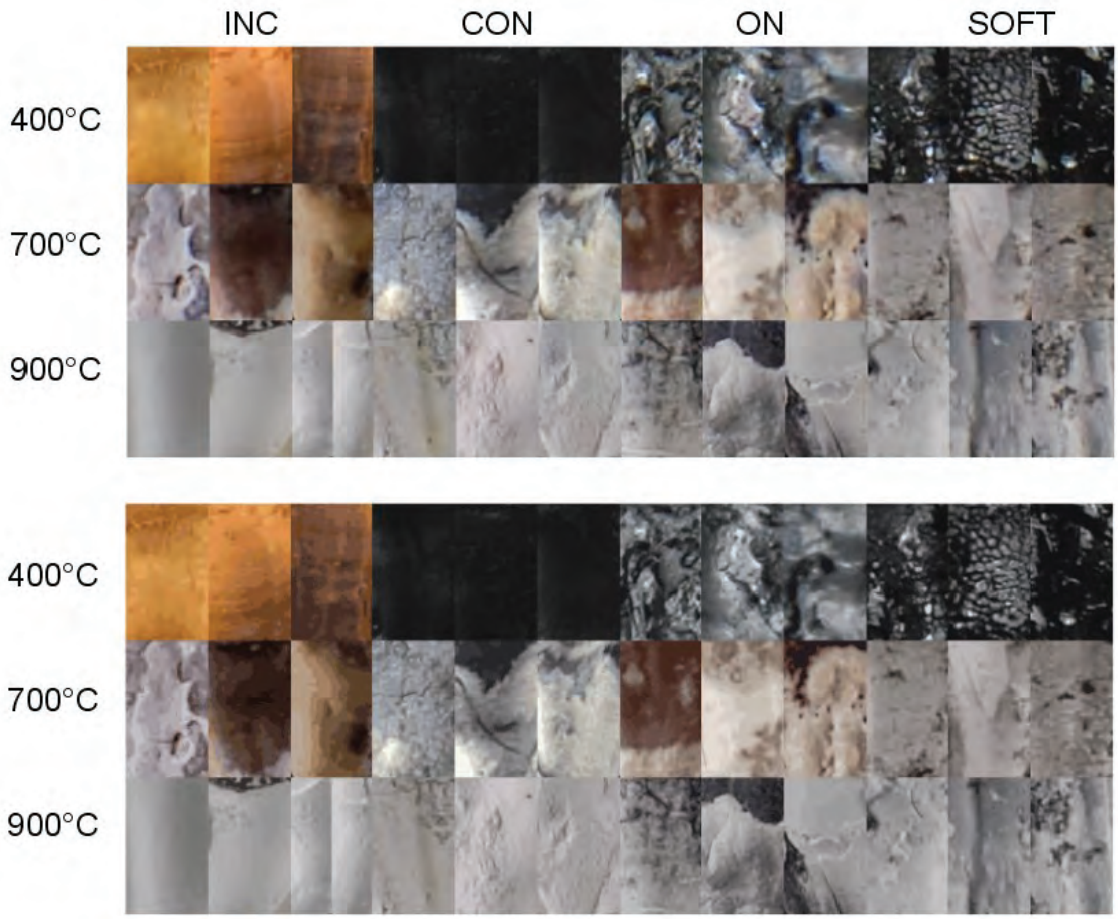

Figure 4.17 Root surface sections of the various heating regime groups before (top) and after the application of the Wu-Chant colour reduction algorithm (16 colours, bottom). Each row represents one temperature group, and triplets indicating the various heating regime groups. (INC) Incremental increase (CON) 30min constant exposure (ON) 30min constant exposure with overnight cooling and (SOFT) 30min constant exposure with soft tissue protection.

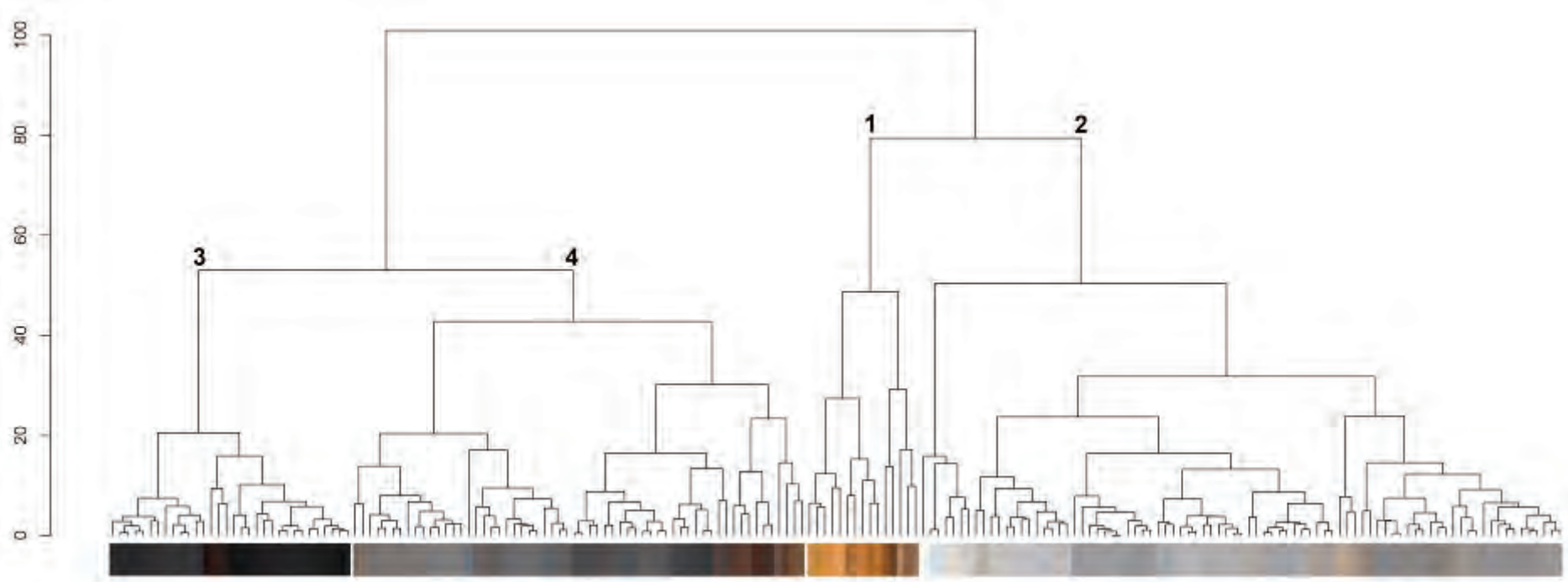

Figure 4.18 Hierarchical cluster analysis of root surface colours after exposure to 400, 700 and 900°C using various heating regimes. The branches of the dendrogram were 'cut' at a distance of 50 to identify four main clusters, containing between 15 and 85 colours.

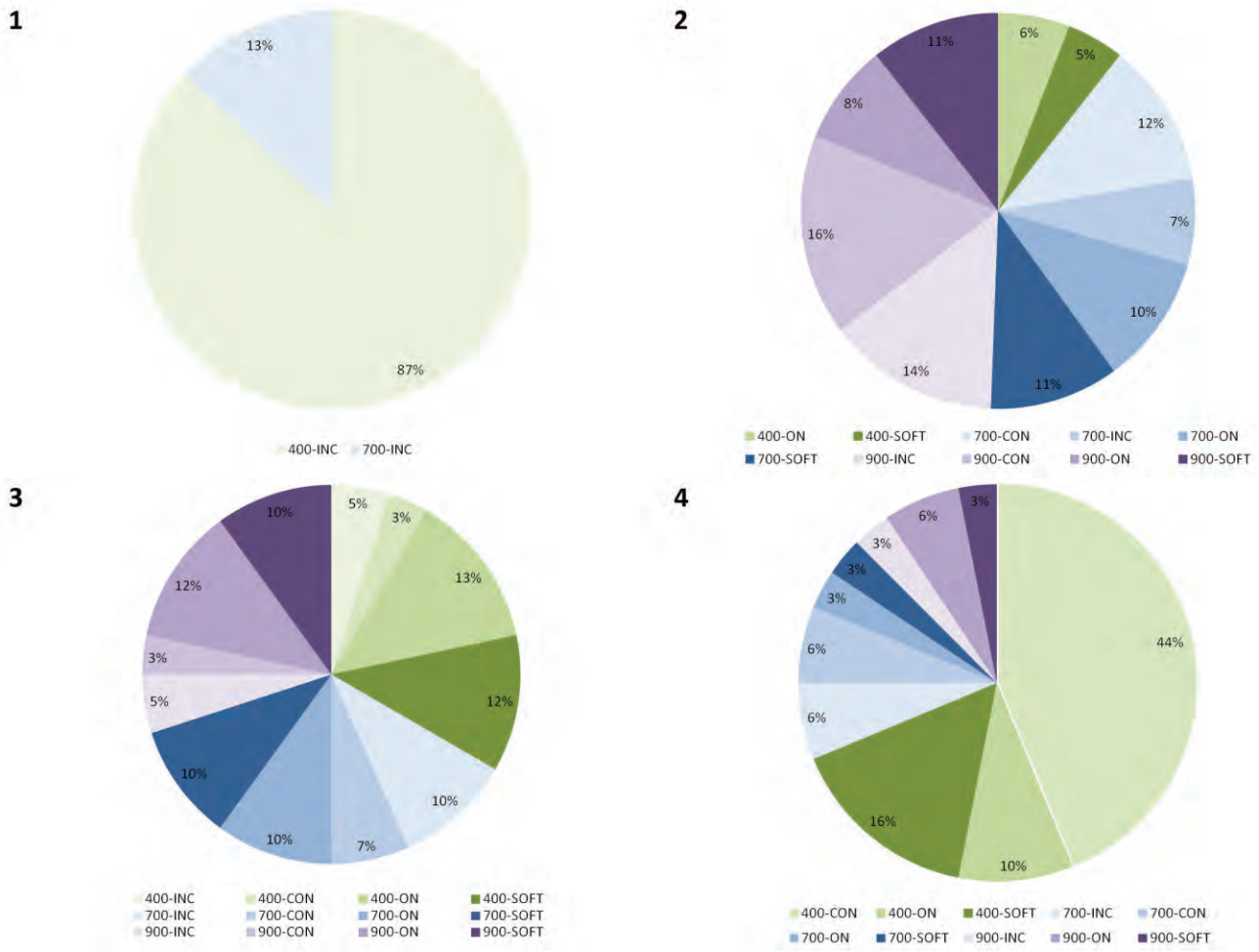

Figure 4.19 Composition of four main clusters of root surface colours after exposure to 400°C, 700°C and 900°C using various heating regimes.

Chapter 5 – Results: Heat-induced structural and dimensional alterations

The quantification of heat-induced structural alterations was made using video imaging and scanning electron microscopy, whilst dimensional and morphological alterations were evaluated with conventional radiography and micro-CT.

5.1. Failure of the dentine-enamel junction

A total of 104 teeth were used in the analysis of heat-induced structural alterations. The enamel remained attached to the dentine in all teeth of the 400°C test groups, partially separated from the coronal dentine or fragmented between 500 and 700°C and fully separated and fragmented in all teeth at or above 800°C (Figure 3.1). The failure of the dentine-enamel junction was captured as a video using a digital camera at 24 frames per second. Figure 5.1 shows subsequent still images of a video, showing the spontaneous separation of dentine and enamel between two frames (within 0.04 seconds). A discolouration of the adjacent coronal dentine was observed shortly before the initial failure. Infrared thermometer measurements indicated a surface temperature between 380 and 450°C when the initial shattering of the enamel occurred.

5.2. Cracks and fractures

Besides the separation and fragmentation of the enamel, heat-induced cracks and fractures were observed at high temperatures. Multiple superficial cracks were visible in SEM images (Figure 5.2). Fractures, referring to cracks that extended over an entire cross-section, could be visualised using conventional radiographs and micro-CT imaging. Micro-CT sections of all teeth of the lower temperature groups (≤ 600°C) showed multiple cracks in the apical dentine and cementum as well as single larger longitudinal cracks. At higher temperatures (700 to 1000°C) multiple larger longitudinal and numerous transversal fractures were visible in the dentine, originating from the root canals and pulp cavity (Figure 5.3).

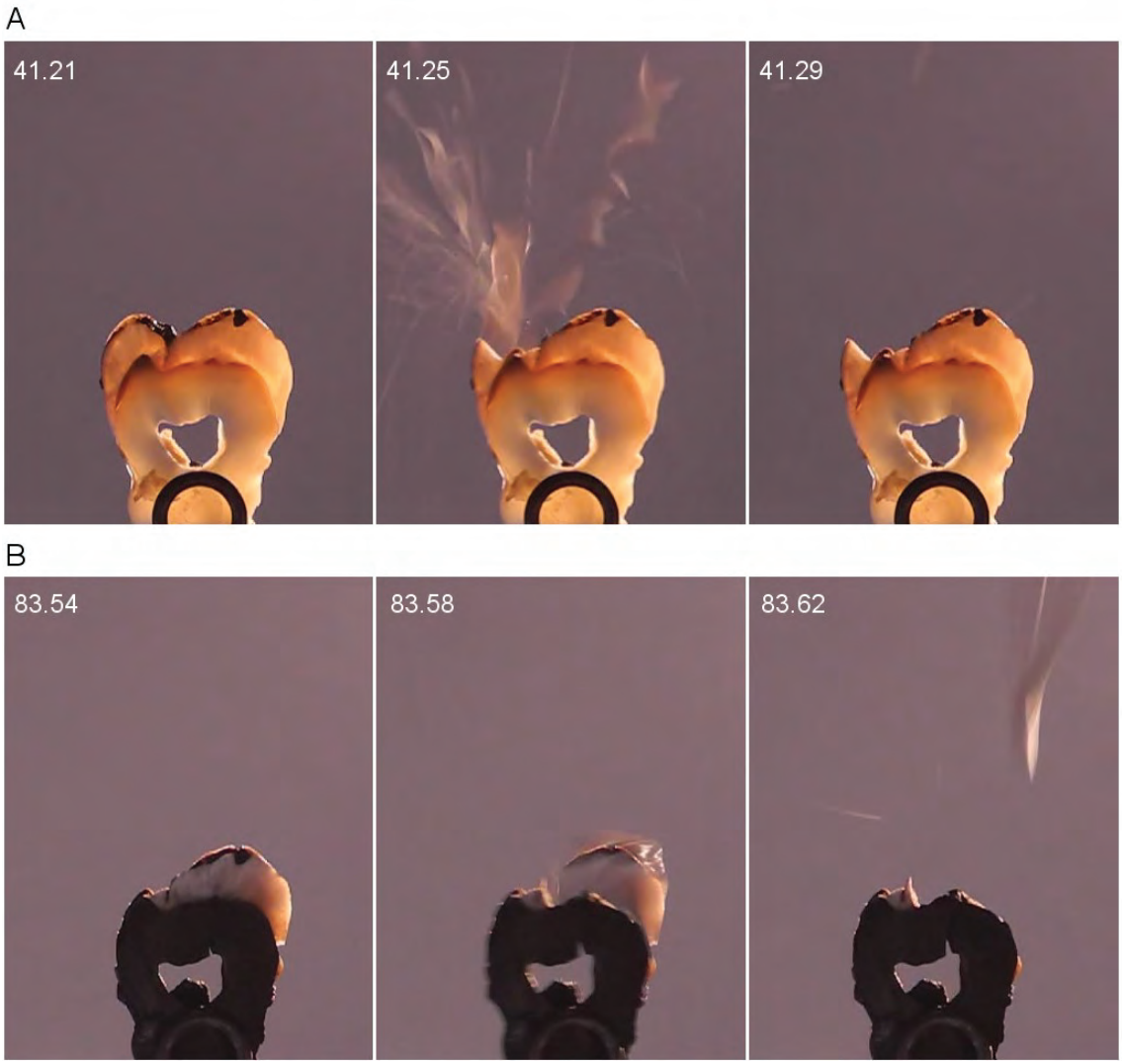

Figure 5.1 Separation of the enamel alongside the dentine-enamel junction

(A) Initial separation after 41 seconds exposure to a blue (Bunsen burner) flame (~600°C). The tooth surface temperature was ~380°C, with a darkening of the adjacent coronal dentine occurring shortly before shattering.

(B) Further separation of the enamel after 83 seconds heat exposure at a surface temperature of ~450°C.

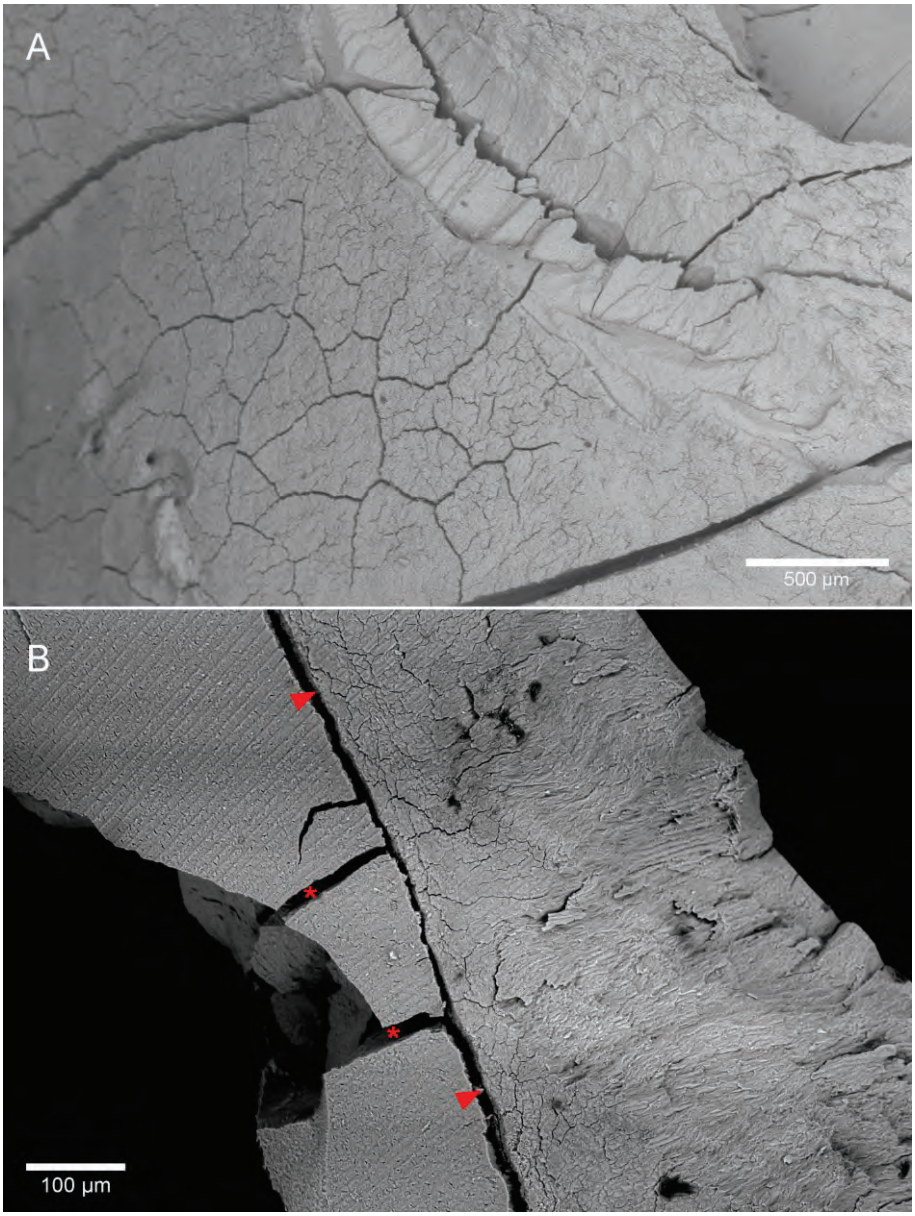

Figure 5.2 Visible cracks and fractures in scanning electron microscopic images

(A) Superficial cracks in the coronal dentine of a tooth from the 600°C 30min constant exposure group. Individual fractures and separation of enamel visible at 40× magnification

(B) Tooth fragment from the 900°C 30min constant exposure group showing the failure of the dentine-enamel junction (arrows) and deep cracks in dentine (asterisks) at 500× magnification.

Figure 5.3 Micro-CT cross-sections of premolars of the **(A)** 400, **(B)** 700 and **(C)** 900°C 30min constant exposure group. Visualisation of the dentinal volume loss using the registered pre- and post-scan sections (left) and cross-sections in the apical (middle) and coronal dentine (right). The cross-sections showed multiple cracks in the apical and coronal dentine and partial or full detachment and fragmentation of the crown. Scale bar = 1mm.

This figure is reprinted from Sandholzer et al. 'Radiologic evaluation of heat-induced shrinkage and shape preservation of human teeth using micro-CT' Journal of Forensic Radiology and Imaging 2013; 1(3), p.107-111, with permission from Elsevier.

5.2. Shrinkage

In total, 104 teeth were included in the statistical data analysis of heat-induced volumetric shrinkage. Due to the fragmentation and separation of enamel, the analysis primarily focused on the root and did not include the measurement of specific tooth dimensions. To prevent a false-positive influence of broken coronal dentine the analysed region of interest (ROI) was limited to non-fragmented dentine and a minimum of 400 micro-CT cross-sections (i.e. 5.4 mm) of the corresponding pre- and post-scans. A two-tailed independent sample t-test showed no statistical difference between the dentinal shrinkage of premolars and molars ($p=0.493$). The mean volumetric shrinkage in the 30min constant exposure groups was found to be between 4.8 (at 400°C) and 32.5% (at 1000°C, Table 5.1). The results indicate that minor shrinkage already occurred at temperatures as low as 400°C (4.8%), with a sharp increase between 700 and 800°C (11.5 to 24.2%). A one-way ANOVA with post-hoc LSD test showed significant differences in the rate of shrinkage at higher temperatures, whereas no significant differences were found between lower temperature groups (400 vs. 500°C ($p=0.642$); 500 vs. 600°C ($p=0.073$); 600 vs. 700°C ($p=0.060$)).

Moreover, the statistical analysis revealed that the heating regime did not influence the volumetric shrinkage at 400°C, however elongated exposure time to higher temperatures (700 and 900°C) was found to significantly increase the rate of shrinkage (Table 5.2).

In order to relate volumetric shrinkage resulting from micro-CT measurements to conventional radiographs, the rate of 2-D shrinkage was calculated. Assuming uniform shrinkage, the axonometric relationship between 2-D and 3-D shrinkage can be calculated independently of the shape of the object as: $(Shrinkage_{Vol})^{2/3}$. The 2-D shrinkage was found to range between 2.8% (at 400°C) and 10.2% (at 1000°C; Tables 5.1 and 5.2)

Table 5.1 Mean dentinal shrinkage after 30min constant exposure (n=56). Statistical significance was evaluated using a one-way ANOVA with 95% confidence interval (significance levels: * $p<0.05$, ** $p<0.005$, *** $p<0.0005$).

Temperature (°C)	**3-D Shrinkage (% ±1 SD)**	**2-D Shrinkage (%)**
400	4.8 ± 0.8	2.8
500	5.9 ± 1.4	3.3
600	8.7 ± 0.8	4.2
700	11.5 ± 1.5 *	5.1
800	24.2 ± 4.2 ***	8.4
900	27.5 ± 4.4 *	9.1
1000	32.5 ± 5.4 **	10.2

Table 5.2 Mean dentinal shrinkage using three different heating regimes (n=72). Statistical significance was evaluated using a one-way ANOVA with 95% confidence interval (significance levels: * $p<0.05$, ** $p<0.005$, *** $p<0.0005$).

Temperature (°C)	**3-D Shrinkage (% ±1 SD)**	**2-D Shrinkage (%)**
400 INC	5.04 ± 0.91	2.94
400 CON	4.78 ± 0.80	2.84
400 ON	5.61 ± 0.75	3.16
700 INC	9.16 ± 1.91	4.38
700 CON	11.53 ± 1.53	5.10
700 ON	16.61 ± 3.60 **	6.51
900 INC	25.47 ± 4.92	8.66
900 CON	27.50 ± 4.35	9.11
900 ON	31.14 ± 2.18 *	9.90

INC Incremental increase, removed from furnace when temperature was reached
CON Constant exposure for 30min, removed from furnace when duration was reached
ON Constant exposure for 30min, removed from furnace after cooling overnight.

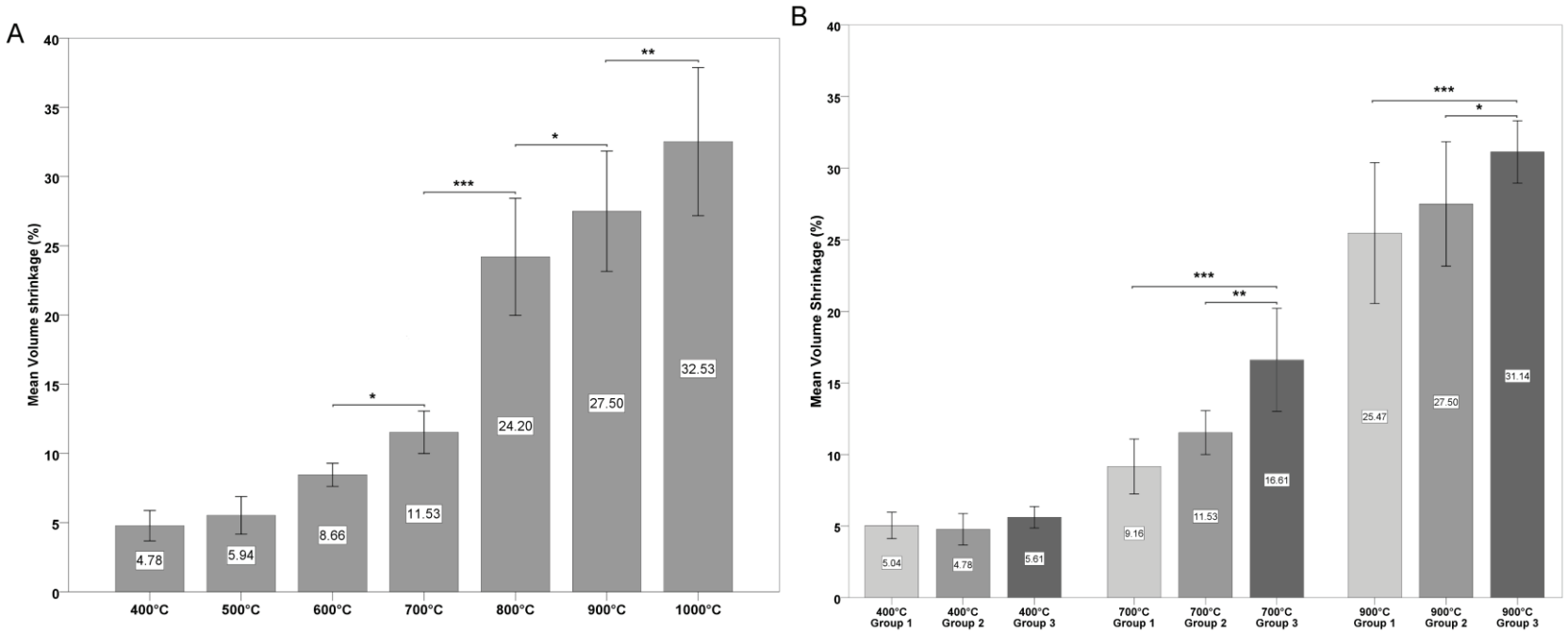

Group 1: Incremental increase, removed from furnace when temperature was reached
Group 2: Constant exposure for 30min, removed from furnace when duration was reached
Group 3: Constant exposure for 30min, removed from furnace after cooling overnight

Figure 5.4 Mean volumetric shrinkage of heat-affected teeth. Statistical significance was evaluated using a one-way ANOVA with 95% confidence interval (significance levels: * $p<0.05$, ** $p<0.005$, *** $p<0.0005$). **(A)** Volumetric shrinkage after 30min constant exposure showing statistically significant differences in higher temperature groups, whilst no significant statistical difference was found between lower temperature groups. **(B)** Influence of the heating regime on volumetric shrinkage present at higher temperatures (700°C and 900°C), whilst no influence found at 400°C.

5.3. Morphological preservation

Shape preservation of the dentine was investigated using digital radiographs, cross-sectional micro-CT images and 3-D models of the co-registered pre- and post-scans. Although fragmentation and cracks at high temperatures often affected the morphology of the root canals and pulp cavity, visually the shrinkage did not appear to influence tooth morphology.

The shrinkage can generally be described as uniform and the overall tooth morphology was well preserved in premolars and molars (Figure 5.5). Minor heat-induced contraction of the distal (apical) portions of the roots was found in the 3-D models of teeth heated at and above 800°C, but was not identifiable on the standard digital radiographs (Figure 5.6).

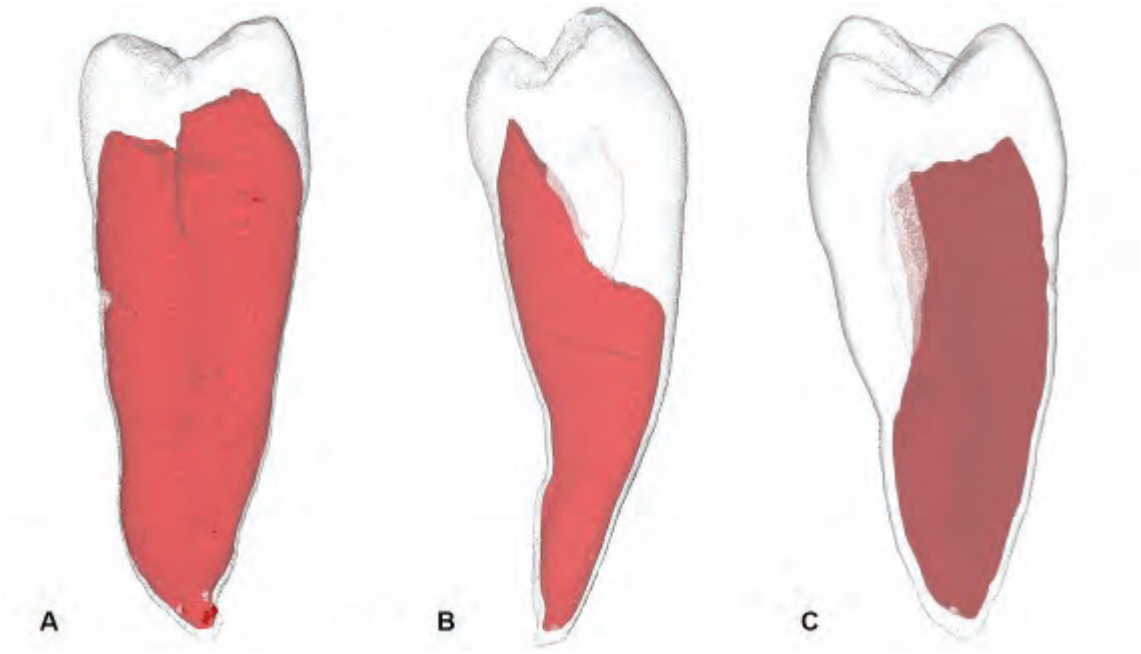

Figure 5.5 Comparative 3-D models indicating shape preservation after exposure to elevated temperatures (700 to 1000°C). Visualisation of dentinal volume loss using registered micro-CT pre- and post-scans at **(A)** 700, **(B)** 900 and **(C)** 1000°C indicating good preservation of tooth morphology.

This figure is reprinted from Sandholzer et al. 'Radiologic evaluation of heat-induced shrinkage and shape preservation of human teeth using micro-CT' Journal of Forensic Radiology and Imaging 2013; 1(3), p.107-111, with permission from Elsevier.

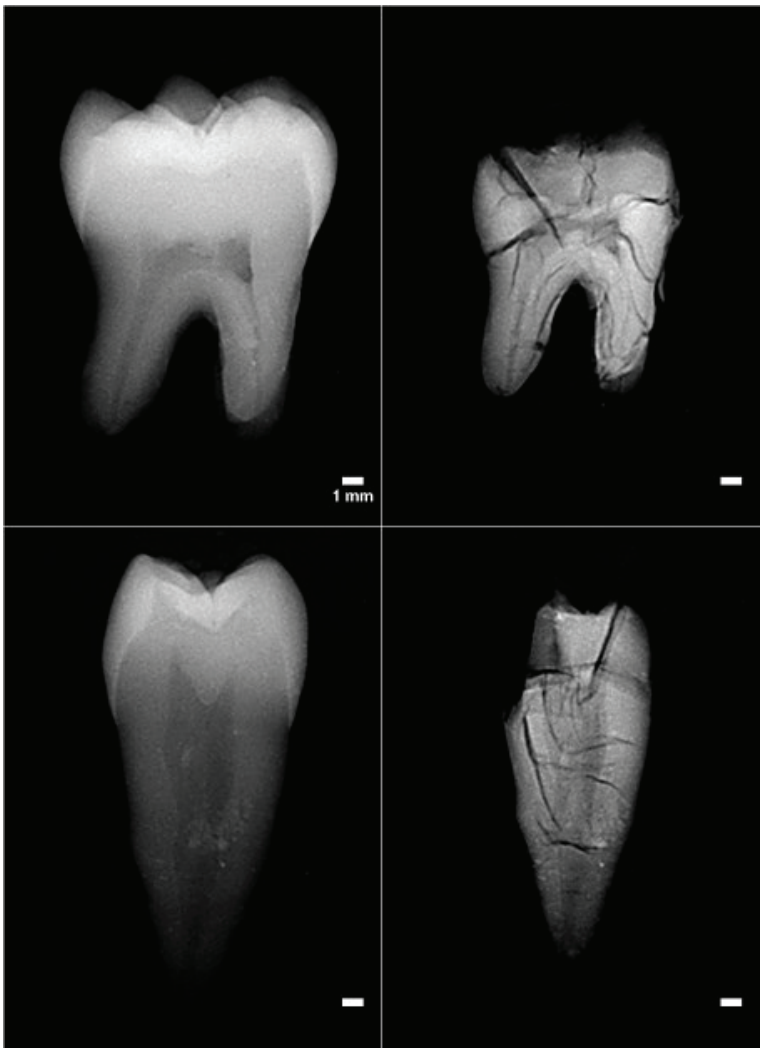

Figure 5.6 Corresponding digital radiographs indicating dentinal shrinkage and shape preservation of molars and premolars after 30min constant exposure at 900°C. Complete fragmentation of the crown and partially fragmented coronal dentine with multiple cracks and fractures present. Scale bar = 1mm.

This figure is reprinted from Sandholzer et al. 'Radiologic evaluation of heat-induced shrinkage and shape preservation of human teeth using micro-CT' Journal of Forensic Radiology and Imaging 2013; 1(3), p.107-111, with permission from Elsevier.

Chapter 6 – Results: Heat-induced crystalline alterations

The heat-induced crystalline alterations of dental tissues were analysed using synchrotron-based X-ray scattering experiments. The small- and wide-angle X-ray scattering (SAXS/WAXS) patterns provided information on crystallite dimensions, the degree of alignment and crystallite shape.

6.1. Macroscopic and microscopic alterations

Fourteen tooth sections (3×1×0.5mm) were analysed in the *ex situ* synchrotron X-ray scattering experiment, and three 1mm bucco-lingual cross-sections were used in the real-time synchrotron X-ray scattering experiment. The *ex situ* samples showed a progressive, temperature-dependent shift in surface colours similar to the changes observed for entire teeth (Figure 6.1). Micro-CT revealed that in all heated *ex situ* samples cracks were present in dentine, with multiple and larger cracks observed in cross-sections at and above exposure to 700°C (Figure 6.1). Fragments of enamel remained attached in samples up to 800°C in the *ex situ* experiment, enabling SAXS/WAXS analysis of enamel and dentine. Due to setup restrictions of the real-time X-ray scattering experiments (i.e. radiation inside the experimental hutch and limited size of observation window of furnace), colour alterations and temperature of enamel separation could not be documented.

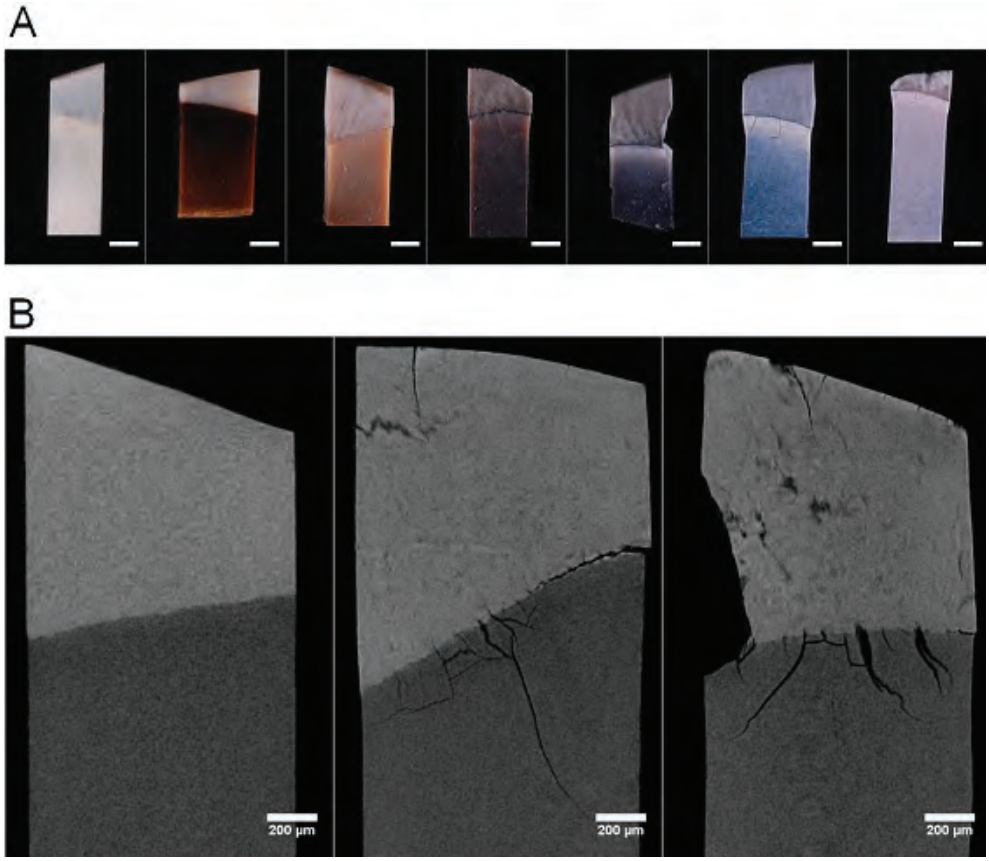

Figure 6.1 Documentation of tooth sections used for the *ex situ* synchrotron X-ray scattering experiment

(A) Surface colour alterations of tooth sections (3×1×0.5mm) heated for 30min at 400 to 900°C (in steps of 100°C). Scale bars = 500µm. Please note that illumination varied from previous surface colour photographs and colour calibration could not be performed due to small specimen size.

(B) Micro-CT maximum-intensity projections of tooth sections (RT, 500 and 700°C) used for the *ex situ* X-ray scattering experiment showing heat-induced cracks within dentine and enamel.

6.2. *Ex situ* synchrotron small-angle X-Ray scattering (SAXS) measurements

Initially, two longitudinal line scans with 14 scattering patterns each were collected in transmission mode from fixed locations within each sample (scan step 100µm). A total of 13 measurements (three in enamel, ten in dentine) that could be clearly attributed to the respective tissue were included in the statistical analysis. Additional transverse line scans with six scattering patterns each were performed for sections of the 400, 600 and 800°C groups. To further document spatial variation of the measurements for all samples, 0.6×0.6mm ROIs including the dentine-enamel junction were mapped (scan step 40µm), resulting in a 15×15 grid containing 225 scattering patterns.

6.2.1. Mean crystallite thickness

The mean crystallite thickness nearly tripled in dentine from 2.01nm at room temperature to 5.58nm at 900°C (2.8-fold increase). Moreover, the mean crystallite thickness of dentine did not vary in the transverse direction at any of the test temperatures ($p=0.875$ for 400°C; $p=0.274$ for 600°C; $p=0.097$ for 800°C). In contrast, the mean crystallite thickness of enamel only increased 1.4-fold from 3.93nm at RT to 5.34nm at 800°C (Figure 6.2). Table 6.1 summarises the mean crystallite thickness variation of all test groups (RT, 400 to 900°C). An overview of the variation of the mean crystallite thickness variation in the 0.6×0.6mm ROIs is given in Figure 6.5, confirming that dentine and enamel could be easily distinguished based on their mean crystallite thickness. Generally, the crystallite dimensions within both tissues were lower around the dentine-enamel junction from room temperature up to 500°C. This trend could also be observed at higher temperatures (<700°C), although the difference of the mean crystallite thickness in dentine and enamel was smaller.

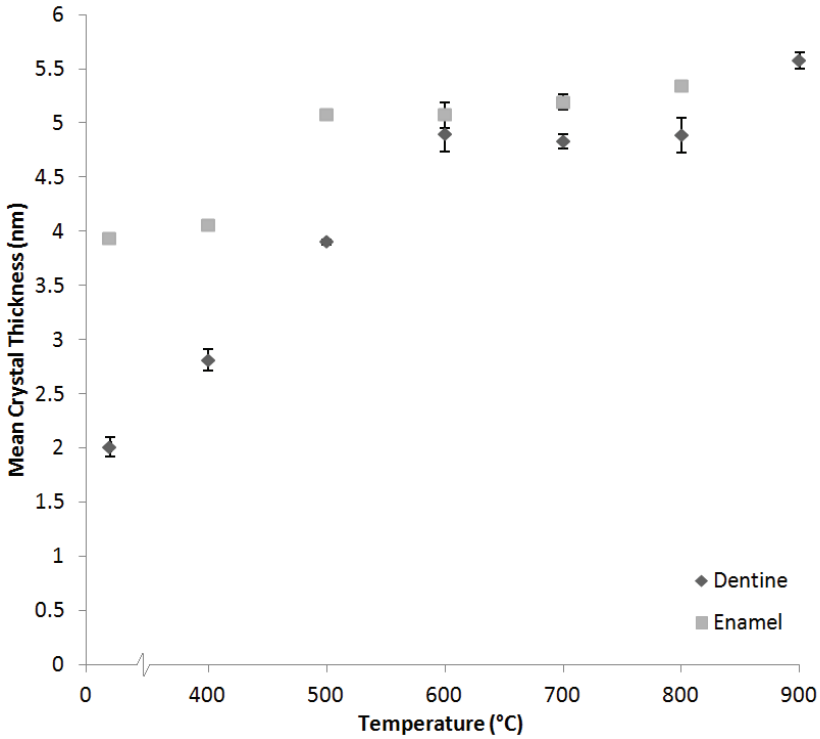

Figure 6.2 Variation of the mean crystallite thickness in dentine and enamel determined by SAXS

Thirteen longitudinal line measurements were included (three for enamel, ten for dentine). The mean crystallite thickness of dentine increased from 2.01nm at RT to 5.58nm at 900°C, and the mean crystallite thickness of enamel increased from 3.93nm at RT to 5.34nm at 800°C. Error bars ± 1SD.

6.2.2. Crystalline degree of alignment

The values for the crystalline degree of alignment can range between 0 and 1, where 0 describes no predominant orientation with the plane of section whilst 1 indicates perfect alignment of all crystallites. Figure 6.3 shows the average degree of alignment derived from ten scanning patterns in dentine and three patterns in enamel of the individual test groups. The overall degree of alignment of crystallites in dentine decreased from 0.27 at RT to 0.15 at 900°C, whilst the degree of alignment in enamel dropped from 0.64 at RT to 0.36 at 800°C, indicating a more disordered orientation of the crystallites as temperature increased (Table 6.1).

The main drop in alignment was seen in the dentine adjacent to the dentine-enamel junction when plotting the individual values of the line measurements (Figure 6.4). In enamel and distant dentine the degree of alignment appeared to be less variable throughout all test groups. Similar trends for the degree of alignment variation were found in the 0.6×0.6mm ROIs (Figure 6.5). The lowest degree of alignment was visible around the dentine-enamel junction, with a decreasing trend of alignment in dentine towards the dentine-enamel junction.

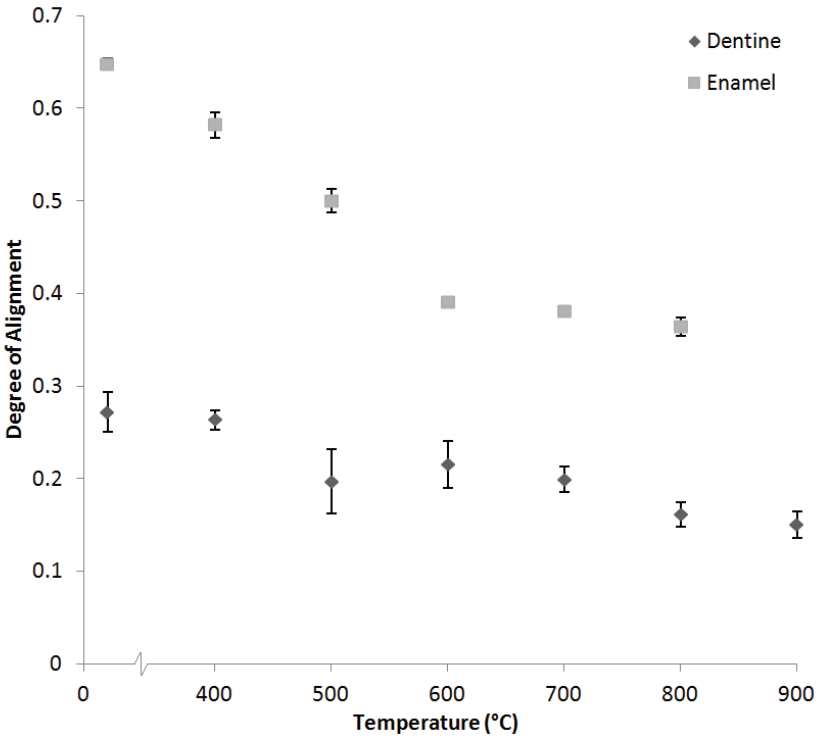

Figure 6.3 Variation of the degree of alignment in dentine and enamel determined by SAXS

Thirteen measurements were taken in longitudinal direction (three for enamel, ten for dentine). The degree of alignment of crystallites in dentine decreased from 0.27 at RT to 0.15 at 900°C and from 0.64 at RT to 0.36 at 800°C in enamel, indicating a more random orientation of the crystallites with increasing temperature. Error bars ± 1SD.

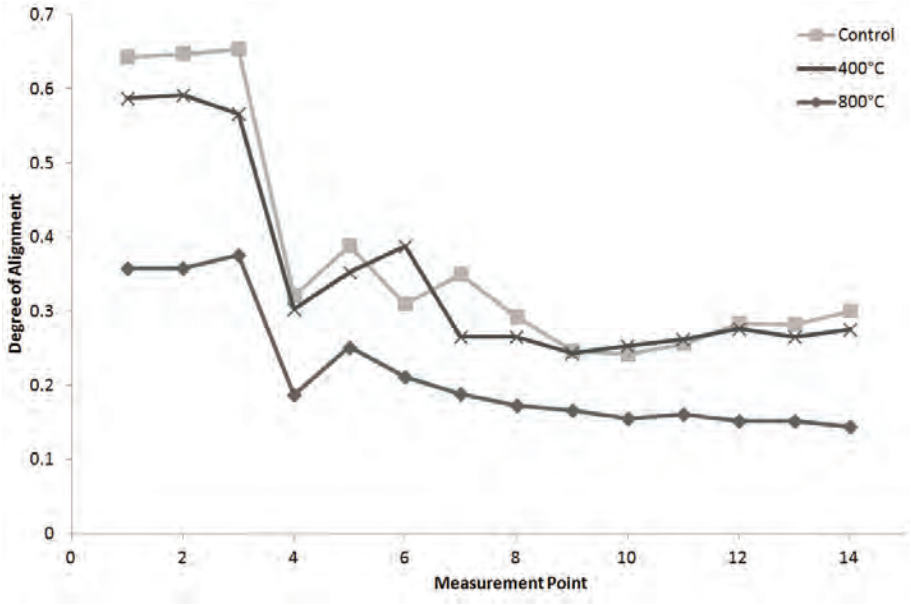

Figure 6.4 Representative variation of degree of alignment in dentine and enamel at RT, 400 and 800°C

Thirteen measurements (step size: 100µm) were taken in longitudinal direction (three for enamel, ten for dentine). A major drop in the degree of alignment was visible around the dentine-enamel junction (Measurement point 4-6), whilst in the enamel (Measurement points 1-3) and distant dentine (Measurement points 7-14) the degree of alignment appeared less variable.

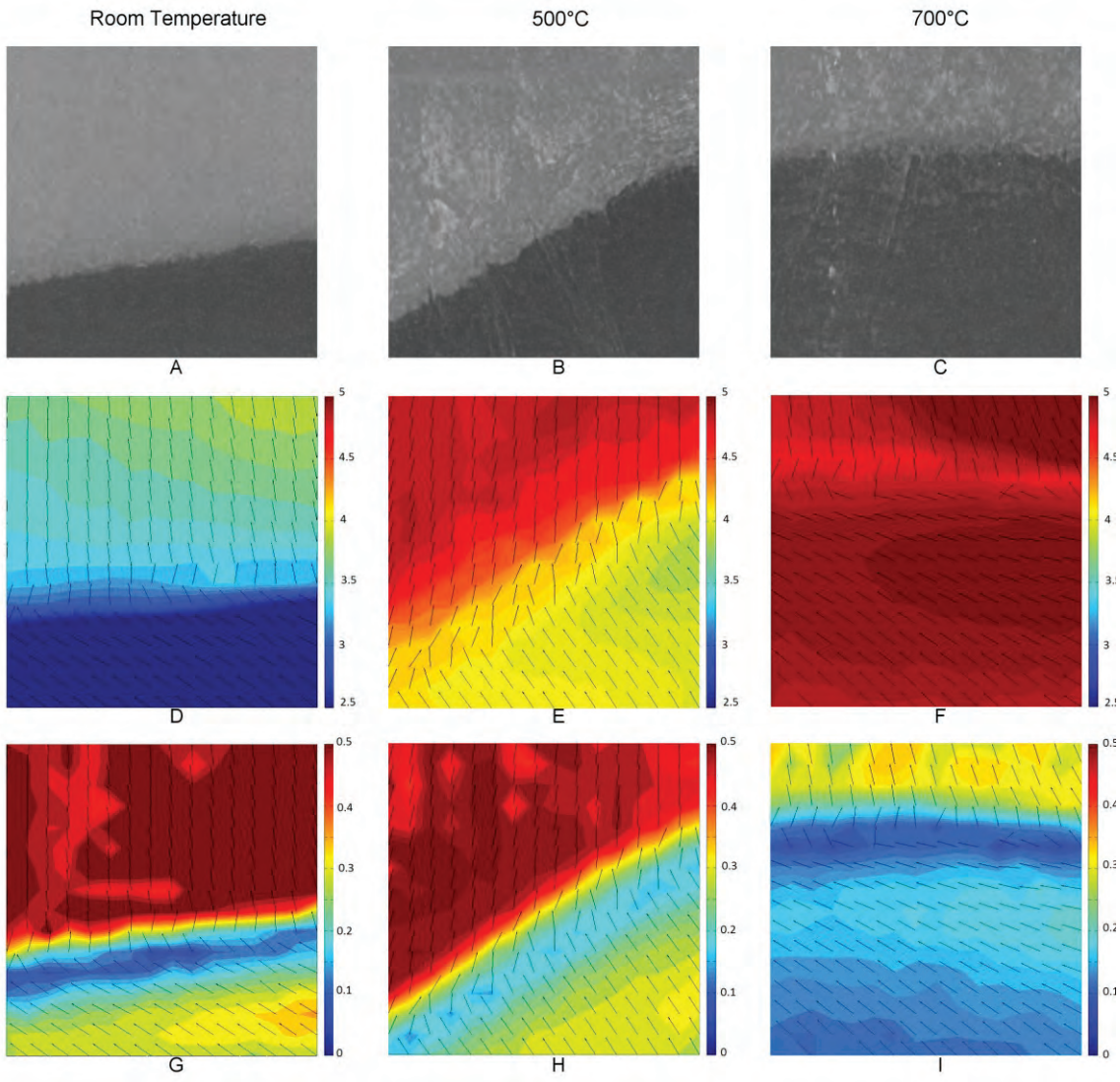

Figure 6.5 Regions of interest (0.6×0.6mm) of tooth section containing 225 SAXS patterns

(A-C) Micro-CT cross-section of the ROI at RT, 500 and 700°C; **(D-F)** Colour-coded mean crystallite thickness (nm) map with crystallite orientation marked as a vector field with black arrows; **(G-I)** Colour-coded degree of alignment map with crystallite orientation marked as a vector field with black arrows.

6.2.3. Crystallite shape

The crystallite shape variation in dentine and enamel computed from the *ex situ* synchrotron SAXS measurements is given in Figure 6.6. The dentine crystallites had a needle-like morphology at room temperature (ρ=1.40), changing to a more platelet-like morphology at 400 to 500°C (ρ=2.03-2.19) and finally to a polydisperse (i.e. complex) morphology at 600 to 900°C (ρ=3.22-3.53). The crystallite shape of enamel was found to be polydisperse (ρ=2.77-3.27) in all test groups (Table 6.1).

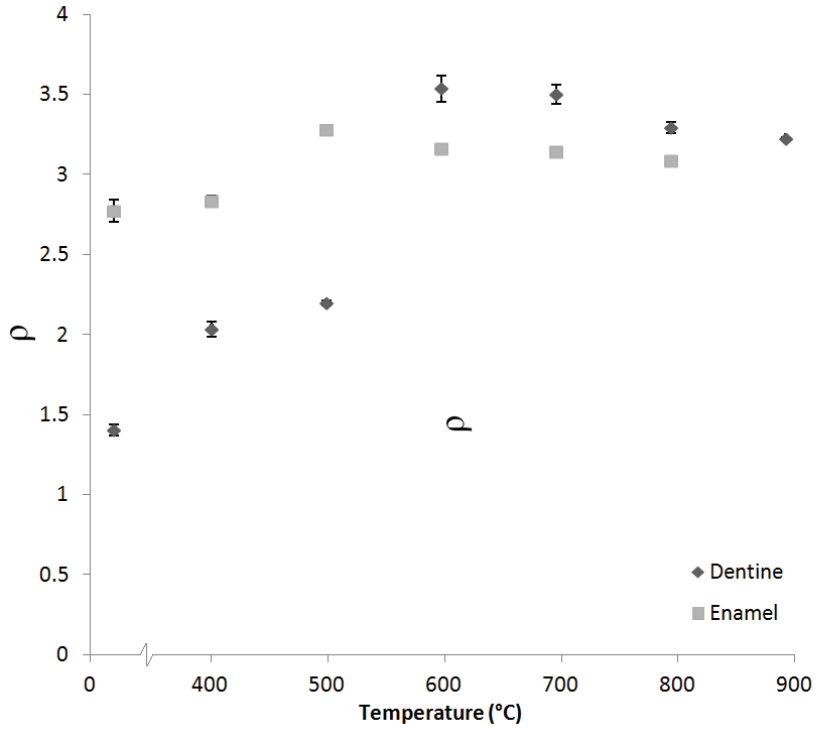

Figure 6.6 Variations of crystallite shape in dentine and enamel determined by SAXS

Thirteen measurements were taken in longitudinal direction (three for enamel, ten for dentine). The calculations indicate that a needle-like morphology (1.40) at RT, changing to a more platelet-like morphology at 400 to 500°C (2.03-2.19) and finally to a polydisperse morphology at 600 to 900°C (3.53-3.22). The shape of enamel crystallites was found to be polydisperse (2.77-3.27) in all test groups. Error bars ± 1SD.

Table 6.1 Overview of *ex situ* synchrotron SAXS results on mean thickness, degree of alignment and shape of dentine and enamel crystallites. Thirteen measurements were taken in longitudinal direction (three for enamel, ten for dentine), Mean thickness results from transverse line scans (trans) with six dentine scattering patterns for selected samples of 400, 600 and 800°C. Statistical significance was evaluated using a one-way ANOVA with 95% confidence interval for the mean thickness results (Significance levels: * $p<0.05$, ** $p<0.005$, *** $p<0.0005$).

Temperature (°C)	**Dentine Mean Thickness (nm ±1 SD)**	**Enamel Mean Thickness (nm ±1 SD)**	**Degree of Alignment Dentine (± 1SD)**	**Degree of Alignment Enamel (± 1SD)**	**Crystallite Shape Dentine (± 1SD)**	**Crystallite Shape Enamel (± 1SD)**
CTL	2.01 ± 0.09	3.93 ± 0.05	0.27 ± 0.02	0.65 ± 0.01	1.40 ± 0.04	2.77 ± 0.07
400	2.81 ± 0.10***	4.05 ± 0.01	0.26 ± 0.01	0.58 ± 0.01	2.03 ± 0.05	2.84 ± 0.03
500	3.90 ± 0.02***	5.08 ± 0.04***	0.20 ± 0.03	0.50 ± 0.01	2.20 ± 0.01	3.28 ± 0.01
600	4.90 ± 0.16***	5.07 ± 0.12	0.22 ± 0.03	0.39 ± 0.01	3.53 ± 0.08	3.16 ± 0.02
700	4.83 ± 0.06	5.19 ± 0.07	0.20 ± 0.01	0.38 ± 0.01	3.50 ± 0.06	3.14 ± 0.07
800	4.88 ± 0.16	5.34 ± 0.03	0.16 ± 0.01	0.36 ± 0.01	3.29 ± 0.04	3.09 ± 0.05
900	5.58 ± 0.08***	---	0.15 ± 0.01	---	3.22 ± 0.09	---
400trans	2.83 ± 0.05					
600trans	4.89 ± 0.01					
800trans	4.80 ± 0.03					

This table is reprinted from Sandholzer et al. 'X-ray scattering evaluation of ultrastructural changes of human dental tissue with thermal treatment' Journal of Forensic Sciences 2014; 59(3) 769-774, DOI 10.1111/1556-4029.12400, with permission from Wiley-Blackwell

6.3. *Ex situ* synchrotron wide-angle X-Ray scattering (WAXS) measurements

Due to the limited size of the 2-D detector in the *ex situ* synchrotron experiment, only the (002) peak could be captured and analysed. Figure 6.7 shows representative WAXS results for dentine from a series of tooth sections (RT, 400, 700, 800 and 900°C) for the particular region of scattering angles associated with the (002) peak (11.2-11.5°). After the disappearance of the organic components, sintering of the hydroxyapatite crystallites led to grain growth and greater crystal perfection between 700 and 800°C, reflecting in a sharpening of the diffraction peaks (Figure 6.7). This indicated an increased diffraction contribution from larger particles above 800°C as well as a peak separation appearing at 900°C.

By fitting the peaks of the control and 900°C sample, a full width at half maximum (FWHM) variation ratio of 0.13:0.039 (dentine) and 0.05:0.04 (enamel) was found. This ratio showed that the crystallites appeared 3.3-fold larger in dentine (at 900°C) and 1.3-fold larger in enamel (at 800°C) compared to the control sample.

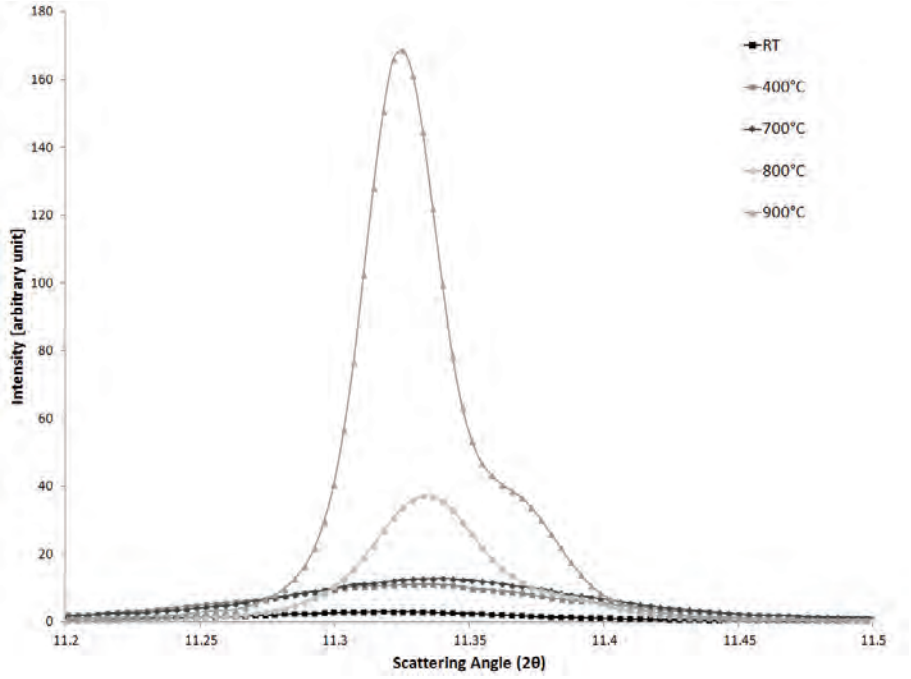

Figure 6.7 WAXS results of the (002) reflection of dentine from a series of tooth sections for a selected region of scattering angles (11.2-11.5°). A sharpening of the diffraction peak at higher temperatures (800 to 900°C) was observed in comparison to the control sample indicating an increased diffraction contribution from larger crystallites.

6.4. Real-time small-angle X-Ray scattering (SAXS) measurements

In the real-time synchrotron X-ray scattering experiment, continuous SAXS measurements were performed at three fixed locations within the dentine of 1mm bucco-lingual cross-sections (scan step 100μm) inside a remotely controlled furnace. In order to evaluate the influence of the heating regime on the mean crystallite thickness and the degree of alignment, temperature increases of 6, 12 and 24°C/min were applied. Forty two to 148 patterns were collected between RT and 880 to 900°C, depending on the heating regime.

6.4.1. Mean crystallite thickness

The mean crystallite thickness was calculated from the SAXS patterns, considering a constant volume fraction of the mineral phase. During the heating process, a shoulder in the diagram was observed between 325 and 375°C, depending on the heating regime (Figure 6.7). A steep increase of the mean crystallite thickness started around 470 to 500°C, with the maximum mean crystallite thickness found between 770 and 820°C, followed by a slight decrease towards 900°C. The standard deviation of crystallite thickness values between the three measurement locations was found to be negligible (≤ ±0.15nm).

6.4.2. Crystalline degree of alignment

As a consequence of the heating process, the crystalline degree of alignment in dentine decreased from 0.18 to 0.05 in the 12°C/min increase group (Figure 6.9). Similar trends were found in the other heating regime groups as well (0.10 to 0.01 in 6°C/min group, 0.10 to 0.06 in 24°C/min group). Up to 280°C the crystallites had a relative stable degree of alignment, with an increase from 0.17 to 0.19 between 280 and 370°C. Between 370 and 700°C the degree of alignment decreased slowly from 0.19 to 0.14, whilst between 700 and 900°C the degree of alignment dropped from 0.14 to 0.05. The standard deviation of the degree of alignment was found to be negligible (≤ ±0.02), indicating a uniform behaviour of the crystallites from the different measurement locations.

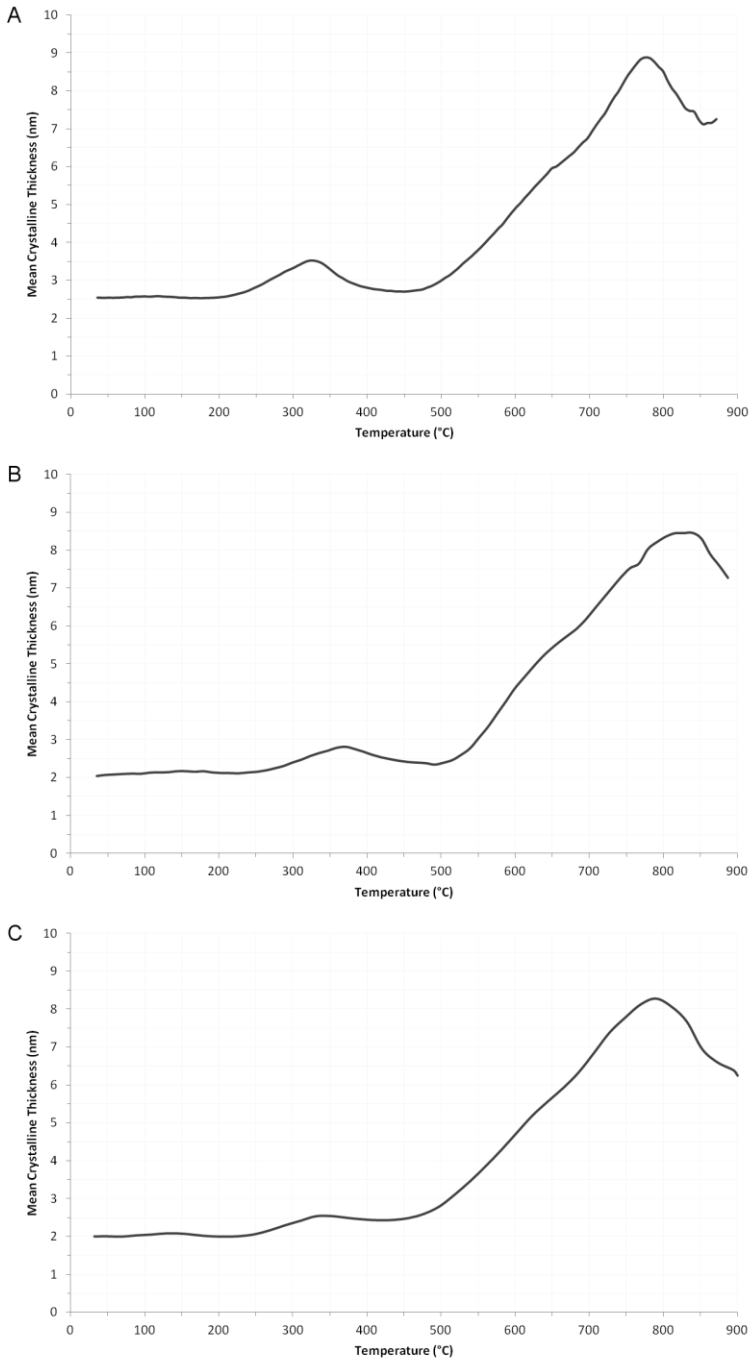

Figure 6.8 *In situ* variation of mean crystallite thickness considering a constant volume fraction of the mineral phase. Between 325 and 375°C a hump was present, followed by a steep increase of the mean crystallite thickness starting around 470 to 500°C. The maximum crystallite thickness was between 770 and 820°C, followed by a slight decrease towards 900°C.

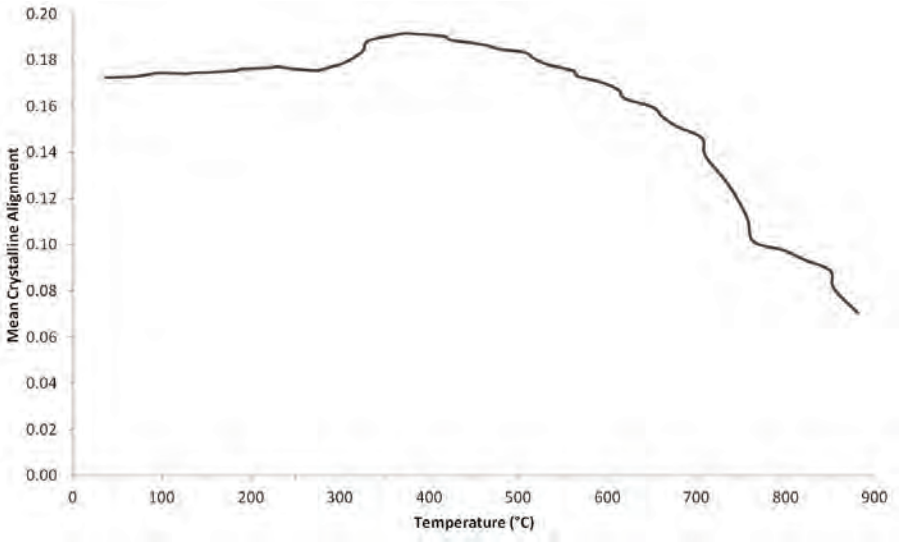

Figure 6.9 *In situ* variation of the crystalline degree of alignment in dentine (12°C/min increase up to 880°C). Up to 280°C dentine had a relative stable degree of alignment, with an increase from 0.17 to 0.19 at 280 to 370°C. Between 370 and 700°C the alignment decreased slowly from 0.19 to 0.14, and a further drop (0.14 to 0.05) was observed between 700 and 900°C.

Chapter 7 – Discussion

The overall aim of the present work was to investigate the influence of duration of heat exposure and heating regimes regarding the macroscopic, compositional, structural and crystalline alterations of dental tissues. A range of analytical approaches was used to evaluate the heat-induced alterations of dentine and enamel. To ensure the comparability of the present work, the selected temperatures and heating regimes of were matched to previous lab-based studies (Beach et al., 2008, Bonavilla et al., 2008, Bush et al., 2006, Fereira et al., 2010, Karkhanis and Franklin, 2009, Merlati et al., 2002, Merlati et al., 2004, Moreno et al., 2009, Myers et al., 1999, Patidar et al., 2010, Rossouw et al., 1999, Savio et al., 2006, Woisetschlager et al., 2011).

7.1. Macroscopic alterations

7.1.1. Failure of the dentine-enamel junction

The fragmentation or 'popping off' of enamel was macroscopically observed in teeth heated at or above 500°C, whilst the micro-CT analysis already revealed a partial de-bonding of the enamel in the 400°C groups. Moreover, tooth sections that were heated over a Bunsen burner flame showed initial shattering of the enamel at a tooth surface temperature between 380°C and 450°C. This temperature range is in accordance with previous studies that reported the 'popping off' of enamel after exposing teeth between 400 and 500°C (Beach et al., 2008, Endris and Berrsche, 1985, Muller et al., 1998). The slight temperature discrepancy of initial shattering between teeth and tooth sections may be explained by the heating procedure as well as the tooth section dimensions allowing an accelerated heat transfer (Lin et al., 2010a, Lin et al., 2010b, Myers et al., 1999). These factors would also explain the fact that some studies reported shattering of the enamel between 650 and 800°C when using a slow incremental increase heating regime (Merlati et al., 2002, Sandholzer et al., 2014).

The shattering of the enamel appeared to be a highly kinetic event (i.e. enamel fragments suddenly shattered off) caused by a combination of factors discussed below. A discolouration of the enamel-adjacent coronal dentine shortly before the initial shattering was observed during the heating of tooth sections could be associated with the loss of organic components (Figure 5.1). The loss of organic

components has been shown to make dentine more brittle due to increased intertubular tensile stress and the dentine-enamel junction weaker, allowing the propagation of cracks (Hughes and White, 2009). However, no significant increase of the weight loss (from the analytical scale measurements) or rates of weight loss (from TGA) were found between 400 and 500°C, where the initial shattering occurred. The boiling and steaming of the absorbed water were also thought to be responsible for an initial separation of the dentine-enamel junction (Botha, 1986). However, FTIR experiments by Reyes-Gasga et al. (2008) indicated that most of the absorbed water evaporates at around 200°C, and therefore most likely does not directly influence the shattering process. Another factor could be the high thermal expansion coefficient of the organic components (Lei et al., 2010). Computational models of the *in situ* SAXS measurements by Sui et al. (Sui et al., 2014b) indicate that the HAp crystallites are be put under stress by the surrounding organic components at temperatures between 300 and 400°C, with a release of this stress at around 500°C. Therefore, a differential expansion of the denaturing organic material within dental tissues followed by a fast contraction might contribute to the de-bonding of the enamel.

Besides dehydration and alterations of the organic components, the partial or full de-bonding of enamel has also been associated with heat-induced dentinal shrinkage (Hughes and White, 2009). The micro-CT analysis, although revealing initial de-bonding of the enamel at 400°C, showed no significant increase in the dentinal shrinkage between 400 and 500°C (4.8 to 5.9%, 30min constant exposure). Overall, the results of the current work indicate that the failure of the dentine-enamel junction is most likely caused by a combination of dentinal shrinkage and denaturation-induced expansion-contraction of organic structures in the enamel-adjacent coronal dentine.

7.1.2. Cracks and fractures

Heat-induced cracks and fractures in dental tissues have been previously investigated using histology, dental radiographs and micro-CT (Fereira et al., 2008, Fereira et al., 2010, Sandholzer et al., 2014, Savio et al., 2006). Based on microscopic examinations, Muller et al. (1998) found superficial and internal cracks in dentine to appear at around 600°C. The micro-CT analysis revealed internal cracks in dentine much earlier, at 400°C (Figure 5.3). The primary location of the cracks was near the pulp chamber, with less cracks visible in the roots, confirming previous investigations (Sandholzer et al., 2014). Hughes and White (2009) indicated that cracks and fractures are caused by the spontaneous evaporation of absorbed water and the intertubular tensile stress, allowing the crack to propagate through compositionally modified dentine and enamel. Most likely the dehydration and stress induced by the loss of organic material supports the formation of these cracks and fractures (Rasmussen et al., 1976). At the current stage of research it is suggested that heat transfers into the pulp chamber leading to the destruction of the organic structures and subsequently to a temperature increase of the air within the pulp chamber. As the air volume expands, cracks form and propagated through the structurally modified dental tissues. Micro-CT imaging has proven to be a useful tool to document cracks in dental tissues and could be used in combination with computational modelling to study crack formation mechanisms. However, it is still unclear at what temperatures initial cracks form. One possible way to explore this could be high-speed X-ray filming of a tooth placed in a furnace fitted with X-ray transmittant windows (similar to the furnace used in the *in situ* synchrotron SAXS experiment).

7.1.3. Preservation of tooth morphology

The changes of root and pulpal morphology were visually assessed using 3-D micro-CT models and digital radiographs. A minor contraction of the distal portions of the roots was visible in the micro-CT models at high temperatures (≥800°C), whilst the resolution of digital radiographs from various angles was not able to visualise the shape changes.

Moreover, the pulpal morphology, a distinct morphological feature important for fire victim identification, did not seem to be influenced by cracks and fractures on the digital radiographs.

Overall, the good preservation of morphological features is somewhat different from observations made for burned animal and human bone, where warping and severe deformation were reported (Gonçalves et al., 2011, Shipman et al., 1984, Thompson, 2005). This could be due to the relatively isotropic distribution of the organic matrix in teeth when compared to bone (Thompson, 2005). Since root and pulpal morphology frequently need to be considered in comparative dental radiography, the shape preservation after exposure to high temperature is crucial to allow positive forensic identifications (Merlati et al., 2002).

7.2. Weight loss

The analytical scale measurements of weight loss (Chapter 3.1) ranged between 7.8 (400°C, incremental heating) and 33.9% (800°C, 45min constant exposure). Beach et al. (2008) previously reported a range between 13.1% (at 204°C, 60min constant exposure) and 36.0% (at 593°C, 30min constant exposure). The higher variation in weight loss of the present work can be explained by a higher sample size (n=179) compared to the study by Beach et al. (n=32). These results indicate that especially during a short exposure at 400 and 500°C (i.e. incremental increase, 5 or 15min constant heating), only a part of the tissue volume might have reached a temperature where weight loss could occur (Endris and Berrsche, 1985, Lin et al., 2010b).

An increased rate of weight loss in dentine was found in the region of 125 to 175°C and 330 to 360°C, depending on the heating protocol (Figure 3.2). The 125 to 175°C region was previously associated with a predominant loss of absorbed water (e.g. trapped in the dentinal tubules) and organic material. The weight loss between 330 and 360°C region was ascribed to the destruction of dentinal carbonates and lattice water (Holager, 1970, Lim and Liboff, 1972). Additionally, a study by Reyes-Gasga et al. (2008) showed that the peak around 200°C relates to the elimination of absorbed water and organic material, whilst the peak around 350°C results from the expulsion of lattice water and carbonates.

Generally, the TGA measurements were in accordance with earlier studies of the thermal behaviour of dental tissues, confirming that the overall weight loss in teeth is derived from dentine rather than enamel. (Brown et al., 1970, Brown et al., 1972, Corcia and Moody, 1974, Holager, 1970, Reyes-Gasga et al., 2008). To date, no TGA measurements have been reported for demineralised dentine. The analysis of these samples showed a weight loss of 99.5 up to 100.0% for the 6, 12 and 20.75°C/min increase groups, with the principal part (i.e. ≥99%) of organic structures destroyed between 660 and 825°C. Only the 24°C/min increase group showed some remnants (97.9% weight loss), most likely due to the fast temperature increase or small mineral residues. Increased rates of weight loss occurred in similar regions found in the dentine samples, with an additional peak in the region of 590 to 640°C (Figure 3.2). This peak of increased weight loss might be due to the missing protective effect of the mineral structures that may slow down the organic degradation process.

7.3. Destruction of organic components

The loss of the organic components and lattice carbonates was previously associated with major macroscopic and microscopic changes like weight loss, surface colour and dimensional changes (Fairgrieve, 2008, Mayne-Correira, 1997, Shipman et al., 1984, Thompson, 2005).

Attenuated total reflectance FTIR (ATR-FTIR) was performed in order to qualitatively confirm that the weight loss found in the analytical scale and TGA measurements are caused by the loss of organic components (Chapter 3.2.1). The related carbonate peaks between 1400 and 1650cm^{-1} diminished with increasing temperature, and a principal loss of organic components and lattice carbonates in dentine was seen at 900°C. These findings were found to be in accordance with previous studies related to compositional alterations in burned animal and human bone (Hollund et al., 2013, Mkukuma et al., 2004, Thompson et al., 2009).

In a novel approach, real-time FTIR allowed evaluating the destruction of the carbonates derived from organic phase (e.g. collagen matrix, cell proteins) and lattice carbonates (i.e. carbonate substitutions in the HAp structure) during the heating process up to 400°C. Peaks related to collagen and cell proteins

diminished by up to 67% during the heating process, with effects seen on these peaks as early as 60°C. Denaturation and alterations of the collagen appearance between 60 and 100°C were previously reported in heat-affected bone (Fernandez Castillo et al., 2013a, Fernandez Castillo et al., 2013b, Holden et al., 1995). In contrast, peaks related to lattice carbonates were less affected by the heat (maximum 22% decrease of peak height) and stable up to 280°C.

The possible preservation of DNA in heat-affected teeth has been previously studied, with the purpose of supporting the fire victim identification process (Barker et al., 2008, da Silva et al., 2012, Duffy et al., 1991, Rees and Cox, 2010). In the present work it was shown that small quantities of organic components related to collagen and cell proteins were still present after the heating up to 400°C. Nonetheless, the performed measurements of the present study can neither implicate the presence nor the quality of DNA. As the knowledge on DNA preservation is crucial to eventually facilitate comparative DNA analysis in cases involving burned and fragmented remains (Interpol, 2009, Williams et al., 2004), further insight could be gained by using high-performance liquid chromatography (HPLC) or TGA coupled mass-spectrometry (TGA-MS) approaches.

7.4. Surface colour alterations

Surface colour alterations, one of the most noticeable macroscopic feature of heat-affected teeth, has been attributed to the loss of organic constituents in dental tissues and combustion of other chemical groups of hydroxyapatite (Berzina-Cimdina and Borodajenko, 2012, Endris and Berrsche, 1985, Fairgrieve, 2008, Herrmann, 1972, Mayne-Correira, 1997, Moreno et al., 2009, Shipman et al., 1984, Thompson, 2005).

Discolouration towards dark brown and black was seen in the 400°C test groups, and after 5min exposure at 500°C. Herrmann (1972) proposed that this initial black discolouration was due to the degradation of carbonates. This could be confirmed by the ATR- and real-time FTIR measurements that showed that the level of carbonates derived from organic structures decreased during the heating process up to 400°C, accompanied by a black discolouration of the tooth cross-section around 340°C.

Between 500 and 600°C shades of brown were observed, which might be caused by further degradation of organic constituents, combined with the combustion of other chemical groups of HAp (Berzina-Cimdina and Borodajenko, 2012). The analytical scale, TGA and FTIR results all indicated that the weight loss process and loss of organic constituents was still in progress around 600°C.

Light grey and white discolourations were observed in most test groups at and above 700°C and were previously associated with the principal loss of organic constituents (Herrmann, 1972, Moreno et al., 2009, Shipman et al., 1984). The analytical scale results of the present work showed that at a temperature of ≥700°C, a plateau of maximum weight loss around 30.5% was reached (range: 27.1 to 34.1%). The dark grey patches present above 700°C did not appear as glossy as the discolourations observed in the 400°C 15 to 45min and 500°C 5min groups, and are likely to be caused by organic remnants, substitutions in the HAp structure, reduced oxygen availability or possible contaminants inside the furnace.

The overall trends in surface colour alterations correspond with previous observations of isolated human teeth exposed to incrementally increase or constant exposure to elevated temperatures (Beach et al., 2008, Karkhanis and Franklin, 2009, Merlati et al., 2002, Moreno et al., 2009, Savio et al., 2006). Nonetheless, a dependency of the surface colour alterations on the duration of heat exposure, the heating regime and soft tissue protection was found. Particularly at temperatures below 800°C, the duration of heat exposure and heating regime strongly influenced the colour changes, which would lead to miss-classification using colour-chart based systems proposed by Shipman et al. (1984) and Karkhanis and Franklin (2009). A constant exposure at 400°C for 5min and incremental increase to 400°C led to a dark yellow/brown discolouration of the root (7.8 to 11.4% weight loss). In contrast, all other 400°C test groups (15, 30, 45min constant exposure, overnight cooling and soft tissue protection) resulted in a glossy dark grey/black appearance (16.1 to 20.2% weight loss). Similar observations were made for the 500 and 600°C 5min constant exposure groups, which appeared similar in root surface colour to the subordinate 15 to 45min constant exposure groups (Figure 4.1). But also at higher temperatures, surface colour alterations were very diverse, mainly reflected in the

weight loss data (e.g. 700°C groups, 20.1 to 30.5% weight loss). At and above 900°C, the weight loss was less influenced by the heating regime, also resulting in more uniform colour appearance.

Quantitative colorimetric measurements using calibrated digital photographs provided a standardised and objective way to document and compare these colour alterations. To evaluate whether certain colours could be used to deduce a temperature range, hierarchical cluster analyses were performed. It could be shown that 99% of colours present in the 28 duration test groups had a ΔE of more than 2.3, and could theoretically be differentiated as separate colours by normal human vision. Nonetheless, many colours within a group and between groups might appear very similar. By grouping the colours of the 28 duration test groups into five clusters, overall trends in the surface colours could be visualised (Figure 4.10). The majority (71.7%) of the colours were grouped into two big clusters. These two clusters mainly incorporated tones of grey and brown that were present in 79 to 100% of the 28 duration test groups and therefore could not be accurately associated with a distinct temperature range. A separate cluster was formed by dark yellow/brown discolourations which were only present in the 400°C 5min constant exposure group. The fact that this cluster only consists of one temperature group can be ascribed to the short heat exposure and lack of experimental groups below 400°C. An additional cluster including shades of dark grey and black consisted mainly of colours from the 400°C 15 to 45min and 500°C 5min groups (86%), associated with the degradation of carbonates. Light grey/white discolourations made up another cluster, and were derived from temperature group of 700°C or above, linked to the predominant loss of organic constituents in dentine.

The hierarchical cluster analysis of the colours present in the test groups of the various heating regimes and soft tissue protection revealed similar trends as the duration test groups (Figure 4.18). Only one of the four clusters could be clearly associated with a distinct temperature range, containing variations of light grey/white, predominantly derived from the 700 and 900°C test groups.

The hierarchical cluster analysis based on quantitative colorimetric measurements was intended to evaluate whether information on the temperature could be elicited based on 16 representative colours

per experimental group. At the current stage of research the computational analysis only indicated three main colour transition stages that can clearly be associated with temperature ranges.

At short exposures to 400°C or below, the root surface colour changed from the natural pale yellow towards a dark yellow/brown. The analytical scale, TGA and FTIR results of the present study indicated an initial loss of organic structures at this stage. With prolonged exposures (15 to 45min) at 400°C or 5min exposure at 500°C the root surface showed a glossy dark grey/black discolouration. This stage can be associated with the degradation of carbonates. Finally, at prolonged exposures at and above 700°C the root surface colour became predominantly light grey/white, which is related to the principal loss of all organic material and lattice carbonates.

Besides a simple description of colours, various researchers used colour reference charts for the documentation and description of surface colour alterations and estimation of temperature exposure (Beach et al., 2008, Endris and Berrsche, 1985, Karkhanis and Franklin, 2009, Muller et al., 1998, Shipman et al., 1984). The description and approach to determine matching colours is highly subjective and dependent on various external factors, such as the positioning of the observer or the illuminant. Therefore, a more standardised and objective way to document and compare these colour alterations using quantitative colorimetric measurements of calibrated digital photographs was tested. The usage of the Gretag Macbeth Color Checker Chart in combination with the 'Chart White Balance' plugin (van der Haeghen and Naeyaert, 2006) ensured an appropriate and repeatable calibration tool. Nonetheless, shadows caused by the curvature of the tooth surface, reflections caused by glossy surfaces, superficial cracks and fractures may also influence the colour analysis. A colour reduction of the original images was necessary to facilitate the computational analysis of the images. Representative colour palettes containing 16 colours per experimental group were computed, which showed similar trends in colour entropy as the original images (Figures 4.6 and 4.7).

One of the aims of the quantitative colorimetric measurements was to create improved colour palettes that could be used in daily forensic practice or as part of archaeological excavations to determine the

temperature range of heat-affected teeth. Analysing colours from calibrated photographs proved to be a practical way of quantitatively determine heat-induced colour alterations; however the significant influence due to duration heating regime did not allow clear distinction of temperatures. That indicates temperature specific colour palettes should only be used with precaution. Although upon visual inspection certain temperature-dependent trends in colour changes were observed, the currently used computational analysis did not reveal these sufficiently (e.g. differences in brown tones at 500 and 600°C). Previous studies using the 'Munsell Soil Colour Chart' or similar colour catalogues, or other colorimetric approaches (digitalised photographs, flatbed scanners, spectrophotometry) to correlate surface colour alterations with temperature ranges were solely based on one duration at the individual temperature steps (Beach et al., 2008, Endris and Berrsche, 1985, Fereira et al., 2008, Karkhanis and Franklin, 2009, Shipman et al., 1984, Walker et al., 2008). The colour entropy in the 15 to 45min constant exposure groups at and above 500°C indicated more homogeneous colour changes. Nonetheless, only aforementioned general trends were found in the hierarchical cluster analysis providing a rough estimation of a cremation temperature range, and are not suitable for precise temperature estimation.

Overall, the observations of surface colour alterations indicate that the tissue temperature may play a more important role than the temperature of the surrounding air. This would also explain why the protection by oral soft tissue and the alveolar bone socket cause a non-uniform colour appearance of the heat-affected teeth by hindering the heat transfer towards the dental tissue (Lain et al., 2011). In order to further understand the influence of temperature, duration and heating regimes on surface colour alterations, investigations using constant exposure times below 5min are proposed. Moreover, the role of the furnace used (i.e. the size of the heating chamber), the presence of contaminants or fire accelerants as well as other external factors (e.g. oxygen availability) and their influence on the surface colours still needs further investigation. Advanced analytical approaches using more elaborate methods of cluster analysis might additionally be useful to classify the colours in a different way, revealing more specific colour patterns.

7.5. Shrinkage

In addition to morphological, compositional and colour alterations, heat-induced shrinkage has also been previously reported for teeth (Maples and Browning, 1995, Norrlander, 1995, Shipman et al., 1984). Whilst the rate of shrinkage for heat-affected bone has been previously investigated, no precise quantitative data on the dimensional changes of human teeth has been available (Großkopf, 2004, Wahl, 1982). The results regarding the volumetric shrinkage of dentine indicated that minor dimensional changes already occurred at 400°C (4.8%), with a major increase between 700 and 800°C (11.5 to 24.2%). The initial shrinkage at 400 and 500°C (4.8 to 5.9%) is possibly caused by the heat-induced dehydration and initial loss of the organic matrix that contains the HAp crystals. Between 500 and 700°C (5.9 to 11.5%) the shrinkage is likely to be related to a combination of the destruction of organic structures and dimensional changes of the crystalline structures, whilst above 700°C (24.2 to 32.5%) sintering and re-crystallisation of HAp crystallites leads to major dimensional changes (Shipman et al., 1984, Thompson, 2005). Although the *in situ* X-ray scattering experiment indicated that crystallite dimensions in dentine started to increase between 470 and 500°C, the effects only became measurable at a microscopic level at higher temperatures. It could also be shown that in the 700 and 900°C overnight groups a prolonged exposure to elevated temperatures led to a significantly increased rate of shrinkage (Figure 5.4). In contrast, at 400°C the overnight cooling did not lead to changes in the shrinkage rate. Additional research is needed to clarify what influence prolonged durations of heat exposure would have on the rate of shrinkage between 500 and 700°C.

Literature values on the heat-induced shrinkage of bone range between 0.5 and 27% (Buikstra and Swegle, 1989, Großkopf, 2004, Thompson, 2005, Ubelaker, 2009). This large variation might be possibly due to the fact that previous authors did not clearly disclose whether 3-D (volumetric) or 2-D shrinkage had been reported. Whilst the volumetric shrinkage for teeth ranged from 4.8 to 32.5%, the corresponding 2-D shrinkage was only between 2.8 and 10.2%. The documentation of dental shrinkage at temperatures as low as 400°C can be attributed to the more precise nature of the micro-CT approach, as earlier studies assessed shrinkage of bone only using calliper measurements (Shipman

et al., 1984, Thompson, 2005). Nevertheless, similar to bone (Thompson, 2005), major dimensional changes were associated with temperatures around 800°C. In the last few years micro-CT has been increasingly used in forensic sciences (Baglivo et al., 2013, Chang et al., 2000, Rutty et al., 2013, Thali et al., 2003). Clinical CTs have been recently used by Bassed and Hill (2011) to estimate the dental age of fire victims, however the current resolution (voxel size of 1mm) and the lack of metal artefact reduction algorithms prevent a detailed analysis of dental morphology. Woisetschläger et al. (2011) used a high-resolution CT (voxel size of 0.1mm) to analyse alterations in grey values of filling materials and dental tissues of isolated human teeth. The findings of these two studies suggest that high-resolution CTs could be useful for the identification of fire victims. Although high-resolution CTs would also be able to detect dimensional changes at elevated temperatures, currently only micro-CT offers a sufficient resolution to analyse the precise shrinkage rate and morphological alterations. Nonetheless, the gold standard for fire victim identification remains comparative dental radiography using panorama, bite wing or single radiographs. The intention of evaluating the rate of shrinkage was also to clarify the implications for the daily forensic practice (Bernstein, 1998, Bush and Bush, 2011, Chang et al., 2000, Hill et al., 2011b, Lain et al., 2011, Merlati et al., 2004, Savio et al., 2006). Overall, the results of the present work show that shrinkage below 800°C is very small (2-D shrinkage ≤5.1%), and is unlikely to be detectable on standard digital radiographs. At temperatures associated with predominant light grey/white discolouration (≥800°C), shrinkage becomes visible in digital radiographs and should be implemented into the standard procedure for the identification of heat-affected dental remains (Fairgrieve, 2008).

7.6. Crystalline alterations

The quantitative analytical approach based on synchrotron radiation, combining SAXS and WAXS allowed the determination of the local crystalline alterations in a tooth cross-section rather than a volume-weighted averaged measurement of pulverised samples. In general, the heating process led to a variation in mean crystallite thickness, alignment and shape in dental tissues. Only a small variation in the SAXS/WAXS measurements in longitudinal line scans as well as the grid mapping was found, indicating a relatively uniform thermal behaviour of the samples. This may be attributed to the dimensions of the tooth sections (0.5 to 1mm thickness) and chosen heating protocol. Entire teeth are expected to exhibit a non-uniform thermal diffusion (i.e. temperature gradient from surface to pulp cavity) and therefore may show spatial variation in heat-induced crystalline changes.

Due to the limited size of the detector used, only the (002) peak data could be interpreted, which has been previously associated with the diffraction by HAp crystallites (Reyes-Gasga et al., 2008). At lower temperatures (400 to 600°C) no significant changes in the (002) peak were observed in dentine. The predominant loss of the organic matrix which supports the mineral phase led to a higher degree of perfection of the HAp crystallites between 700 and 800°C, visible as sharper and stronger peaks. At and above 800°C sintering of the crystallites led to a significant growth and sharpening of the WAXS peaks. Similar phenomena have been reported for XRD heating experiments on animal bone and teeth (Greenwood et al., 2012, Hiller et al., 2003, Piga et al., 2009, Rogers and Daniels, 2002, Shipman et al., 1984).

Besides the sintering of the crystallites, a mineral phase change from HAp [$Ca_5(PO_4)_3(OH)$] to TCP [$Ca_3(PO_4)_2$] has been reported in XRD studies of bone heated at 900°C (Beckett et al., 2011, Herliansyah et al., 2009). The *ex situ* synchrotron X-ray scattering experiment did not reveal a mineral phase change in dentine or enamel when heated for 30min at 900°C, possibly relating to the high dependency of the mineral phase change on the sintering temperature and duration of heat exposure (Hiller et al., 2003, Reyes-Gasga et al., 2008).

Crystalline degree of alignment

In accordance with earlier SAXS results, the control samples showed a more disordered orientation of HAp crystallites in dentine than enamel (Jiang et al., 2005). The longitudinal line scans as well as the grid mapping of the *ex situ* samples showed a tissue-dependent variation in the degree of alignment. A major drop in the alignment was observed in the dentine adjacent to the dentine-enamel junction, whilst in the deeper dentine, the degree of alignment appeared less variable. This observation can be related to the gradient properties of dentine reported by Tesch et al. (2001) and can be explained as the optimisation of the mechanical functions of dentine (Marten et al., 2010). The gradual disappearance of the organic matrix may explain the decrease of the degree of alignment, where a trend towards more random orientation with increasing temperatures was found in dentine and enamel. The overall reduction of the degree of alignment in dental tissues during the heating process may be associated with the arrangement of the crystallites, as well as the changes in crystallite dimensions and shape at elevated temperatures (Greenwood et al., 2012, Hiller et al., 2003, Pramanik et al., 2013).

The real-time synchrotron SAXS experiments showed a stable degree of alignment ranging from room temperature up to 280°C in dentine, corresponding to the absence of crystallite rotation or growth. Once the organic components degraded (280 to 370°C), a small increase in the crystalline degree of alignment was noted in dentine. This temperature range also reflected in a slight increase of mean crystallite thickness, which may correspond to a gradual expansion of organic matrix leading to a compression of the crystal structure (Sui et al., 2014b). Between 370 and 700°C the degree of alignment decreased slowly, most likely due to the gradual loss of supporting organic components. Above 700°C the predominant loss of the structural organic components caused the collapse and rearrangement of crystallites, which might be associated with rotations and the anisotropic (i.e. non-uniform) sintering of hydroxyapatite crystallites.

Crystallite shape

The changes of crystallite shape were determined using SAXS data interpretation. At room temperature, dentine showed a needle-like morphology, gradually increasing to more platelet-like at 400 to 500°C and finally to a polydisperse morphology at 600 to 900°C. In contrast to dentine, enamel showed polydisperse morphology in all test groups (RT to 800°C). The precise polydisperse crystallite morphology that was found at elevated temperatures could be determined by the simplistic needle or platelet model used in this study (Hiller et al., 2003). The heat-induced shape changes of HAp crystallites were previously shown in a transmission electron microscopy (TEM) study by Reiche et al. (2002). Although on a different scale, the shape alterations are also in accordance with SEM results showing more complex appearance of the crystals and sintering of the mineral structure above 700°C (Holden et al., 1995, Shipman et al., 1984).

Mean crystallite thickness

The mean crystallite thickness of the control samples is consistent with previously reported TEM and XRD results (Piga et al., 2009, Reiche et al., 2002). The SAXS-derived increase of the mean crystallite thickness was found to be 2.8-fold in dentine (RT to 900°C) and 1.4-fold (RT to 800°C) in enamel. These results were emphasised by the corresponding WAXS data derived from the width at half maximum (FWHM) variation ratio. This ratio indicated that crystallites appear 3.3-fold larger in dentine (at 900°C) and 1.3-fold larger in enamel (at 800°C) compared to the control sample. In general, the small increase in mean crystallite thickness for enamel may be due to a more dense arrangement of hydroxyapatite crystallites compared to dentine, allowing only a limited increase in size. A 3.7-fold increase of average crystallite size (RT to 900°C) was previously reported when analysing pulverised teeth using XRD, however the independent contributions of dentine and enamel were not taken into account (Piga et al., 2009). In bone, previous SAXS studies indicated a 5 to 10.7-fold increase of mean crystallite thickness between room temperature and 900°C (Etok et al., 2007, Hiller et al., 2003). These discrepancies may be related to the structural difference between bone and

dental tissues, prolonged heat exposure used in these studies (45min to 6h) as well as grinding as part of the sample preparation process (Etok et al., 2007, Hiller et al., 2003, Piga et al., 2009).

The real-time synchrotron SAXS measurements provided a further understanding of the thermal kinetics, as it allowed documenting a complete and continuous evolution of the crystalline structure during the heating process. Moreover, the influence of the heating regime on the mean crystallite thickness could be evaluated. A temporal increase of the mean crystallite thickness was observed between 325 and 375°C which may be due to a gradual expansion of organic components leading to a compression of the crystallites (Sui et al., 2014b). A steep increase in mean crystallite thickness was observed between 470 and 500°C with maxima found between 770 and 820°C, which were independent of the heating protocol. Overall, a 2.6 to 3.5-fold increase of the mean crystallite thickness between RT and 900°C was observed, confirming the results of the *ex situ* synchrotron X-ray scattering experiment. To keep the real-time results comparable to *ex situ* results, a constant volume fraction was considered. The volume fraction describes the fraction of particles within the volume created by the X-ray beam transmitting through the sample. However, as the TGA, FTIR and micro-CT experiments indicate, the volume fraction is likely to change due to the loss of organic constituents, sintering of the crystallites and overall shrinkage of dentine. By using a refined analytical approach and advanced computational model, a more detailed understanding of the heat-induced changes of the crystallite size could be computed which would lead to a creation of reference values for heat-affected dental tissues(Sui et al., 2014b).

Overall, the synchrotron-based SAXS/WAXS experiments support previous lab-based studies that characterised the heat-induced alterations of crystallite size in archaeological and experimentally altered animal bone and teeth (Etok et al., 2007, Hiller and Wess, 2006, Piga et al., 2009). Moreover, the results of the present work emphasise the need to investigate bone and dental tissues separately, as they appear to react differently on a crystalline level (Greenwood et al., 2012, Hollund et al., 2013, Piga et al., 2008, Shipman et al., 1984).

Chapter 8 - Conclusions

The overall aim of the present work was to investigate the influence of duration of heat exposure and heating regimes regarding the macroscopic, compositional, structural and crystalline alterations of dental tissues, which was addressed with a range of combined novel analytical approaches.

The investigation of heat-induced destruction of organic components using high-precision measurements of weight loss and compositional alterations revealed a strong dependency on the duration of heat exposure and the heating regime. This dependency was also reflected in the variation of surface colour alterations. Below 800°C, the duration of heat exposure strongly influenced the surface colour alterations. Walker et al. (2008) have previously showed that a combination of multiple conditions in the cremation environment (e.g. duration, temperature and oxygen availability) determine the extent of the surface colour alterations. Additional factors, such as the fast increase or fluctuation of temperature as well as the presence of contaminants are likely to have effects on the surface colour alterations of dental tissues. Overall, as established here by quantitative colorimetric measurements, surface colour alterations are assumed to be of minor value for forensic investigations as only rough estimations of the cremation temperature range can be achieved.

A more precise determination of the cremation temperature is possible using the analysis of crystalline alterations of hydroxyapatite. A temperature-dependent increase of the mean crystallite thickness of HAp in dentine and enamel was found to start around 500°C, independently of the chosen heating regime. Whilst the access to synchrotron facilities is limited for routine forensic work, especially the mean crystallite thickness results can also be utilised as reference values for the more commonly used lab-based XRD and SAXS approaches. This would benefit the examination of isolated dental remains to determine the circumstances of cremation during forensic investigations. For example, wooden campfires do normally not reach more than 700°C, so if an increased crystallite size this could mean that fire accelerants might have been used during the attempt to dispose a body.

The combination of real-time analytical approaches also gave an insight into the kinetics of the heating process. The gradual degradation of carbonates derived from the structural organic components caused

a dark grey/black discolouration around 400°C and are also believed to cause some initial shrinkage. Between 400 and 500°C the differential expansion of the denaturing organic material in combination with initial shrinkage, is likely to lead to the failure of the dentine-enamel junction. Finally, the combination of crystalline alterations and loss of organic constituents led to an increased rate of shrinkage between 700 and 800°C.

The results of the present work also gave important implications for the daily forensic practice of fire victim identification. The heat-induced dehydration and loss of organic constituents led to a fragile nature of the teeth that required careful handling. It was found to be pivotal to follow the guidelines given by Hill et al. (2011b) to preserve dental structures. The experimental results showed the principal loss of organic constituents between 660 and 825°C, reinforcing the importance of comparative dental radiography for fire victim identification. The 'popping off' of the enamel necessitates focussing on other morphological features found in panorama, bite wing or single radiographs. Although cracks and fractures occurred, the root curvature and pulpal morphology was overall well preserved at elevated temperatures. Predominately light grey/white discolouration (≥800°C) can also be associated with the visibility of shrinkage in digital radiographs. As comparative radiography forms a cornerstone of fire victim identification, the rates of shrinkage should be kept in mind when matching *antemortem* dental records and *postmortem* findings during forensic investigations.

Overall, the findings resulting from the present work have to be considered in the fire victim identification process and as they eventually facilitate the identification in cases where only dental remains are present.

Chapter 9 - Future Work

In previous studies, factors such as the protection of soft and hard tissues, fast increase of temperature, fast cooling due to fire extinguishing agents or the presence of contaminants have generally not been taken into account by lab-based research and it is possible that they might have important effects on the changes observed in dental tissues (Muller et al., 1998). Therefore, future research on this subject should primarily focus on the influence of further heating regimes (e.g. short heat exposures) and the presence of protective hard- and soft tissue to allow more precise conclusions regarding the characterisation of the associated alterations.

Besides the investigation of the influence of external factors, further advances are likely to be made in the documentation and recovery of heat-affected dental remains. Recent studies by Waterhouse (2013a, 2013b) on the influences of weather factors on the post-burning fragmentation of skeletal remains imply the necessity for a careful and prompt recovery of dental remains. Although recovery protocols have been proposed, further studies on the optimisation of the stabilisation and transportation process could help to preserve dental material. Portable handheld X-ray systems (e.g. NOMAD Pro, Aribex Inc.) would be beneficial to document the dental remains already on-site. Moreover, 3-D laser scanning could be used to document the location of dental remains at crime scenes in order to reconstruct the circumstances of the heating event (Sandholzer et al., 2013). Due to the wide availability, conventional radiography will always be a cornerstone of dental identification, nonetheless over the next decades CT imaging is likely to gain importance for the dental identification of fire victims. Mobile CT scanner units, which already form part of the equipment of disaster victim identification teams, could additionally help to document human remains and support the identification process (Bassed et al., 2011, Bassed and Hill, 2011, O'Donnell et al., 2011, Rutty et al., 2009). With an increasing number of medical and dental CT scans performed during the life time, computer assisted systems are likely to be used after disasters to facilitate victim identification (Campobasso et al., 2007).

Technical innovations will further shed light on the heat-induced alterations in dental tissues and dental materials. A database of dental materials based on XRF and EDS measurements, as proposed

by Bush and Bush (2011), could support the identification process by providing reference values for dental materials used worldwide. Future research to study the preservation of proteins related to DNA, could be carried out by using HPLC or TGA-MS. These techniques would allow an insight into the components that are destroyed during the heating process and give a more detailed idea of DNA preservation.

Moreover, synchrotron-based X-ray scattering has shown to be a viable approach to support the estimation of the cremation temperature. Lab-based SAXS/WAXS investigations using heating chambers would allow the usage of a larger sample size and provide an improved understanding on the effects of heat on the crystalline structures. Additionally, future developments in the setup for synchrotron-based investigations would allow further investigating of thermal crystallisation kinetics of dental tissues. For example, 3-D SAXS tomography could provide a more precise indication of the changes in crystal dimension, orientation and morphological alterations.

Finally, future research should include the investigation of various external factors (e.g. soft and hard tissue protection, contaminants) and perform additional analytical experiments (e.g. high-speed X-ray filming, HPLC, MS-TGA, *in situ* SAXS/WAXS) to further understand the macroscopic, compositional, structural and crystalline alterations of heat-affected dental tissues. Such lab-based results should ideally be compared to dental remains derived from other experimental (e.g. crematoria-based) studies and forensic settings. Ultimately, it is hoped that this will allow reconstructing the circumstances of the heating event and further facilitate the odontological identification process of fire victims.

Chapter 10 - References

ADAMS, B. J. 2003a. The diversity of adult dental patterns in the United States and the implications for personal identification. *J Forensic Sci,* 48**,** 497-503.

ADAMS, B. J. 2003b. Establishing personal identification based on specific patterns of missing, filled, and unrestored teeth. *J Forensic Sci,* 48**,** 487-496.

AL-AMAD, S. H., CLEMENT, J. G., MCCULLOUGH, M. J., MORALES, A. & HILL, A. J. 2007. Evaluation of two dental identification computer systems: DAVID and WinID3. *J Forensic Odontostomatol,* 25**,** 23-29.

AL-JAWAD, M., ADDISON, O., KHAN, M. A., JAMES, A. & HENDRIKSZ, C. J. 2012. Disruption of enamel crystal formation quantified by synchrotron microdiffraction. *J Dent,* 40**,** 1074-1080.

ALQAHTANI, S. J., HECTOR, M. P. & LIVERSIDGE, H. M. 2010. Brief communication: The London atlas of human tooth development and eruption. *Am J Phys Anthropol,* 142**,** 481-490.

ANDERSEN, L., JUHL, M., SOLHEIM, T. & BORRMAN, H. 1995. Odontological identification of fire victims--potentialities and limitations. *Int J Legal Med,* 107**,** 229-234.

ANDERSON, S. G. S., BERNSTEIN, M., BERRYMAN, H. E. & BOWERS, C. M. 2007. Human identification. *In:* HERSCHAFT, E. E., ALDER, M. E., ORD, D. K., RAWSON, R. D. & SMITH, E. S. (eds.) *Manual of Forensic Odontology*. 4th ed. Boca Raton: CRC Press.

BAGLIVO, M., WINKLHOFER, S., HATCH, G. M., AMPANOZI, G., THALI, M. J. & RUDER, T. D. 2013. The rise of forensic and post-mortem radiology - Analysis of the literature between the year 2000 and 2011. *J Forensic Radiol Imaging,* 1(1), 3-9.

BARKER, C., COX, M., FLAVEL, A., LAVER, J., LEWIS, M. & MCKINLEY, J. I. 2008. Mortuary procedures III - Skeletal analysis 2: Techniques for determining identity. *In:* COX, M., FLAVEL, A., HANSON, I., LAVER, J. & WESSLING, R. (eds.) *The Scientific Investigation of Mass Graves: Towards Protocols and Standard Operating Procedures.* Cambridge: Cambridge University Press.

BARTHEL, K. U. 2007. *3D Color Inspector/Color Histogram* [Online]. Available: http://rsb.info.nih.gov/ij/plugins/color-inspector.html [Accessed 15.09.2013].

BASSED, R. B., BRIGGS, C. A. & DRUMMER, O. H. 2011. Age estimation using CT imaging of the third molar tooth, the medial clavicular epiphysis, and the spheno-occipital synchondrosis: A multifactorial approach. *Forensic Sci Int,* 212**,** 273.e1-273.e5.

BASSED, R. B. & HILL, A. J. 2011. The use of computed tomography (CT) to estimate age in the 2009 Victorian Bushfire Victims: A case report. *Forensic Sci Int,* 205**,** 48-51.

BASTIAAN, R. J. 1984. Dental identification of the Victorian bushfire victims. *Aust Dent J,* 29**,** 105-110.

BEACH, J. J., PASSALACQUA, N. V. & CHAPMAN, E. N. 2008. Heat-related changes in tooth color: Temperature versus duration of exposure. *In:* SCHMIDT, C. & SYMES, S. (eds.) *The Analysis of Burned Human Remains.* 1st ed. San Diego: Academic Press.

BECK, J. J. W. 2011. What is the future of imaging in forensic practice? *Radiography,* 17**,** 212-217.

BECKETT, S., ROGERS, K. D. & CLEMENT, J. G. 2011. Inter-Species Variation in Bone Mineral Behavior upon Heating. *J Forensic Sci,* 56**,** 571-579.

BERKETA, J. 2014. Maximizing postmortem oral-facial data to assist identification following severe incineration. *Forensic Sci Med Pathol***,** 10(2), 208-216.

BERKETA, J., JAMES, H. & MARINO, V. 2011. Dental implant changes following incineration. *Forensic Sci Int,* 207**,** 50-54.

BERKETA, J. W., HIRSCH, R. S., HIGGINS, D. & JAMES, H. 2010. Radiographic Recognition of Dental Implants as an Aid to Identifying the Deceased. *J Forensic Sci,* 55**,** 66-70.

BERMAN, G. M., BUSH, M. A., BUSH, P. J., FREEMAN, A. J., LOOMIS, P. W. & MILLER, R. G. 2013. Dental Identification. *In:* SENN, D. R. & WEEMS, R. A. (eds.) *Manual of Forensic Odontology.* 5th ed. Boca Raton, FL, USA: CRC Press.

BERNSTEIN, M. 1998. Radiologic Applications in Forensic Dentistry. *In:* BROGDON, B. (ed.) *Forensic Radiology.* 1st ed. Boca Raton: CRC Press.

BERZINA-CIMDINA, L. & BORODAJENKO, N. 2012. Research of Calcium Phosphates Using Fourier Transform Infrared Spectroscopy. *In:* THEOPHANIDES, T. (ed.) *Infrared Spectroscopy - Materials Science, Engineering and Technology.* InTech.

BOHNERT, M. 2007. Kraftfahrzeugbrand. *Rechtsmedizin,* 17**,** 175-186.

BOHNERT, M., ROST, T. & POLLAK, S. 1998. The degree of destruction of human bodies in relation to the duration of the fire. *Forensic Sci Int,* 95**,** 11-21.

BONAVILLA, J. D., BUSH, M. A., BUSH, P. J. & PANTERA, E. A. 2008. Identification of incinerated root canal filling materials after exposure to high heat incineration. *J Forensic Sci,* 53**,** 412-418.

BOTHA, C. T. 1986. The dental identification of fire victims. *J Forensic Odontostomatol,* 4**,** 67-75.

BOYDE, A. 1989. Enamel. *In:* BERKOVITZ, B. K. B., BOYDE, A., FRANK, R. M., HÖBLING, H. J., MOXHAM, B. J., NALBANDIAN, J. & TOGE, C. H. (eds.) *Teeth.* 1 ed. Berlin: Springer.

BRANDAO, R. B., MARTIN, C. C., CATIRSE, A. B., DE CASTRO, E. S. M., EVISON, M. P. & GUIMARAES, M. A. 2007. Heat induced changes to dental resin composites: a reference in forensic investigations? *J Forensic Sci,* 52**,** 913-919.

BROUGH, M. D. 1991. The king's cross fire. Part 1: the physical injuries. *Burns,* 17**,** 6-9.

BROWN, W. S., DEWEY, W. A. & JACOBS, H. R. 1970. Thermal properties of teeth. *J Dent Res,* 49**,** 752-755.

BROWN, W. S., JACOBS, H. R. & THOMPSON, R. E. 1972. Thermal fatigue in teeth. *J Dent Res,* 51**,** 461-467.

BUIKSTRA, J. E. & SWEGLE, M. 1989. Bone modification due to burning: experimental evidence. *In:* BONNISCHEN, R. & SORG, M. H. (eds.) *Bone Modification.* Orono: Peopling of the Americas Publications, University of Maine.

BUSH, M. A. & BUSH, P. J. Dental materials as an aid for victim identification: examination of calcined remains by SEM/EDS. *In:* POSTEK, M. T., NEWBURY, D. E., PLATEK, S. F. & JOY, D. C., eds., 2010. SPIE, 772914.

BUSH, M. A., BUSH, P. J. & MILLER, R. G. 2006. Detection and classification of composite resins in incinerated teeth for forensic purposes. *J Forensic Sci,* 51**,** 636-642.

BUSH, P. J. & BUSH, M. A. 2011. The Next Level in Victim Identification: Materials Properties as an Aid in Victim Identification. *In:* BOWERS, C. (ed.) *Forensic Dental Evidence.* 2nd ed. Amsterdam: Elsevier Academic Press.

CABRERA, J. E. 2013. *Texture Analyzer* [Online]. Available: http://rsbweb.nih.gov/ij/plugins/texture.html [Accessed 24/12/2013].

CAMPBELL, M. N. & FAIRGRIEVE, S. I. 2011. Differentiation of traumatic and heat-induced dental tissue fractures via SEM analysis. *J Forensic Sci,* 56**,** 715-719.

CAMPOBASSO, C. P., DELL'ERBA, A. S., BELVISO, M. & DI VELLA, G. 2007. Craniofacial Identification by Comparison of Antemortem and Postmortem Radiographs: Two Case Reports Dealing with Burnt Bodies. *Am J Forensic Med Path,* 28**,** 182-186.

CHANG, Y. L., STANFORD, C. M. & KELLER, J. C. 2000. Calcium and phosphate supplementation promotes bone cell mineralization: Implications for hydroxyapatite (HA)-enhanced bone formation. *J Biomed Mat Res,* 52**,** 270-278.

CLEMENT, J. G. 1998. Dental identification. *In:* CLEMENT, J. G. & RANSON, D. L. (eds.) *Craniofacial identification in forensic medicine.* London: Arnold.

CORCIA, J. T. & MOODY, W. E. 1974. Thermal Analysis of Human Dental Enamel. *J Dent Res,* 53**,** 571-580.

CORDNER, S. M., WOODFORD, N. & BASSED, R. 2011. Forensic aspects of the 2009 Victorian Bushfires Disaster. *Forensic Sci Int,* 205**,** 2-7.

DA SILVA, R. H. A., QUIEZI, R., BERTOLACINI, C. D. P., CARVALHO, S. P. M., DA SILVAGASQUE, K. C., DE ALMEIDA-E.-SILVA, C. T. & BICUDO, L. A. R. 2012. Human identification analysis using PCR from the root portion of dental elements under different conditions of temperature and exposure time. *RSBO,* 9**,** 67-73.

DENT, A. J., GREAVES, G. N., ROBERTS, M. A., SANKAR, G., WRIGHT, P. A., JONES, R. H., SHEEHY, M., MADILL, D., CATLOW, C. R. A., THOMAS, J. M. & RAYMENT, T. 1995. A New Furnace Design for Use in Combined X-Ray-Absorption and Diffraction of Catalysis and Ceramics Studies - Formation from Carbonate Precursors of Cu, Co, Mn Spinels for the Oxidation of Co and the Formation of Plzt, a Piezoelectric Ceramic. *Nucl Intstrum Meth B,* 97**,** 20-22.

DEYMIER-BLACK, A. C., ALMER, J. D., STOCK, S. R., HAEFFNER, D. R. & DUNAND, D. C. 2010. Synchrotron X-ray diffraction study of load partitioning during elastic deformation of bovine dentin. *Acta Biomater,* 6**,** 2172-2180.

DIJKSTRA, B. K. S. 1938. Die Skelettreste aus dem Kreisgrabenfriedhof von Sleen, Provinz Drente. *Mannus, Zeitschrift fur Vorgeschichte,* 30**,** 548-561.

DODWELL, N. 2012. Early Bronze Age Busta in Cambridgeshire? On-Site experiments to investigate the effects of fires and pryes on pits. *In:* MITCHELL, P. D. & BUCKBERRY, J. (eds.) *Proceedings of the Twelfth Annual Conference of the British Association for Biological Anthropology and Osteoarchaeology. Department of Archaeology and Anthropology University of Cambridge 2010.* Oxford: Archaeopress.

DOLINAK, D. & MATSHES, E. 2005. Identification. *In:* MATSHES, E., LEW, E. & DOLINAK, D. (eds.) *Forensic Pathology: Principles and Practice.* Amsterdam: Elsevier Academic Press.

DUFFY, J. B., WATERFIELD, J. D. & SKINNER, M. F. 1991. Isolation of tooth pulp cells for sex chromatin studies in experimental dehydrated and cremated remains. *Forensic Sci Int,* 49**,** 127-141.

ELLIOTT, J. C. 1994. *Structure and Chemistry of the Apatites and Other Calcium Orthophosphates*, Amsterdam: Elsevier.

ENDRIS, R. & BERRSCHE, R. 1985. Farbenwandel der Zahnhartgewebe als Zeichen thermischer Schädigung. *Z Rechtsmed,* 94**,** 109-120.

ETOK, S., VALSAMI-JONES, E., WESS, T. J., HILLER, J. C., MAXWELL, C., ROGERS, K. D., MANNING, D., WHITE, M., LOPEZ-CAPEL, E., COLLINS, M. J., BUCKLEY, M., PENKMAN, K. & WOODGATE, S. 2007. Structural and chemical changes of thermally treated bone apatite. *J Mater Sci,* 42**,** 9807-9816.

FAIRGRIEVE, S. 2008. *Forensic Cremation: Recovery and Analysis*, 1st ed. Boca Raton: CRC Press.

FEDOROV, A., BEICHEL, R., KALPATHY-CRAMER, J., FINET, J., FILLION-ROBIN, J. C., PUJOL, S., BAUER, C., JENNINGS, D., FENNESSY, F., SONKA, M., BUATTI, J., AYLWARD, S. R., MILLER, J. V., PIEPER, S. & KIKINIS, R. 2012. 3D Slicer as an Image Computing Platform for the Quantitative Imaging Network. July PMID: 22770690. *Magn Reson Imaging,* 30**,** 1323-1341.

FEREIRA, J. L., DE FEREIRA, A. E. & ORTEGA, A. I. 2008. Methods for the analysis of hard dental tissues exposed to high temperatures. *Forensic Sci Int,* 178**,** 119-124.

FEREIRA, J. L., ORTEGA, A. I., BARRIOS, F. A. & ESPINA-FEREIRA, A. I. 2010. Structural analysis of the indicators of dental age in hard dental tissues submitted to high temperatures. *Acta Microsc,* 19**,** 291-304.

FERNANDEZ CASTILLO, R., UBELAKER, D. H., ACOSTA, J. A. L. & DE LA FUENTE, G. A. C. 2013a. Effects of temperature on bone tissue. Histological study of the changes in the bone matrix. *Forensic Sci Int,* 226**,** 33-37.

FERNANDEZ CASTILLO, R., UBELAKER, D. H., ACOSTA, J. A. L., DE LA ROSA, R. J. E. & GARCIA, I. 2013b. Effect of Temperature on Bone Tissue: Histological Changes. *J Forensic Sci,* 58**,** 578-582.

FRANK, R. M. & NALBANDIAN, J. 1989. Structure and Ultrastructure of Dentine. *In:* BERKOVITZ, B. K. B., BOYDE, A., FRANK, R. M., HÖBLING, H. J., MOXHAM, B. J., NALBANDIAN, J. & TOGE, C. H. (eds.) *Teeth.* 1 ed. Berlin: Springer.

FRATZL, P., GROSCHNER, M., VOGL, G., PLENK, H., ESCHBERGER, J., FRATZL-ZELMAN, N., KOLLER, K. & KLAUSHOFER, K. 1992. Mineral crystals in calcified tissues: a comparative study by SAXS. *J Bone Miner Res,* 7**,** 329-334.

GLATTER, O. & KRATKY, O. 1982. *Small angle x-ray scattering,* 1st ed. London: Academic Press.

GONÇALVES, D., THOMPSON, T. J. U. & CUNHA, E. 2011. Implications of heat-induced changes in bone on the interpretation of funerary behaviour and practice. *J Archaeol Sci,* 38**,** 1308-1313.

GREENWOOD, C., ROGERS, K., BECKETT, S. & CLEMENT, J. 2012. Bone mineral crystallisation kinetics. *J Mater Sci Mater Med,* 23**,** 2055-2060.

GRIFFITHS, C. J. & BELLAMY, G. D. 1993. Protection and radiography of heat affected teeth. *Forensic Sci Int,* 60**,** 57-60.

GROßKOPF, B. 2004. *Leichenbrand. Biologisches und kulturhistorisches Quellenmaterial zur Rekonstruktion vor- und frühgeschichtlicher Population und ihrere Funeralpraktiken.* Disseration, University of Leipzig.

GÜNTHER, H. & SCHMIDT, O. 1953. Die Zerstörung des menschlichen Gebisses im Verlauf der Einwirkung hoher Temperaturen. *Deut Z gerichtl Med,* 42**,** 108-188.

HAMMERSLEY, A. P. 1997. *FIT2D: An Introduction and Overview* [Online]. Available: http://www.esrf.eu/computing/scientific/FIT2D/FIT2D_INTRO/fit2d.html [Accessed 20/09/2013].

HARSANYI, L. 1975. Scanning eletron microscopic investigation of thermal damage of the teeth. *Acta Morphol Acad Sci Hung,* 23**,** 271-281.

HERLIANSYAH, M. K., HAMDI, M., IDE-EKTESSABI, A., WILDAN, M. W. & TOQUE, J. A. 2009. The influence of sintering temperature on the properties of compacted bovine hydroxyapatite. *Materials Science & Engineering C-Biomimetic and Supramolecular Systems,* 29**,** 1674-1680.

HERRMANN, B. 1972. Zur Beurteilung von Kohlenstoffverfärbungen bei Leichenbränden. *Ausgrabungen Funde,* 17**,** 275-277.

HERSCHAFT, E. E., ALDER, M. E., ORD, D. K., RAWSON, R. D. & SMITH, E. S. 2006. *Manual of Forensic Odontology,* 4th ed. Albany: Impress Printing & Graphics.

HIGGINS, D. & AUSTIN, J. J. 2013. Teeth as a source of DNA for forensic identification of human remains: A Review. *Sci Justice,* 53(4), 433-441.

HILL, A. J., HEWSON, I. & LAIN, R. 2011a. The role of the forensic odontologist in disaster victim identification: Lessons for management. *Forensic Sci Int,* 205**,** 44-47.

HILL, A. J., LAIN, R. & HEWSON, I. 2011b. Preservation of dental evidence following exposure to high temperatures. *Forensic Sci Int,* 205**,** 40-43.

HILLER, J. C., THOMPSON, T. J. U., EVISON, M. P., CHAMBERLAIN, A. T. & WESS, T. J. 2003. Bone mineral change during experimental heating: An X-ray scattering investigation. *Biomater,* 24**,** 5091-5097.

HILLER, J. C. & WESS, T. J. 2006. The use of small-angle X-ray scattering to study archaeological and experimentally altered bone. *J Archaeol Sci,* 33**,** 560-572.

HILLSON, S. 1996. *Dental anthropology,* 1st ed. Cambridge: Cambridge University Press.

HOLAGER, J. 1970. Thermogravimetric examination of enamel and dentin. *J Dent Res,* 49**,** 546-548.

HOLDEN, J. L., PHAKEY, P. P. & CLEMENT, J. G. 1995. Scanning electron microscope observations of heat-treated human bone. *Forensic Sci Int,* 74**,** 29-45.

HOLLUND, H. I., ARIESE, F., FERNANDES, R., JANS, M. M. E. & KARS, H. 2013. Testing an alternavite high-throughput tool for investigating bone diagenesis: FTIR in attenuated total reflection (ATR) mode. *Archaeometry,* 55**,** 507-532.

HUGHES, C. E. & WHITE, C. A. 2009. Crack Propagation in Teeth: A Comparison of Perimortem and Postmortem Behavior of Dental Materials and Cracks. *J Forensic Sci,* 54**,** 263-266.

INTERPOL. 2009. *Disaster Victim Identification Guide* [Online]. Available: http://www.interpol.int/INTERPOL-expertise/Forensics/DVI-Pages/DVI-guide [Accessed 15/07/2013].

INTERPOL. 2013. *Fingerprints* [Online]. Available: http://www.interpol.int/INTERPOL-expertise/Forensics/Fingerprints [Accessed 15/07/2013].

JABLONSKI, N. G. & SHUM, B. S. 1989. Identification of unknown human remains by comparison of antemortem and postmortem radiographs. *Forensic Sci Int,* 42**,** 221-30.

JACKOWSKI, C., AGHAYEV, E., SONNENSCHEIN, M., DIRNHOFER, R. & THALI, M. 2006a. Maximum intensity projection of cranial computed tomography data for dental identification. *Int J Legal Med,* 120**,** 165-167.

JACKOWSKI, C., LUSSI, A., CLASSENS, M., KILCHOER, T., BOLLIGER, S., AGHAYEV, E., CRISTE, A., DIRNHOFER, R. & THALI, M. J. 2006b. Extended CT scale overcomes restoration caused streak artifacts for dental identification in CT-3D color encoded automatic discrimination of dental restorations. *J Comput Assist Tomo,* 30**,** 510-513.

JAIN, A. K. & CHEN, H. 2004. Matching of dental X-ray images for human identification. *Pattern Recogn,* 37**,** 1519-1532.

JAMESON, M. W., HOOD, J. A. A. & TIDMARSH, B. G. 1993. The Effects of Dehydration and Rehydration on Some Mechanical-Properties of Human Dentin. *J Biomech,* 26**,** 1055-1065.

JIANG, H. D., LIU, X. Y., LIM, C. T. & HSU, C. Y. 2005. Ordering of self-assembled nanobiominerals in correlation to mechanical properties of hard tissues. *Appl Phys Lett,* 86**,** 163901.

JOHANSEN, R. J. & BOWERS, C. 2012. Positive Dental Identification Using Tooth Anatomy and Digital Superimposition. *J Forensic Sci***,** 58(2), 534-536.

KARKHANIS, S. & FRANKLIN, D. 2009. Macroscopic and microscopic changes in incinerated deciduous teeth. *J Forensic Odontostomatol,* 27**,** 9-19.

KNIGHT, B. 1984. How radiography aids forensic medicine. *Radiography,* 50**,** 5-10.

LABORIER, C., BONNETAIN, J. C. & RÖTZSCHER, K. 2004. Das Concorde-Flugzeug-Unglück. *Rechtsmed,* 14**,** 11-13.

LAIN, R., TAYLOR, J., CROKER, S., CRAIG, P. & GRAHAM, J. 2011. Comparative dental anatomy in Disaster Victim Identification: Lessons from the 2009 Victorian Bushfires. *Forensic Sci Int,* 205**,** 36-39.

LEI, H. J., LIU, B. & FANG, D. N. 2010. The coefficient of thermal expansion of biomimetic composite. *Frontiers of Materials Science in China,* 4**,** 234-238.

LIM, J. J. & LIBOFF, A. R. 1972. Thermogravimetric Analysis of Dentin. *J Dent Res,* 51**,** 509-514.

LIN, M., LIU, Q. D., KIM, T., XU, F., BAI, B. F. & LU, T. J. 2010a. A new method for characterization of thermal properties of human enamel and dentine: Influence of microstructure. *Infrared Phys Techn,* 53**,** 457-463.

LIN, M., XU, F., LU, T. J. & BAI, B. F. 2010b. A review of heat transfer in human tooth-Experimental characterization and mathematical modeling. *Dent Mater,* 26**,** 501-513.

LIN, P. L., LAI, Y. H. & HUANG, P. W. 2012. Dental biometrics: Human identification based on teeth and dental works in bitewing radiographs. *Pattern Recogn,* 45**,** 934-946.

LINDBLOOM, B. 2009. *Delta E (CIE 2000)* [Online]. Available: http://www.brucelindbloom.com/ [Accessed 17/09/2013].

LIPTON, B. E., MURMANN, D. C. & PAVLIK, E. J. 2013. History of Forensic Odontology. *In:* SENN, D. R. & WEEMS, R. A. (eds.) *Manual of Forensic Odontology.* 5th ed. Boca Raton: CRC Press.

MAHNY, M., VANEYCKEN, L. & OOSTERLINCK, A. 1994. Evaluation of Uniform Color Spaces Developed after the Adoption of Cielab and Cieluv. *Color Res Appl,* 19**,** 105-121.

MAPLES, W. R. & BROWNING, M. 1995. *Dead Men Do Tell Tales: The Strange and Fascinating Cases of a Forensic Anthropologist,* 1st ed. New York: Broadway Books.

MARELLA, G. L. & ROSSI, P. 1999. An approach to person identification by means of dental prostheses in a burnt corpse. *J Forensic Odontostomatol,* 17**,** 16-19.

MARET, D., PETERS, O. A., DEDOUIT, F., TELMON, N. & SIXOU, M. 2011. Cone-Beam Computed Tomography: A useful tool for dental age estimation? *Med Hypotheses,* 76**,** 700-702.

MARTEN, A., FRATZL, P., PARIS, O. & ZASLANSKY, P. 2010. On the mineral in collagen of human crown dentine. *Biomater,* 31**,** 5479-5490.

MATOSO, R. I., BENEDICTO, E. N., DE LIMA, S. H. R., PRADO, F. B., DARUGE, E. & DARUGE JUNIOR, E. 2013. Positive identification of a burned body using an implanted orthopedic plate. *Forensic Sci Int,* 229**,** 168.e1-168.e5.

MAYNE-CORREIRA, P. M. 1997. Fire Modification of Bone: A review of the Literature. *In:* HAGLUND, W. D. & SORG, M. H. (eds.) *Forensic Taphonomy: The Postmortem Fate of Human Remains.* 1st ed. Boca Raton: CRC Press.

MCKINLEY, J. I. 2000. The analysis of cremated bone. *In:* COX, M. & MAYS, S. (eds.) *Human Osteology in Archaeology and Forensic Science.* 1st ed. London: Greenwich Medical Media.

MECKEL, A. H., GRIEBSTEIN, W. J. & NEAL, R. J. 1965. Structure of mature human dental enamel as observed by electron microscopy. *Arch Oral Biol,* 10**,** 775-783.

MERLATI, G., DANESINO, P., SAVIO, C., FASSINA, G., OSCULATI, A. & MENGHINI, P. 2002. Observations on dental prostheses and restorations subjected to high temperatures: experimental studies to aid identification processes. *J Forensic Odontostomatol,* 20**,** 17-24.

MERLATI, G., SAVLO, C., DANESINO, P., FASSINA, G. & MENGHINI, P. 2004. Further study of restored and un-restored teeth subjected to high temperatures. *J Forensic Odontostomatol,* 22**,** 34-39.

MEYER, H. J. 2003. The Kaprun cable car fire disaster - aspects of forensic organisation following a mass fatality with 155 victims. *Forensic Sci Int,* 138**,** 1-7.

MINCER, H. H., BERRYMAN, H. E., MURRAY, A. & DICKENS, R. L. 1990. Methods for Physical Stabilization of Ashed Teeth in Incinerated Remains. *J Forensic Sci,* 35**,** 971-974.

MKUKUMA, L. D., SKAKLE, J. M., GIBSON, I. R., IMRIE, C. T., ASPDEN, R. M. & HUKINS, D. W. 2004. Effect of the proportion of organic material in bone on thermal decomposition of bone mineral: an investigation of a variety of bones from different species using thermogravimetric analysis coupled to mass spectrometry, high-temperature X-ray diffraction, and Fourier transform infrared spectroscopy. *Calcif Tissue Int,* 75**,** 321-328.

MOODY, G. H. & BUSUTTIL, A. 1994. Identification in the Lockerbie Air Disaster. *Am J Forensic Med Path,* 15**,** 63-69.

MORENO, S., MERLATI, G., MARIN, L., SAVIO, C. & MORENO, F. 2009. Effects of high temperatures on different dental restorative systems: Experimental study to aid identification processes. *J Forensic Dent Sci,* 1**,** 17-23.

MULLER, M., BERYTRAND, M. F., QUATREHOMME, G., BOLLA, M. & ROCCA, J. P. 1998. Macroscopic and microscopic aspects of incinerated teeth. *J Forensic Odontostomatol,* 16**,** 1-7.

MURRAY, C. A., BOYD, P. T., YOUNG, B. C., DICKSON, S. D. M. & CURRIE, J. N. W. 2007. A survey of denture identification marking within the United Kingdom. *Brit Dent J,* 203, E24.

MYERS, S. L., WILLIAMS, J. M. & HODGES, J. S. 1999. Effects of extreme heat on teeth with implications for histologic processing. *J Forensic Sci,* 44**,** 805-809.

NOMIR, O. & ABDEL-MOTTALEB, M. 2007. Human Identification From Dental X-Ray Images Based on the Shape and Appearance of the Teeth. *IEEE T Inf Foren Security,* 2**,** 188-197.

NORRLANDER, A. L. 1995. Burned and incinerated remains. *In:* BOWERS, C. M. & BELL, G. (eds.) *Manual of Forensic Odontology.* 3rd ed. Ann Arbor: Forensic Press.

O'DONNELL, C., IINO, M., MANSHARAN, K., LEDITSCKE, J. & WOODFORD, N. 2011. Contribution of postmortem multidetector CT scanning to identification of the deceased in a mass disaster: Experience gained from the 2009 Victorian bushfires. *Forensic Sci Int,* 205**,** 15-28.

PALLAGATTI, S., SHEIKH, S., AGGARWAL, A., GUPTA, R. S. D. & KAUR, A. 2011. Maxillofacial Radiology in Forensic Science. *J Forensic Res,* 2**,** 100134.

PATIDAR, K. A., PARWANI, R. & WANJARI, S. 2010. Effects of high temperature on different restorations in forensic identification: Dental samples and mandible. *J Forensic Dent Sci,* 2**,** 37-43.

PIGA, G., MALGOSA, A., THOMPSON, T. J. U. & ENZO, S. 2008. A new calibration of the XRD technique for the study of archaeological burned human remains. *J Archaeol Sci,* 35**,** 2171-2178.

PIGA, G., THOMPSON, T. J. U., MALGOSA, A. & ENZO, S. 2009. The Potential of X-Ray Diffraction in the Analysis of Burned Remains from Forensic Contexts. *J Forensic Sci,* 54**,** 534-539.

PRAMANIK, S., HANIF, A. S. M., PINGGUAN-MURPHY, B. & ABU OSMAN, N. A. 2013. Morphological Change of Heat Treated Bovine Bone: A Comparative Study. *Materials,* 6**,** 65-75.

PRETTY, I. A. 2007. Forensic dentistry: 1. Identification of human remains. *Dent Update,* 34**,** 621-630.

PRETTY, I. A., BARSLEY, R. E., BOWERS, C. M., BUSH, M. A., BUSH, P., CLEMENT, J., DORION, R., FREEMAN, A. J., LEWIS, J., SENN, D. R. & WRIGHT, F. A. 2013. Odontology - dentistry's contribution to truth and justice. *In:* UBELAKER, D. H. (ed.) *Forensic Science: Current Issues, Future Directions.* 1st ed. Hoboken: Wiley-Blackwell.

PRETTY, I. A. & SWEET, D. 2001. A look at forensic dentistry--Part 1: The role of teeth in the determination of human identity. *Brit Dent J,* 190**,** 359-366.

PURVES, J. D. 1975. Dental identification of fire victims. *Forensic Sci,* 6**,** 217-219.

R CORE TEAM. 2013. *R: A language and environment for statistical computing* [Online]. Available: http://www.R-project.org/ [Accessed 15/10/2013].

RASBAND, W. S. 1997-2013. *ImageJ, U.S. National Institutes of Health, Bethesda, Maryland, USA* [Online]. Available: http://imagej.nih.gov/ij/ [Accessed 12/09/2013].

RASMUSSEN, S. T., PATCHIN, R. E., SCOTT, D. B. & HEUER, A. H. 1976. Fracture Properties of Human Enamel and Dentin. *J Dent Res,* 55**,** 154-164.

RAUE, L., GERSDORFF, N., RÖDIGER, M. & KLEIN, H. 2012. New insights in prism orientation within human enamel. *Arch Oral Biol,* 57**,** 271-276.

REES, K. A. & COX, M. J. 2010. Comparative Analysis of the Effects of Heat on the PCR-Amplification of Various Sized DNA Fragments Extracted from Sus Scrofa Molars*. *J Forensic Sci,* 55**,** 410-417.

REICHE, I., VIGNAUD, C. & MENU, M. 2002. The crystallinity of ancient bone and dentine: new insights by transmission electron microscopy. *Archaeometry,* 44**,** 447-459.

REYES-GASGA, J., GARCÍA-GARCÍA, R., ARELLANO-JIMÉNEZ, M. J., SANCHEZ-PASTENES, E., TIZNADO-OROZCO, G. E., GIL-CHAVARRIA, I. M. & GÓMEZ-GASGA, G. 2008. Structural and thermal behaviour of human tooth and three synthetic hydroxyapatites from 20 to 600 °C. *J Phys D Appl Phys,* 41**,** 225407.

RINNERTHALER, S., ROSCHGER, P., JAKOB, H. F., NADER, A., KLAUSHOFER, K. & FRATZL, P. 1999. Scanning small angle X-ray scattering analysis of human bone sections. *Calcif Tissue Int,* 64**,** 422-429.

ROBINSON, J. P., LUMLEY, P. J., CLARIDGE, E., COOPER, P. R., GROVER, L. M., WILLIAMS, R. L. & WALMSLEY, A. D. 2012. An analytical Micro CT methodology for quantifying inorganic dentine debris following internal tooth preparation. *J Dent,* 40**,** 999-1005.

ROGERS, K., BECKETT, S., KUHN, S., CHAMBERLAIN, A. & CLEMENT, J. 2010. Contrasting the crystallinity indicators of heated and diagenetically altered bone mineral. *Palaeogeogr Palaeocl,* 296**,** 125-129.

ROGERS, K. D. & DANIELS, P. 2002. An X-ray diffraction study of the effects of heat treatment on bone mineral microstructure. *Biomater,* 23**,** 2577-2585.

ROSSOUW, R. J., GROBLER, S. R., PHILLIPS, V. M. & VAN, W. K. T. J. 1999. The effects of extreme temperatures on composite, compomer and ionomer restorations. *J Forensic Odontostomatol,* 17**,** 1-4.

RUTTY, G. N., BROUGH, A., BIGGS, M. J. P., ROBINSON, C., LAWES, S. D. A. & HAINSWORTH, S. V. 2013. The role of micro-computed tomography in forensic investigations. *Forensic Sci Int,* 225**,** 60-66.

RUTTY, G. N., ROBINSON, C., MORGAN, B., BLACK, S., ADAMS, C. & WEBSTER, P. 2009. Fimag: The United Kingdom Disaster Victim/Forensic Identification Imaging System. *J Forensic Sci,* 54**,** 1438-1442.

SANDHOLZER, M. A., BARON, K., HEIMEL, P. & METSCHER, B. D. 2014. Volume analysis of heat-induced cracks in human molars: A preliminary study. *J Forensic Dent Sci,* 6**,** 53-58.

SANDHOLZER, M. A., ERRICKSON, D. & WALTER, B. S. 2013. AAFS 2013: Current issues and future trends in forensic radiology and imaging. *J Forensic Radiol Imaging,* 1**,** 88-90.

SANDHOLZER, M. A., SUI, T., KORSUNSKY, A. M., WALMSLEY, A. D., LUMLEY, P. J. & LANDINI, G. 2014, in press. X-ray scattering evaluation of ultrastructural changes of human dental tissue with thermal treatment *J Forensic Sci*.

SAVIO, C., MERLATI, G., DANESINO, P., FASSINA, G. & MENGHINI, P. 2006. Radiographic evaluation of teeth subjected to high temperatures: experimental study to aid identification processes. *Forensic Sci Int,* 158**,** 108-16.

SCHINDELIN, J., ARGANEDA-CARRERAS, I., FRISE, E., KAYNIG, V., LONGAIR, M., PIETZSCH, T., PREIBISCH, S., RUEDEN, C., SAALFELD, S., SCHMID, B., TINEVEZ, J. Y., WHITE, D. J., HARTENSTEIN, V., ELICEIRI, K., TOMANCAK, P. & CARDONA, A. 2012. Fiji: an open-source platform for biological-image analysis. *Nat Methods,* 9**,** 676-682.

SCHMID, B., SCHINDELIN, J., CARDONA, A., LONGAIR, M. & HEISENBERG, M. 2010. A high-level 3D visualization API for Java and ImageJ. *BMC Bioinformatics,* 11**,** 274.

SCHMIDT, C. 2008. The recovery and study of burned human teeth. *In:* SCHMIDT, C. & SYMES, S. (eds.) *The Analysis of Burned Human Remains.* 1st ed. San Diego: Academic Press.

SCHULLER-GOTZBURG, P. & SUCHANEK, J. 2007. Forensic odontologists successfully identify tsunami victims in Phuket, Thailand. *Forensic Sci Int,* 171**,** 204-207.

SCHWARTZ, T. R., SCHWARTZ, E. A., MIESZERSKI, L., MCNALLY, L. & KOBILINSKY, L. 1991. Characterization of deoxyribonucleic acid (DNA) obtained from teeth subjected to various environmental conditions. *J Forensic Sci,* 36**,** 979-990.

SCHWEITZER, H. & EICHENHOFER, W. 1980. Temperaturen in der Mundhöhle bei Verbrennungen mit hohen Temperaturen. *Zbl Rechtsmed,* 20**,** 38.

SENN, D. R. & WEEMS, R. A. 2013. *Manual of Forensic Odontology,* 5th ed. Boca Raton: CRC Press.

SHIPMAN, P., FOSTER, G. & SCHOENINGER, M. 1984. Burnt bones and teeth: an experimental study of color, morphology, crystal structure and shrinkage. *J Archaeol Sci,* 11**,** 307-325.

SILVA, R., BOTELHO, T., PRADO, F., KAWAGUSHI, J., DARUGE JÚNIOR, E. & BÉRZIN, F. 2011. Human identification based on cranial computed tomography scan — a case report. *Dentomaxillofacial Radiology,* 40**,** 257-261.

SQUIRES, K. E., THOMPSON, T. J. U., ISLAM, M. & CHAMBERLAIN, A. 2011. The application of histomorphometry and Fourier Transform Infrared Spectroscopy to the analysis of early Anglo-Saxon burned bone. *J Archaeol Sci,* 38**,** 2399-2409.

SUI, T., SANDHOLZER, M. A., BAIMPAS, N., DOLBNYA, I. P., LANDINI, G. & KORSUNSKY, A. M. 2013a. Hierarchical modelling of elastic behaviour of human enamel based on synchrotron diffraction characterisation. *J Struct Biol,* 184**,** 136-146.

SUI, T., SANDHOLZER, M. A., BAIMPAS, N., DOLBNYA, I. P., WALMSLEY, A., LUMLEY, P. J., LANDINI, G. & KORSUNSKY, A. M. 2013b. Multiscale modelling and diffraction-based characterization of elastic behaviour of human dentine. *Acta Biomater,* 9**,** 7937-7947.

SUI, T., LUNT, A. J., BAIMPAS, N., SANDHOLZER, M. A., HU, J., DOLBNYA, I. P., LANDINI, G. & KORSUNSKY, A. M. 2014a. Hierarchical modelling of in situ elastic deformation of human enamel based on photoelastic and diffraction analysis of stresses and strains. *Acta Biomater,* 10**,** 343-354.

SUI, T., SANDHOLZER, M. A., LUNT, A. J., BAIMPAS, N., SMITH, A., LANDINI, G. & KORSUNKSY, A. 2014b. In-situ X-ray scattering evaluation of heat-induced ultrastructural changes in dental tissues and synthetic hydroxyapatite. *J R Soc Interf,* 11, 20130928

SUN, J., ZHANG, X., CUI, J. & ZHOU, L. 2006. Image retrieval based on color distribution entropy. *Pattern Recogn Lett,* 27**,** 1122-1126.

SWEET, D. 2000. Dental DNA Evidence. *In:* WILLEMS, G. (ed.) *Forensic Odontology: Proceedings of the European Iofos Millennium Meeting Leuven, Belgium August 23-26, 2000*. Leuven: Leuven University Press.

SWEET, D. 2010. Forensic dental identification. *Forensic Sci Int,* 201**,** 3-4.

SWEET, D., HILDEBRAND, D. & PHILLIPS, D. 1999. Identification of a skeleton using DNA from teeth and a PAP smear. *J Forensic Sci,* 44**,** 630-633.

SYMES, S. A., RAINWATER, C. W., CHAPMAN, E. N., GIPSON, D. R. & PIPER, A. L. 2008. Patterned Thermal Destruction of Human Remains in a Forensic Setting. *In:* SCHMIDT, C. W. & SYMES, S. A. (eds.) *The Analysis of Burned Human Remains.* 1st ed. San Diego: Academic Press.

TAYLOR, P. T., WILSON, M. E. & LYONS, T. J. 2002. Forensic odontology lessons: multishooting incident at Port Arthur, Tasmania. *Forensic Sci Int,* 130**,** 174-182.

TESCH, W., EIDELMAN, N., ROSCHGER, P., GOLDENBERG, F., KLAUSHOFER, K. & FRATZL, P. 2001. Graded microstructure and mechanical properties of human crown dentin. *Calcif Tissue Int,* 69**,** 147-157.

THALI, M. J., MARKWALDER, T., JACKOWSKI, C., SONNENSCHEIN, M. & DIRNHOFER, R. 2006. Dental CT imaging as a screening tool for dental profiling: Advantages and limitations. *J Forensic Sci,* 51**,** 113-119.

THALI, M. J., TAUBENREUTHER, U., KAROLCZAK, M., BRAUN, M., BRUESCHWEILER, W., KALENDER, W. A. & DIRNHOFER, R. 2003. Forensic microradiology: micro-computed tomography (Micro-CT) and analysis of patterned injuries inside of bone. *J Forensic Sci,* 48**,** 1336-1342.

THOMPSON, T. J. U. 2004. Recent advances in the study of burned bone and their implications for forensic anthropology. *Forensic Sci Int,* 146 Suppl**,** S203-5.

THOMPSON, T. J. U. 2005. Heat-induced dimensional changes in bone and their consequences for forensic anthropology. *J Forensic Sci,* 50**,** 1008-1015.

THOMPSON, T. J. U., GAUTHIER, M. & ISLAM, M. 2009. The application of a new method of Fourier Transform Infrared Spectroscopy to the analysis of burned bone. *J Archaeol Sci,* 36**,** 910-914.

THOMPSON, T. J. U., ISLAM, M. & BONNIERE, M. 2013. A new statistical approach for determining the crystallinity of heat-altered bone mineral from FTIR spectra. *J Archaeol Sci,* 40**,** 416-422.

THOMPSON, T. J. U., ISLAM, M., PIDURU, K. & MARCEL, A. 2011. An investigation into the internal and external variables acting on crystallinity index using Fourier Transform Infrared Spectroscopy on unaltered and burned bone. *Palaeogeogr Palaeocl,* 299**,** 168-174.

TOHNAK, S., MEHNERT, A. J., MAHONEY, M. & CROZIER, S. 2011. Dental CT metal artefact reduction based on sequential substitution. *Dentomaxillofac Radiol,* 40**,** 184-190.

UBELAKER, D. H. 2009. The forensic evaluation of burned skeletal remains: A synthesis. *Forensic Sci Int,* 183**,** 1-5.

VAN DER GRAAF, E. R. & TEN BOSCH, J. J. 1993. Changes in dimensions and weight of human dentine after different drying procedures and during subsequent rehydration. *Arch Oral Biol,* 38**,** 97-99.

VAN DER HAEGHEN, Y. & NAEYAERT, J. M. 2006. Consistent cutaneous imaging with commercial digital cameras. *Arch Dermatol,* 142**,** 42-46.

VON HOFMANN, E. 1875. Beobachtungen an verbrannten Leichentheilen. *Wien Med Wochenschr,* 25.

VON WURMB-SCHWARK, N., RINGLEB, A., GEBUHR, M. & SIMEONI, E. 2005. Genetic analysis of modern and historical remains. *Anthropol Anz,* 63**,** 1-12.

WAHL, J. 1982. Leichenbranduntersuchungen. Ein Überblick über die Bearbeitungs- und Aussagemöglichkeiten von Brandgräberen. *Prähistorische Z,* 57**,** 2-125.

WALKER, P. L., MILLER, K. W. P. & RICHMAN, R. 2008. Time, temperature and oxygen availability: an experimental study of the effects of environmental conditions on the color and organic content of cremated bone. *In:* SCHMIDT, C. & SYMES, S. (eds.) *The Analysis of Burned Human Remains.* 1st ed. San Diego: Academic Press.

WARREN, M. 2008. Detection of Commingling in Cremated Human Remains. *In:* ADAMS, B. J. & BYRD, J. E. (eds.) *Recovery, Analysis, and Identification of Commingled Human Remains.* Totowa: Humana Press.

WATERHOUSE, K. 2013a. The effect of weather conditions on burnt bone fragmentation. *J Forensic Leg Med,* 20**,** 489-495.

WATERHOUSE, K. 2013b. Post-burning fragmentation of calcined bone: Implications for remains recovery from fatal fire scenes. *J Forensic Leg Med,* 20**,** 1112-1117.

WILLIAMS, D., LEWIS, M., FRANZEN, T., LISSETT, V., ADAMS, C., WHITTAKER, D., TYSOE, C. & BUTLER, R. 2004. Sex determination by PCR analysis of DNA extracted from incinerated, deciduous teeth. *Science & Justice,* 44**,** 89-94.

WOISETSCHLAGER, M., LUSSI, A., PERSSON, A. & JACKOWSKI, C. 2011. Fire victim identification by post-mortem dental CT: radiologic evaluation of restorative materials after exposure to high temperatures. *Eur J Radiol,* 80**,** 432-440.

WOOD, R. E. & KOGON, S. L. 2010. Dental radiology considerations in DVI incidents: A review. *Forensic Sci Int,* 201**,** 27-32.

YAMAMOTO, K., OHTANI, S., KATO, S., SUGIMOTO, H., MIAKE, K. & NAKAMURA, T. 1990. Morphological Changes in Human and Animal Enamel Rods with Heating - Especially Limits in Temperature Allowing Discrimination between Human and Animal Teeth. *Bull Kanagawa Dental College,* 18**,** 55-61.

ZHONG, X., YU, D., WONG, Y. S., SIM, T., LU, W. F., FOONG, K. W. C. & CHENG, H. L. in press. 3D dental biometrics: Alignment and matching of dental casts for human identification. *Comput Ind.*

Chapter 11 - Appendix

11. 1. ImageJ/Fiji macros

11.1.1. Create mask for uniform black background

This Fiji macro creates a uniform black background to facilitate colorimetric image analysis. The original picture had a green background, a colour that was not present in the surface colour alterations and therefore could be used to produce a binary (i.e. black and white) mask (Figure 2.3).

```
min=newArray(3);
max=newArray(3);
filter=newArray(3);
a=getTitle();
run("HSB Stack");
run("Convert Stack to Images");
selectWindow("Hue");
rename("0");
selectWindow("Saturation");
rename("1");
selectWindow("Brightness");
rename("2");
min[0]=48;
max[0]=130;
filter[0]="pass";
min[1]=0;
max[1]=255;
filter[1]="pass";
min[2]=0;
max[2]=255;
filter[2]="pass";
for (i=0;i<3;i++){
  selectWindow(""+i);
  setThreshold(min[i], max[i]);
  run("Convert to Mask");
  if (filter[i]=="stop")  run("Invert");
}
imageCalculator("AND create", "0","1");
imageCalculator("AND create", "Result of 0","2");
for (i=0;i<3;i++){
  selectWindow(""+i);
  close();
}
selectWindow("Result of 0");
close();
selectWindow("Result of Result of 0");
run("Erode");
run("Fill Holes");
rename(a);
```

11.1.2. Create colour palettes from *.txt files

The following Fiji macro produces colour palettes based on a list of RGB values (saved as a tab-delimited *.txt file). A set number (maximum: 256) of 8-bit images are created, and put together as a montage with parameters (e.g. number of columns/rows, size, border) as desired. Subsequently, the *.txt file is selected and the RGB values get set as colours for the individual tiles of the montage using the lookup table (LUT) function.

```
newImage("Untitled", "8-bit Black", 300, 300, 6);
for (i=1;i<=nSlices;i++){
 setSlice(i);
 run("Set...", "value="+i-1+" slice");
}

run("Make Montage...", "columns=1 rows=6 scale=1 first=1 last=6 increment=1 border=1 font=12");
getLut(reds, greens, blues);

text = File.openAsString("");
  lines = split(text,"\n");
  text = "";
nl=lines.length;
for (i=1;i<nl;i++){
 rgb= split(lines[i], "\t");
 reds[i]=rgb[0];
 greens[i]=rgb[1];
 blues[i]=rgb[2];
}
setLut(reds, greens, blues);
```

11.1.3. Extraction of colour entropy from RGB images

This ImageJ macro was written by G. Landini and allows the extraction of the colour entropy from RGB images. The RGB value of each individual pixel of an image is recorded, and combined with the information of the area of an image size (i.e. number of pixels) to finally calculate the colour entropy as outlined in Chapter 2.8.1.

```
hist=newArray(16777216);
h=getHeight();
w=getWidth();

for (y=0;y<h;y++){
  for (x=0;x<w;x++){
       p=getPixel(x,y);
        i=(p&0xff0000)+(p&0x00ff00)+(p&0x0000ff);
        hist[i]=hist[i]+1;
  }
}

pix=w*h; //number of pixels in image
log2=log(2);

s=0;
for (i=0;i<16777216;i++){
  if(hist[i]>0) {
      // avoid log(0)
      p=hist[i]/pix; // probability of colour j
      s=s+(p*(log(p)/log2));
  }
}
print ("Entropy: "+(-s));
```

11.2. Reprints of peer-reviewed publications

Publication 1:
Sandholzer MA, Walmsley AD, Lumley PJ, Landini G. *Radiologic evaluation of heat-induced shrinkage and shape preservation of human teeth using micro-CT*. Journal of Forensic Radiology and Imaging 2013; 1(3) 107-111, DOI 10.1016/j.jofri.2013.05.003.

Publication 2:
Sandholzer MA, Sui T, Korsunsky A, Walmsley AD, Lumley PJ, Landini G. *X-ray scattering evaluation of ultrastructural changes of human dental tissue with thermal treatment* Journal of Forensic Sciences 2014; 59(3) 769-774, DOI 10.1111/1556-4029.12400.

Publication 3:
Sui T, **Sandholzer MA**, Le Bourhis E, Baimpas N, Landini G, Korsunsky AM. *Structure-mechanical function relations at nano-scale in heat-affected human dental tissue.*Journal of the Mechanical Behavior of Biomedical Materials 2014, 32 113-124, DOI 10.1016/j.jmbbm.2013.12.014.

Publication 4:
Sui T, **Sandholzer MA**, Lunt AJG, Baimpas N, Smith A, Landini G, Korsunsky AM. *In-situ X-ray scattering evaluation of heat-induced ultrastructural changes in dental tissues and synthetic hydroxyapatite* Journal Royal Society Interface 2014, 11(95), 20130928, DOI 10.1098/rsif.2013.0928

Publication 5:
Sui T, Lunt A, Baimpas N, **Sandholzer MA**, Hu J, Dolbnya IP, Landini G, Korsunsky AM. *Hierarchical modelling of in situ elastic deformation of human enamel based on photoelastic and diffraction analysis of stresses and strains.* Acta Biomaterialia 2014, 10(1) 343-354, DOI 10.1016/j.actbio.2013.09.043.

Publication 6:
Sui T, **Sandholzer MA**, Baimpas N, Dolbnya IP, Landini G, Korsunsky AM. *Hierarchical modelling of elastic behaviour of human enamel based on synchrotron diffraction characterization.* Journal of Structural Biology 2013; 184(2) 136-146, DOI 10.1016/j.jsb.2013.09.023.

Publication 7:
Sui T, **Sandholzer MA**, Baimpas N, Dolbnya IP, Walmsley AD, Lumley PJ, Landini G, Korsunsky AM. *Multi-scale modelling and diffraction-based characterization of elastic behaviour of human dentine* Acta Biomaterialia 2013; 9(8) 7937-7947, DOI 10.1016/j.actbio.2013.04.020.

Journal of Forensic Radiology and Imaging 1 (2013) 107–111

Contents lists available at SciVerse ScienceDirect

Journal of Forensic Radiology and Imaging

journal homepage: www.elsevier.com/locate/jofri

Radiologic evaluation of heat-induced shrinkage and shape preservation of human teeth using micro-CT

Michael A. Sandholzer*, Anthony D. Walmsley, Philip J. Lumley, Gabriel Landini

School of Dentistry, College of Medical and Dental Sciences, University of Birmingham, St Chads Queensway, Birmingham B4 6NN, United Kingdom

ARTICLE INFO

Article history:
Received 3 March 2013
Received in revised form
15 April 2013
Accepted 17 May 2013
Available online 1 July 2013

Keywords:
X-ray microtomography
Forensic dentistry
Victim identification
Heat-induced alterations
Burned teeth
Cremains

ABSTRACT

Introduction: The most reliable and frequently applied method for identification of fire victims is comparative dental radiography. Forensic investigators are often confronted with fragmented and isolated remains, frequently removed from their anatomical position. Whilst the heat-induced dimensional and morphological changes in bone have been previously studied, precise data for heat-induced changes of human teeth is still lacking.

Objective: The aim of this study was to obtain quantitative micro-CT data to evaluate the three-dimensional shrinkage and shape preservation of human teeth to provide an improved understanding on heat-induced alterations of dental tissues.

Materials and methods: High-resolution micro-CT scans and digital radiographs were carried out on 66 freshly extracted human teeth before and after 30 min exposure to temperatures of 400–1000 °C. Image analysis was performed using 3D Slicer and Fiji imaging packages.

Results: The average volumetric shrinkage ranged between 4.78% (at 400 °C) and 32.53% (at 1000 °C). A major increase in shrinkage occurs between 700 °C and 800 °C, while no significant statistical difference (ANOVA post-hoc LSD, $\alpha < 0.05$) was found between lower temperature groups. Tooth morphology was generally well preserved even at high temperatures, in contrast to observation made for burned bone, where warping and strong deformation can occur.

Conclusions: The results of this micro-CT study add relevant information on shape preservation and allow forensic investigators to account for heat-induced alterations of size, eventually facilitating the odontological identification process in cases where only isolated teeth or dental fragments are present.

1. Introduction

Radiological imaging plays a vital role in the identification process of deceased persons [1–4]. The most reliable and frequently applied radiologic method for identification in cases involving high temperature exposure is comparative dental radiography, which compares features of the dentition (e.g. missing teeth, pathologies and restorations) between ante-mortem and post-mortem dental radiographs [5–7]. Burned human remains are often found after natural disasters, airplane crashes or house fires, as a result of either direct contact with open flames or the exposure to high temperatures [5,6,8]. The positive identification and investigation of severely burned human remains requires careful examination, forensic experience and excellent skills in comparative dental anatomy [5].

Since the thermal stress or the surrounding environment (e.g. destroyed airplane, collapsed building) can lead to extreme fragmentation of the skeletal remains, forensic investigators are often confronted with isolated teeth or fragments thereof [5,9]. Posterior teeth tend to be better preserved than anterior teeth due to their size and the heat protection, offered by layers of skin, mucosa, muscle and fatty tissue and are therefore more likely to be used in the odontological identification process [6]. It has been reported that teeth shrink due to the heat exposure and are therefore often removed from their anatomical position [5,8]. However, whilst heat-induced dimensional changes in animal and human bone have been previously studied, there is no precise data available for the heat-induced dimensional changes of human teeth [10,11]. Therefore, the first aim of this study was to evaluate the volumetric heat-induced shrinkage for a variety of temperatures found in possible archaeological and forensic scenarios by means of quantitative X-ray microtomography (micro-CT).

High-resolution CT imaging has become of increasing importance in forensic radiography [1,12–14]. Recently, Woisetschläger et al. reported on the specific heat-induced alterations of HU

* Corresponding author. Tel.: +44 121 4665527; fax: +44 121 625 8815.
E-mail addresses: mxs142@bham.ac.uk, m.sandholzer@gmail.com (M.A. Sandholzer).

2212-4780/$ - see front matter © 2013 Elsevier Ltd. All rights reserved.
http://dx.doi.org/10.1016/j.jofri.2013.05.003

values in dental tissues and a number of restoration materials analysed with high-resolution CT, providing important information on the characterisation of filling materials exposed to heat [15]. However, with increasing trends in oral health, growing numbers of patients have low incidence of caries and consequently lack restorations, so other features, like the external enamel shape and root morphology need to be considered in the ante-mortem–post-mortem comparison [6,7]. Merlati et al. [16] indicated the importance of qualitative aspects of structural features for positive dental identification, emphasising tooth morphology as a very significant characteristic. In animal and human bone heat-induced warping and deformation can occur at higher temperatures, whilst the extent of morphological changes in human teeth over a large range of temperatures has not been previously evaluated [10,11,16–18]. Therefore, the second aim of this study was to look at shape preservation of dental tissues after exposure to high temperatures, which can add relevant information for comparative dental radiography of isolated teeth and fragments.

2. Material and methods

2.1. Human teeth sampling and preparation

A total of 66 (33 premolars, 33 molars) freshly extracted sound human teeth (ethical approval obtained from the National Research Ethics Committee; NHS-REC reference 09.H0405.33/Consortium R&D No. 1465) were disinfected and cleaned to eliminate residues. Fifty-six teeth were subdivided into seven different temperature groups (400 °C–1000 °C in steps of 100 °C), with 8 teeth each (4 PM, 4 M). Ten teeth (5 PM, 5 M) were burned at 900 °C for further analysing shape alterations at high temperatures. A Carbolite ashing furnace AAF 11/3 (Carbolite, Sheffield, United Kingdom) was used to simulate the thermal stress. The teeth were exposed to the various high temperatures for 30 min and subsequently cooled down to room temperature according to earlier publications [17,18].

2.2. Standard X-ray protocol

Digital radiographs were taken of 10 teeth before and after heat exposure at 900 °C using a customised Kodak 2100 Intraoral X-ray system (Carestream Health Inc., Rochester, NY, USA) using 60 kV voltage, 7 μA current and 0.1 s exposure time. The setup allowed fixed object-detector distance and size calibration was performed using high-precision ball bearings.

2.3. Micro-CT protocol

The pre- and postscans of 56 teeth were carried out with a SkyScan 1172 micro-CT scanner (SkyScan, Kontich, Belgium) at 13.5 μm resolution using 80 kV voltage, 100 μA current and a 0.5 mm Aluminium filter. The resulting slices were reconstructed with SkyScan's NSRECON package using a uniform attenuation coefficient.

2.4. Image analysis

Following the reconstruction the micro-CT image stacks were converted and a 3-D fast rigid registration of pre- and postscans was performed using 3D Slicer version 3.6.4 (available online: http://www.slicer.org) [19]. After the manual determination of the region of interest (ROI) the registered image stacks were cropped, the images binarised by using the same thresholding values [20] and the resulting values exported to SPSS version 19 (IBM SPSS Inc., Chicago, USA) for further statistical analysis. Three-dimensional models were produced using the Fiji imaging package [20].

2.5. Statistical analysis

The computed differences of the pre- and postscan volumes were statistically analysed with a student t-test, a one-way analysis of variance (ANOVA) and post-hoc Least Significant Difference (LSD) tests using SPSS version 19. Significance levels of $p < 0.05$ (95% confidence interval) were used as an index of statistical significance.

3. Results

3.1. Macroscopic evaluation

A progressive, temperature-dependent shift from a natural colour to predominantly black/dark brown (400 °C), brown (500–600 °C), greyish-blue (700 °C), light grey (800 °C), chalky-white (900 °C) and patches of white, black and pink (1000 °C) was observed (see Fig. 1).

The enamel was fully preserved and attached to the dentine in the 400 °C group, partially separated from the coronal dentine or fragmented between 500 °C and 700 °C and fully separated and fragmented in all teeth ≥800 °C. At temperatures ≥500 °C, the teeth became more fragile, with visible crack formation and fragmentation within the dentine.

3.2. Radiological evaluation

In all teeth of the lower temperature groups (≤600 °C) the micro-CT sections showed multiple small cracks in the apical

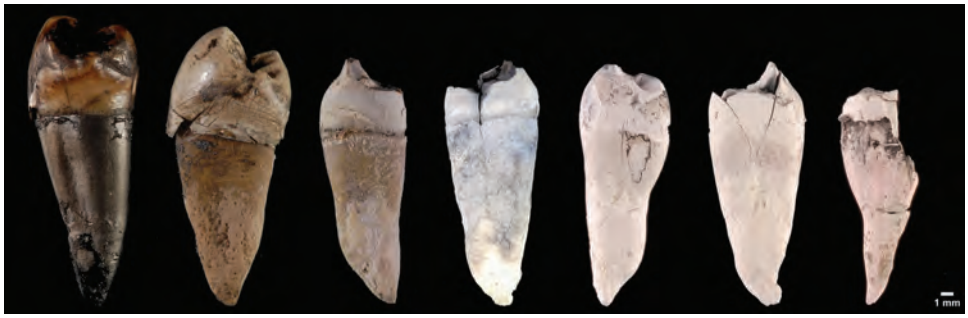

Fig. 1. Heat-induced colour alterations. Progressive, temperature-dependent shifts from a natural colour to black/dark brown (400 °C), brown (500–600 °C), greyish-blue (700 °C), light grey (800 °C), chalky-white (900 °C) and white/pink (1000 °C). (For interpretation of the references to colour in this figure legend, the reader is referred to the web version of this article.)

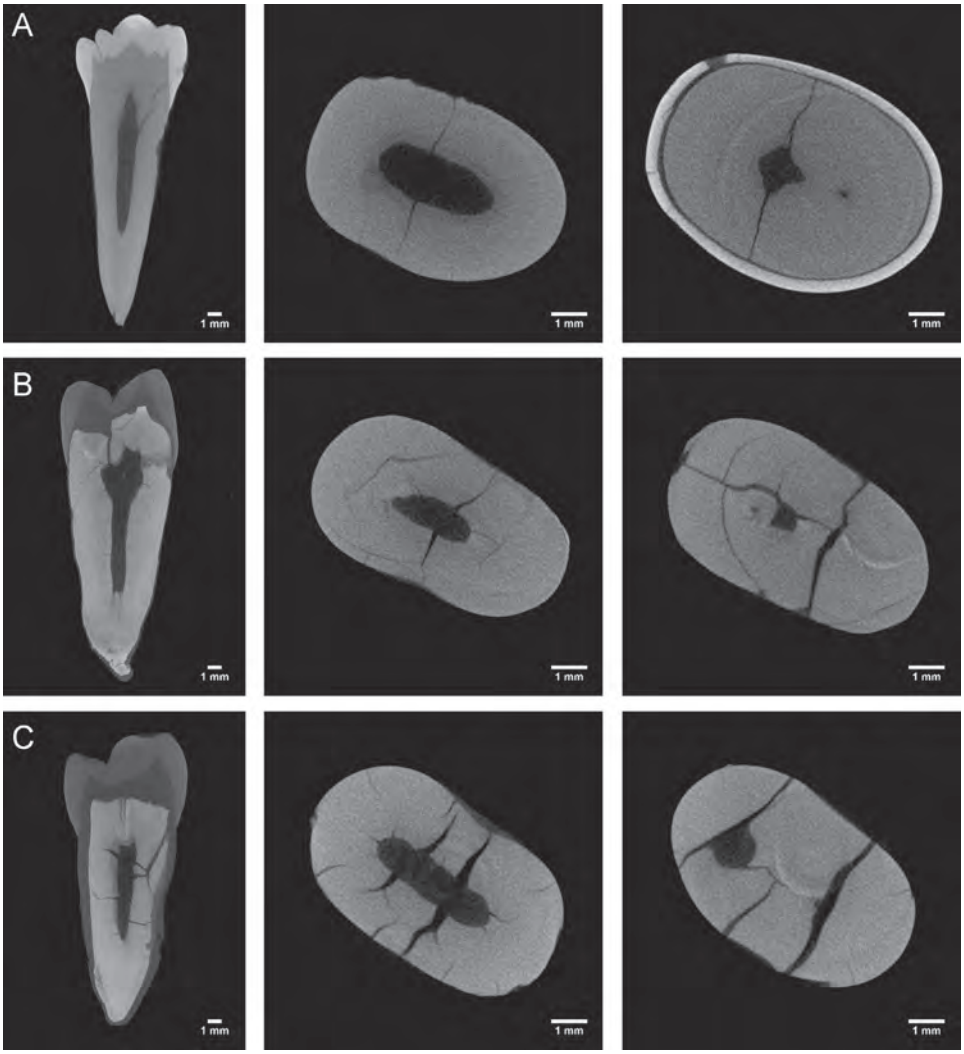

Fig. 2. Micro-CT cross-sections of premolars of the 400,700 and 900 °C group. Visualisation of the dentinal volume loss using the registered pre- and postscans sections (left) and cross-sections in the apical (middle) and coronal dentine (right). (A) 400 °C: cross-sections of the root show multiple small cracks in the dentine and cementum. Single bigger cracks in the crown region and detachment of the crown alongside the dentine–enamel border. Shrinkage: 4.78 ± 0.80%, (B) 700 °C: cross-sections of the root show multiple bigger longitudinal small cracks in the dentine and cementum as well as multiple transversal cracks coming from the canals and pulp chamber. Partial or full detachment and fragmentation of the crown. Shrinkage: 11.53 ± 1.53%, and (C) 900 °C: cross-sections of the root show multiple cracks and longitudinal fractures in the dentine and multiple transversal cracks coming from the canals and pulp chamber. Full detachment and fragmentation of the crown. Shrinkage: 27.50 ± 4.35%.

dentine and cementum as well as single larger longitudinal cracks. At higher temperatures (700 °C–1000 °C) multiple larger longitudinal and numerous transversal cracks were visible in the dentine, mainly deriving from the canals and the pulp chamber (see Fig. 2).

3.3. Shape preservation

Shape preservation of the dentine was investigated using digital radiographs, cross-sectional micro-CT images and 3D models of the co-registered pre- and postscans. Although fragmentation and cracks at elevated temperatures often affected the pulp chamber and root canals, the shrinkage can be described as uniform and overall tooth morphology was well preserved (see Figs. 3 and 4, Electronic Supplementary Material 1). Minor heat-induced contraction ≥800 °C of the distal portions of the roots was found in the micro-CT models, but was generally not identifiable on the standard digital radiographs.

Supplementary material related to this article can be found online at http://dx.doi.org/10.1016/j.jofri.2013.05.003.

3.4. Shrinkage evaluation

In total, 56 teeth were included in the statistical data analysis (Table 1). A student's t-test showed no statistical difference between the dentinal shrinkage of premolars and molars ($p=0.737$).

To prevent a false-positive influence of broken coronal dentine on dentinal shrinkage the analysed ROI was limited to non-fragmented dentine parts. A minimum of 400 slices (equal to 5.4 mm) of the corresponding pre- and postscans were included in the analysis and no statistical difference between number of analysed slices and dentinal shrinkage was found ($p=0.396$). Pearson's correlation coefficient demonstrated a clear correlation between temperature and dentinal shrinkage at the 0.01 level (adjusted $R^2=0.859$). The average shrinkage ranged between 4.78% (at 400 °C) and 32.53% (at 1000 °C) (see Table 1).

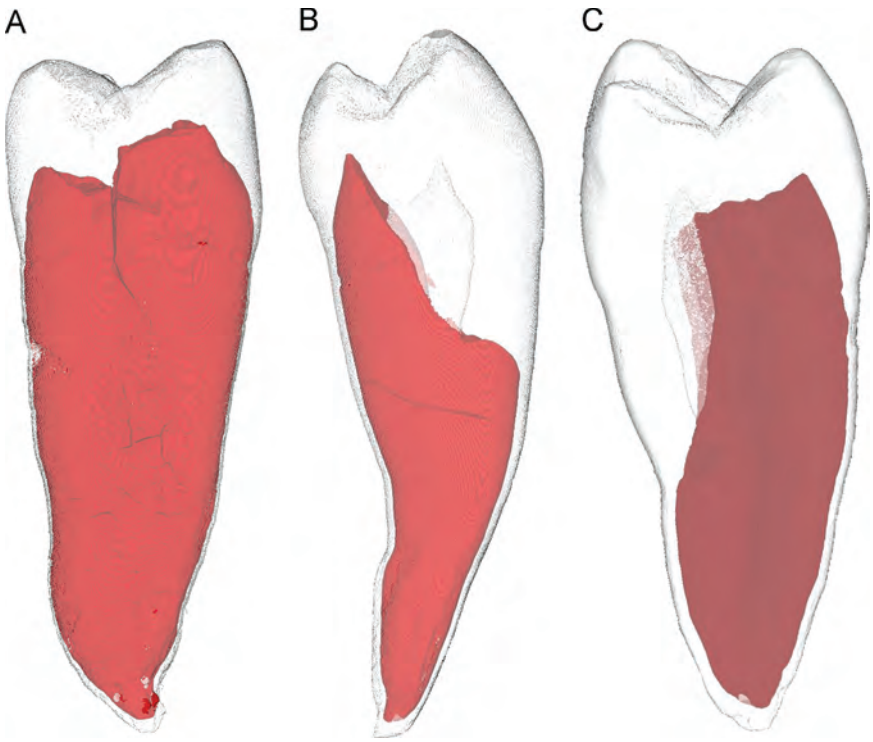

Fig. 3. Comparative 3-D models indicating shape preservation after exposure to elevated temperatures (700–1000 °C). Visualisation of dentinal volume loss using registered micro-CT pre-and postscans at 700 °C (A), 900 °C (B) and 1000 °C (C) indicating good preservation of tooth morphology.

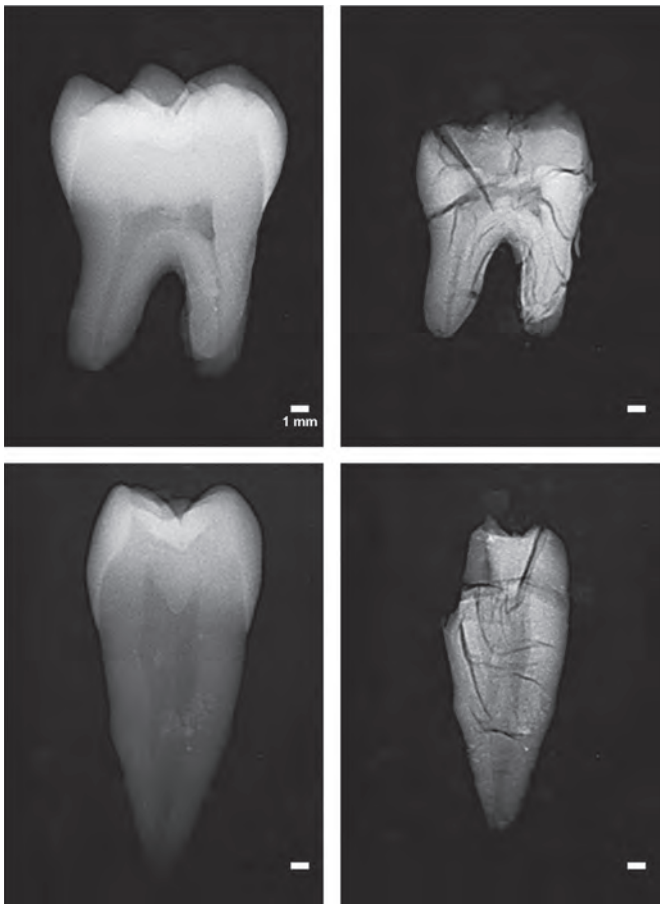

Fig. 4. Corresponding digital radiographs indicating dentinal shrinkage and shape preservation of molars and premolars. Complete fragmentation of the crown and partially broken dentine with multiple cracks present after constant exposure at 900 °C for 30min.

Table 1
Mean dentinal volume shrinkage at seven temperatures (400 °C–1000 °C) after constant exposure of 30 min. The mean difference of dentinal shrinkage is significant for higher temperatures (ANOVA post-hoc LSD test, 95% confidence interval).

Temperature (°C)	Shrinkage (% ± 1 SD)
400	4.78 ± 0.80
500	5.94 ± 1.36
600	8.66 ± 0.83
700	11.53 ± 1.53*
800	24.20 ± 4.23***
900	27.50 ± 4.35*
1000	32.53 ± 5.35**

* $p < 0.05$.
** $p < 0.005$.
*** $p < 0.0005$.

Highly significant differences in the dentinal shrinkage were present in higher temperature groups, whilst no significant statistical difference was found between lower temperature groups (400 °C vs. 500 °C ($p=0.642$); 500 °C vs. 600 °C ($p=0.073$); 600 °C vs. 700 °C ($p=0.060$)).

4. Discussion

4.1. Macroscopic results

Factors such as the presence of soft tissue, fast increase of temperature, fast cooling due to fire extinguishing agents or the presence of contaminants have generally not been taken into account by lab-based research, although they might also have important effects on the appearance of hard tissues [6,10]. To ensure the comparability of the results, the selected temperatures, heating regimes and durations were matched to previous studies [17,18]. The macroscopic results, i.e. surface colour alteration and

crown detachment, correspond with previous observations of isolated unrestored human teeth exposed to high temperatures [6,8,15–18].

4.2. Radiological results

As the enamel was partially or fully fragmented in the majority of the teeth, this study has primarily focused on the shape preservation and shrinkage of dentine.

A minor contraction of the distal portions of the roots is visible in the high-resolution CT images at elevated temperatures (≥800 °C), whilst the resolution of digital radiographs from various angles has shown to be not sufficient to visualise those small shape changes. The good preservation of the tooth morphology is somewhat different from the observation made for severely burned bone, where warping and strong deformation can occur [10,11]. This could be ascribed to the relatively isotropic distribution of the collagen matrix within teeth in comparison to bone [10]. As the root morphology needs to be frequently considered in comparative dental radiography, the good shape preservation after exposure to high temperature could proof to be crucial for positive identification [16].

A summary of grouped results (Table 1) indicate a major increase in shrinkage between 700 °C and 800 °C, which is expected to be due to the complete loss of the organic content, facilitating the sintering and recrystallisation of the hydroxyapatite crystals [10,11]. Major dimensional changes in bone have also been associated with temperatures around 800 °C, which correspond with the results of this study [10]. The micro-CT results indicate that volumetric shrinkage can already be documented at temperatures as low as 400 °C, but this can be ascribed to the more precise nature of the approach used, whilst earlier studies assessed shrinkage of bone using calliper measurements [10,11].

In the last few years micro-CT has been increasingly used in forensic sciences [2,3,12]. Although micro-CT provides high-resolution data for image analysis, allowing the visualisation of alterations of internal structures, teeth fillings with metal components are expected to lead to artefacts influencing the image analysis [2]. Computed tomography has been recently used by Bassed and Hill to estimate the dental age of fire victims, however its current resolution (voxel size of 1 mm) and metal artefact reduction algorithms prevent a detailed analysis of morphology [13]. Woisetschläger et al. used high-resolution CT (voxel size of 0.1 mm) to analyse alterations in HU values of filling materials and dental tissues of isolated human teeth [15]. The findings of those two studies suggest that high-resolution CTs could be used in the future for the purpose of identification of fire victims. Those high-resolution CTs would also be able to detect changes at higher temperatures; nevertheless micro-CT was chosen in this study to determine the precise rate of shrinkage and analysis of shape changes over a large range of temperatures in sufficient resolution.

However, the gold standard still remains comparative dental radiography using panorama radiographs, bite wing or single x-ray images and therefore the intention was to produce results that can be translated into daily forensic practice [2,5–9,18]. The results of this study implicate that shrinkage below 800 °C is practically negligible, as it cannot or only hardly be detected in standard digital radiographs. However, at higher temperatures which can be associated with light grey and white discolouration (see Fig. 1 and [17]), shrinkage is clearly visible in digital radiographs and this should be vigilantly implemented into the standard procedure for the identification of burned dental remains proposed by Fairgrieve [21].

In conclusion, the findings of this study support earlier findings on the macroscopic changes (surface colour alteration and crown detachment), adding information on the specific dentinal shrinkage and shape preservation over a large range of temperatures found in possible archaeological and forensic scenarios. The combination of knowledge on the progressive colour changes and the results of micro-CT evaluation on the specific dentinal shrinkage and shape preservation eventually facilitate the odontological identification process of fire victims in cases where only isolated teeth are present.

References

[1] M.J. Thali, T. Markwalder, C. Jackowski, M. Sonnenschein, R. Dirnhofer, Dental CT imaging as a screening tool for dental profiling: advantages and limitations, Journal of Forensic Sciences 51 (1) (2006) 113–119.

[2] J.J.W. Beck, What is the future of imaging in forensic practice? Radiography 17 (3) (2011) 212–217.

[3] M. Baglivo, S. Winklhofer, G.M. Hatch, G. Ampanozi, M.J. Thali, T.D. Ruder, The rise of forensic and post-mortem radiology—analysis of the literature between the year 2000 and 2011, Journal of Forensic Radiology and Imaging 1 (1) (2013) 3–9.

[4] G.N. Rutty, A. Brough, M.J.P. Biggs, C. Robinson, S.D.A. Lawes, S.V. Hainsworth, The role of micro-computed tomography in forensic investigations, Forensic Science International 225 (1–3) (2013) 60–66.

[5] R. Lain, J. Taylor, S. Croker, P. Craig, J. Graham, Comparative dental anatomy in Disaster Victim Identification: lessons from the 2009 Victorian Bushfires, Forensic Science International 205 (1–3) (2011) 36–39.

[6] C. Savio, G. Merlati, P. Danesino, G. Fassina, P. Menghini, Radiographic evaluation of teeth subjected to high temperatures: experimental study to aid identification processes, Forensic Science International 158 (2–3) (2006) 108–116.

[7] M. Bernstein, Radiologic applications in forensic dentistry, in: B. Brogdon (Ed.), Forensic Radiology, CRC Press, Boca Raton, FL, 1998, pp. 98–140.

[8] P.J. Bush, M.A. Bush, The next level in victim identification: materials properties as an aid in victim identification, in: C. Bowers (Ed.), Forensic Dental Evidence, Elsevier Academic Press, London, 2011, pp. 55–72.

[9] A.J. Hill, R. Lain, I. Hewson, Preservation of dental evidence following exposure to high temperatures, Forensic Science International 205 (1–3) (2011) 40–43.

[10] T.J.U. Thompson, Heat-induced dimensional changes in bone and their consequences for forensic anthropology, Journal of Forensic Sciences 50 (5) (2005) 1008–1015.

[11] P. Shipman, G. Foster, M. Schoeninger, Burnt bones and teeth: an experimental study of color, morphology, crystal structure and shrinkage, Journal of Archaeological Science 11 (4) (1984) 307–325.

[12] M.J. Thali, U. Taubenreuther, M. Karolczak, et al., Forensic microradiology: micro-computed tomography (Micro-CT) and analysis of patterned injuries inside of bone, Journal of Forensic Sciences 48 (6) (2003) 1336–1342.

[13] R.B. Bassed, A.J. Hill, The use of computed tomography (CT) to estimate age in the 2009 Victorian Bushfire Victims: a case report, Forensic Science International 205 (1–3) (2011) 48–51.

[14] R. Silva, T. Botelho, F. Prado, J. Kawagushi, E. Daruge Júnior, F. Bérzin, Human identification based on cranial computed tomography scan—a case report, Dentomaxillofacial Radiology 40 (4) (2011) 257–261.

[15] M. Woisetschläger, A. Lussi, A. Persson, C. Jackowski, Fire victim identification by post-mortem dental CT: radiologic evaluation of restorative materials after exposure to high temperatures, European Journal of Radiology 80 (2) (2011) 432–440.

[16] G. Merlati, P. Danesino, C. Savio, G. Fassina, A. Osculati, P. Menghini, Observations on dental prostheses and restorations subjected to high temperatures: experimental studies to aid identification processes, Journal of Forensic Odonto-Stomatology 20 (2) (2002) 17–24.

[17] S. Karkhanis, D. Franklin, Macroscopic and microscopic changes in incinerated deciduous teeth, Journal of Forensic Odonto-Stomatology 27 (2) (2009) 9–19.

[18] G. Merlati, C. Savio, P. Danesino, G. Fassina, P. Menghini, Further study of restored and un-restored teeth subjected to high temperatures, Journal of Forensic Odonto-Stomatology 22 (2) (2004) 34–39.

[19] J.P. Robinson, P.J. Lumley, E. Claridge, P.R. Cooper, L.M. Grover, R.L. Williams, et al., An analytical Micro CT methodology for quantifying inorganic dentine debris following internal tooth preparation, Journal of Dentistry 40 (11) (2012) 999–1005.

[20] K.W. Eliceiri, M.R. Berthold, I.G. Goldberg, L. Ibanez, B.S. Manjunath, M. E. Martone, et al., Biological imaging software tools, Nature Methods 9 (7) (2012) 697–710.

[21] S. Fairgrieve, Forensic Cremation: Recovery and Analysis, 1st ed., CRC Press, Boca Raton, FL, 2008.

X-ray scattering evaluation of ultrastructural changes of human dental tissues with thermal treatment*

Michael A. Sandholzer M.Sc. [1], Tan Sui B.Sc. [2], Alexander M. Korsunsky Ph.D. [2], A. Damien Walmsley Ph.D. BDS [1], Philip J. Lumley Ph.D. BDS [1], Gabriel Landini Ph.D. DrOdont [1]

[1] School of Dentistry, College of Medical and Dental Sciences, University of Birmingham, St Chad's Queensway, Birmingham B4 6NN, United Kingdom

[2] Department of Engineering Science, University of Oxford, Parks Road, Oxford OX1 3PJ, United Kingdom

*****Presented at the 19th European Meeting of the Paleopathology Association, August 27-29 2012, in Lille, France.

Abstract

Micro- and ultrastructural analysis of burned skeletal remains is crucial for obtaining a reliable estimation of cremation temperature. Earlier studies mainly focused on heat-induced changes in bone tissue, whilst this study extends this research to human dental tissues using a novel quantitative analytical approach. Twelve tooth sections were burned at 400-900°C (30min exposure, increments of 100°C). Subsequent combined small and wide angle X-ray scattering (SAXS/WAXS) experiments were performed at the Diamond Light Source synchrotron facility, where 28 scattering patterns were collected within each tooth section. In comparison with the control sample, an increase of mean crystal thickness was found in burned dentine (2.8-fold) and enamel (1.4-fold), however at a smaller rate than reported earlier for bone tissue (5 -10.7-fold). The results provide a structural reference for traditional X-ray scattering methods and emphasize the need to investigate bone and dental tissues separately to obtain a reliable estimation of cremation temperature.

Keywords

Forensic Science, Cremated Remains, Burned bones and teeth, Heat-induced changes, X-ray microtomography, X-Ray Diffraction, Small Angle Scattering, Forensic Odontology, Forensic Anthropology

Introduction

Burned human remains are frequently recovered from forensic settings and archaeological sites as a result of ritual cremations, natural disasters, accidents or crime (1-3). In general, skeletal hard tissues undergo macroscopic and microscopic alterations (2, 4), and a variety of factors (e.g. duration, temperature and oxygen availability) in the cremation environment determine the extent of those alterations (5). A fire can cause a number of substantial alterations within skeletal hard tissues, but forensic analysis of burned human remains can give important information about the context and conditions of a fire (e.g. fire temperature, fire position or presence of fire accelerants) and eventually facilitates victim identification (6). While macroscopic alterations (e.g. surface colour) can be used to deduce an approximate temperature range, the investigation of the micro- and ultrastructural alterations of skeletal hard tissue exposed to high temperatures has proven to be crucial to get a reliable estimation of temperature (2, 6, 7).

Multiple techniques have been used to investigate the micro- and ultrastructural heat-induced alterations of skeletal hard tissue, where the most frequently applied techniques are based on the absorbance spectra of infrared radiation (Fourier transform infrared spectroscopy, FTIR) or X-ray diffraction (XRD) (3, 6, 8-10). The crystallinity index (CI), frequently reported in literature and quantified by FTIR, XRD or Raman Spectroscopy, gives information about the mean changes in hydroxyapaptite (HAp) crystal size and microscopic structural order of tissue (7-9, 11, 12). However, the CI does not characterise individual crystal features (e.g. size, morphology) and may fail to describe adequately the complexity and heterogeneity of heat-induced processes. In particular, CI values can be influenced by sample preparation (10, 13, 14). Although recently improved FTIR approaches (9) and statistical methods for the comparability of CI results have been established (7), there have been ongoing debates on the general limitations and validity of CI measurements (6, 9, 10, 14).

X-ray diffraction/scattering (XRD or wide angle X-ray scattering, WAXS) of crystals is capable of showing distinct differences in crystal size and a sharpening of diffraction peaks at higher temperatures, enabling reliable temperature estimations (3, 9, 14).

Beckett et al. (15) and Rogers et al. (10) reported a significant difference in HAp characteristics between animal and human bone mineral upon heating analysed with XRD, however those results have recently been contested (16). In general, XRD involves the grinding and chemically altering of a sample and subsequently obtaining a volume-weighted average result that does not provide local fine-scale changes of skeletal ultrastructure (13).

Most of the research to date has focused on the heat-induced compositional and structural alterations of bone tissue (13, 15), and there is only limited data about the changes in hard dental tissues (6). The ultrastructural changes of human bone and teeth using XRD, showed that crystallites derived from bone and dental tissue react differently to heat, implicating that those tissues have to be separately investigated when precise temperature estimation is desired (6). However, Piga et al. (6) pulverised entire teeth, neither taking into account a possibly non-uniform thermal treatment nor the ultrastructural differences of dentine and enamel (17).

Small angle X-ray scattering (SAXS) provides information about the thickness, degree of alignment and shape of crystallites (18). Synchrotron-based SAXS/WAXS have been used for the investigation of local mineralized tissue ultrastructure, providing nano- and sub-nano-scale information at the spatial resolution required to simultaneously characterize and understand the internal architecture and hierarchical properties of materials (19). Synchrotron facilities allow simultaneous SAXS/WAXS data collection, whereas the combined approach allows a high throughput of samples within a short time of analysis and the identification of local ultrastructural alterations without grinding or chemically altering the sample. The obtained quantitative X-ray scattering information is the precise average within the illuminated volume projected along the X-ray beam direction, allowing more sensitive measurements of crystalline size, shape and orientation when compared with traditional XRD (18, 20). Hiller and Wess (18) and Etok et al. (4) successfully applied lab-based SAXS to characterise the heat-induced alterations of crystalline size in archaeological and experimentally altered bone, however there is no SAXS data available for hard dental tissues. In this study an analytical approach,

combining SAXS and WAXS is used to investigate the heat-induced alterations of dentine and enamel, in order to develop a structural reference for heat-affected dental tissues that can be useful in forensic investigations involving traditional methods.

Material and Methods

Four freshly extracted healthy posterior human teeth (ethical approval obtained from the National Research Ethics Committee; NHS-REC reference 09.H0405.33/ Consortium R&D No. 1446) were used to prepare 14 tooth sections according to Marten et al. (21), with the individual section dimensions of 3×1×0.5mm. Teeth were excluded from the study because of apparent damages (e.g. broken roots), endodontic treatments, dental restorations or caries. Twelve tooth sections were subdivided into six temperature groups for 30min constant exposure at 400°C-900°C (increments of 100°C) in an ashing furnace (Carbolite AAF 11/3, Sheffield, United Kingdom), and two additional unheated sections were used as controls. The teeth were removed as the desired duration was reached and subsequently cooled down to room temperature.

For the purpose of planning the exact measuring positions of the SAXS/WAXS, micro-CT scans of the samples were performed with a SkyScan 1172 scanner (SkyScan, Kontich, Belgium) at 1.9µm resolution using 80kV voltage, 120uA current and a 0.5mm Aluminium filter. The resulting slices were reconstructed with SkyScan NSRECON package and subsequently 3-D planning models were created with Fiji imaging software (22).

The X-ray scattering experiment was carried out on the I22 microfocus SAXS beamline at Diamond Light Source (Oxford Harwell Campus, Didcot, UK) using a monochromatic beam (18keV) focused down to beam size of 14.5×19µm. The sample-detector distance was 1040mm, enabling the entire SAXS and a partial WAXS pattern to be captured on a 2-D Pilatus 2M detector (Dectris Ltd., Baden, Switzerland). Two longitudinal line scans with 14 scattering patterns each (3 in enamel, 11 for dentine) were collected in transmission mode from fixed locations within each sample (scan step 100µm).

Additionally, transverse line scans with 6 scattering patterns each were performed for selected samples of 400°C, 600°C and 800°C.

SAXS data analysis

SAXS data provides information about crystallite thickness, degree of alignment and shape. For an initial quantitative analysis 2-D diffraction images are converted into 1-D intensity profiles and pre-processed using the Fit2D software package (23).

Crystallite thickness

In order to determine the mean crystal thickness, the scattering intensity $I(q,\varphi)$ was radially integrated around the entire range of the azimuthal angle φ to obtain the function of $I(q)$, where q is the scattering vector.

Based on Porod's law, which is valid in a two-phase system, the Porod chord length T is defined as:

$$T = \frac{4}{\pi}\frac{Q}{P} \qquad \text{(Eq. 1)}$$

where P is the Porod constant given by $I(q) = Pq^{-4}$ (Porod's law at large q range), which can be determined from the $Iq^4 \sim q^4$ plot, and Q representing the area integration of the $Iq^2 \sim q$ plot. T is used as the definition of mean thickness without any assumption of the particle shape (13). However, for the special case of needle/platelet shape, T can be interpreted as an average measurement of the smallest dimension of crystallites. By taking further factors (e.g. volume fraction) into account, the actual thickness of the crystals can be calculated using the mean thickness results (24).

Degree of alignment

For evaluating particle orientation, the degree of alignment ρ is used to describe the percentage of the aligned particles. In order to quantify the degree of alignment, the SAXS patterns were integrated along all concerned scattering vectors *q*.

This results in a function $I(\varphi)$ with the azimuthal angle φ, normally with two peaks upon a constant background (24, 25). The definition for the degree of alignment is:

$$\rho = \frac{A_{oriented}}{A_{oriented} + A_{unoriented}} \qquad \text{(Eq. 2)}$$

where $A_{unoriented}$ is the area of the constant background area accounting for the scattering from unoriented particles and $A_{oriented}$ (resulting from scattering of oriented particles) depicts the total area of $I(\varphi) \sim \varphi$ subtracting $A_{unoriented}$. The value of ρ ranges from 0 to 1, with $\rho = 0$ indicating no predominant orientation within the plane of the section and $\rho = 1$ corresponding to a perfect alignment of all crystals (24, 25).

Crystalline Shape

In dental tissue two typical shapes of HAp are usually considered, needle-like shape and platelet-like shape (21). In a monodisperse system, the determination of crystalline shape can be directly obtained from the $I(q) \sim q$ plot. The shape calculation is based on the cylindrical shapes (radius R and height H) assumption in random distribution, taking all orientations with equal probability (26). Especially for needle-like particles with infinitesimal transverse dimensions ($R<<H$), and for platelet-like shape particles with infinitesimal thickness ($R>>H$), the intensity can be simplified, as $I_{av}(q) \sim q^{-1}$ (for needle-like), and $I_{av}(q) \sim q^{-2}$ (for platelet-like). Therefore, if the absolute value of the slope in the logarithmic format of $I \sim q$ plot is close to 1, the particle has needle-like shape, whilst if it is close to 2, the shape is platelet-like. Values >2 correspond to a more polydisperse crystal morphology (18).

WAXS data analysis

Identical to XRD, the peaks in WAXS patterns are represented by separated rings with various width and intensity levels, containing characteristic information related to the crystal structure. The analysis of wide angle scattering patterns is performed using Bragg's law, which establishes the relationship between the spacing of atomic planes in crystals and the scattering angle at which these planes produce intense reflections.

$$n\lambda = 2d^{hkl} \sin\theta \qquad \text{(Eq. 3)}$$

where λ is the wavelength, d^{hkl} is the interplanar distance between planes with Miller indices (*hkl*), θ is one half of the scattering angle and *n* is the order of the reflection. Each peak corresponds to a

certain family of lattice planes within a certain crystallographic phase. Therefore, diffraction pattern analysis can be used to identify and quantify the crystallographic phases and structure parameters.

A strong and distinct ring obtained from HAp (the main inorganic component of hard dental tissues) is that of the (002) lattice planes. The (002) reflection contains the information on the orientation of the principal axis (hexagonal c-axis) as well as the fibril orientation due to their parallel orientation (27).

Based on the Scherrer Equation, the width of the peaks in the diffraction pattern is related to the mineral crystal, thus the length of the mineral particles can be derived from the WAXS patterns.

$$L = \frac{k\lambda}{B\cos\theta} \qquad \text{(Eq. 4)}$$

where L is the particle length, B is the full-width at half maximum (FWHM) of (002) peaks, which is contributed from both mineral structure, and instrument broadening. The factor k is a constant related to the crystalline shape while λ and θ have the same as meaning as described above.

Statistical Analysis

The computed mean crystalline thickness were statistically analysed with two-tailed paired sample t-tests using SPSS version 19 (IBM SPSS Inc., Chicago, USA). Probability levels of $p<0.05$ (95% confidence interval) were considered statistically significant.

Results and Discussion

Macroscopic and microscopic alterations

To ensure the comparability of our results, the selected temperature range (400°C-900°C) and duration were matched to previous studies to include possible forensic and archaeological scenarios (6, 28).

Additional factors such as the presence of soft tissues, fast increase or fluctuation of temperature or the presence of contaminants, have generally so far not been taken into account in lab-based research but they might also have some effects on skeletal hard tissues. Progressive, temperature-dependent shifts in colour from a yellowish/white (control) to dark brown (400°C), brown (500-600°C), dark grey (700°C), light greyish-blue (800°C) and chalky-white (900°C) in dentine were observed. In all

burned samples the micro-CT models showed small cracks within the dental slices, while in groups treated at ≥700°C additional multiple larger longitudinal and numerous transversal cracks were visible in the dentine too. In contrast to observations made on entire teeth (6), where the enamel entirely lifted off at the dentine-enamel junction (DEJ) at ~700°C, the enamel was preserved in all our samples treated at ≤800°C, enabling the combined analysis of enamel and dentine. Although the exact mechanisms of the enamel shattering in teeth are unclear, the preservation in our samples can be ascribed to the small slice dimensions which might minimise heat-induced stress around the DEJ.

Wide-angle X-ray scattering (WAXS)

Due to the limited size of the 2D detector, only the (002) peak could be captured and analysed, which result from the diffraction by HAp crystallites. WAXS measurements revealed a variation of the peaks and Fig. 1 shows the results of the (002) reflection of dentine from a selected series of burned dental slices (400°C-900°C) as well as the control sample for a selected region of scattering angles (11.2-11.5°). Increasing temperature leads to the disappearance of the organic components in between the mineral phase and a higher degree of perfection of the HAp crystallite can be observed, accompanied by further crystallisation of the amorphous part (3). In general, a sharpening of diffraction peaks at higher temperatures (800°C-900°C) can be observed in comparison to the control sample, indicating an increased diffraction contribution from larger particles as well as a peak separation appearing at 900°C. Finally, at high temperatures (≥800°C) sintering of HAp crystallites leads to grain growth and improved crystal quality, resulting in significant growth and sharpening of the diffraction peaks (13).

By fitting the peaks of the control and 900°C sample, a FWHM variation ratio of 0.13/0.039 (dentine) and 0.05/0.04 (enamel) could be shown; indicating in Eq.4 that the crystals appear 3.3-fold larger in dentine (at 900°C) and 1.3-fold larger in enamel (at 800°C) compared to the control sample.

Small-angle X-ray scattering (SAXS)

Table 1 summarises the mean crystalline thickness variation from a series of burned dental slices (400°C -900°C) and the control group. Fig. 2 shows the average value of 10 scanning patterns in dentine and 3 patterns in enamel. The mean crystalline thickness (T) of the control samples (2.01 ± 0.09 nm) is consistent with earlier transmission electron microscopy (TEM) studies and XRD data (6, 11). Whilst the SAXS-derived increase of the mean crystalline thickness in bones was reported earlier

to be 5 to 10.7-fold at 900°C compared to the original crystal size (4, 13), it was found to be 2.8-fold in dentine (2.01nm (RT) to 5.58nm (900°C)) and only 1.4-fold (3.93nm (RT) to 5.34nm (800°C)) in enamel (for additional values see Table 1). Therefore, our results emphasize the need to separately investigate bone and dental tissues when precise temperature estimation is desired.

A 3.7-fold increase of average crystalline size (RT to 900°C) was reported when analysing pulverised teeth with XRD (6), however the independent contributions of dentine and enamel were not taken into account.

In general, the small increase in crystal size for enamel may be due to a more dense arrangement of HAp compared with dentine, allowing only a limited size increase. Overall, the results of mean crystalline thickness indicate the most influential structural changes occurred in dentine. The SAXS results reinforce a comparable increase of particle thickness, supporting the WAXS analysis derived FWHM variation ratio.

Moreover, the mean crystalline thickness of dentine does not significantly vary in the transverse direction at any of the temperatures tested here, indicating a relatively uniform thermal treatment ($p=0.875$ for 400°C; $p=0.274$ for 600°C; $p=0.097$ for 800°C). The analysis of an intact dental slice enabled us to study possible local variations, however the analysis of variation in longitudinal and transverse direction indicating a uniform thermal treatment and behaviour of the samples. Teeth derived from a forensic setting or archaeological site are expected to have a non-uniform thermal treatment and show spatial variation in ultrastructural changes. This will likely affect the results of traditional X-ray scattering measurements, where a relatively large amount of powder is needed for analysis (6, 13). In order to document the spatial variation multiple measurements on a thin cross-section of an entire tooth, ideally 2D SAXS/WAXS mapping, would be necessary. To overcome the issue of spatial variation within the sample and more accurately determine the maximum cremation temperature, XRD/SAXS/FTIR samples should generally be taken from the hard tissue surface.

Fig. 3 and Fig. 4 show the variation in the degree of alignment determined by SAXS within the burned dental slices (400°C -900°C) as well as the control group, which is the average value of 10 scanning patterns in dentine and 3 patterns in enamel.

The degree of alignment values range between 0 and 1, where 0 describes no predominant orientation with the plane of section whilst 1 indicates perfect alignment of all crystals (24). In the control sample, dentine (0.27) shows a more random orientation of HAp crystals than in enamel (0.64), consistent with earlier SAXS results of dental tissues (29). The overall degree of alignment of crystals in dentine decreases from 0.27 at RT to 0.15 at 900°C, while the degree of alignment in enamel dropped from 0.64 at RT to 0.36 at 800°C indicating a more random orientation of the crystals as temperature increases (see Table 1). Gradual disappearance of the structural organic components may explain the decrease of the degree of alignment, where a trend towards more random orientation can be found in dentine and enamel as temperature increases.

The degree of alignment might vary depending on the measurement location, and in order to obtain the complete three-dimensional information of the nanostructure multiple measurements, ideally under various rotation angles, would be necessary (20). A major drop in alignment is visible in the zone around the dentine-enamel junction (DEJ), whilst in the enamel and distant dentine the degree of alignment appeared less variable throughout all test groups (Fig. 3). This observation is in accordance with the gradient properties of human dentine reported by Tesch et al. (24) and can be explained as the optimization of the mechanical functions of dentine, which serves as a functional material (21).

Fig. 5 shows the shape variation of the crystals within dentine and enamel determined by SAXS, and the absolute value of the slope in the logarithmic form of $I(q) \sim q$ plot for dentine indicates a needle-like morphology at RT (1.40), changing to a more platelet-like morphology at 400-500°C (2.03-2.19) and finally to a more complex (polydisperse) morphology at 600-900°C (3.53-3.22).

The variation of the absolute value of the slope for enamel is limited, with the scattering results appearing polydisperse (2.77-3.27) in all test groups (see Table 1). The precise polydisperse crystallite morphology identified at higher temperatures cannot be determined by the simplistic needle or platelet model used in this study (13). Although on a different scale, the ultrastructural shape alterations are in accordance with electron microscopic results showing only small structural variance at lower temperatures and more a complex appearance >700°C (3).

Conclusions

A quantitative analytical approach based on synchrotron radiation, combined small and wide angle X-ray scattering (SAXS/WAXS), was used to investigate the heat-induced ultrastructural alterations of dentine and enamel. In contrast to other previously used methods, this approach allows a non-destructive analysis of entire samples to determine local alterations rather than a volume-weighted averaged measurement used in traditional X-ray scattering methods.

The results indicate a specific temperature-dependent increase of the mean thickness of HAp crystals in dentine and enamel that can be used to determine a temperature range. Moreover, a decrease of the degree of alignment and change of crystalline shape, as well as greater crystal perfection with larger grain growth could be documented. Whilst the access to synchrotron facilities is limited for routine forensic work, the results of this study, especially the mean crystalline thickness, can be utilised in the more commonly used lab-based X-ray scattering analysis of burned human remains. Overall, a structural reference was developed for heat-affected dental tissues that can be useful in investigations of forensic and archaeological samples, once again emphasizing the need to separately investigate bone and dental tissues when precise temperature estimation is desired.

Acknowledgments

The authors would like to thank Nikos Baimpas (Department of Engineering Science, University of Oxford) and Dr. Jen Hiller (Diamond Light Source, Oxford) for helpful instructions regarding the beamline setup. Diamond Light Source is acknowledged for provision of synchrotron beamtime through allocation SM7919.

References

1. Gonçalves D, Thompson TJU, Cunha E. Implications of heat-induced changes in bone on the interpretation of funerary behaviour and practice. Journal of Archaeological Science 2011;38(6):1308-13.
2. Thompson TJU. Heat-induced dimensional changes in bone and their consequences for forensic anthropology. Journal of Forensic Sciences 2005;50(5):1008-15.
3. Shipman P, Foster G, Schoeninger M. Burnt bones and teeth: an experimental study of color, morphology, crystal structure and shrinkage. Journal of Archaeological Science 1984;11(4):307-25.
4. Etok S, Valsami-Jones E, Wess TJ, Hiller JC, Maxwell C, Rogers KD, et al. Structural and chemical changes of thermally treated bone apatite. Journal of Materials Science 2007;42(23):9807-16.
5. Walker P, Miller K, Richman R. Time, temperature and oxygen availability: an experimental study of the effects of environmental conditions on the color and organic content of cremated bone. In: Schmidt CW, Symes SA, editors. The Analysis of Burned Human Remains. London: Academic Press, 2008:129-35.
6. Piga G, Thompson TJU, Malgosa A, Enzo S. The Potential of X-Ray Diffraction in the Analysis of Burned Remains from Forensic Contexts. Journal of Forensic Sciences 2009;54(3):534-9.
7. Thompson TJU, Islam M, Bonniere M. A new statistical approach for determining the crystallinity of heat-altered bone mineral from FTIR spectra. Journal of Archaeological Science 2013;40(1):416-22.
8. Squires KE, Thompson TJU, Islam M, Chamberlain A. The application of histomorphometry and Fourier Transform Infrared Spectroscopy to the analysis of early Anglo-Saxon burned bone. Journal of Archaeological Science 2011;38(9):2399-409.
9. Hollund HI, Ariese F, Fernandes R, Jans MME, Kars H. Testing an alternavite high-throughput tool for investigating bone diagenesis: FTIR in attenuated total reflection (ATR) mode. Archaeometry 2013;55(3) 507-32.
10. Rogers K, Beckett S, Kuhn S, Chamberlain A, Clement J. Contrasting the crystallinity indicators of heated and diagenetically altered bone mineral. Palaeogeography, Palaeoclimatology, Palaeoecology 2010;296(1-2):125-9.
11. Reiche I, Vignaud C, Menu M. The crystallinity of ancient bone and dentine: new insights by transmission electron microscopy. Archaeometry 2002;44(3):447-59.
12. Thompson TJU, Islam M, Piduru K, Marcel A. An investigation into the internal and external variables acting on crystallinity index using Fourier Transform Infrared Spectroscopy on unaltered and burned bone. Palaeogeography, Palaeoclimatology, Palaeoecology 2011;299(1-2):168-74.
13. Hiller JC, Thompson TJU, Evison MP, Chamberlain AT, Wess TJ. Bone mineral change during experimental heating: An X-ray scattering investigation. Biomaterials 2003;24(28):5091-7.

14. Piga G, Malgosa A, Thompson TJU, Enzo S. A new calibration of the XRD technique for the study of archaeological burned human remains. Journal of Archaeological Science 2008;35(8):2171-8.
15. Beckett S, Rogers KD, Clement JG. Inter-Species Variation in Bone Mineral Behavior upon Heating. Journal of Forensic Sciences 2011;56(3):571-9.
16. Piga G, Solinas G, Thompson TJU, Brunetti A, Malgosa A, Enzo S. Is X-ray diffraction able to distinguish between animal and human bones? Journal of Archaeological Science 2013;40(1):778-86.
17. Kugler M. X-ray diffraction analysisin the forensic science: The last resort in many criminal cases. Advances in X-Ray Analysis 2003;46:1-16.
18. Hiller JC, Wess TJ. The use of small-angle X-ray scattering to study archaeological and experimentally altered bone. Journal of Archaeological Science 2006;33(4):560-72.
19. Daniels JE, Pontoni D, Hoo RP, Honkimaki V. Simultaneous small- and wide-angle scattering at high X-ray energies. Journal of Synchrotron Radiation 2010;17:473-8.
20. Gaiser S, Deyhle H, Bunk O, White S, Müller B. Understanding Nano-Anatomy of Healthy and Carious Human Teeth: a Prerequisite for Nanodentistry. Biointerphases 2012;7(1):1-14.
21. Marten A, Fratzl P, Paris O, Zaslansky P. On the mineral in collagen of human crown dentine. Biomaterials 2010;31(20):5479-90.
22. Eliceiri KW, Berthold MR, Goldberg IG, Ibanez L, Manjunath BS, Martone ME, et al. Biological imaging software tools. Nature Methods 2012;9(7):697-710.
23. Hammersley AP. FIT2D: An Introduction and Overview. ESRF Internal Report, ESRF97HA02T 1997.
24. Tesch W, Eidelman N, Roschger P, Goldenberg F, Klaushofer K, Fratzl P. Graded microstructure and mechanical properties of human crown dentin. Calcified Tissue International 2001;69(3):147-57.
25. Rinnerthaler S, Roschger P, Jakob HF, Nader A, Klaushofer K, Fratzl P. Scanning small angle X-ray scattering analysis of human bone sections. Calcified Tissue International 1999;64(5):422-9.
26. Guinier A, Fournet G. Small-angle scattering of X-rays. New York: Wiley, 1955.
27. Deymier-Black AC, Almer JD, Stock SR, Haeffner DR, Dunand DC. Synchrotron X-ray diffraction study of load partitioning during elastic deformation of bovine dentin. Acta Biomaterialia 2010;6(6):2172-80.
28. Myers SL, Williams JM, Hodges JS. Effects of extreme heat on teeth with implications for histologic processing. Journal of Forensic Sciences 1999; 44(4):805-9.
29. Jiang HD, Liu XY, Lim CT, Hsu CY. Ordering of self-assembled nanobiominerals in correlation to mechanical properties of hard tissues. Applied Physics Letters 2005; 86(16): 163901.

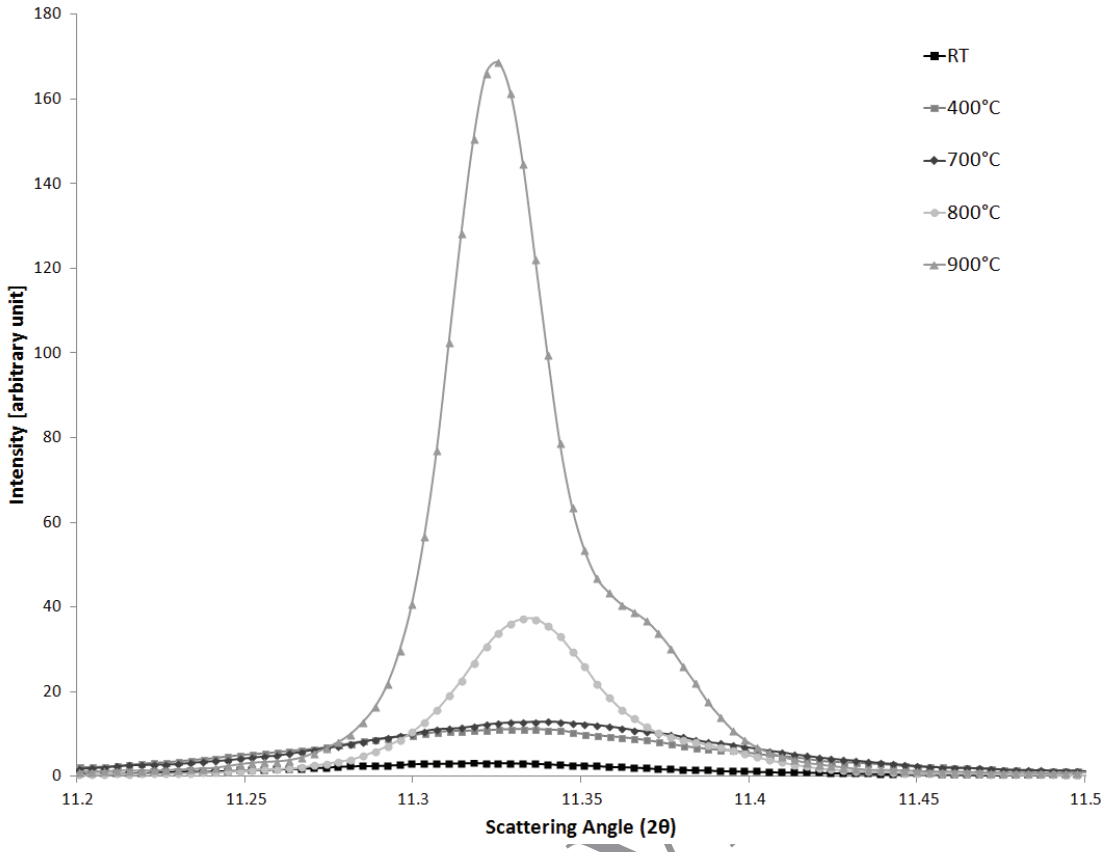

FIG. 1 WAXS results of the (002) reflection of dentine from a series of burnt dental slices (control, 400°C-900°C) for a selected region of scattering angles (11.2-11.5°). In general, a sharpening of peaks at higher temperatures (800°C-900°C) can be observed in comparison to the control sample, indicating an increased diffraction contribution from larger particles. The peaks at low temperatures appear not as smooth due to the influence from an organic phase, gradually decreasing and completely disappearing at between 700° and 800°C.

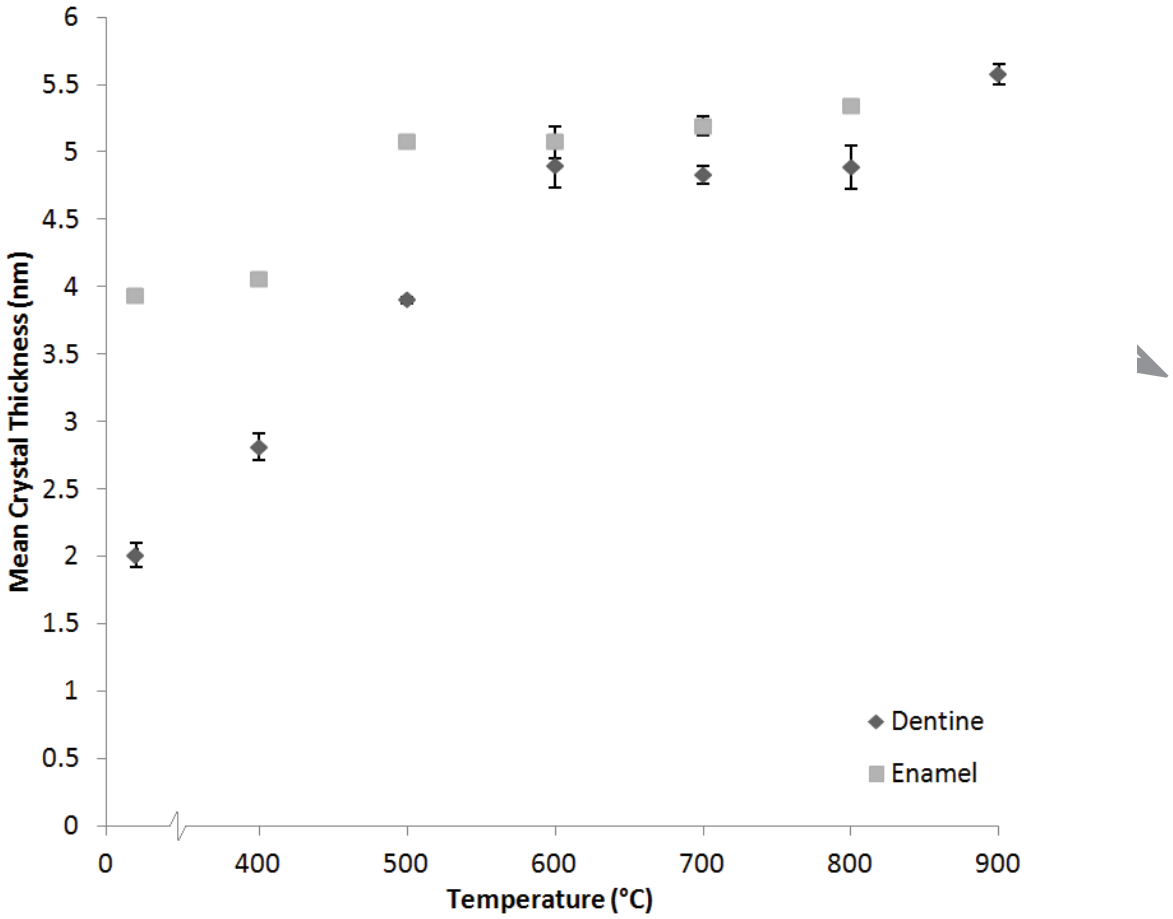

FIG. 2 Variation of the mean crystal thickness in enamel and dentine determined by SAXS. Multiple measurements were taken in longitudinal direction, averaging the values of 10 scanning patterns in dentine and 3 patterns in enamel. The mean crystalline thickness of dentine increases from 2.01nm at room temperature (RT) to 5.58nm at 900°C, and the mean crystalline thickness of enamel increases from 3.93nm at RT to 5.34nm at 800°C. Error bars ± 1SD.

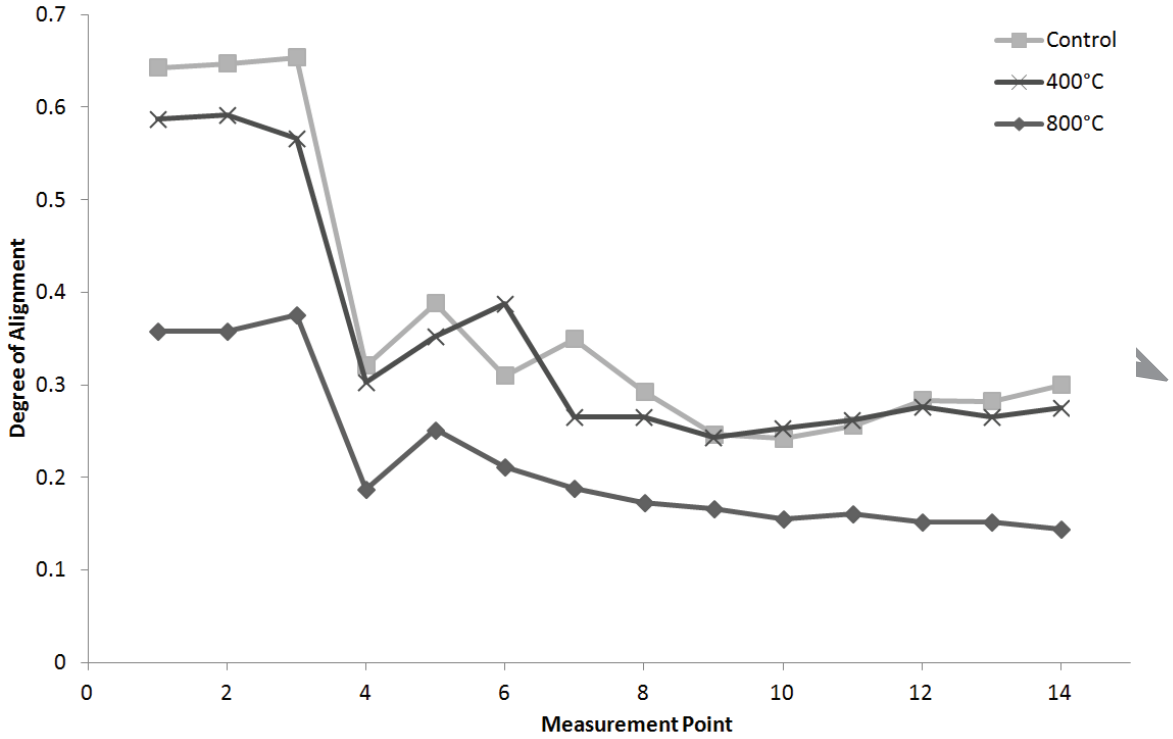

FIG. 3 Representative variation of degree of alignment in enamel and dentine at room temperature (RT), 400° and 800°C. Longitudinal line scans with 13 scattering patterns each (3 in enamel, 10 for dentine) were collected in transmission mode from fixed locations within each sample (scan step 100 µm). A major drop in alignment is visible around the dentine-enamel junction (DEJ, Measurement point 4-6), whilst in the enamel (Measurement points 1-3) and distant dentine (Measurement points 7-14) the degree of alignment appeared less variable.

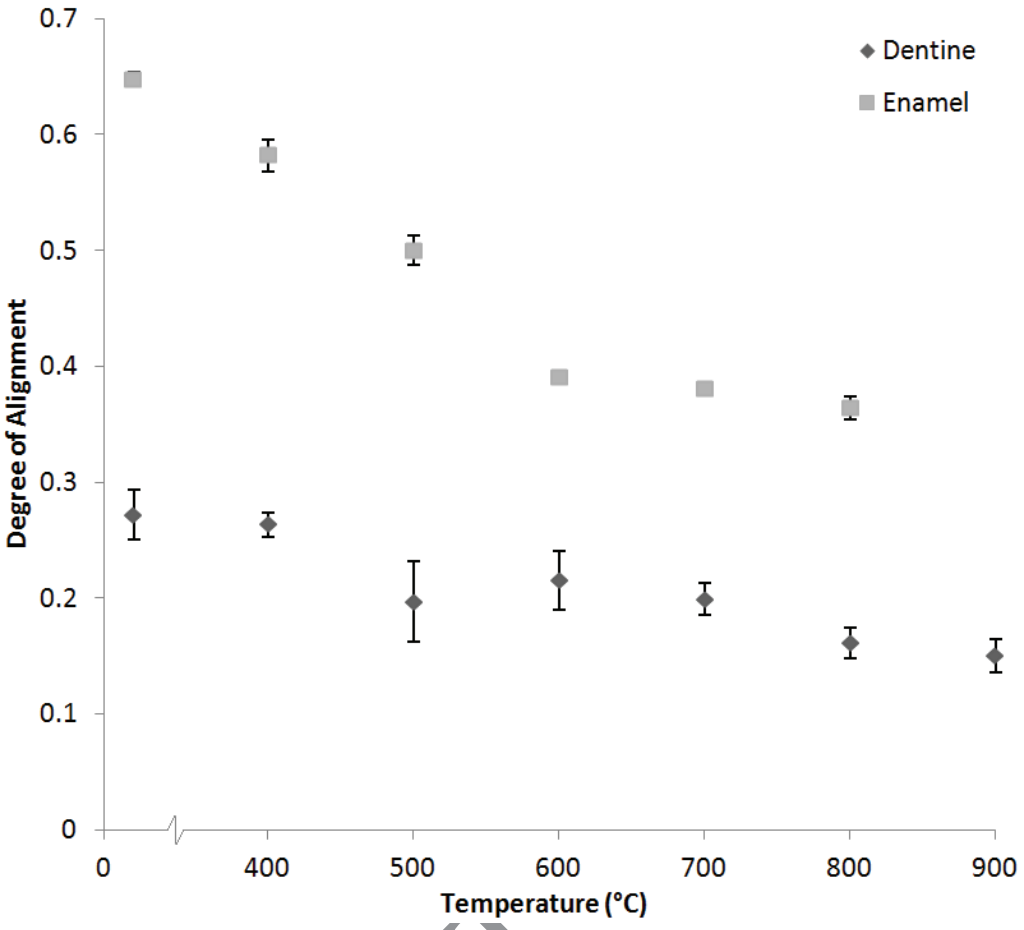

FIG. 4 Variation of degree of alignment in enamel and dentine determined by SAXS. Multiple measurements were taken in longitudinal direction, averaging the values of 10 scanning patterns in dentine and 3 patterns in enamel. The overall degree of alignment of crystals in dentine decreases from 0.27 at RT to 0.15 at 900°C, and the degree of alignment in enamel dropped from 0.64 at RT to 0.36 at 800°C indicating a more random orientation of the crystals as temperature increases. Error bars ± 1SD.

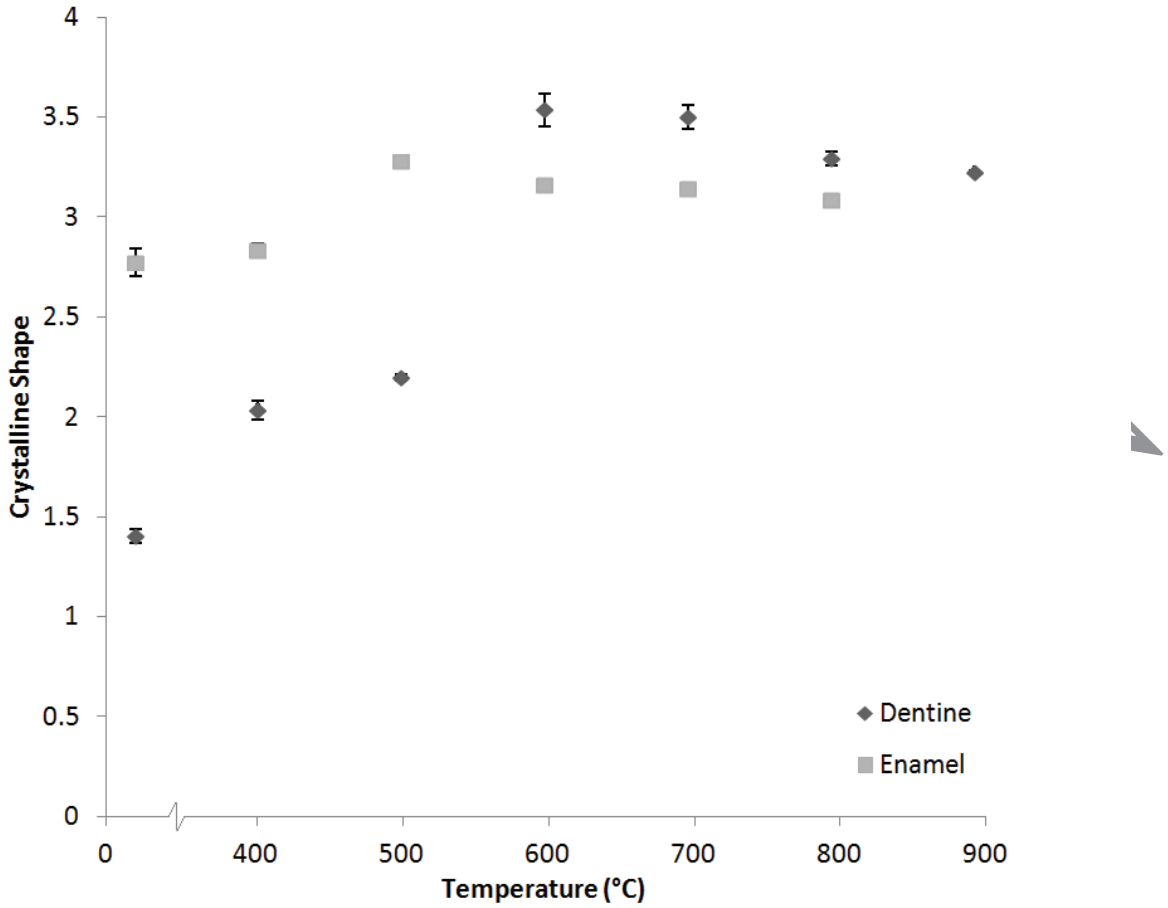

FIG. 5 Variations of crystalline shape in enamel and dentine with increasing temperature determined by SAXS. The absolute value of the slope for dentine indicates a needle-like morphology at RT (1.40), changing to a more platelet-like morphology at 400-500°C (2.03-2.19) and finally to a more complex (polydisperse) morphology at 600-900°C (3.53-3.22). Error bars ± 1SD.

Table 1 Overview of SAXS measurement results. Mean thickness, degree of alignment and shape of dentine and enamel crystallites collected from longitudinal line scans with 13 scattering patterns each (10 for dentine, 3 in enamel). Mean thickness results from transverse line scans (trans) with 6 dentine scattering patterns for selected samples of 400°C, 600°C & 800°C. Statistical significance was evaluated using two-tailed paired sample t-tests with 95% confidence interval for the mean thickness results (*p<0.05, **p<0.005, ***p<0.0005).

Temperature (°C)	**Dentine Mean Thickness (nm ±1 SD)**	**Enamel Mean Thickness (nm ±1 SD)**	**Degree of Alignment Dentine (± 1SD)**	**Degree of Alignment Enamel (± 1SD)**	**Crystalline Shape Dentine (± 1SD)**	**Crystalline Shape Enamel (± 1SD)**
CTL	2.01 ± 0.09	3.93 ± 0.05	0.27 ± 0.02	0.65 ± 0.01	1.40 ± 0.04	2.77 ± 0.07
400	2.81 ± 0.10***	4.05 ± 0.01	0.26 ± 0.01	0.58 ± 0.01	2.03 ± 0.05	2.84 ± 0.03
500	3.90 ± 0.02***	5.08 ± 0.04***	0.20 ± 0.03	0.50 ± 0.01	2.20 ± 0.01	3.28 ± 0.01
600	4.90 ± 0.16***	5.07 ± 0.12	0.22 ± 0.03	0.39 ± 0.01	3.53 ± 0.08	3.16 ± 0.02
700	4.83 ± 0.06	5.19 ± 0.07	0.20 ± 0.01	0.38 ± 0.01	3.50 ± 0.06	3.14 ± 0.07
800	4.88 ± 0.16	5.34 ± 0.03	0.16 ± 0.01	0.36 ± 0.01	3.29 ± 0.04	3.09 ± 0.05
900	5.58 ± 0.08***	---	0.15 ± 0.01	---	3.22 ± 0.09	---
400trans	2.83 ± 0.05					
600trans	4.89 ± 0.01					
800trans	4.80 ± 0.03					

JOURNAL OF THE MECHANICAL BEHAVIOR OF BIOMEDICAL MATERIALS 32 (2014) 113–124

Available online at www.sciencedirect.com

ScienceDirect

www.elsevier.com/locate/jmbbm

Research Paper

Structure-mechanical function relations at nano-scale in heat-affected human dental tissue

Tan Sui[a,*], Michael A. Sandholzer[b], Eric Le Bourhis[c], Nikolaos Baimpas[a], Gabriel Landini[b], Alexander M. Korsunsky[a]

[a]Department of Engineering Science, University of Oxford, Parks Road, Oxford OX1 3PJ, United Kingdom
[b]School of Dentistry, College of Medical and Dental Sciences, University of Birmingham, St Chad's Queensway, Birmingham B4 6NN, United Kingdom
[c]Institut P',CNRS UPR 3346, University of Poitiers, SP2MI, BP 30179, F86962 Futuroscope Chasseneuil Cedex, France

ARTICLE INFO

Article history:
Received 15 August 2013
Received in revised form
30 November 2013
Accepted 14 December 2013
Available online 20 December 2013

Keywords:
Dental tissue
Thermal treatment
SAXS/WAXS
Nanoindentation
Mechanical-structural correlation

ABSTRACT

The knowledge of the mechanical properties of dental materials related to their hierarchical structure is essential for understanding and predicting the effect of microstructural alterations on the performance of dental tissues in the context of forensic and archaeological investigation as well as laser irradiation treatment of caries. So far, few studies have focused on the nano-scale structure-mechanical function relations of human teeth altered by chemical or thermal treatment. The response of dental tissues to thermal treatment is thought to be strongly affected by the mineral crystallite size, their spatial arrangement and preferred orientation. In this study, synchrotron-based small and wide angle X-ray scattering (SAXS/WAXS) techniques were used to investigate the microstructural alterations (mean crystalline thickness, crystal perfection and degree of alignment) of heat-affected dentine and enamel in human dental teeth. Additionally, nanoindentation mapping was applied to detect the spatial and temperature-dependent nanomechanical properties variation. The SAXS/WAXS results revealed that the mean crystalline thickness distribution in dentine was more uniform compared with that in enamel. Although in general the mean crystalline thickness increased both in dentine and enamel as the temperature increased, the local structural variations gradually reduced. Meanwhile, the hardness and reduced modulus in enamel decreased as the temperature increased, while for dentine, the tendency reversed at high temperature. The analysis of the correlation between the ultrastructure and mechanical properties coupled with the effect of temperature demonstrates the effect of mean thickness and orientation on the local variation of mechanical property. This structural–mechanical property alteration is likely to be due to changes of HAp crystallites, thus dentine and enamel exhibit different responses at different temperatures. Our results enable an improved understanding of the mechanical properties correlation in hierarchical biological materials, and human dental tissue in particular.

*Corresponding author. Tel.: +44 18652 83447; fax: +44 18652 73010.
E-mail address: tan.sui@eng.ox.ac.uk (T. Sui).

1751-6161/$ - see front matter © 2013 Elsevier Ltd. All rights reserved.
http://dx.doi.org/10.1016/j.jmbbm.2013.12.014

1. Introduction

The bulk of human teeth consists of two main mineralised tissues, collagen-rich dentine and highly mineralised enamel. They join forming a complex and mechanically durable dentine–enamel junction (DEJ) that contributes to the life-long success of the tooth structure under thermo-mechanical loadings encountered in the oral cavity under the conditions such as mastication, chemically active environment and thermal shock (He and Swain, 2009; Marshall et al., 1998; Ten Cate, 1998). This remarkable performance provides the motivation for numerous investigations into the detail of the micro- and nano-structure of enamel, dentine and the DEJ. The knowledge of the mechanical properties related to the hierarchical structure of dentine, enamel and the DEJ is essential for understanding and predicting the effects of microstructural alterations due to disease, treatment, or environmental or thermal exposure on the performance of dental tissues and their artificial replacements.

The use of advanced high-energy techniques is increasing in modern dentistry. With the advent of a variety of new laser systems spanning by a range of energy densities and pulse durations, clinical treatments such as laser-assisted caries protection were proposed and developed. Local temperature induced by laser as high as 1000 °C may be achieved during laser treatment (Fried et al., 2002; Zuerlein et al., 1999). Improved caries prevention is surmised to be associated with increased mineralisation and HAp crystallite sintering that leads to the sealing of dentinal tubules. However, the confirmation of this by direct microscopic characterisation of the very thin surface layer affected by laser therapies is an extremely challenging experimental task. In addition, in the context of archaeological and forensic investigations, the macroscopic alterations (e.g. surface colour) can be used to deduce an approximate temperature range, while the investigation of the micro- and ultrastructural alterations of skeletal hard tissues exposed to high temperatures turned out to be an excellent means of obtaining reliable estimates of the temperatures of exposure (Piga et al., 2009; Thompson, 2005; Thompson et al., 2011). The above considerations provide a strong motivation for a detailed study into the effect of thermal exposure on the nano-structure properties of human dental tissue. In order to understand and quantify more precise information about the evolution of the hierarchical nano/micro-structure under in situ thermal exposure, the application of advanced non-destructive techniques offers an appropriate route.

Synchrotron based X-ray diffraction, small- and wide angle X-ray scattering (SAXS and WAXS, respectively), are advanced non-destructive techniques that enable characterising the ultrastructure, mechanical property and texture evaluation of mineralised tissues (Al-Jawad et al., 2007; Daniels et al., 2010; Deymier-Black et al., 2010). WAXS (XRD) has been proved to be capable of showing the distinct differences of HAp of animal and human bone mineral upon heating (Beckett et al., 2011; Piga et al., 2008; Piga et al., 2013; Rogers et al., 2010), however most lab-based XRD usually involves the mechanical destruction of a sample and estimation of a subsequent volume-weighted averaged result, without providing local fine-scale changes of ultrastructure (Hiller et al., 2003). Compared with conventional high-magnification microscopic methods, SAXS allows a far higher throughput of samples with shorter time of analysis and non-destructive identification of local structural alterations at the nano-scale. However, the investigation of thermal treated mineralised tissues using SAXS technique is still lacking, and only recently, lab-based SAXS was used to characterize the structural changes in human bone for forensic and archaeological purposes (Hiller et al., 2003), but few in the corresponding SAXS data analysis on human dental tissues in particular.

Nanoindentation has recently emerged as a powerful tool for measuring the nano-scale mechanical properties in biomaterials (Ebenstein and Pruitt, 2006). Nanoindentation in mineralised tissues have been extensively studied and reviewed by Kinney et al. (Kinney et al., 2003) and Haques et al. (Haque, 2003). In teeth, a primary focus has been to map mechanical properties across the normal dental tissues to understand the role of local properties and hierarchical structure, and has also been coupled with chemical mapping (Fong et al., 2000; Marshall et al., 2001; Roy and Basu, 2008). However, to date, no studies have been reported on the investigation of the variation of mechanical properties on thermally treated dental tissues. Tesch et al. (Tesch et al., 2001) successfully applied SAXS and nanoindentation to characterize non-treated dentine and observed variations of mechanical and structural properties in correlations but the resolution is low. In the present investigation of heat-induced alterations of hard dental tissues with high resolution, a SAXS mapping setup was combined with nanoindentation mapping. The results obtained here are likely to help in a better understanding of the internal architecture alterations and hierarchical properties changes due to heat exposure. In addition, the effect of exposure of human skeletal hard tissues to high temperatures is an important topic of study in the context of forensic investigations and archaeological analysis (Beckett et al., 2011; Enzo et al., 2007; Piga et al., 2009; Rogers and Daniels, 2002; Shipman et al., 1984).

The aim of this study was to have a medium resolution mapping using synchrotron-based SAXS/WAXS technique to characterise the structural features both in dentine and enamel, as well as in the region near the DEJ of human teeth samples with various thermal treatments in order to analyse the ultrastructural variation (mean crystalline thickness, crystal perfection, orientation and degree of alignment) and their correlation with the reduced modulus and hardness properties (measured by nanoindentation).

2. Materials and methods

2.1. *Sample preparation*

Four freshly extracted intact human molars (ethical approval obtained from the National Research Ethics Committee; NHS-REC reference 09.H0405.33/ Consortium R&D No. 1446) were disinfected in 15 mM sodium azide solution and washed under running water for 5–6 h before mechanically cleaned to eliminate residues. Teeth were excluded from the study

because of damage (e.g. broken roots), endodontic treatment, dental restorations or caries. Details such as age, sex and patients ethnic background remained anonymous as part of patient confidentiality regulations. In total, twelve teeth sections ($3 \times 1 \times 0.5\ mm^3$) were prepared and kept in a hydrated state in Phosphate Buffer Solution (PBS) at 4 °C before the experiment (Marten et al., 2010). Of these, 10 sections were allocated into five temperature groups for 30 min constant exposure at 400 °C–800 °C (in steps of 100 °C), and two additional unheated sections were used as controls. An ashing furnace (Carbolite AAF 11/3, Sheffield, United Kingdom) was used to generate the thermal treatment. Each tooth sample was then subjected to a thermal history that heated the sample to the final (maximum) temperature (constant exposure) and were then removed from the furnace after the desired duration of exposure was reached, and subsequently cooled down in the crucibles to room temperature and stored in padded containers.

For the purpose of planning the measuring positions and Region of Interests (ROIs) of the SAXS/WAXS mapping, micro-CT scans of the samples were performed with a SkyScan 1172 scanner (SkyScan, Kontich, Belgium) at 1.9 μm resolution using 80 kV voltage, 120 μA current and a 0.5 mm Aluminium filter (Fig. 2a–c). The resulting data were reconstructed with SkyScan NRECON package and subsequent models were recreated with Fiji imaging software (Eliceiri et al., 2012). In addition, it should be noted that the micro-CT scan was also used on the selection of samples in order to largely guarantee that the DEJ plane of the selected samples was almost parallel to the X-ray beam.

The nanoindentation measurements were performed on the same teeth sections after embedding in Epoxy resin (Buehler Epo-Kwick, Buehler Ltd., Lake Bluff, IL) to preserve their integrity and were analysed in the dry condition. The maximum peak temperatures of the epoxy during curing the manufacturer is 145 °C with a short period of time, which the influence on the sample is thought to be limited. Furthermore, the sections are carefully ground with a series of grinding papers (P800-P4000) to expose the surface and finally polished with 3 μm diamond polishing compound. This way, it was made sure that properties of the tissue were measured, and not properties of the epoxy resin.

In summary, six samples (RT, 400 °C, 500 °C, 600 °C, 700 °C and 800 °C) were used for the SAXS/WAXS mapping measurements and three out of those six samples including RT, 500 °C and 700 °C were further selected for the nano-indentation mapping, since these temperatures were representatives of major compositional changes and weight loss (Pramanik et al., 2013).

2.2. Micro-focus small angle X-ray scattering experiment

Micro-focus SAXS experiments were performed on the I22 beamline at Diamond Light Source (DLS, Oxford, UK) using monochromatic 18 keV X-rays. The distance between detector and sample was 1040 mm, guaranteeing that clear and complete SAXS patterns and a partial WAXS pattern could be captured on the 2D detector (Pilatus 2 M, Dectris Ltd., Baden, Switzerland) positioned downstream of the sample. The use of the incident X-ray beam focused down to the spot size of $14.5 \times 19\ \mu m^2$ allowed the achievement of the required spatial resolution. Each sample was mounted upright in air and scattering patterns were collected in transmission mode while the sample was repeatedly shifted in the plane perpendicular to the X-ray incident beam travelling in the z-direction to collect the map of SAXS patterns. The mapping area of region of interest (ROI) for the control sample and samples from 400 °C to 800 °C was $0.6 \times 0.6\ mm^2$. The spacing between each two measurement points of the mapping scans was 40 μm both in longitudinal (y-direction) and transverse (x-direction) directions, resulting in a total of 225 scattering patterns per sample (see Fig. 1a).

The experiment allows us to consider the DEJ a functionally and structurally gradient layer – a common approximation that is used with considerable success in the study of inhomogeneous materials, interfaces, surface treated systems, etc. Since the main interest is in-plane variation, therefore, all possible efforts have been made to ensure that the X-ray beam travelling through the sample is close to parallel to the DEJ and the beam size ($14.5 \times 19\ \mu m^2$) is able to provide a result averaged over the gauge volume that moves across the DEJ. Samples of the thickness ~500 μm represent the practical limit in terms of survival of thermal exposure. As for the SAXS measurements conducted in transmission mode in these experiments, sample thinner than that is likely to result in low intensity of the SAXS signal.

2.3. Scattering data analysis

2.3.1. SAXS

Quantitative interpretation of SAXS patterns provides insight into the mean thickness, orientation and degree of alignment of dense particles. For initial quantitative analysis, 2-D diffraction images were converted into 1-D intensity profiles and pre-processed using the Fit2D software package (Hammersley, 1997).

a) Mean crystalline thickness
The scattering intensity $I(q, \varphi)$ was radially integrated over the entire range of the azimuthal angle φ to obtain a function of $I(q)$, where q represents the scattering vector. The crystal mean thickness T is defined as the *Porod* chord length based on *Porod's law* valid in a two-phase system

$$T = \frac{4}{\pi \frac{Q}{P}} \tag{1}$$

where P is the *Porod* constant given by $I(q) = Pq^{-4}$ (*Porod's law* at large q range), which can be determined from the $Iq^4 \sim q^4$ plot, and Q is the integrated area of the $Iq^2 \sim q$ plot. Note that the definition of T was used without any assumption of the particle shape. However, for specific cases of needle or platelet shape, T can be interpreted as an average measurement of the smallest dimension of crystallites. The actual mean crystalline thickness can be further calculated based on T and other factors like volume fraction (Fratzl et al., 1996).

b) Orientation and degree of alignment
The degree of alignment (ρ) of HAp crystalline particles is used to describe the percentage of aligned particles. To quantify it as well as the preferred orientation, the SAXS

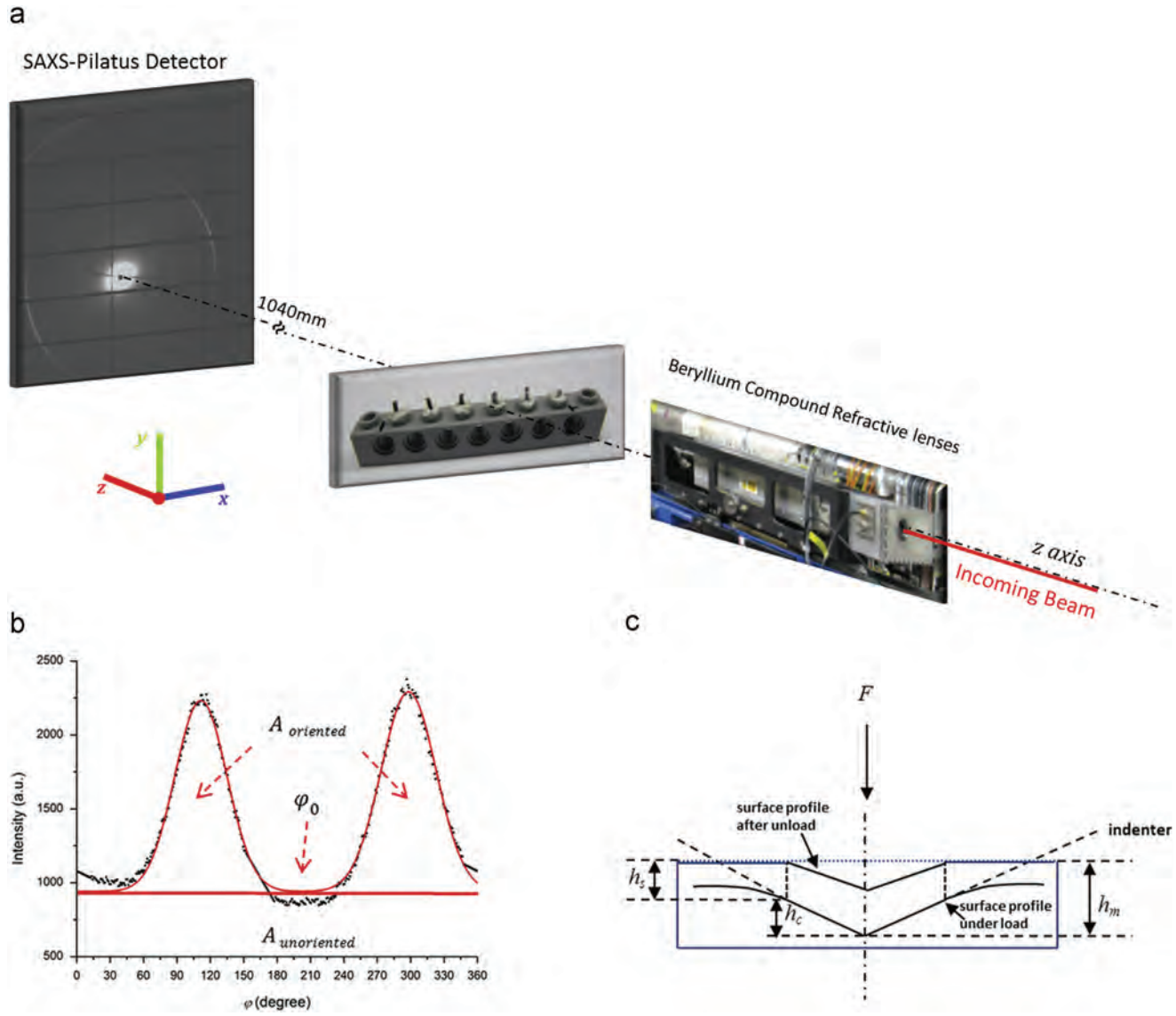

Fig. 1 – Schematic diagram of the experimental setup. (a) micro-focus SAXS setup, WAXS patterns can also be partly obtained on the SAXS-Pilatus detector, (b) A plot of the integrated curve $I(\varphi)$ (black points). The Gauss fit is also shown in the figure (red line). The predominant orientation $\varphi_0$is the average position of the two peaks. The ratio $A_{oriented}/(A_{oriented}+A_{unoriented})$ gives the degree of alignment and (c) nanoindentation profile showing the quantities used in the analysis. (For interpretation of the references to color in this figure legend, the reader is referred to the web version of this article).

patterns were integrated over all the available scattering vectors q, resulting in a function $I(\varphi)$ with the azimuthal angle φ (Rinnerthaler et al., 1999; Tesch et al., 2003), which is shown in Fig. 1b. The Gauss fit is also shown in the figure (red line). In the plot of $I(\varphi)$, the average position of the two peaks determines the predominant orientation φ_0, and the degree of alignment is defined as the ratio

$$\rho = \frac{A_{oriented}}{A_{oriented} + A_{unoriented}} \quad (2)$$

where $A_{unoriented}$ is the area of the constant background level and $A_{oriented}$ is the overall area under the curve of $I(\varphi)$ subtracting the background. The value of the degree of alignment ranges from 0 to 1, where $\rho = 0$ indicates no predominant orientation within the plane of the section and $\rho = 1$ indicates a perfect alignment of all crystallites (Rinnerthaler et al., 1999; Tesch et al., 2003).

2.3.2. WAXS

WAXS patterns are represented by separated diffraction rings, containing characteristic information related to the crystal structure. The analysis of WAXS patterns is performed using the *Bragg's law*, which establishes the relationship between the spacing of atomic planes in crystals and the scattering angle at which these planes produce intense reflections (Bragg and Bragg, 1933). The (002) lattice plane reflection ring from HAp contains the information on the orientation of the c-axis of the crystals as well as the fibril orientation due to their parallel orientation, which is strong

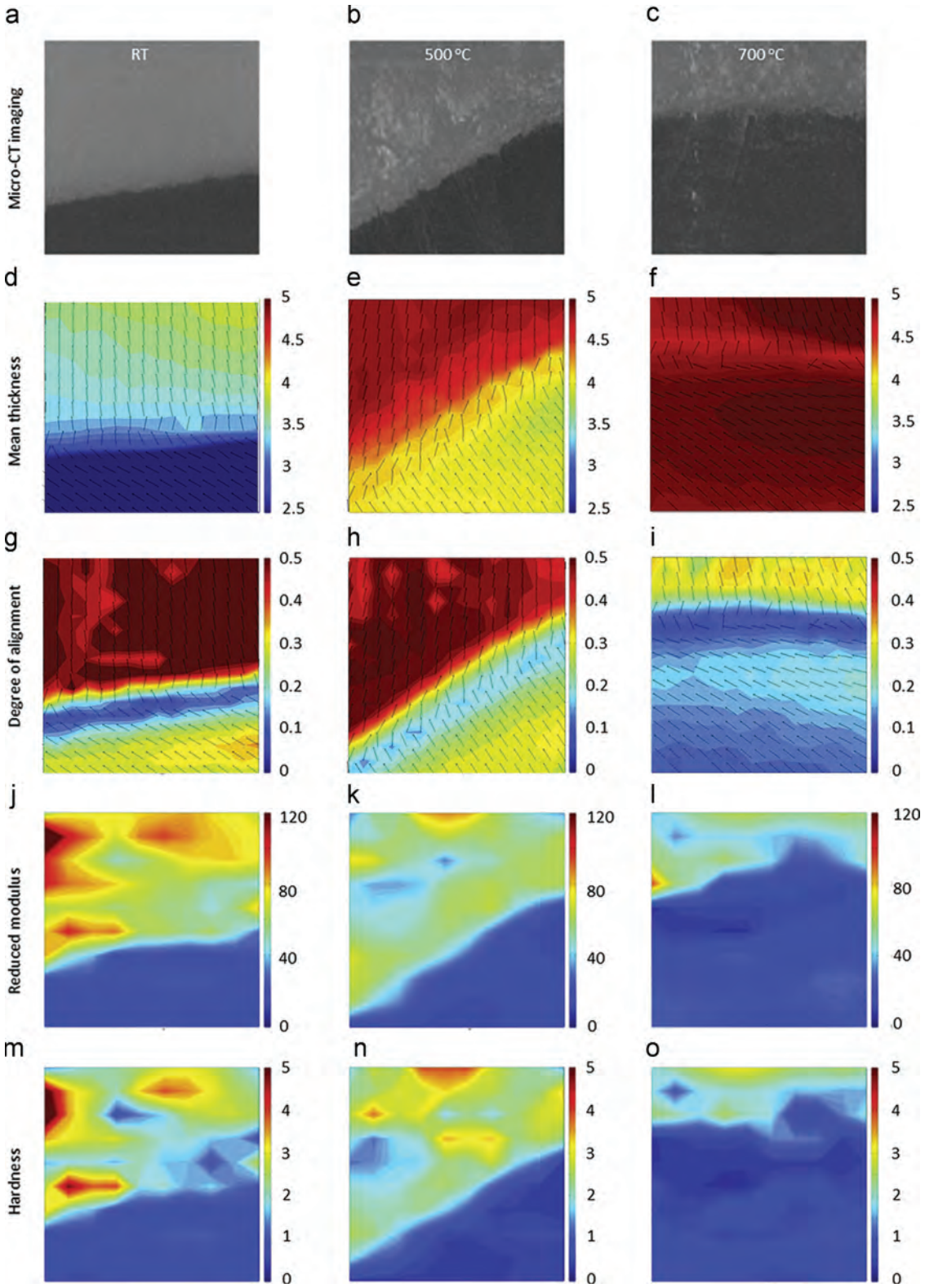

Fig. 2 – Region of interest (0.6 × 0.6 mm^2) of dental slice mapped with SAXS and nanoindentation techniques. Each column represents the results within the same area under a certain temperature as labelled. (a–c) ROI of RT (room temperature), 500 °C and 700 °C samples revealed by Micro-CT; 2D colour coded of SAXS results: (d–f) mean thickness (nm) and (g–i) degree of alignment of HAp crystallites, with the crystal orientation marked by the black lines. The mean thickness of the crystallites in both dentine and enamel increases as the temperature increases (from light blue to red for enamel and from dark blue to red for dentine). However, the spatial difference between dentine and enamel decreases with temperature. The degree of alignment drops as the temperature increases (from red to yellow for enamel and from yellow to blue for dentine); 2D colour coded of nanoindentation results: (j–l) reduced modulus (GPa) and (m–o) hardness (GPa); The reduced modulus and hardness of enamel is observed to decrease significantly with the increasing temperature (from yellow–red mixture to light blue). (For interpretation of the references to color in this figure legend, the reader is referred to the web version of this article).

and distinct (Deymier-Black et al., 2010) Therefore, only the (002) peak of interest is selected for interpretation.

2.4. Nanoindentation experiment

A nanohardness tester (NHT) with a Berkovich diamond probe from CSM (CSM, Neuchatel, Switzerland) was utilised to perform nanoindentation on the thermally treated samples. The calibration was done by fused silica and the procedure suggested by Oliver and Pharr (Oliver and Pharr, 1992) was used to correct for the load-frame compliance of the apparatus and the imperfect shape of the indenter tip. The tests were performed at room temperature under force control feedback mode to a peak force of 2 mN. A load function composed of 30 s loading, followed by 30 s holding and 30 s unloading was used (Le Bourhis et al., 2004; Patriarche et al., 2004). The hold period at maximum load (30 s) is used to limit creep upon unloading, and thereby allow for a more reliable extraction of mechanical properties from the unloading curve (Angker et al., 2005). The contact depth was between 100 and 400 nm that is much lower than the tooth sample thickness (0.5 mm), so that the properties obtained can be confidently assigned to the bulk. Maps of indents were performed along the same ROI used for the scattering experiment. The indents were spaced approximately 60 μm apart both in the x- and y-directions and performed using automation.

Nanoindentation tests are widely used to determine some material properties. Every nano-indent operation involves a loading and unloading process, and the indentation load-depth data is recorded for each operation (Hsu et al.). A schematic diagram of nanoindentation process (Fig. 1c) is shown, where indentation depth h is the summation of h_s (displacement due to elastic deformation) and h_c (contact depth). S is the contact stiffness at maximum penetration and is the initial slope of the unloading curve. Using the compliance method, the hardness H and reduced modulus E_r can be determined directly from analysis of load-displacement data (Ebenstein and Pruitt, 2006). The hardness of the sample can be obtained by dividing the load by the projected area of indentation

$$H = \frac{F_m}{A_c} \tag{3}$$

where A_c ($A_c = 24.5h_c^2$ for a perfect tip) is the contact area, F_m is the force at maximum load. The composite modulus E^* (sample and diamond) is extracted from

$$\frac{1}{E^*} = \frac{2\beta}{S}\sqrt{\frac{A_c}{\pi}} \tag{4}$$

where β is a correction factor depending on the rip geometry ($\beta = 1.034$ for a Berkovich one). The relation with diamond and sample properties is given by

$$\frac{1}{E^*} = \frac{1-\nu_D^2}{E_D} + \frac{1-\nu_S^2}{E_S} \tag{5}$$

where E and ν are Young's modulus and Poisson ratio and the subscripts D and S are for diamond and sample respectively ($E_D = 1141$ GPa, $\nu_D = 0.07$). The reduced modulus is referred to as

$$\frac{1}{E_r} = \frac{1-\nu_s^2}{E_s} \tag{6}$$

which is reported in (Le Bourhis and Patriarche, 2007; Lim et al., 2005; Oliver and Pharr, 1992).

2.5. Statistical analysis

The calculated mean crystalline thickness values were statistically analysed with two-tailed paired sample t-tests using SPSS version 19 (IBM SPSS Inc., Chicago, USA). Probability levels of $p < 0.05$ (95% confidence interval) were considered statistically significant.

3. Results

Colour coded 2D mapping provides a general qualitative understanding of the spatial distribution of the ultrastructural and mechanical properties and their variations with temperature. It also offers a validation on extracting the line measurements or 1D plot with the detailed quantitative information of the changes and correlation of the results. For reasons of consistency, the central line values were chosen in all samples and no dependency of the measurement results on the line position was found. In this section, both the 2D mapping results and the line plot were presented.

3.1. Ultrastructural observations

3.1.1. Mean crystalline thickness

The spatial mean thickness variations of HAp crystallites in the control sample (RT, room temperature), samples heat treated at 500 °C and 700 °C were visualized in Fig. 2d–f as colour coded 2D-plot. Similar features from the three samples were observed, of which the mean crystalline thickness decreased from enamel to DEJ, and further down through deeper dentine. From Fig. 2d–f, it was found that the mean thickness of HAp crystallites increases with temperature, which was reflected through the 2D colour changes (enamel from blue in Fig. 2d to red in Fig. 2f, while dentine from dark blue to red). In addition, the spatial difference of the crystalline thickness between enamel and dentine was found to gradually decrease with temperature since in Fig. 2f, enamel and dentine almost shared the same colour.

In order to trace the average mean crystalline thickness alteration with increasing temperature, the thickness values along the central line of dentine and enamel in the mapping area were extracted from the 2D mapping results, which are shown in Fig. 3a. The variation of the averaged mean crystalline thickness of the central line of dentine and enamel with increasing temperature are illustrated in Fig. 4a and b, from which the crystallites in dentine is nearly tripled from 1.94 (SD: 0.06) nm at room temperature (RT) to 5.16 (SD: 0.06) nm at 800 °C, while that of crystallites in enamel increased from 3.81 (SD: 0.28) nm at RT to 4.90 (SD: 0.04) nm at 800 °C (for additional values see Table 1).

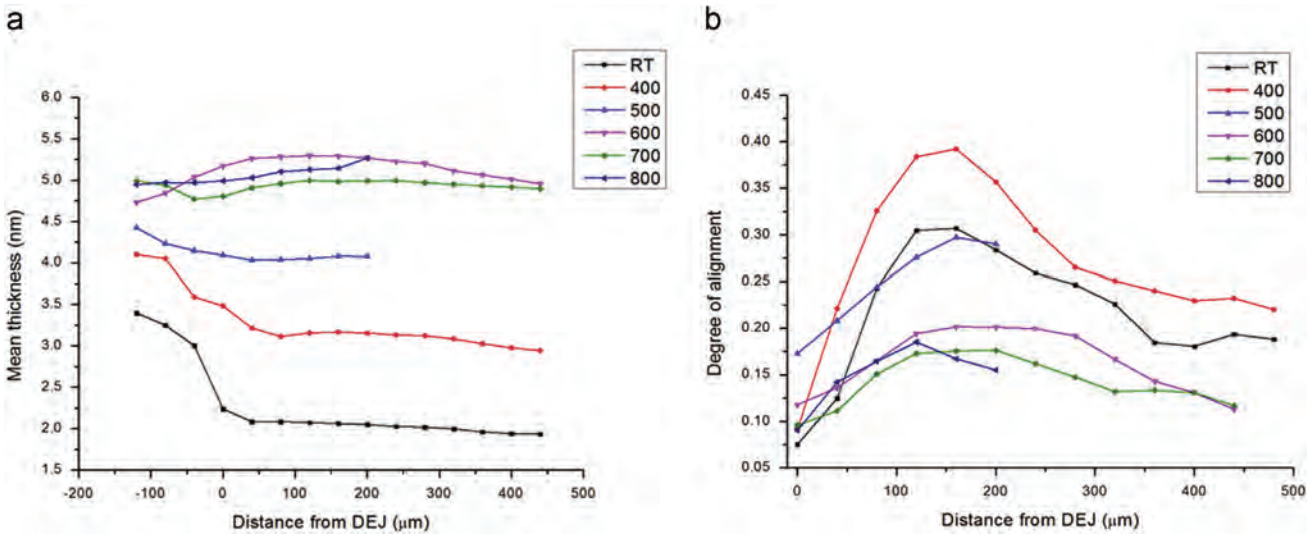

Fig. 3 – Ultrastructural variations along the central line from the 2D mapping result of ROI as a function of temperature and distance from DEJ. (a) results of the mean thickness of HAp. The first three measurement points (with minus distances from DEJ) represent the results in enamel; (b) results of the degree of alignment of HAp. Only the results of crystals in dentine are shown due to the complex variation happened beneath the DEJ.

3.1.2. *Orientation and degree of alignment*

The 2D maps of the degree of alignment variation of the same three samples (RT, 500 °C and 700 °C) within the interested region were shown respectively in Fig. 2g–i. The enamel and dentine show distinctive results visualized by the colour coding. Similar gradient features as the mean thickness results were observed. Generally, enamel has higher degree of alignment than dentine. However, it was found that the degree of alignment of both enamel and dentine decreased with temperature as the colour changed mostly from red to yellow in enamel and yellow to blue in dentine.

The angular orientation of the mineral particles in the 2D teeth slices is depicted by the small black lines superimposed on the degree of alignment mapping (shown in Fig. 2g–i). In enamel, all the particles are almost orthogonal to the DEJ plane. Same features can be observed for the particles in dentine but only for the region far beneath the transition area of the DEJ. It appears that mineral particles gradually become parallel to the DEJ plane through the region near DEJ.

The same central line of dentine and enamel as presented in the mean thickness visualization were selected from 2D mapping results. Only the line variation of the result in dentine is of the most interest and is shown in Fig. 3b. It is found that in the specific area in dentine just beneath the DEJ, the degree of alignment is relatively higher than the area far away from DEJ, shown as a bump in Fig. 3b. However, the overall degree of alignment of crystals in dentine decreased (also see Fig. 4c and d) and the bump gradually disappeared with increasing temperature. This indicates a tendency towards more random distribution of crystals as the temperature increased (see Table 1).

3.2. *Mechanical properties characterization*

3.2.1. *Reduced modulus*

Fig. 2j–l demonstrate the results of the spatial distribution of reduced modulus within the 2D interested area of the three samples (RT, 500 °C and 700 °C). The DEJ is clearly visible whereas the distribution inside the enamel and dentine is limited. It was found that only enamel has a pronounced colour change (from yellow–red in Fig. 2j to light blue in Fig. 2l), indicating a significant decrease of reduced modulus in enamel with temperature.

The variations of the averaged reduced modulus of the central line of dentine and enamel with respect to all the tested temperatures are illustrated in Fig. 4a and c. From the figure, it is found that the averaged reduced modulus of dentine decreased from 20 (SD: 6) GPa at RT to 15 (SD: 2) GPa at 500 °C and then increased to 29 (SD: 10) GPa at 800 °C, while in enamel it decreased from 70 (SD: 17) GPa at RT to 56 (SD: 17) GPa at 500 °C, and then further down to 47 (SD: 18) GPa at 800 °C (see Table 1).

3.2.2. *Hardness*

The overall spatial distribution of hardness of the three samples (RT, 500 °C and 700 °C) in the ROI can be observed in Fig. 2m–o. The DEJ is still recognisable, but the spatial changes are not as clearly shown as in the structural mapping of thickness and degree of alignment. Similar tendency as the reduced modulus was found that the hardness of enamel dropped significantly with temperature, which is reflected from the pronounced colour change.

The detailed alteration of the hardness with increasing temperature is also reflected in the variation of the averaged hardness of the selected central line of dentine and enamel (Fig. 4b and d). It was found that the averaged hardness variations have the similar tendency of variation as that of the averaged reduced modulus both in dentine and enamel. The averaged hardness in dentine decreased from 0.7 (SD: 0.1) GPa at RT down to 0.4 (SD: 0.1) GPa at 500 °C and then increased to 0.8 (SD: 0.3) GPa at 800 °C, while in enamel the averaged hardness decreased from 3.0 (SD: 1.3) GPa at RT to

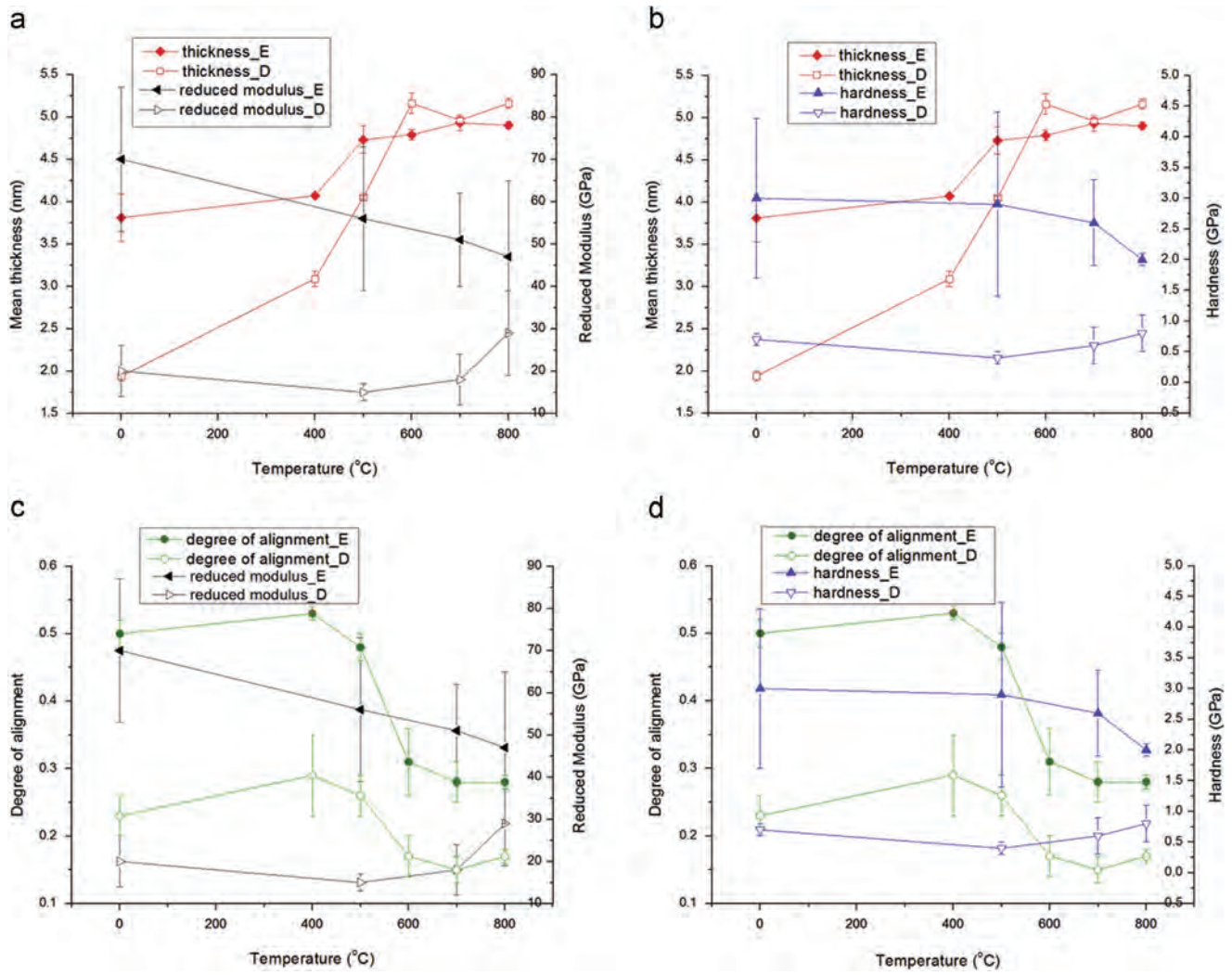

Fig. 4 – Correlation analysis between structural–mechanical parameters coupled with increasing temperature ("E" means enamel while "D" means dentine). All the results are the averaged values of different regions along the selected central line in ROI. (a) mean thickness vs. reduced modulus; (b) mean thickness vs. hardness; (c) degree of alignment vs. reduced modulus; (d) degree of alignment vs. hardness. Error bars ± 1 SD. (For interpretation of the references to color in this figure, the reader is referred to the web version of this article).

Table 1 – Overview of SAXS and nanoindentation measurement results collected from central line from 2D mapping results. Statistical significance was evaluated using two-tailed paired sample *t*-tests with a 95% confidence interval for the mean thickness results (*$p<0.05$, **$p<0.005$, ***$p<0.0005$).

Temperature (°C)		Mean crystalline thickness (nm)	Degree of alignment	Hardness (GPa)	Reduced modulus (GPa)
RT	Enamel	3.81(SD: 0.28)	0.50(SD: 0.02)	3.0(SD: 1.3)	70(SD:17)
400		4.07(0.02)	0.53(0.01)		
500		4.73(0.16)*	0.48(0.02)	2.9(1.5)	56(17)
600		4.79(0.06)	0.31(0.05)		
700		4.93(0.09)	0.28(0.03)	2.6(0.7)	51(11)
800		4.90(0.04)	0.28(0.01)	2.0(0.1)	47(18)
RT	Dentine	1.94(0.06)	0.23(0.03)	0.7(0.1)	20(6)
400		3.09(0.09)***	0.29(0.06)		
500		4.05(0.02)***	0.26(0.03)	0.4(0.1)	15(2)
600		5.16(0.12)***	0.17(0.03)		
700		4.96(0.03)***	0.15(0.02)	0.6(0.3)	18(6)
800		5.16(0.06)	0.17(0.01)	0.8(0.3)	29(10)

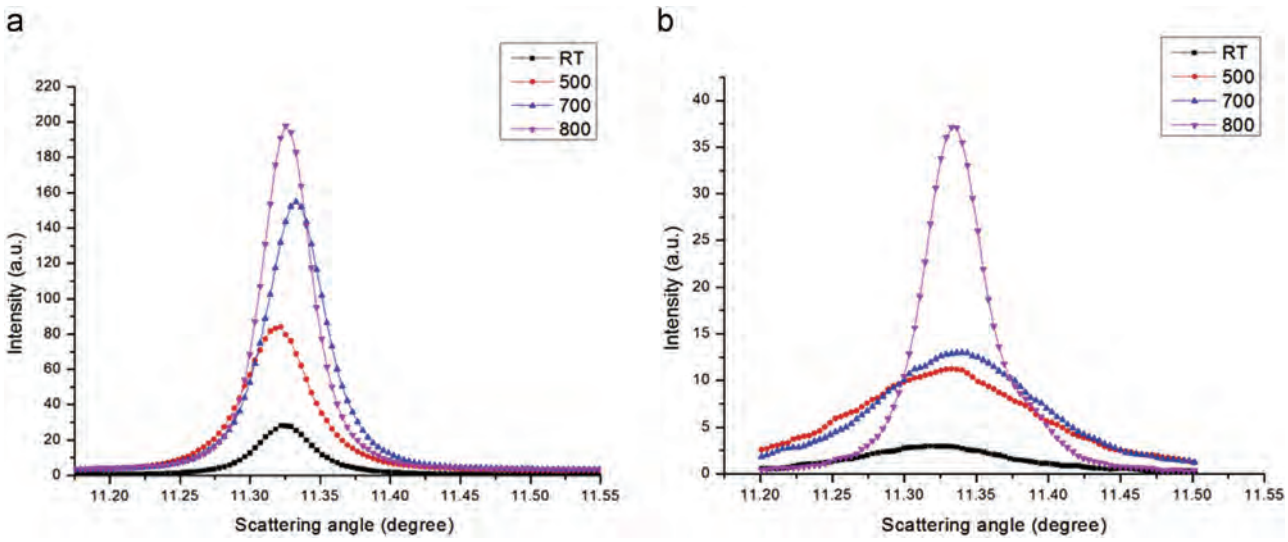

Fig. 5 – Intensity variation of the (002) reflection in the WAXS patterns of different regions at different temperatures: (a) enamel and (b) dentine. The observed peak sharpening and higher intensity at higher temperatures compared with the control sample indicates an increased diffraction contribution from HAp crystallites.

2.9 (SD:1.5) GPa at 500 °C and then to 2.0 (SD:0.1) GPa at 800 °C (see Table 1).

3.3. *Crystal perfection*

The WAXS patterns diffracted from HAp crystals in both the enamel and dentine provide information about the crystalline perfection difference in different regions. Due to the limited size of the 2D detector, only the (002) peak could be captured and analyzed. Fig. 5 shows the diffraction intensity variation of (002) peak for a selected region of scattering angles (11.2°–11.5°) with the temperature change. A sharpening of the peak at higher temperatures was observed, compared to the broad one of the control sample at lower temperature. This represents an increased diffraction contribution from HAp crystals within this scattering angle range as the temperature increased, which indicates that the crystal perfection increased remarkably during the heating. Note that the peak sharpening in dentine is more obvious than that in enamel.

4. Discussion

The ultrastructural alteration of skeletal hard tissues exposed to the thermal treatment process developed in the present study provides a better, more reliable basis for deducing the heating history, compared with the conventional methods based on monitoring the macro- and microstructural colour (Piga et al., 2009; Thompson, 2005; Thompson et al., 2013) in the forensic and archaeological investigation. In the clinical application like caries prevention, the present study offers an opportunity to characterise the microstructural features affected by laser therapies.

The previous analysis of the entire powdered tooth analysis obscures the sharpness of ultrastructural variations in dentine and enamel (Kugler, 2003; Piga et al., 2009). The present study clearly illustrates how the observed evolution of ultrastructure reflects the differences between dentine and enamel, suggesting that enamel and dentine must be investigated separately in order to evaluate the exposure temperature precisely in the forensic cases as well as optimise laser-assistant treatment in clinical application.

The structural–mechanical properties correlation to the temperature provides an additional guidance to track the heating history in the forensic study. In addition, for caries prevention, it provides the evidence that the alteration of mechanical properties should also be taken into account during the sintering process, since the decreased hardness may induce micro-cracks with increasing temperature.

4.1. *Ultrastructural observations*

4.1.1. *Mean crystalline thickness*

Overall the mean crystalline thickness distribution in dentine was more uniform compared with that in enamel. The mean crystalline thickness was observed to obviously decrease in enamel and slightly increase in dentine towards DEJ at low temperature, which may be ascribed to the gradient properties of human dental slice (Jacobs et al., 1973) as illustrated in Fig. 3a. However, as temperature increases, this gradient becomes smaller, which can be clearly seen in Fig. 3a. Besides the visible gradient features, the major drop was visible near the transition area around the DEJ, indicating the spatial structural variation in the human dental slice.

The mean crystalline thickness of the control sample (3.81 (SD: 0.28) nm in dentine and 1.94 (SD: 0.06) nm in enamel) is consistent with the earlier transmission electron microscopy (TEM) studies and XRD data (Marten et al., 2010; Reiche et al., 2002). The increase of mean crystalline thickness happened after 400 °C which implied the HAp crystallites starting to sinter, leading to grain size growth. This process becomes dramatic after 600 °C, as can be confirmed by tracking the WAXS peak variation as illustrated in the

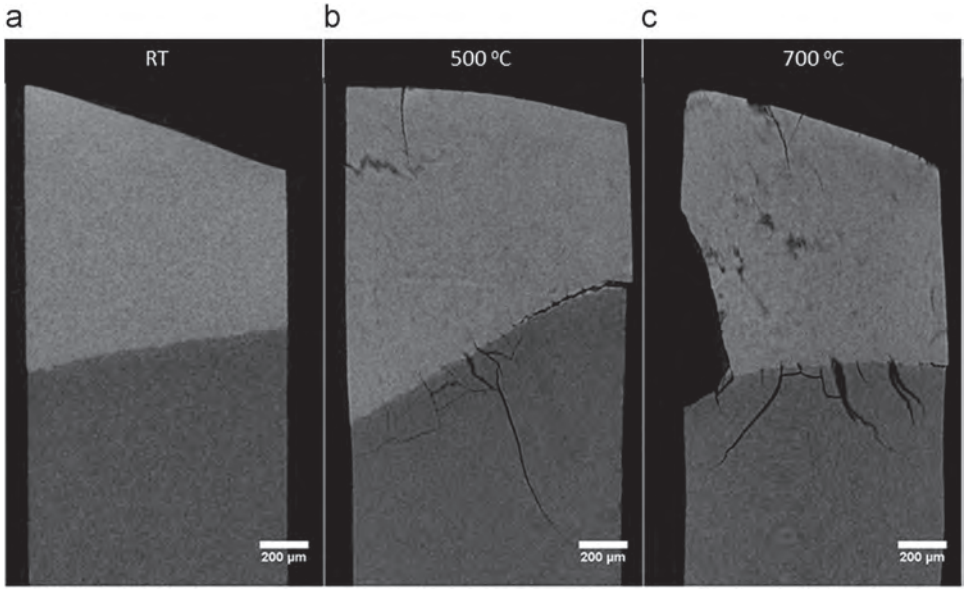

Fig. 6 – Crack development revealed by micro-CT cross-sectional images. The control sample (a) shows no cracks around the DEJ; whilst an increase in number of cracks and lifting of the enamel can be seen at 500 °C (b) and 700 °C (c).

Fig. 5 (Pramanik et al., 2013). In addition, the small increase in crystallite size for enamel with increasing temperature is likely to be related to the denser arrangement of HAp crystallites compared with dentine.

4.1.2. *Orientation and degree of alignment*

The local structural variation of the degree of alignment in dentine with distance from DEJ (Fig. 3b) represents an internal ultra- and micro-structural adaptation matching the geometry of the human tooth. The higher degree of alignment of HAp crystallites near DEJ is expected to stiffen the dentine. Thus the higher mineral particle co-alignments beneath the chewing surface cusps may be important for the transfer or the redistribution of mastication loads from the much harder, highly mineralised enamel deep into bulk dentine (Eliceiri et al., 2012).

The degree of alignment in dentine (0.23 (SD: 0.03)) from the control sample (room temperature, Fig. 4c and d) shows an almost random orientation of HAp crystallites, while the result in enamel indicates a stronger textured orientation (0.50 (SD: 0.02)). This is consistent with earlier SAXS results for dental tissue (Eliceiri et al., 2012; Jiang et al., 2005), where the internal architecture in dentine was observed to be net-like fibrils wound around tubules with decorated HAp crystallites. If it is observed along tubule direction, the fibrils will display an almost random distribution (Bozec et al., 2005). Therefore, when the beam illuminates perpendicular to the dental slice, i.e. perpendicular to the cross section of tubule, the HAp crystallites will have a much lower degree of alignment than that of well-packed HAp crystallites in enamel, which crystallites partially aligned along the prisms (or rods) (Macho et al., 2003). It is noted that in both dentine and enamel, there is a reduction in the degree of alignment as the temperature increased. The reduction of the overall degree of alignment as well as the bump gradient of the central line observed in Fig. 3b with increasing temperature may be explained by the burning-off or gradual disappearance of the organic phase most of which is collagen. Since the organic phase serves as the support of the structure, such disappearance may lead to the rearrangement of crystallites associated with rotation or anisotropic sintering. In addition, the rearrangement of crystallites may increase the crystal perfection, especially in dentine (Fig. 5), due to its larger amount of organic phase than in enamel.

4.2. *Mechanical properties characterization*

Both hardness and reduced modulus mapping showed the obvious contrast of properties between the dentine and enamel. The boundary between dentine and enamel is clearly shown in Fig. 2j–o and regions with large reduced modulus and hardness match very well as expected. However, it was found that the transition feature of mechanical properties in dentine was not as clear as the ultrastructural visualization, which was partly due to the low resolution of nanoindentation compared with SAXS/WAXS and the mechanical-response dispersion of both enamel and dentine. In addition, the existing cracks or surface defects in all the samples may affect the indentation results, and increase the relatively large error bounds in Fig. 4.

The hardness (0.7 (SD: 0.1) GPa in dentine and 3.0 (SD: 1.3) GPa in enamel) and reduced modulus (20 (SD: 6) GPa in dentine and 70 (SD: 17) GPa in enamel) of the control sample were consistent with the earlier nanoindentation studies on dental tissues (Roy and Basu, 2008; Tesch et al., 2001). The different behaviours of dentine and enamel might result from their different mineral contents. The initial reduction of the mechanical properties in dentine might be due to the gradual disappearance of collagen and the subsequent increase at higher temperatures might be explained by the occurrence of sintering and significantly increased crystal perfection, which

was partly reflected in the sharper peak variation in dentine in Fig. 5.

4.3. *Ultrastructure and mechanical properties correlation*

The relationship between the variations of the ultrastructure and mechanical properties with respect to different temperatures are reflected in Fig. 4a–d. As illustrated in Fig. 4a and b, in the enamel the reduced modulus (solid black symbols) and hardness (solid blue symbols) decrease as the mean thickness (solid red symbols) goes up. Similar phenomenon can also be observed in the dentine as illustrated in the empty symbols. The bigger the mean crystalline thickness is, the lower the mechanical properties would be, as reported by Tesch et al. (Tesch et al., 2001). Thus, the mean thickness was found to be a good predictor of the reduced modulus and hardness.

No obvious correlation between the degree of alignment and the mechanical properties can be observed in Fig. 4c and d except that the region with higher modulus as shown in Fig. 2 almost matches the region with higher degree of alignment of HAp crystallites, which indicates that the local structural variation may result in the local change of modulus in the same area. Furthermore, the distribution of the orientation of HAp crystallites may indicate a correlation between the orientation effect or texture effect and the mechanical property variation, as discussed in our previous work (Sui et al., 2013; Sui et al., 2014).

The consistent tendency of reduced modulus and hardness (Bao et al., 2004) is observed in Fig. 4. The observed alteration of the mechanical properties within the dental slice as the temperature increases may facilitate the crack propagation, since the decrease of hardness indicates the reduction of the ultimate strength (Krishna et al., 2013), which is visible in micro-CT observation (see Fig. 6).

5. Conclusions

The effects of heat treatment on human dental tissues were successfully elucidated by a systematic study of the combined SAXS/WAXS mapping and nanoindentation mapping techniques. Quantitative analysis of SAXS patterns of human teeth samples revealed a temperature-dependent variation of the mean thickness and the degree of alignment of nanoscale mineral phase (HAp crystallites) both in dentine and enamel. Furthermore, nanoindentation mapping captured the remarkable decrease of the hardness and modulus as the temperature increased. The relationship between the ultrastructural changes and mechanical behaviour changes with increasing temperature indicates that the structure has a strong effect on the mechanical properties.

In conclusion, the combination of synchrotron-based SAXS/WAXS and nanoindentation mapping methods has been shown to be a powerful method for the determination of the variation of the structural–mechanical property relationship in human dental tissues induced by the thermal treatment. Ultimately, the SAXS mapping approach developed in the present study might allow further design and optimization of laser treatment strategies for clinical applications, and will possibly provide an effective approach to deduce the heating history for teeth samples in the forensic and archaeological context.

Acknowledgements

AMK acknowledges the support of EPSRC through grants EP/I020691 “Multi-disciplinary Centre for In-situ Processing Studies (CIPS)”, EP/G004676 “Micromechanical Modelling and Experimentation”, and EP/H003215 “New Dimensions of Engineering Science at Large Facilities”. Diamond Light Source is acknowledged for providing the beam time.

REFERENCES

Al-Jawad, M., Steuwer, A., Kilcoyne, S.H., Shore, R.C., Cywinski, R., Wood, D.J., 2007. 2D mapping of texture and lattice parameters of dental enamel. Biomaterials 28, 2908–2914.

Angker, L., Swain, M.V., Kilpatrick, N., 2005. Characterising the micro-mechanical behaviour of the carious dentine of primary teeth using nano-indentation. J. Biomech. 38, 1535–1542.

Bao, Y.W., Wang, W., Zhou, Y.C., 2004. Investigation of the relationship between elastic modulus and hardness based on depth-sensing indentation measurements. Acta Mater. 52, 5397–5404.

Beckett, S., Rogers, K.D., Clement, J.G., 2011. Inter-species variation in bone Mineral behavior upon heating. J. Forensic Sci. 56, 571–579.

Bozec, L., de Groot, J., Odlyha, M., Nicholls, B., Nesbitt, S., Flanagan, A., Horton, M., 2005. Atomic force microscopy of collagen structure in bone and dentine revealed by osteoclastic resorption. Ultramicroscopy 105, 79–89.

Bragg, W.H., Bragg, W.L., 1933. The Crystalline State, Vol. 1. A General Survey Bell, London.

Daniels, J.E., Pontoni, D., Hoo, R.P., Honkimaki, V., 2010. Simultaneous small- and wide-angle scattering at high X-ray energies. J. Synchrotron Radiat. 17, 473–478.

Deymier-Black, A.C., Almer, J.D., Stock, S.R., Haeffner, D.R., Dunand, D.C., 2010. Synchrotron X-ray diffraction study of load partitioning during elastic deformation of bovine dentin. Acta Biomater. 6, 2172–2180.

Ebenstein, D.M., Pruitt, L.A., 2006. Nanoindentation of biological materials. Nano Today 1, 26–33.

Eliceiri, K.W., Berthold, M.R., Goldberg, I.G., Ibanez, L., Manjunath, B.S., Martone, M.E., Murphy, R.F., Peng, H., Plant, A.L., Roysam, B., Stuurmann, N., Swedlow, J.R., Tomancak, P., Carpenter, A.E., 2012. Biological imaging software tools. Nat. Methods 9, 697–710.

Enzo, S., Bazzoni, M., Mazzarello, V., Piga, G., Bandiera, P., Melis, P., 2007. A study by thermal treatment and X-ray powder diffraction on burnt fragmented bones from tombs II, IV and IX belonging to the hypogeic necropolis of “Sa Figu” near Ittiri, Sassari (Sardinia, Italy). J. Archaeol. Sci. 34, 1731–1737.

Fong, H., Sarikaya, M., White, S.N., Snead, M.L., 2000. Nano-mechanical properties profiles across dentin-enamel junction of human incisor teeth. Mater. Sci. Eng. C-Biomimetic Supramol. Syst. 7, 119–128.

Fratzl, P., Schreiber, S., Boyde, A., 1996. Characterization of bone Miner. crystals in horse radius by small-angle X-ray scattering. Calcif. Tissue Int. 58, 341–346.

Fried, D., Zuerlein, M.J., Le, C.Q., Featherstone, J.D.B., 2002. Thermal and chemical modification of dentin by 9–11-mu m CO_2 laser pulses of 5–100-mu s duration. Lasers Surg. Med. 31, 275–282.

Hammersley, A.P. 1997. "FIT2D: An Introduction and Overview" ESRF Internal Report.
Haque, F., 2003. Application of nanoindentation to development of biomedical materials. Surf. Eng. 19, 255–268.
He, L.H., Swain, M.V., 2009. Enamel—A functionally graded natural coating. J. Dentistry 37, 596–603.
Hiller, J.C., Thompson, T.J., Evison, M.P., Chamberlain, A.T., Wess, T.J., 2003. Bone Mineral change during experimental heating: an X-ray scattering investigation. Biomaterials 24, 5091–5097.
Hsu, C.M., Lin, A.D., Chien, H.L., Hung, T.P., Kuang, J.H., Using nanoindentation techniques to investigate the Young's moduli for human teeth of different ages.
Jacobs, H.R., Thompson, R.E., Brown, W.S., 1973. Heat-transfer in teeth. J. Dent. Res. 52, 248–252.
Jiang, H.D., Liu, X.Y., Lim, C.T., Hsu, C.Y., 2005. Ordering of self-assembled nanobiominerals in correlation to mechanical properties of hard tissues. Appl. Phys. Lett., 86.
Kinney, J.H., Marshall, S.J., Marshall, G.W., 2003. The mechanical properties of human dentin: a critical review and re-evaluation of the dental literature. Crit. Rev. Oral Biol. Med. 14, 13–29.
Krishna, S.C., Gangwar, N.K., Jha, A.K., Pant, B., 2013. On the prediction of strength from hardness for copper alloys. J. Mater. 2013, 1–6.
Kugler, M., 2003. X-ray diffraction analysis in forensic science: the last resort in many criminal cases. Adv. X-ray Anal., 46.
Le Bourhis, E., Patriarche, G., 2007. TEM-nanoindentation studies of semiconducting structures. Micron 38, 377–389.
Le Bourhis, E., Patriarche, G., Largeau, L., Riviere, J.P., 2004. Polarity-induced changes in the nanoindentation response of GaAs. J. Mater. Res. 19, 131–136.
Lim, C.T., Hairul Nizam, B.R., Omar, B.H.B., Chng, H.K., Yap, A.U.J., 2005. Probing the nanomechanical properties of teeth. ICF11 proceeding.
Macho, G.A., Jiang, Y., Spears, I.R., 2003. Enamel microstructure–a truly three-dimensional structure. J. Human Evol. 45, 81–90.
Marshall, G.W., Balooch, M., Gallagher, R.R., Gansky, S.A., Marshall, S.J., 2001. Mechanical properties of the dentinoenamel junction: AFM studies of nanohardness, elastic modulus, and fracture. J. Biomed. Mater. Res. 54, 87–95.
Marshall, S.J., Balooch, M., Breunig, T., Kinney, J.H., Tomsia, A.P., Inai, N., Watanabe, L.G., Wu-Magidi, I.C., Marshall, G.W., 1998. Human dentin and the dentin–resin adhesive interface. Acta Mater. 46, 2529–2539.
Marten, A., Fratzl, P., Paris, O., Zaslansky, P., 2010. On the Miner. in collagen of human crown dentine. Biomaterials 31, 5479–5490.
Oliver, W.C., Pharr, G.M., 1992. An Improved technique for determining hardness and elastic-modulus using load and displacement sensing indentation experiments. J. Mater. Res. 7, 1564–1583.
Patriarche, G., Le Bourhis, E., Khayyat, M.M.O., Chaudhri, M.M., 2004. Indentation-induced crystallization and phase transformation of amorphous germanium. J. Appl. Phys. 96, 1464–1468.
Piga, G., Malgosa, A., Thompson, T.J.U., Enzo, S., 2008. A new calibration of the XRD technique for the study of Archaeological burned human remains. J. Archaeol. Sci. 35, 2171–2178.
Piga, G., Thompson, T.J.U., Malgosa, A., Enzo, S., 2009. The potential of X-Ray diffraction in the analysis of burned remains from forensic contexts. J. Forensic Sci. 54, 534–539.
Piga, G., Solinas, G., Thompson, T.J.U., Brunetti, A., Malgosa, A., Enzo, S., 2013. Is X-ray diffraction able to distinguish between animal and human bones?. J. Archaeol. Sci. 40, 778–785.
Pramanik, S., Hanif, A.S.M., Pingguan-Murphy, B., Abu Osman, N.A., 2013. Morphological change of heat treated bovine bone: a comparative study. Materials 6, 65–75.
Reiche, I., Vignaud, C., Menu, M., 2002. The crystallinity of ancient bone and dentine: new insights by transmission electron microscopy. Archaeometry 44, 447–459.
Rinnerthaler, S., Roschger, P., Jakob, H.F., Nader, A., Klaushofer, K., Fratzl, P., 1999. Scanning small angle X-ray scattering analysis of human bone sections. Calcif. Tissue Int. 64, 422–429.
Rogers, K., Beckett, S., Kuhn, S., Chamberlain, A., Clement, J., 2010. Contrasting the crystallinity indicators of heated and diagenetically altered bone Mineral. Palaeogeogr. Palaeoclimatol. Palaeoecol. 296, 125–129.
Rogers, K.D., Daniels, P., 2002. An X-ray diffraction study of the effects of heat treatment on bone mineral microstructure. Biomaterials 23, 2577–2585.
Roy, S., Basu, B., 2008. Mechanical and tribological characterization of human tooth. Mater. Charact. 59, 747–756.
Shipman, P., Foster, G., Schoeninger, M., 1984. Burnt bones and teeth—an experimental-study of color, morphology, crystal-structure and shrinkage. J. Archaeol. Sci. 11, 307–325.
Sui, T., Sandholzer, M.A., Baimpas, N., Dolbnya, I.P., Walmsley, A.D., Lumley, P.J., Landini, G., Korsunsky, A.M., 2013. Multi-scale modelling and diffraction-based characterization of elastic behaviour of human dentine. Acta Biomater. 9, 7937–7947.
Sui, T., Lunt, A.J., Baimpas, N., Sandholzer, M.A., Hu, J., Dolbnya, I.P., Landini, G., Korsunsky, A.M., 2014. Hierarchical modelling of in situ elastic deformation of human enamel based on photoelastic and diffraction analysis of stresses and strains. Acta Biomater. 10, 343–354.
Ten Cate, A.R., 1998. Oral histology: development, structure, and function, 5th Ed. Mosby, St. Louis, Mo., London.
Tesch, W., Eidelman, N., Roschger, P., Goldenberg, F., Klaushofer, K., Fratzl, P., 2001. Graded microstructure and mechanical properties of human crown dentin. Calcif. Tissue Int. 69, 147–157.
Tesch, W., Vandenbos, T., Roschgr, P., Fratzl-Zelman, N., Klaushofer, K., Beertsen, W., Fratzl, P., 2003. Orientation of mineral crystallites and mineral density during skeletal development in mice deficient in tissue nonspecific alkaline phosphatase. J. Bone Miner. Res. 18, 117–125.
Thompson, T.J.U., 2005. Heat-induced dimensional changes in bone and their consequences for forensic anthropology. J. Forensic Sci. 50, 1008–1015.
Thompson, T.J.U., Islam, M., Bonniere, M., 2013. A new statistical approach for determining the crystallinity of heat-altered bone Miner. from FTIR spectra. J. Archaeol. Sci. 40, 416–422.
Thompson, T.J.U., Islam, M., Piduru, K., Marcel, A., 2011. An investigation into the internal and external variables acting on crystallinity index using Fourier Transform Infrared Spectroscopy on unaltered and burned bone. Palaeogeogr. Palaeoclimatol. Palaeoecol. 299, 168–174.
Zuerlein, M.J., Fried, D., Featherstone, J.D.B., 1999. Modeling the modification depth of carbon dioxide laser-treated dental enamel. Lasers in Surg. Med. 25, 335–347.

In situ X-ray scattering evaluation of heat-induced ultrastructural changes in dental tissues and synthetic hydroxyapatite

Tan Sui[1], Michael A. Sandholzer[2], Alexander J.G. Lunt[1], Nikolaos Baimpas[1], Andrew Smith[3], Gabriel Landini[2], Alexander M. Korsunsky[1]

[1] Department of Engineering Science, University of Oxford, Parks Road, Oxford OX1 3PJ, United Kingdom

[2] School of Dentistry, College of Medical and Dental Sciences, University of Birmingham, St. Chad's Queensway, Birmingham B4 6NN, United Kingdom

[3]Diamond Light Source Ltd, Harwell Science and Innovation Campus, Didcot OX11 0DE, United Kingdom

Abstract

Human dental tissues consist of inorganic constituents (mainly crystallites of hydroxyapatite, HAp) and organic matrix. In addition, synthetic HAp powders are frequently used in medical and chemical applications. Insight into the ultrastructural alterations of skeletal hard tissues exposed to thermal treatment is crucial for the estimation of temperature of exposure in forensic and archaeological studies. However, at present only limited data exist on the heat-induced structural alterations of human dental tissues. In this paper, advanced non-destructive Small- and Wide Angle X-ray Scattering (SAXS/WAXS) synchrotron techniques were used to investigate the *in situ* ultrastructural alterations in thermally treated human dental tissues and synthetic HAp powders. The crystallographic properties were probed by WAXS, whilst HAp grain size distribution changes were evaluated by SAXS. The results demonstrate the important role of the organic matrix that binds together the HAp crystallites in responding to heat exposure. This is highlighted by the difference in the thermal behaviour between human dental tissues and synthetic HAp powders. The X-ray analysis results are supported by thermogravimetric analysis (TGA). The results concerning the HAp crystalline architecture in natural and synthetic HAp powders provide a reliable basis for deducing the heating history for dental tissues in the forensic and archaeological context, and the foundation for further development and optimization of biomimetic material design.

Keywords: in situ thermal treatment; dental tissue; hydroxyapatite; SAXS/WAXS

1. Introduction

Hydroxyapatite (HAp) crystallites that are closely integrated in the organic matrix at the nano-scale are the main inorganic constituents of the hierarchical mineralized human dental tissues, namely, enamel and dentine. Such natural HAp crystallites are understood to be crucial to the physiology and function of dental tissues [1]. In parallel, recent developments in synthetic biomineralization have demonstrated that synthetic HAp powders can play an important role for medical applications, especially for the replacement or treatment of dental tissues [2].

Advanced high-energy treatment techniques are finding increasing use in modern dentistry. In the early 1970s, Kantola et al. [3] showed that laser treatment of dental tissues can be used to increase the mineral content and crystallinity of dentine by preferential removal of the inherent water and protein. With the advent of a variety of new laser systems spanning a range of energy densities and pulse durations, clinical treatments such as laser-assisted caries protection were proposed and developed. Local temperature induced by short pulse laser treatment leads to local heating to temperatures between several hundred °C to over 1000°C. The alteration of dental tissue remains highly localised and improved caries prevention is surmised to be associated with increased mineralisation and HAp crystallite sintering that leads to the sealing of dentinal tubules, whilst leaving the remaining tissues intact due to the confined effect of less than 10 μm in depth (at the fluence of 2 J/cm^2)[4, 5].

Any change in the local environment of HAp crystallites, e.g. through laser illumination or direct heating, is bound to affect the mineral ultrastructure. In the context of archaeological and forensic investigations, while macroscopic alterations (e.g. surface colour) can be used to deduce an approximate temperature range, the investigation of the micro- and ultrastructural alterations of skeletal hard tissue to high temperatures has proven to be crucial to obtain a reliable estimation of the temperature of exposure [6-8]. This, in turn, sheds light on the attendant circumstances, e.g. the presence and nature of combustible agent used. Dental tissues, being the most highly mineralised part of the human body, can withstand longer

thermal exposure and survive higher temperatures, thus offering the possibility of extending the range of applicability of this technique [9].

The above considerations provide strong motivation for a detailed study into the effect of thermal exposure on the nano-structure (the arrangement of HAp crystallites) of human dental tissue, as well as the role of the organic phase. Whilst much research has been carried out into the heat-induced changes that occur in bone, in connection with human remains studied in the context of archaeology, anthropology and paleontology [10-13], the corresponding range and depth of study of the thermal response of dental tissues remains lacking [6, 14].

Multiple techniques have been used to study heat-induced ultrastructural alterations of skeletal hard tissues. Most widely applied techniques are based on the absorption spectra of infrared radiation (Fourier transform infrared spectroscopy, FTIR), or lab-based X-ray powder diffraction (XRD) and lab-based small angle X-ray scattering (SAXS) [6, 10, 15-17]. However, there has been on-going debate regarding the general limitations and validity of the results quantified by FTIR [6, 15, 16]. Lab-based XRD has been shown to be capable of showing the distinct differences in the response of HAp crystallites to heating between animal and human bone [6, 16, 18]. As a complementary method, lab-based SAXS allows the identification of local structural alterations at the nano-scale, and is also capable of a fast throughput of samples [19]. However, both methods usually involve the grinding of a sample into powder to obtain volume-averaged results that do not provide appropriately spatially resolved information on the local changes of skeletal ultrastructure within the tissue [19, 20]. In order to understand and quantify more precisely the mechanism of such ultrastructural alterations with temperature, the application of advanced non-destructive techniques offers an appropriate route. One of the most advanced non-destructive techniques is synchrotron based X-ray diffraction, namely, WAXS and SAXS. These methods have been used to characterise human dental tissues [21, 22], which enabled the characterisation of the ultrastructure of mineralized tissue using intact (not ground) samples, rather than powdered samples used with lab-based techniques.

Recently, the non-destructive synchrotron based techniques (WAXS/SAXS) have been applied to the study of previously thermally treated human dental tissues [9]. However, these tests were conducted *ex situ*, where it was possible to consider only a limited number of samples after exposure to temperatures in the range in 400°C -900°C. In addition, by necessity, different samples were used for each measurement and thus the sample-to-sample ultrastructure variation could not be excluded. This aspect may weaken the reliability of the conclusions drawn regarding the mechanism of local ultrastructural changes. Furthermore, the *ex situ* mode of sample characterisation is only applied after heating and cooling the samples to/from different temperatures. Obviously, no information is available on the structure evolution during heating, nor cooling. To the best of our knowledge no results have been reported on monitoring heat-induced ultrastructural changes of HAp crystallites using an *in situ* experimental protocol spanning the entire relevant range of heating and cooling, nor has the comparison been made between the naturally occurring HAp crystallites within human dental tissues and synthetic HAp powders. Thus *in situ* thermal measurement will help to understand the internal architecture of complex natural materials (highly mineralised human tissues), and its evolution during thermal exposure.

In this paper we report the evaluation of the crystallographic properties (*d*-spacing and crystal perfection and size) and the nano-structure (thickness, orientation and degree of alignment) of HAp crystallites embedded within the dental-tissue, as well as synthetic HAp powders subjected to *in situ* thermal treatment. The combination of synchrotron X-ray scattering techniques (WAXS/SAXS) was employed. The results were analysed in order to understand how the internal ultrastructure within the human dental tissues and the synthetic HAp powders evolves during the heating and cooling schedule.

2. Materials and methods

2.1. Sample preparation

Freshly extracted intact human third molars (ethical approval obtained from the National Research Ethics Committee; NHS-REC reference 09.H0405.33/ Consortium R&D No. 1465) were washed and cleaned in distilled water to eliminate residues so that the possibility of contamination or other chemical effects was excluded. The samples were cut into 1mm-thick cross-sectional slices in the bucco-lingual orientation including dentine and enamel (see Figure 1a) using a low speed diamond saw (Isomet Buehler Ltd., Lake Bluff, Illinois, USA) and polished using a sequence of grit papers to minimise the induced residual strain. In total, four cross-sections were prepared and were kept in distilled water in a commercial fridge at 4°C until the experiment was performed. Low temperature storage conditions ensured relatively low diffusion rates so as to impede or exclude any possibility of superficial demineralization effect of water.

A mould was filled with 100mg of commercially available HAp powder (Hydroxyapatite HTP powder, Bio-Rad, Hercules, CA, USA) and compacted with using an Instron 5544 machine (Instron Ltd., Bucks, United Kingdom) at 1.8kN force. The resulting disk was 1.2mm thick and 8 mm in diameter, with an approximate density of 1150 mg/cm^3.

The weight-loss over time was additionally evaluated using Thermogravimetry (TGA) at a rate of 12˚C/min using three cube-shaped dental samples (3×3×3mm) extracted from two molars. The weight fraction of the organic component was determined with TGA using one cubic dentine sample that was placed in a rotating 10% formic acid bath for 14 days to eliminate the mineral content, thus producing a purely organic sample.

2.2. In-situ scattering measurements

2.2.1. Thermal treatment setup

In situ thermal treatment of the samples was performed using a remotely operated and monitored furnace that allows collection of SAXS/WAXS data at temperatures up to 1000˚C. This furnace is a modification of the design used at Daresbury laboratory [23]. The samples were fixed in specially designed ceramic sample holders. A Kapton window in the furnace

allowed a high-energy X-ray transmission setup to be used, as illustrated in Figure 1a. The heating and cooling protocols were controlled using a Eurotherm controller. The protocols incorporated ramps at 12^{o}C/min, and constant temperature holds of 200 seconds for each temperature level within dental slice samples studied (enamel and dentine in Figure 1d). The protocol for synthetic HAp powders is also shown in Figure 1e. Slightly different thermal protocols were used for natural and synthetic materials due to the limitations of the experimental set-up (furnace heating rates accessible for different samples). However, preliminary measurements carried out showed that, within the range of heating rates considered, the resulting differences were negligible. The temperature output by the furnace controller and thermocouple was of high accuracy (one decimal point, approximately 0.1° nominal precision). Overall, the measurements were conducted at three different points in dentine, one measurement point in enamel and one point in the synthetic HAp sample. Larger number of data sets would improve the quality of data and provide better statistical information on data quality. However, due to the limited availability of synchrotron beamtime, the collection of additional datasets was not possible. The statistical error analysis of dentine has been included in the results, and is reported below.

2.2.2. Beamline experimental setup

The experiment was carried out on the I22 experimental beamline at Diamond Light Source, Oxford Harwell Campus, Didcot, UK. A monochromatic X-ray beam (photon energy of 18keV) was used to illuminate the samples with the beam size of 65×120μm^2 as illustrated schematically in Figure 1a. At each heating or cooling step, WAXS and SAXS patterns were simultaneously collected at consecutive heating and cooling increments at enamel and dentine or synthetic HAp crystallite across the specimens. A lightly compacted disk of NIST standard silicon powder was used for the WAXS data calibration and a disk of Silver Behenate (AgBe) powder was used for the SAXS data calibration [24].

WAXS diffraction patterns (Figure 1b) were recorded using a Pilatus 100K detector (Dectris, Baden, Switzerland) placed at a sample-to-camera distance of 275.55mm (Figure 1a). Further downstream of the beam a Pilatus 2M detector (Dectris, Baden, Switzerland) was

positioned at a distance of 2892mm to collect the SAXS patterns (Figure 1c). In order to record simultaneously the WAXS and SAXS patterns at each scanning location, the WAXS detector was titled and offset at 11.5^{o} to the incident beam.

2.3. X-ray scattering data analysis

2.3.1. WAXS data analysis

WAXS patterns appear graphically as separated rings with different widths and intensity levels, which contain characteristic information related to the crystalline structure. The analysis of WAXS patterns is performed using *Bragg's law*, which establishes the relationship between the spacing of atomic planes in crystals and the scattering angle at which these planes produce intense reflections.

$$n\lambda = 2d_{spacing}^{hkl} \sin\theta \quad \text{(Eq. 1)}$$

where λ is the wavelength, $d_{spacing}^{hkl}$ (*d-spacing*) is the interplanar distance between planes with *Miller indices* {*hkl*}, θ is one half of the scattering angle and *n* is the order of the reflection. Each peak corresponds to a certain family of lattice planes within a certain crystallographic phase. The changes of *d-spacing* could be utilized to examine the residual lattice strain and trace the phase transformation. Therefore, diffraction pattern analysis can be used to identify and quantify the crystallographic phases and structure parameters. The typical WAXS pattern is shown in Figure 1b can be used to extract and compare the crystallographic properties (e.g. degree of crystal perfection) between different samples or the same samples at different stages of its evolution [20].

In Figure 1b, the ring with the strongest intensity represents the diffraction from the (002) family of lattice planes. Moreover, the (002) lattice plane reflection is the most distinct ring that is reliably present in all three materials studied (dentine, enamel, synthetic HAp). WAXS data can be interpreted in terms of the shift of the diffraction peak obtained from a cluster of HAp crystallites. The variation of interplanar spacing (*d*-spacing) with respect to the temperature between the corresponding lattice planes was captured using WAXS. The (002) peak represents the orientation of the scattering vector along the hexagonal *c*-axis (parallel to

the long direction) within the HAp crystallites. It also corresponds to the organic fibril orientation due to the parallel orientation of fibrils to the long direction in HAp crystallites. The (002) peak is frequently used in determining the crystalline length in the bio-apatite and thus was chosen as the principal peak considered in the present study [25]. In detail, each 2D diffraction image was firstly pre-processed using Fit2D [26]. The (002) peak of interest from each pattern was "caked" (i.e. binned in the radial-azimuthal coordinates) within the range of 20^{o} in the y direction (Figure 1b). Subsequently the (002) peak was fitted with the Gaussian curve to obtain the peak centre position of $d_{spacing}^{002}$. Finite dimensions of the scattering volumes (crystallites) cause diffraction peak broadening that can be used to deduce the particle size. Diffraction peak width is related to the grain size (e.g. HAp crystallite) by the *Scherrer equation* that is widely used for the characterisation of heat-treated mineralised tissues [9, 10].

$$L = \frac{k\lambda}{B_{hkl}\cos\theta} \qquad \text{(Eq. 2)}$$

where L is the particle dimension in the direction of the {*hkl*} crystallographic plane normal, and B_{hkl} is the full-width at half maximum (FWHM) of the (*hkl*) peak. The (002) peak width is associated with the crystallite length and thus *L* deduced from the above equation of (002) peak could be used to estimate the average length of HAp crystallites [25]. The factor k is a constant related to the crystallite shape, while λ and θ have their usual meaning in *Bragg's law*. By monitoring the variation of FWHM during different heating-cooling procedures, the normalized length of the HAp crystallites was deduced.

2.3.2. SAXS data analysis

Quantitative interpretation of SAXS patterns provides insight into the mean thickness and degree of alignment of HAp crystallites. 2-D diffraction images were initially converted into 1-D intensity profiles and processed using Fit2D software package [26].

a) Mean thickness

In order to determine the mean crystal thickness, the scattering intensity $I(q,\varphi)$ was radially integrated around the entire range of the azimuthal angle φ to obtain the function $I(q)$, where q is the scattering vector. Based on *Porod's law*, which is valid in a two-phase system, the *Porod* chord length T is defined as:

$$T = \frac{4}{\pi}\frac{Q}{P} \qquad \text{(Eq. 3)}$$

where P is the *Porod* constant given by $I(q) = Pq^{-4}$ (*Porod's law* describes the decay of intensity for large values of q), and Q represents the integrated area under the $Iq^2 \sim q$ plot. Here T is used as the definition of the mean crystal thickness without any assumption of the particle shape. Based on this, the actual thickness of the crystals can be calculated by taking further factors (e.g. volume fraction) into account. The length (period) of the scattering objects forming phase 1 ($\bar{l}_1$) and of phase 2 ($\bar{l}_2$) in a two-phase system is defined as [27]

$$\bar{l}_1 = \frac{T}{(1-\varphi_1)} \quad \text{and} \quad \bar{l}_2 = \frac{T}{\varphi_1} \qquad \text{(Eq. 4)}$$

where φ_1 is the volume fraction of the scattering object. T can be interpreted as an average measure of the thickness and is close to the smaller dimension of the two phases. With the knowledge of φ_1, T can be used to deduce the thickness of the scattering objects, with $\bar{l}_1$ or $\bar{l}_2$ used as the guideline values for the mean thickness of crystallites.

b) Degree of alignment

The degree of alignment (ρ) of HAp crystallites (percentage of aligned particles) can also be determined from the SAXS patterns. It should be noted that for the enamel, due to the dense distribution of crystals, the shortest range electron density changes occur in the gaps between crystalline particles, giving rise to the scattering signal [28]. The high volume fraction of HAp crystallites in enamel implies highly aligned tight packing, so that the orientation of the gaps between HAp crystallites corresponds closely to that of the HAp

crystallites within the rods [28]. Thus, the information obtained from the value of ρ that describes the degree of alignment of the inter-crystallite gaps can be used to deduce the degree of alignment of HAp crystallites in enamel.

Figure 1c gives an example SAXS pattern of enamel at room temperature. In order to quantify the degree of alignment, SAXS patterns were integrated over all spanned scattering vectors *q*, resulting in a function $I(\varphi)$ that depends on the azimuthal angle φ [29, 30]. The degree of alignment was determined as the ratio of the peak area to the overall area under the curve of $I(\varphi)$, as has been explained and illustrated in previously published work [21]. The value of the degree of alignment ranges from 0 to 1, where $\rho = 0$ indicates no predominant orientation within the plane of the section (normal to the beam) and $\rho = 1$ indicates a perfect alignment of all crystallites [29, 30].

c) Scattering object analysis

The scattering contrast in SAXS arises mainly due to the fluctuation of electron density. The intensity of SAXS signal is proportional to the square of the difference of electron density between the scattering object(s), as well as the volume fraction of the scattering object(s) [27]

$$\bar{\eta} = (\rho_1 - \rho_2)^2 \varphi_1 (1 - \varphi_1) \qquad \text{(Eq. 5)}$$

where $\bar{\eta}$ is the mean square fluctuation of electron density, ρ_1 and ρ_2 are the electron densities of the two scattering phases, and φ_1 is the volume fraction of the scattering object(s) as defined in Eq. 4. According to the Babinet principle [27], in terms of scattering a system with a relatively low volume fraction of particles is equivalent to the dense system filled with particles but having the same volume fraction and arrangement of voids (i.e. the low density phase). In the former system, the particles act as scattering objects, whereas in the latter it is the voids.

3. Results

3.1. WAXS data

3.1.1. d-spacing variation

The thermally induced variation of *d*-spacing of HAp crystallites in human dentine and enamel samples is illustrated in Figures 2a & b. This is observed to be almost reversible during heating and cooling, although a visible drop at ~200^{o}C is seen in the plot for dentine. In contrast, the synthetic HAp powders display a distinct irreversible change of *d*-spacing (see Figure 2c).

3.1.2 Crystal perfection

The sharp diffraction peaks of the natural enamel and the synthetic HAp powders show very small changes during the heating process (Figures 2d & f). In contrast, the diffraction peaks of natural HAp crystallites in dentine are broad as shown in Figure 2e. Furthermore, it is obvious that the peaks start to split and sharpen as temperature increases, which indicates that the perfection increases remarkably during the heating, similar to the behaviour found in human bone [16, 20]. During cooling the degree of crystal perfection remained unchanged for all three materials. The peaks were indexed by reference to standard HAp patterns (JCPDS 9-432) [31].

3.1.3. Crystalline length

The interpretation of the (002) peak width provides information on the evolution of the crystallite length. Figures 3a-c demonstrate the variation of the normalized crystallite length of HAp crystallites in dentine and enamel and in synthetic HAp powders, with the value at the initial temperature serving as the reference (unity). Overall, not much change is observed in the HAp crystallite length in the enamel, although some oscillation is seen at medium temperatures (from ~300^{o}C to ~600^{o}C). In dentine, the HAp crystalline length remains almost constant until above ~600^{o}C. Upon further heating, a significant length increase occurs, followed by the size remaining almost constant during cooling. In synthetic HAp powders, however, an apparent change of crystallite length occurs above ~500^{o}C. The thermal history is

different from that in dentine, with the crystallite length continuing to grow even during the cooling process (see Figure 3c).

3.2. SAXS data

3.2.1. Scattering intensity and volume fraction variation

In the context of the Babinet principle, initially the scattering objects in the dentine and synthetic HAp polycrystalline samples are the HAp crystallites. In contrast, in the enamel, initially the scattering objects are the gaps between HAp crystallites filled with organic matter. However, due to the gradual denaturing and disappearance of the organic matrix as well as the accompanying process of crystal growth, the scattering objects in the dentine and HAp polycrystalline samples may also change to gaps. In order to verify the hypothesis that such change in the nature of the scattering objects in human dentine and synthetic HAp polycrystalline samples indeed takes place, the overall intensity variations from the SAXS patterns of the human dentine, enamel and synthetic HAp polycrystalline samples are plotted in Figures 4 a-c using open markers. The overall low intensity for the enamel sample indicates that the volume fraction of the scattering objects (gaps between crystallites) remains low. As for dentine and synthetic HAp crystallites, the observed large increase in the intensity coincides with the stage at which the HAp crystallites undergo fast growth, as reflected in the crystalline mean thickness plots in Figures 3 e and f.

Meanwhile, the volume fraction of the scattering objects, the HAp crystallites also increases until the transition temperature (~612^{o}C for dentine and ~745^{o}C for synthetic HAp powders). At this point the increased volume fraction of particles (and the reduced volume fraction of gaps) leads to the gaps between particles becoming the principal scattering objects, resulting in the dramatic decrease of intensity.

3.2.2. Crystalline mean thickness with constant volume fraction

The normalized crystallite mean thickness results for samples was calculated by SAXS interpretation using constant volume fraction of constituent phases (Figures 3d-f). During the heating process, a hump is observed in Figure 3e for dentine at ~300^{o}C. Upon further heating, the mean thickness starts to increase in the range from ~500^{o}C to ~700^{o}C. This is followed by

a slight decrease up to ~900°C. The mean thickness remains almost constant during cooling. The variation for the synthetic HAp powders (Figure 3f) is similar, but appears smoother compared with that of HAp crystallites in dentine (Figure 3e). Crystal growth in dentine appears to be faster than in the synthetic HAp powders. In addition, no obvious hump is observed at low temperature in the graph of the synthetic HAp powders (Figure 3f). As for the mean thickness variation of HAp crystallites in the enamel, a drop is visible at low temperature (Figure 3d). Beyond this drop, the overall variation is much smaller compared to the results for dentine and synthetic HAp crystallites.

3.2.3. Crystalline mean thickness with varied volume fraction

Based on the above analysis of the scattering objects, we postulate the variation of the volume fraction during heating and cooling as shown in Figure 4, starting with the initial volume fraction obtained by TGA analysis. The volume fraction is assumed to remain constant during cooling. Note that the dramatic changes of intensity observed are associated with the change of the principal scattering objects that occurs when the volume fraction passes 50%. By taking the volume fraction variation of HAp crystallites in dentine, enamel and the synthetic HAp polycrystalline sample into account, the updated results of the crystalline mean thickness based on Eq. 4 are shown in Figures 3 g-i.

3.2.4. Degree of alignment

Since the synthetic HAp powders were produced from powdered HAp crystallites, they show an orientation distribution that is close to random at all temperatures. Thus, only the evolution of the degree of alignment of HAp crystallites in dentine and enamel is presented (Figure 5). During heating, the overall degree of alignment of HAp crystallites decreases from 0.75 to 0.29 in the enamel, and from 0.17 to 0.05 in dentine. In more detail, in enamel the degree of alignment remains almost constant at very low (~0-100°C) and very high temperatures (~800-900°C), while an increase occurs above ~300-400°C, followed by the decrease up to ~800°C. Contrary to the result for the enamel, dentine exhibited a longer low temperature range (~0-300°C) with constant degree of alignment. Afterwards, the evolution follows a similar trend to that in the enamel, with an increase from ~300-400°C and a

decrease from ~400-800^{o}C. However, a more dramatic decrease occurred at ~800-900^{o}C compared with that in the enamel at the same temperature range. The degree of alignment remained unchanged during cooling.

3.3. TGA

Figure 6a shows the weight loss of dentine, enamel and the organic tooth sample (with most mineral content removed chemically) with increasing temperature. Two dramatic drops are visible in the pure organic tissue, at ~300^{o}C and ~650^{o}C respectively. Around 750^{o}C the organic phase in the tooth almost completely disappears. As for dentine and enamel, the weight loss is observed to be less significant than in the pure organic tooth tissue. A dramatic drop is still apparent at ~350^{o}C, and the rate of weight loss continues to decrease slowly at high temperature after ~750^{o}C. The initial weight fraction of HAp crystallites in dentine and enamel can be calculated by monitoring the weight remaining at 750^{o}C in dentine (70.3%) and enamel (95.8%), since the weight loss up to this temperature corresponds to that of water and the organic phase. Using the reported HAp density of 3.16 g/cm^{3} and the methods described in the literature [25], the initial volume fractions of HAp crystallites were calculated to be 45% (dentine) and 90% (enamel).

4. Discussion

The *in situ* thermal treatment in the current study revealed the complete history of the evolution of the ultrastructure of bio-apatite samples during a continuous heating-cooling schedule. In a previous *ex situ* study [9], only point-wise (in terms of temperature) and post-treatment data could be collected. This led to a fragmented and incomplete picture of the process. In comparison, the present study provides reliable information on the sample heating history and ultrastructural response, with the consistency between samples assured by a degree of cross-comparison, full coverage of the entire temperature range, and complete observation of the cooling procedure.

In general, SAXS patterns are more sensitive to the nano-scale structure, allowing the determination of the mean thickness of the crystallites by considering the scattering from two-phase systems [19]. The precise nature of the particles involved (e.g. amorphous vs. crystalline) is not important in this instance. In contrast, WAXS information is extracted from crystal lattice diffraction, and its clarity depends on the degree of perfection of the crystallites.

The principal outcome of quantitative analysis of SAXS and WAXS patterns was to reveal the temperature-dependent variation of the nano-structure (thickness, orientation and degree of alignment) of HAp crystallites, as well as the crystallographic properties (*d*-spacing, crystal perfection and length) variation during the heating and cooling processes. It is interesting to note how the observed evolution reflects the differences between dentine and enamel, and also the differences between the natural HAp crystallites embedded within organic matrix in human dental tissues, on the one hand, and synthetic HAp powders on the other. The role played by the organic matrix during heating is particularly important, as it turns out to govern the evolution of size and strain of HAp crystallites. It is also important to draw the conclusion that in order to evaluate the exposure temperature precisely (e.g. in forensic cases), enamel and dentine must be investigated separately: the analysis of the entire powdered tooth obscures the sharpness of ultrastructural variations in dentine and enamel [6, 32].

4.1. d-spacing variation

In the case of unconsolidated and unconstrained thermal expansion and contraction during heating and cooling, the *d*-spacing variation curves shown in Figures 2 a-c would be fully reversible. The observed difference between the heating-cooling curves in Figure 2 may arise due to the existence and relaxation or development of residual micro-stresses, and in conjunction with structural and compositional (e.g. phase) changes. The reduction in the lattice spacing that occurs in dentine at low temperature (see the curves in Figures 2a and b), is likely to be related to the changes that take place in the organic matrix in dentine. The changes that occur in this matrix during heating are illustrated by the schematic diagram in Figure 6b. At low temperatures the organic matrix expands (swells) more than the HAp crystallites due to its superior thermal expansion coefficient [33]. As a result, the HAp crystallites experience compression (as marked by the red arrow in Figure 6b) that reaches a maximum when the protein matrix begins to denature at ~200^{o}C. Above that temperature the protein matrix begins to burn off and gradually disappears with increasing temperature, which is consistent with the TGA plot in Figure 6a. In parallel with that the compression in the HAp crystallites becomes relieved and the crystallites experience additional expansion over and above the purely thermal strain.

Furthermore, it appears that the synthetic HAp powders experience a larger initial residual stress than HAp powders found in human dental tissue (see Figures 2 a-c). Such difference may be the consequence of two phenomena. Firstly, during sample preparation, a significant compressive stress was applied to the HAp powder to obtain powder disks with a similar density to the dentine tissue. In contrast, in the human dental tissue samples some residual stresses may have been relaxed during the cutting of slices. Secondly, in the synthetic HAp powders the appearance of a new phase is observed above 760^{o}C (β-TCP, tricalcium phosphate). Such decomposition of HAp crystallites to β-TCP has been reported [34]. The phase change leads to large and irreversible changes of the lattice parameters, providing an explanation of the considerable difference in the *d*-spacing traces during heating and cooling. It is noted that although the β-TCP has also been observed in dentine (900^{o}C) and enamel

(800^{o}C) as shown in Figure 2 d & e, its concentration is very low, and its effect on *d*-spacing variation can be ignored within the bounds of experimental accuracy, so that the curves appear reversible. The different transformation temperatures indicate an intrinsic difference in the characteristics between the bio-apatites (like the HAp crystallites in dentine and enamel) and the pure synthetic hydroxyapatites.

4.2. Crystal perfection

A high degree of crystal perfection is observed in the enamel and synthetic HAp crystallites compared to dentine, as shown in Figures 2d-f. The difference arises from the different micro-morphology of HAp crystallites between the three materials studied. The improved perfection (sharper and stronger peaks) in the dentine with increasing temperature (see Figure 2e) is due to the sintering of HAp crystallites that takes place at high temperatures (above ~800^{o}C). During the heating process, as the organic matrix is gradually burnt off, the interlayers of adjacent HAp crystallites disappear. Further heating leads to crystal growth and annealing of crystal defects, resulting in the significant peak sharpening. Further crystallization of the amorphous part observed in bone alteration [16, 20] may also contribute to this effect.

4.3. Degree of alignment

The overall reduction of the degree of alignment in enamel and dentine during heating may be associated with the polydisperse distribution of the particles associated with the changes of crystalline size or shape at high temperature [20]. The initial stage of constant degree of alignment observed both in the enamel (RT-100^{o}C) and dentine (RT-300^{o}C) in Figure 5b may correspond to the absence of crystallite rotation or growth. Once the organic matrix begins to denature, a slight increase in the degree of alignment is noted at ~300-400^{o}C for both dentine and enamel. Such increase corresponds to the gradual disappearance of the organic matrix accompanied by the relaxation of the residual strain. The greater reduction in the degree of alignment observed in dentine compared to enamel in the ~800-900^{o}C range reflects the difference in the composite structures. At very high temperatures the degree of alignment in the enamel remains high, due to the highly directional structure of long prismatic

HAp crystallites that remain aligned even after the organic matrix has been fully burnt off. In contrast, in dentine the disappearance of the large amount (~45% by volume) of organic matrix is likely to correspond to the loss of the supporting structure, causing the collapse and rearrangement of HAp crystallites that is associated with large rotation and anisotropic sintering.

4.4. Intensity variation

In the analysis of synchrotron-based SAXS data that has so far been reported in the literature, the volume fraction of HAp crystallites was always assumed to remain constant during heating [20]. However, the volume fraction in fact varies due to the burning off of the protein matrix, and the sintering of crystallites during heating (that influences the calculation of the mean crystallite thickness). The overall low intensity change indicates a small ultrastructural alteration, which may reflect the limited space for crystal expansion and growth within the enamel sample. The difference between the dentine sample and synthetic HAp powders is also reflected in the scattering behavior, where the comparatively lower value of intensity for dentine at low temperatures is likely to be associated with the presence of the protein matrix in dentine. Given the similar volume fractions of HAp crystallites in the two materials and close initial density values, the difference in the intensity is ascribed to the electron density contrast between the protein matrix and the crystals, which is smaller than that between gaps and the crystals (see Eq.5).

4.5. Crystallite size determined by SAXS/WAXS

Combined with the WAXS characterization on the length calculation of HAp crystallites, a schematic illustration of how the crystallite dimensions change in the dentine and enamel during heating is depicted in Figure 7. Two temperature ranges are identified based on the processes taking place in the organic matrix (the separation temperature is around 500^{o}C). As the organic phase gradually disappears, in “temperature range II”, crystal growth becomes unconstrained. Unlike the crystals in enamel, it is also observed that the crystallites in dentine gradually become misaligned, as indicated by the drop in the degree of alignment. Similar phenomena have been observed in ex-situ bone characterization [35].

It is interesting to observe that in the synthetic HAp powders, continued sintering takes place during high temperature hold and even continues during cooling. This is probably due to the fact that sintering is driven by the overall change in the free energy of the system [36].

5. Conclusions

The effects of *in situ* heat treatment on the hydroxyapatite (HAp) crystallites (human dental tissues) and synthetic HAp crystallites were explored using combined synchrotron based small/wide angle X-ray scattering (SAXS/WAXS) techniques. From the quantitative analysis of SAXS and WAXS patterns, multi-scale characterization of the hierarchical structure of enamel and dentine allows establishing the temperature-dependent variation of the nano-structural parameters (thickness, orientation and the degree of alignment) of HAp crystallites from SAXS and crystallographic properties (*d*-spacing, crystal perfection and length) from WAXS during the heating and cooling processes. The results generally reflect the difference between dentine and enamel, natural and synthetic HAp crystallites. In the analysis presented, the emphasis is placed on understanding the role of the organic matrix during heating. An important observation is made of the fact that the scattering object may change with the volume fraction variation of HAp crystallites during heating.

In conclusion, the synchrotron-based combined SAXS/WAXS analysis has been shown to be a powerful method for the determination of nano-structure variation induced by thermal treatment in human enamel and dentine, as well as in synthetic HAp crystallites. The *in situ* thermal treatment conducted in the present study covered the entire relevant temperature range and revealed the complete continuous history of ultrastructure evolution within a single sample during a continuous heating-cooling schedule. It was clearly demonstrated that insignificant structural changes occur during cooling, indicating that relevant conclusions can be drawn when dental remains samples are analysed as part of archaeological or forensic studies. The approach to the study of ultrastructural alteration in skeletal hard tissues exposed to *in situ* thermal treatment developed in the present study provides a better, more reliable basis for deducing the heating history compared with conventional methods based on the monitoring the macro- and microstructural colour [6, 7, 37]. Furthermore, it allows the

interaction between the mineral crystallites and the organic phase during heating to be captured. These advantages show the superior utility of *in situ* thermal treatment analysis over previous *ex situ* tests. Statistical error analysis of multiple measurement points in dentine confirmed the reliability of the conclusions drawn. The results of this work will also be beneficial to the optimization of the laser fluence used in dental practice, and in the future design of biomimetic materials.

Acknowledgement

AMK acknowledges the support of EPSRC through grants EP/I020691 "Multi-disciplinary Centre for In-situ Processing Studies (CIPS)", EP/G004676 "Micromechanical Modelling and Experimentation", and EP/H003215 "New Dimensions of Engineering Science at Large Facilities". Diamond Light Source is acknowledged for providing the beam time allocation under experiment number SM7981.

References

1. Marshall SJ, Balooch M, Habelitz S, Balooch G, Gallagher R, Marshall GW. 2003 The dentin-enamel junction - a natural, multilevel interface. *J Eur Ceram Soc*. **23**, 2897-2904. (Doi 10.1016/S0955-2219(03)00301-7)
2. Dorozhkin SV. 2010 Nanosized and nanocrystalline calcium orthophosphates. *Acta Biomater*. **6**, 715-734. (DOI 10.1016/j.actbio.2009.10.031)
3. Kantola S. 1973 Laser-Induced Effects on Tooth Structure .8. X-Ray-Diffraction Study of Dentin Exposed to a Co2-Laser. *Acta Odontol Scand*. **31**, 381-386. (Doi 10.3109/00016357309002525)
4. Fried D, Zuerlein MJ, Le CQ, Featherstone JDB. 2002 Thermal and chemical modification of dentin by 9-11-mu m CO2 laser pulses of 5-100-mu s duration. *Laser Surg Med*. **31**, 275-282. (Doi 10.1002/Lsm.10100)
5. Zuerlein MJ, Fried D, Featherstone JDB. 1999 Modeling the modification depth of carbon dioxide laser-treated dental enamel. *Laser Surg Med*. **25**, 335-347. (Doi 10.1002/(Sici)1096-9101(1999)25:4<335::Aid-Lsm8>3.0.Co;2-F)
6. Piga G, Thompson TJU, Malgosa A, Enzo S. 2009 The Potential of X-Ray Diffraction in the Analysis of Burned Remains from Forensic Contexts. *J Forensic Sci*. **54**, 534-539. (DOI 10.1111/j.1556-4029.2009.01037.x)
7. Thompson TJU. 2005 Heat-induced dimensional changes in bone and their consequences for forensic anthropology. *J Forensic Sci*. **50**, 1008-1015.
8. Thompson TJU, Islam M, Piduru K, Marcel A. 2011 An investigation into the internal and external variables acting on crystallinity index using Fourier Transform Infrared Spectroscopy on unaltered and burned bone. *Palaeogeogr Palaeocl*. **299**, 168-174. (DOI 10.1016/j.palaeo.2010.10.044)
9. Sandholzer MA, Sui T, Korsunsky AM, Walmsley AD, Lumley PJ, Landini G. 2014 X-ray scattering evaluation of ultrastructural changes of human dental tissues with thermal treatment.
10. Shipman P, Foster G, Schoeninger M. 1984 Burnt Bones and Teeth - an Experimental-Study of Color, Morphology, Crystal-Structure and Shrinkage. *J Archaeol Sci*. **11**, 307-325. (Doi 10.1016/0305-4403(84)90013-X)
11. Enzo S, Bazzoni M, Mazzarello V, Piga G, Bandiera P, Melis P. 2007 A study by thermal treatment and X-ray powder diffraction on burnt fragmented bones from tombs II, IV and IX belonging to the hypogeic necropolis of "Sa Figu" near Ittiri, Sassari (Sardinia, Italy). *J Archaeol Sci*. **34**, 1731-1737. (DOI 10.1016/j.jas.2006.12.011)
12. Rogers KD, Daniels P. 2002 An X-ray diffraction study of the effects of heat treatment on bone mineral microstructure. *Biomaterials*. **23**, 2577-2585. (Pii S0142-9612(01)00395-7; Doi 10.1016/S0142-9612(01)00395-7)
13. Beckett S, Rogers KD, Clement JG. 2011 Inter-Species Variation in Bone Mineral Behavior upon Heating. *J Forensic Sci*. **56**, 571-579. (DOI 10.1111/j.1556-4029.2010.01690.x)
14. Reyes-Gasga J, Garcia-Garcia R, Arellano-Jimenez MJ, Sanchez-Pastenes E, Tiznado-Orozco GE, Gil-Chavarria IM, et al. 2008 Structural and thermal behaviour of human tooth and three synthetic hydroxyapatites from 20 to 600 degrees C. *J Phys D Appl Phys*. **41**. (Artn 225407; Doi 10.1088/0022-3727/41/22/225407)
15. Hollund HI, Ariese F, Fernandes R, Jans MME, Kars H. 2013 Testing an Alternative High-Throughput Tool for Investigating Bone Diagenesis: Ftir in Attenuated Total Reflection (Atr) Mode. *Archaeometry*. **55**, 507-532.
16. Rogers K, Beckett S, Kuhn S, Chamberlain A, Clement J. 2010 Contrasting the crystallinity indicators of heated and diagenetically altered bone mineral. *Palaeogeogr Palaeocl*. **296**, 125-129. (DOI 10.1016/j.palaeo.2010.06.021)
17. Squires KE, Thompson TJU, Islam M, Chamberlain A. 2011 The application of histomorphometry and Fourier Transform Infrared Spectroscopy to the analysis of early Anglo-Saxon burned bone. *J Archaeol Sci*. **38**, 2399-2409.

18. Piga G, Malgosa A, Thompson TJU, Enzo S. 2008 A new calibration of the XRD technique for the study of archaeological burned human remains. *J Archaeol Sci*. **35**, 2171-2178.
19. Hiller JC, Wess TJ. 2006 The use of small-angle X-ray scattering to study archaeological and experimentally altered bone. *J Archaeol Sci*. **33**, 560-572.
20. Hiller JC, Thompson TJ, Evison MP, Chamberlain AT, Wess TJ. 2003 Bone mineral change during experimental heating: an X-ray scattering investigation. *Biomaterials*. **24**, 5091-5097. (S0142961203004277 [pii])
21. Sui T, Sandholzer MA, Baimpas N, Dolbnya IP, Walmsley AD, Lumley PJ, et al. 2013 Multi-scale modelling and diffraction-based characterization of elastic behaviour of human dentine. *Acta Biomater*. **9**, 7937-7947. (DOI 10.1016/j.actbio.2013.04.020)
22. Sui T, Sandholzer MA, Baimpas N, Dolbnya IP, Landini G, Korsunsky AM. 2013 Hierarchical modelling of elastic behaviour of human enamel based on synchrotron diffraction characterization. *J Struct Biol*. **In press**. (DOI 10.1016/j.jsb.2013.09.023)
23. Dent AJ, Greaves GN, Roberts MA, Sankar G, Wright PA, Jones RH, et al. 1995 A New Furnace Design for Use in Combined X-Ray-Absorption and Diffraction of Catalysis and Ceramics Studies - Formation from Carbonate Precursors of Cu, Co, Mn Spinels for the Oxidation of Co and the Formation of Plzt, a Piezoelectric Ceramic. *Nucl Instrum Meth B*. **97**, 20-22. (Doi 10.1016/0168-583x(94)00369-6)
24. Calibration DLS. 2013 Diamond Light Source Calibration.
25. Deymier-Black AC, Almer JD, Stock SR, Haeffner DR, Dunand DC. 2010 Synchrotron X-ray diffraction study of load partitioning during elastic deformation of bovine dentin. *Acta Biomater*. **6**, 2172-2180. (DOI 10.1016/j.actbio.2009.11.017)
26. Hammersley AP. "FIT2D: An Introduction and Overview". ESRF Internal Report1997.
27. Glatter O, Kratky O. 1982 *Small angle x-ray scattering*. London ; New York: Academic Press.
28. Tanaka T, Yagi N, Ohta T, Matsuo Y, Terada H, Kamasaka K, et al. 2010 Evaluation of the Distribution and Orientation of Remineralized Enamel Crystallites in Subsurface Lesions by X-Ray Diffraction. *Caries Res*. **44**, 253-259. (Doi 10.1159/000314672)
29. Tesch W, Vandenbos T, Roschgr P, Fratzl-Zelman N, Klaushofer K, Beertsen W, et al. 2003 Orientation of mineral crystallites and mineral density during skeletal development in mice deficient in tissue nonspecific alkaline phosphatase. *J Bone Miner Res*. **18**, 117-125. (DOI 10.1359/jbmr.2003.18.1.117)
30. Tesch W, Eidelman N, Roschger P, Goldenberg F, Klaushofer K, Fratzl P. 2001 Graded microstructure and mechanical properties of human crown dentin. *Calcified Tissue Int*. **69**, 147-157. (DOI 10.1007/s00223-001-2012-z)
31. Ooi CY, Hamdi M, Ramesh S. 2007 Properties of hydroxyapatite produced by annealing of bovine bone. *Ceram Int*. **33**, 1171-1177.
32. Kugler M. 2003 X-ray diffraction analysis in forensic science: the last resort in many criminal cases. *Advances in X-ray Analysis*. **46**.
33. Lei HJ, Liu B, Fang DN. 2010 The coefficient of thermal expansion of biomimetic composite. *Front Mater Sci China*. **4**, 234-238.
34. Elliott JC. 1994 *Structure and chemistry of the apatites and other calcium orthophosphates*. Amsterdam ; London: Elsevier.
35. Pramanik S, Hanif ASM, Pingguan-Murphy B, Abu Osman NA. 2013 Morphological Change of Heat Treated Bovine Bone: A Comparative Study. *Materials*. **6**, 65-75. (Doi 10.3390/Ma6010065)
36. Kingery WD, Bowen HK, Uhlmann DR. 1976 *Introduction to ceramics*. 2nd ed. New York ; London: Wiley.
37. Thompson TJU, Islam M, Bonniere M. 2013 A new statistical approach for determining the crystallinity of heat-altered bone mineral from FTIR spectra. *J Archaeol Sci*. **40**, 416-422. (DOI 10.1016/j.jas.2012.07.008)

Figures

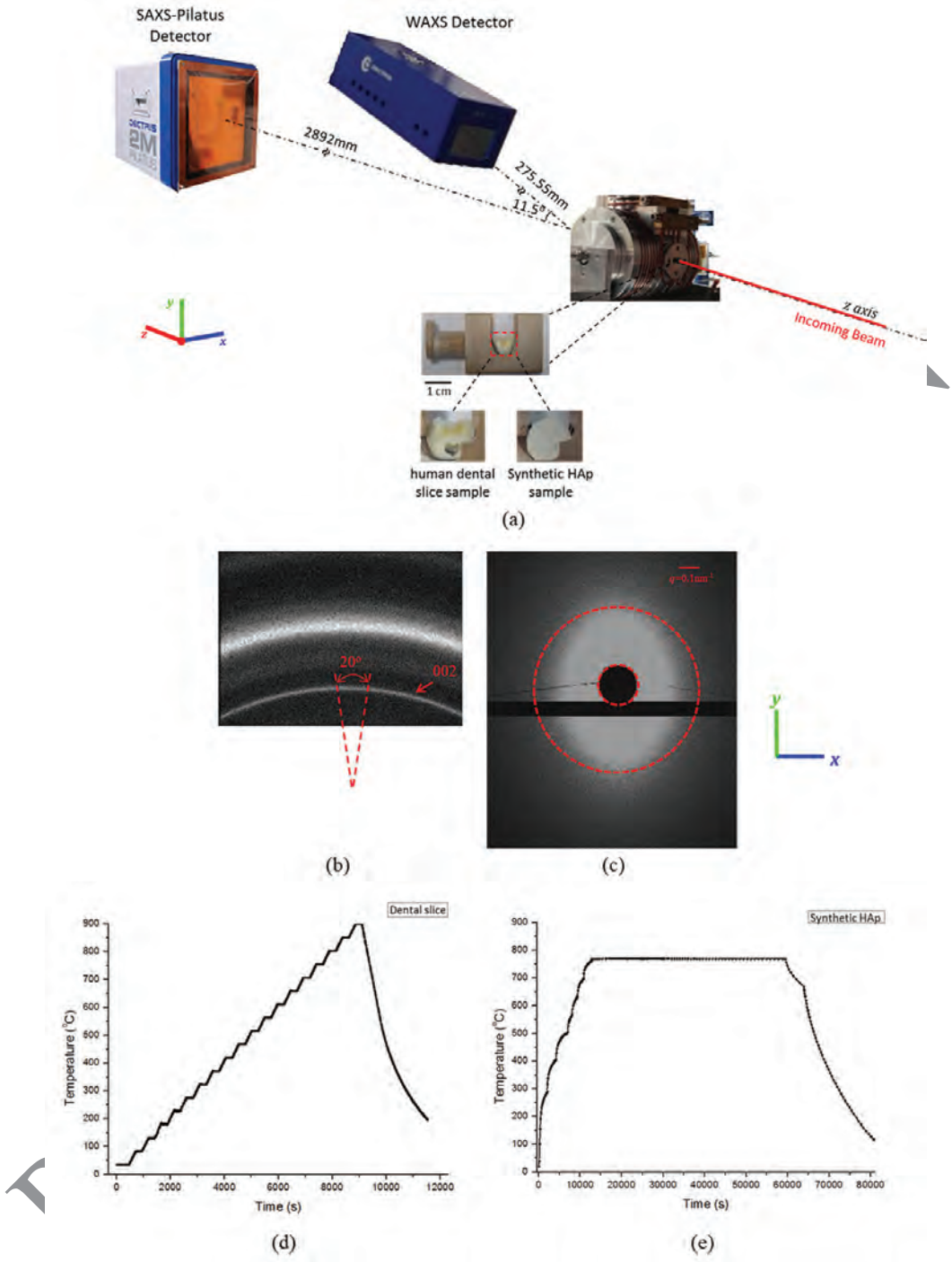

Figure 1

(a) Schematic illustration of the *in situ* SAXS/WAXS experimental set-up that ensured that the WAXS and SAXS patterns were collected simultaneously. (b) A representative WAXS pattern showing the Debye-Sherrer ring corresponding to the (002) peak indicated by the red arrow. On the ring, the section along the y-axis in (a) was "caked" (see text) with a 20^{o} range in order to capture the peak shift upon heating and cooling process. (c) A representative SAXS pattern. The dark region in the middle is the beamstop. The ellipsoidal shape of the pattern indicates a partial alignment of HAp crystallites. The pattern for randomly distributed crystals is a round disc with the outline marked with red dashed circle. (d) and (e) illustrate the different heating and cooling protocols used for the human dental slice samples and the synthetic HAp powders sample.

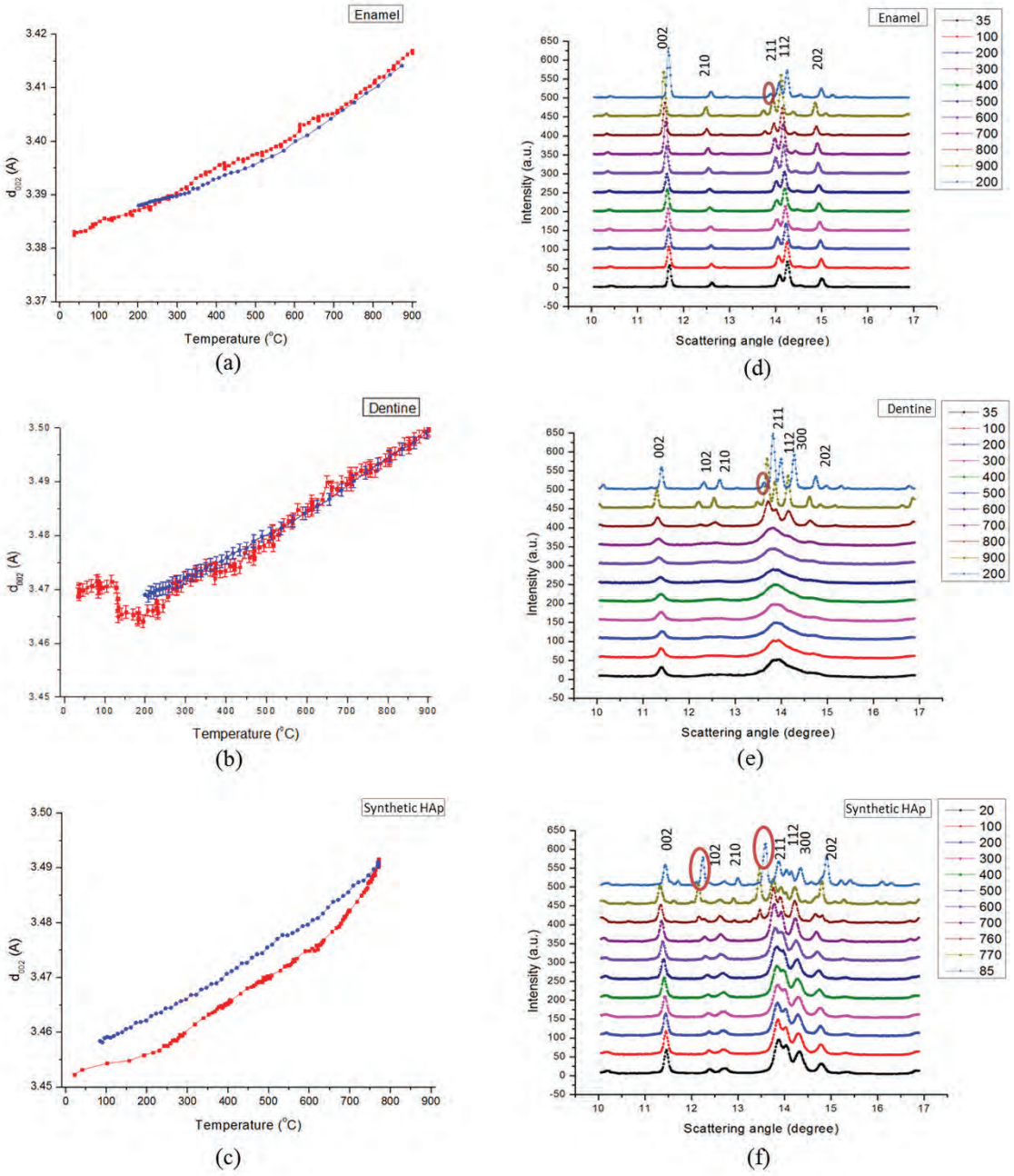

Figure 2

(a)-(c) The changes in the d_{002}-spacing of HAp crystallites in enamel, dentine and synthetic HAp powders samples, respectively, during heating and cooling stages (heating: red points; cooling: blue points). Intensity variation upon heating and cooling, caused by (d) HAp crystallites in enamel; (e) HAp crystallites in dentine and (f) synthetic HAp powders. The red marks in (f) indicate the occurrence of two new peaks.

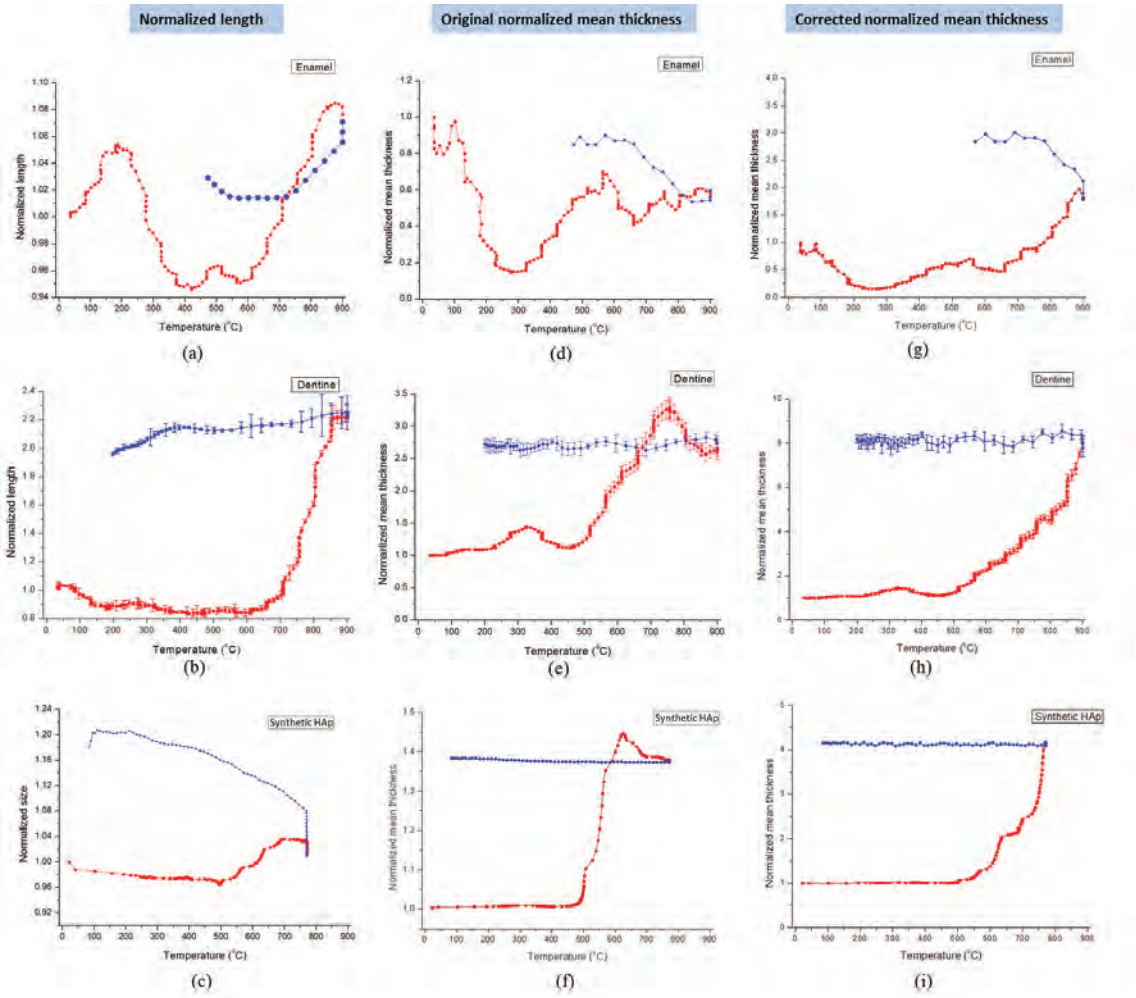

Figure 3

(a)-(c) The variation of the normalized length of HAp crystallites in human enamel, dentine and synthetic HAp powders (red points for heating and blue points for cooling). (d)-(f) The normalized mean thickness (with constant volume fraction) of HAp crystallites in enamel, dentine and synthetic HAp powders. (g)-(i) The normalized mean thickness accounting for the mineral volume fraction variation of HAp crystallites in enamel, dentine and synthetic HAp powders.

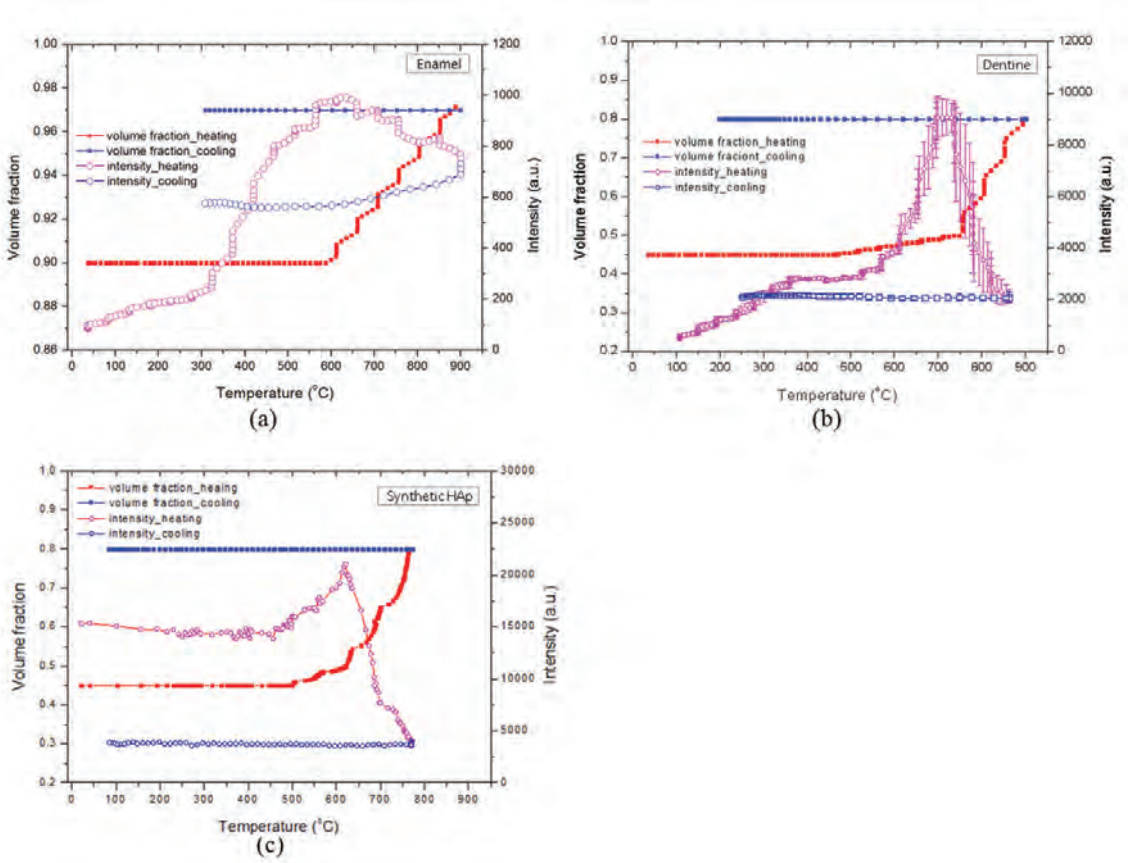

Figure 4

The correlation of the peak intensity variation from SAXS patterns with the mineral volume fraction for (a) human enamel (b) human dentine and (c) synthetic HAp powders. Open purple markers (heating) and open blue markers (cooling) in (a)-(c) represent the results obtained from constant mineral volume fraction, while the red points (heating) and blue points (cooling) in (a)-(c) correspond to the results obtained with the variation of mineral volume fraction taken into account.

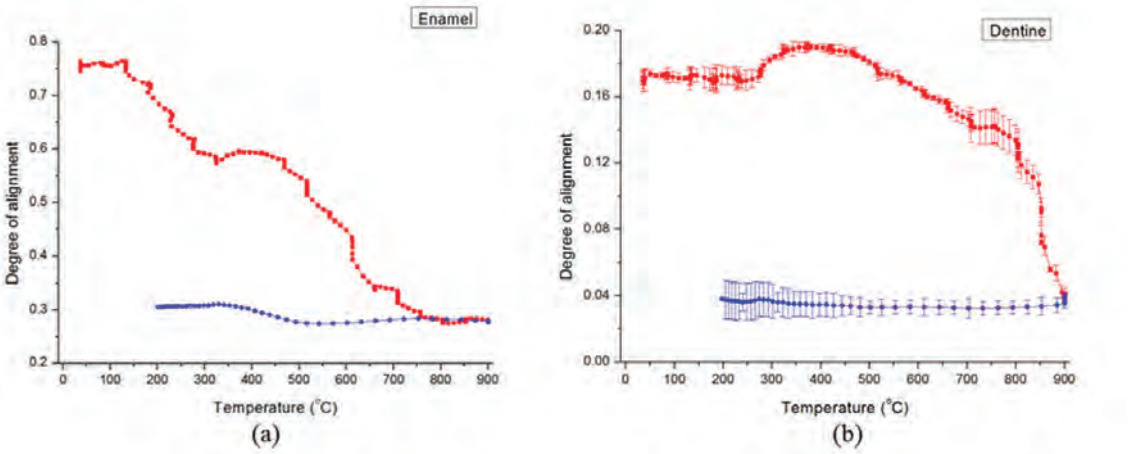

Figure 5

The variation of the degree of alignment of HAp crystallites upon heating/cooling in (a) human enamel and (b) human dentine (red points for heating and blue points for cooling).

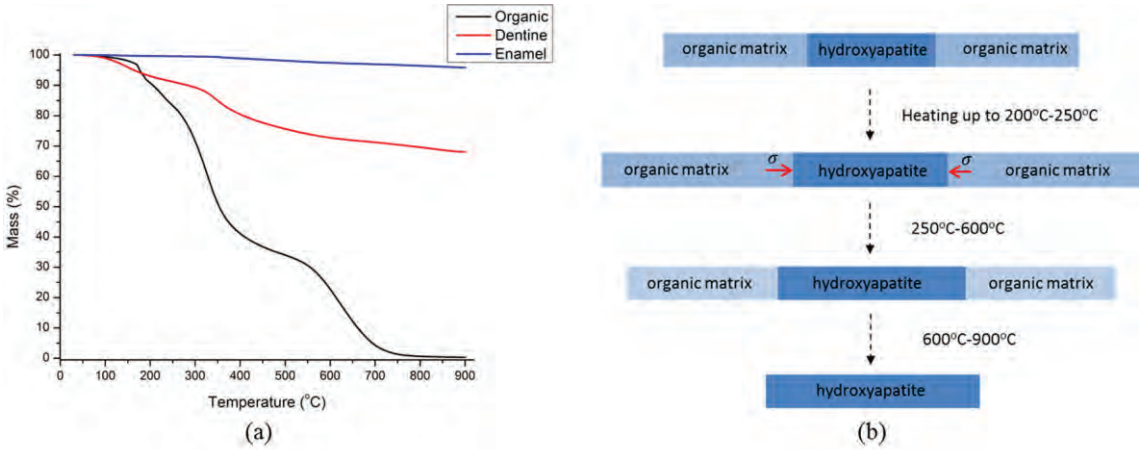

Figure 6

(a) TGA plot of weight loss of dental tissues: pure organic tooth with the inorganic content removed (black line), dentine (red line) and enamel (blue line). (b) A schematic diagram of the ultrastructural alteration of organic matrix and HAp crystallites in human dentine upon heating. The process begins with the superior thermal expansion of the organic matrix compared with the HAp crystallites, resulting in compression of HAp during heating (red arrow). The compression will relaxes gradually as the organic matrix begins to denature and burn off, leading to the additional expansion in the HAp crystallites in excess of the pure thermal strain.

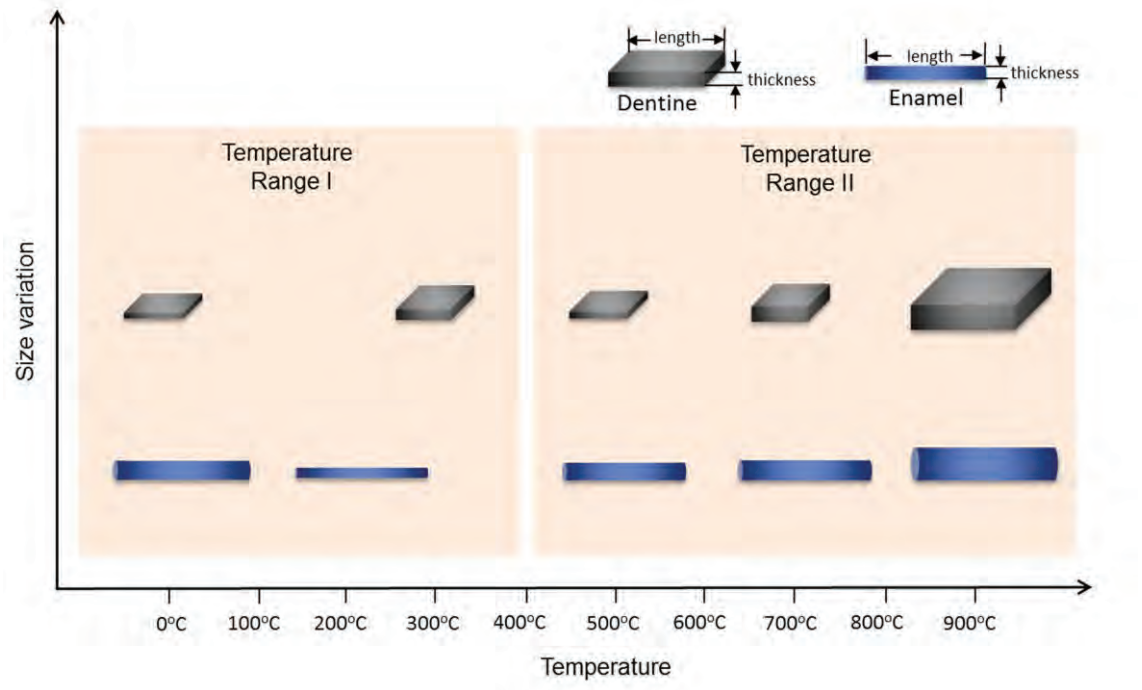

Figure 7

A schematic illustration of the size variation of HAp crystals within human enamel and dentine upon heating. The crystals in enamel are needle-shaped while those in dentine are platelet-shaped. In temperature range I, the interaction between crystals and the protein matrix occurs, while in temperature range II, the protein matrix gradually disappears and the interaction is weakened.

Acta Biomaterialia 10 (2014) 343–354

Contents lists available at ScienceDirect

Acta Biomaterialia

journal homepage: www.elsevier.com/locate/actabiomat

Hierarchical modelling of in situ elastic deformation of human enamel based on photoelastic and diffraction analysis of stresses and strains

Tan Sui [a,*], Alexander J.G. Lunt [a], Nikolaos Baimpas [a], Michael A. Sandholzer [b], Jianan Hu [a], Igor P. Dolbnya [c], Gabriel Landini [b], Alexander M. Korsunsky [a]

[a] Department of Engineering Science, University of Oxford, Parks Road, Oxford OX1 3PJ, UK
[b] School of Dentistry, College of Medical and Dental Sciences, University of Birmingham, St Chad's Queensway, Birmingham B4 6NN, UK
[c] Beamline B16, Diamond Light Source, Harwell Oxford Campus, Didcot OX11 0DE, UK

ARTICLE INFO

Article history:
Received 27 May 2013
Received in revised form 25 September 2013
Accepted 30 September 2013
Available online 9 October 2013

Keywords:
Enamel
WAXS
Photoelasticity
Mechanical behaviours
Eshelby model

ABSTRACT

Human enamel is a typical hierarchical mineralized tissue with a two-level composite structure. To date, few studies have focused on how the mechanical behaviour of this tissue is affected by both the rod orientation at the microscale and the preferred orientation of mineral crystallites at the nanoscale. In this study, wide-angle X-ray scattering was used to determine the internal lattice strain response of human enamel samples (with differing rod directions) as a function of in situ uniaxial compressive loading. Quantitative stress distribution evaluation in the birefringent mounting epoxy was performed in parallel using photoelastic techniques. The resulting experimental data was analysed using an advanced multiscale Eshelby inclusion model that takes into account the two-level hierarchical structure of human enamel, and reflects the differing rod directions and orientation distributions of hydroxyapatite crystals. The achieved satisfactory agreement between the model and the experimental data, in terms of the values of multidirectional strain components under the action of differently orientated loads, suggests that the multiscale approach captures reasonably successfully the structure–property relationship between the hierarchical architecture of human enamel and its response to the applied forces. This novel and systematic approach can be used to improve the interpretation of the mechanical properties of enamel, as well as of the textured hierarchical biomaterials in general.

1. Introduction

The increasing need to understand and predict the effect of structural alterations on the performance of dental tissues and their artificial replacements arises both in the context of clinical treatment, and the development of novel dental prosthetic materials [1]. The elucidation of the dependence of the mechanical behaviour of human enamel on its complex hierarchical structure remains a challenging task. Two different length scales dominate the structure and the mechanical behaviour of the enamel: At the microscale, ~5 μm diameter keyhole-like cross-section aligned prisms (or rods) are oriented towards the crown of the tooth [2]. At the nanoscale level, the rod is known to be a composite made from needle-like biological hydroxyapatite (HAp) crystals (~25–30 nm thick and of length known to be more than 1000 nm, or even spanning the entire thickness of the enamel layer) [3,4], which are held together by the protein matrix between the rods [5–7]. The orientation of HAp needle-like crystals within the rod is known to be a gradual variation on the length scale of the rod diameter [8,9].

The focus of most research to date has been on the mechanical properties of the enamel at the macroscale, with microstructural effects rarely taken into account [2,10]. Very few studies have focused on the multiscale analyses required to determine the influence of the nanoscale structure on the macroscopic mechanical response [11]. In fact, both the crystal shape and orientation of the mineral phase nanocrystals have previously been shown to have an effect on the anisotropy of overall stiffness and strength [12]. Therefore, in order to establish a firm understanding of this hierarchical structure–property relationship, further application of advanced nanoscale techniques and the formulation and refinement of systematic models are required.

Synchrotron-based wide-angle X-ray scattering (WAXS) is a non-destructive analytical technique used to quantify the internal strain of atomic lattices on (poly)crystals, both residually stressed and subjected to external loading in situ [13,14]. In addition, WAXS techniques are able to reveal quantitative information about the orientation distribution of crystals (texture) [15]. For example, recent applications of WAXS include the determination of the

* Corresponding author. Tel.: +44 18652 83447; fax: +44 18652 73010.
E-mail address: tan.sui@eng.ox.ac.uk (T. Sui).

1742-7061/$ - see front matter © 2013 Acta Materialia Inc. Published by Elsevier Ltd. All rights reserved.
http://dx.doi.org/10.1016/j.actbio.2013.09.043

mechanical behaviour of mineralized biological composites such as bone and bovine teeth [14,16–18] while simultaneously providing insight into the crystallographic parameters and textures of such materials [8]. The strain distribution across the amelo-dentinal junction (ADJ) in bovine teeth was investigated by Almer and Stock [16]. However, this was limited to the strain in the loading direction [16,19]. In practice, the external mastication load is not perfectly aligned with the longitudinal direction due to the complex tooth geometries (e.g. on transverse ridges and cusps in first molars), and also due to the local orientation variation of HAp crystals within the rods. Therefore, the analysis of the relationship between the orientation of the applied load and strain needs to be sought. Moreover, the studies reported earlier did not take into account the nanoparticle distribution effect on the mechanical response. In addition, very few studies devoted to human enamel have ever been published [20]. It is therefore unsurprising that there is a lack of understanding of the effects of different growth histories, species or race on the mineralized tissue morphology, and the corresponding mechanical properties [21].

In order to carry out the in situ mechanical loading experiments in a versatile manner, i.e. allowing different directions of loading with respect to the preferred directions of structural orientation within the tissue, the sample was embedded in a photoelastic epoxy disk. The enamel cubes studied in our preliminary experiments could not withstand high external load applied by direct compression between the platens. Without the protection of the epoxy disk, samples were likely to develop local stress concentrations and/or microcracks that reduce the accuracy of measuring the mechanical behaviour of enamel. Furthermore, due to its birefringent properties, epoxy offers the possibility of deducing information about the stress distribution around the sample using photoelastic techniques. Photoelasticity is a non-destructive, whole-field method widely applied in stress distribution analysis. The fringe pattern arises when the sample is viewed between crossed polarizing plates, with the colour or brightness of the fringe being related to the difference between the principal stresses, which is in turn proportional to the maximum shear stress, or Tresca stress, in the material [22]. We combine the photoelastic analysis technique with WAXS analysis during in situ loading in order to establish the relationship between the external stress distribution and the internal crystal lattice strain.

A number of different models of composite deformation have been previously used to describe the elastic response of mineralized biological tissues that arises through the interaction between different constituent phases [11]. This approach also allowed the unknown properties of the component phases to be determined [23]. However, these models mainly focused on the analysis of deformation in only one direction (loading direction) and therefore were not able to provide adequate consideration of the elastic anisotropy. Recently, a multiscale Eshelby inclusion model has been established and successfully applied for the evaluation of the mechanical response of human dentine [12] and of the enamel subjected to compression along the longitudinal direction of the rods [19] by capturing the relationship between the nanoscale structure and the macroscopic loading. The multiscale modelling approach was shown to capture the micromechanical response reasonably well using the two-level hierarchical description of the structure of dentine and enamel, with each level consisting of an isotropic matrix and a group of anisotropic inclusions.

In this study, in situ photoelasticity and synchrotron WAXS techniques were applied simultaneously to measure the applied stress, the internal HAp crystalline orientation distribution and the elastic lattice strain for three samples of human enamel. The samples were prepared so that the primary rod direction was at a different orientation with respect to the external compressive loading that was applied diametrically to the epoxy disk containing the tissue sample (see Fig. 1). The multiscale Eshelby inclusion model was then applied to the analysis of the results, and the capability of the model to capture the relationship between the nanoscale structure and macroscopic loading was investigated.

2. Materials and methods

2.1. Sample preparation

Freshly extracted human third molars with no apparent damage, caries or other dental treatments were used for this study (ethical approval obtained from the National Research Ethics Committee; NHS-REC reference 09.H0405.33/Consortium R&D No. 1465). An enamel disk 2 mm thick was cut from the each tooth using a low-speed diamond saw (Isomet Buehler Ltd., Lake Bluff, IL, USA) and further prepared into smaller bars. A series of polishing papers were used to refine the final 2 mm × 2 mm × 2 mm cube of enamel. The cubes were placed in the centre of a 12 mm diameter cylindrical mould and embedded in epoxy resin (Buehler Epokwick, ITW Test & Measurement GmbH, Dusseldorf, Germany). The disks' surfaces were subsequently polished to expose the enamel surfaces.

In total, the three cubic enamel samples were prepared (designated #6, #7 and #3) with different rod directions with respect to the loading direction (x-direction in Fig. 1a). The predominant direction of rods in sample #6 was parallel to the loading direction with rods lying in the x–y plane, in sample #7 it was perpendicular to the loading direction with rods lying in the x–y plane, and in sample #3 it was perpendicular to the loading direction with rods lying in the y–z plane.

2.2. In situ X-ray diffraction measurements

2.2.1. Photoelasticity setup

A Sharples S-12 demonstration polariscope was used to collect the in situ photoelastic images. The setup consisted of light source, polarizers, quarter-wave plates and a digital SLR camera as shown in Fig. 1. The quarter-wave plates remained crossed and polarizers were aligned crossed to establish the dark field. A green-light filter was also placed between the light source and the camera lens in order to obtain monochromatic fringes to simplify the analysis. A solid epoxy disk (without the sample in the centre) produced from the same batch of epoxy resin was used as a common calibration specimen.

2.2.2. Mechanical loading setup

A schematic diagram of the experimental setup is shown in Fig. 1a. The epoxy disk which contained the cubic sample of human enamel was slowly deformed along the x-direction in laboratory coordinates (Fig. 1a). Compressive loading was applied along the x-direction at the load levels from 0 to 400 N using a remotely operated and monitored compression rig (Deben, Suffolk, UK) with a 5 kN calibrated load cell. The rig was equipped with custom-made jaws, allowing a high-energy transmission X-ray setup to be used. The load was incrementally increased (in 25 N steps and a loading rate of 3.8 N s^{-1}) and held constant while the WAXS and photoelastic patterns were collected.

2.2.3. Beamline diffraction setup

The experiment was performed on the B16 test beamline at Diamond Light Source (DLS, Oxford, UK). A monochromatic X-ray beam of 20 keV photon energy (wavelength: $\lambda = 0.062$ nm) was collimated by slits to a spot size of 0.5 mm × 0.5 mm. Radiographic images of the samples were initially used to align the samples and determine the position of interest. The incident beam on the

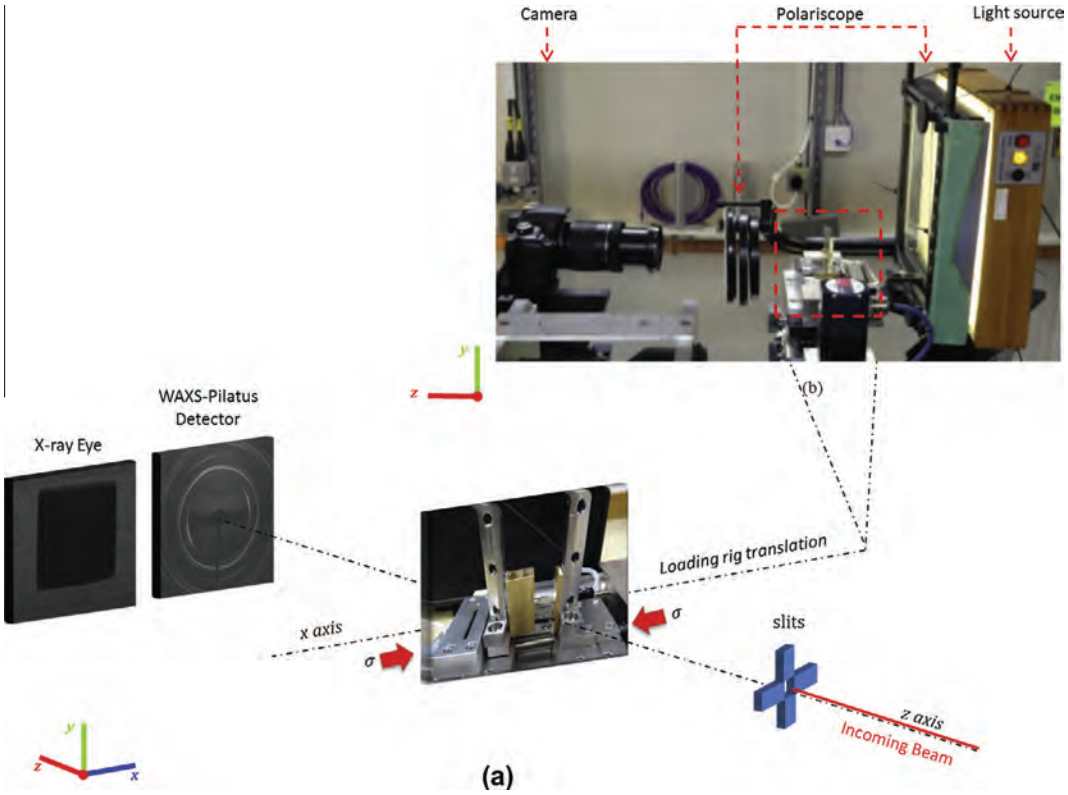

Fig. 1. Schematic diagram of the experimental setup composed of (a) synchrotron beam setup and (b) photoelastic setup. The sample was subjected to uniaxial compressive loading on the compression stage along the *x* direction. The monochromatic X-ray beam was collimated by slits and oriented perpendicular to the sample surface and the loading direction. An X-ray eye detector was used to ensure that the beam was illuminating the cetral position of the enamel specimen. At each detection point, following centring, the X-ray eye detector was translated laterally out of the beam to expose the WAXS detector. WAXS diffraction patterns were recorded at each loading step in three locations on the sample. After each WAXS pattern collection, the compression stage was laterally translated to the photoelastic setup to collect the photoelastic patterns.

sample was perpendicular to the loading direction. Space restrictions of the beamline meant that the sample had to be translated laterally from the WAXS configuration into the photoelastic setup at each consecutive loading increment. WAXS diffraction patterns were recorded using a Photonic Science Image Star 9000 detector (Photonic Science Ltd., UK) which was placed 177.33 mm downstream of the sample. A lightly compacted disk of NIST standard silicon powder was used for precise calibration of the sample-to-detector distance using diffraction pattern analysis [24].

2.3. Data analysis

2.3.1. Photoelasticity data analysis [22]

The use of a diametrically loaded disk is a standard calibration technique which can be used either to obtain the photoelastic properties of the birefringent material, or to determine the calibration constants if these properties are known. The fringe constant of the material is defined as:

$$f = \frac{8}{\pi D}\frac{P}{N_1}, \tag{1}$$

where D is the diameter of the epoxy disk (12 mm), N_1 is the number of fringes for the calibration sample and P is the applied load (N). In order to obtain an estimate for f, a series of known loads was applied to an empty epoxy disk and the corresponding fringe numbers recorded. An average value for f was then determined by taking the mean of the f term calculated at each load.

The stress distribution in the disk is characterized in terms of the difference between the principal stresses (or Tresca shear stress) using the following expression:

$$\sigma_2 - \sigma_1 = N_2\frac{f}{h}, \tag{2}$$

where h is the thickness of epoxy (2 mm), and N_2 is the number of fringes for the sample of interest. The deformation state of the plate-shaped epoxy corresponds closely to the plane stress state approximation in two-dimensional photoelasticity. Since the loading was applied along the x-axis, with the epoxy disk lying in the x–y plane, the principal stresses were $\sigma_1 < 0$, $\sigma_2 > 0$ and $\sigma_3 = 0$.

2.3.2. WAXS data analysis

WAXS analysis relies on interpreting the shift of the diffraction peaks obtained from a bundle of HAp crystals, so that the average lattice strain in the crystals can be deduced [13,25]. Typical WAXS patterns of HAp are shown in Fig. 2a–c and only the peaks of interest were selected for interpretation (#6 (002) peak, #7 (002) peak and #3 (210) peak). For samples #6 and #7, the (002) lattice plane reflection ring from HAp contains information on the orientation of the *c*-axis of the crystals as well as the fibril orientation. This is due to the fact that the enamel structure has a characteristic strong and distinct parallel orientation of needle-shaped crystals [14]. For sample #3 the *c*-axes of the crystals lie perpendicular to the measurement plane, so that the (002) peak is absent or weak. Therefore, another peak (210) needed to be selected. At each compressive loading step, the X-ray eye detector was used to verify the central position. The Deben compression rig applied the load by displacing the two platens in a balanced way, so as to preserve the centre position approximately stationary. This ensured that a consistent sample position in the centre of the sample was interrogated throughout the WAXS data collection. The elastic lattice

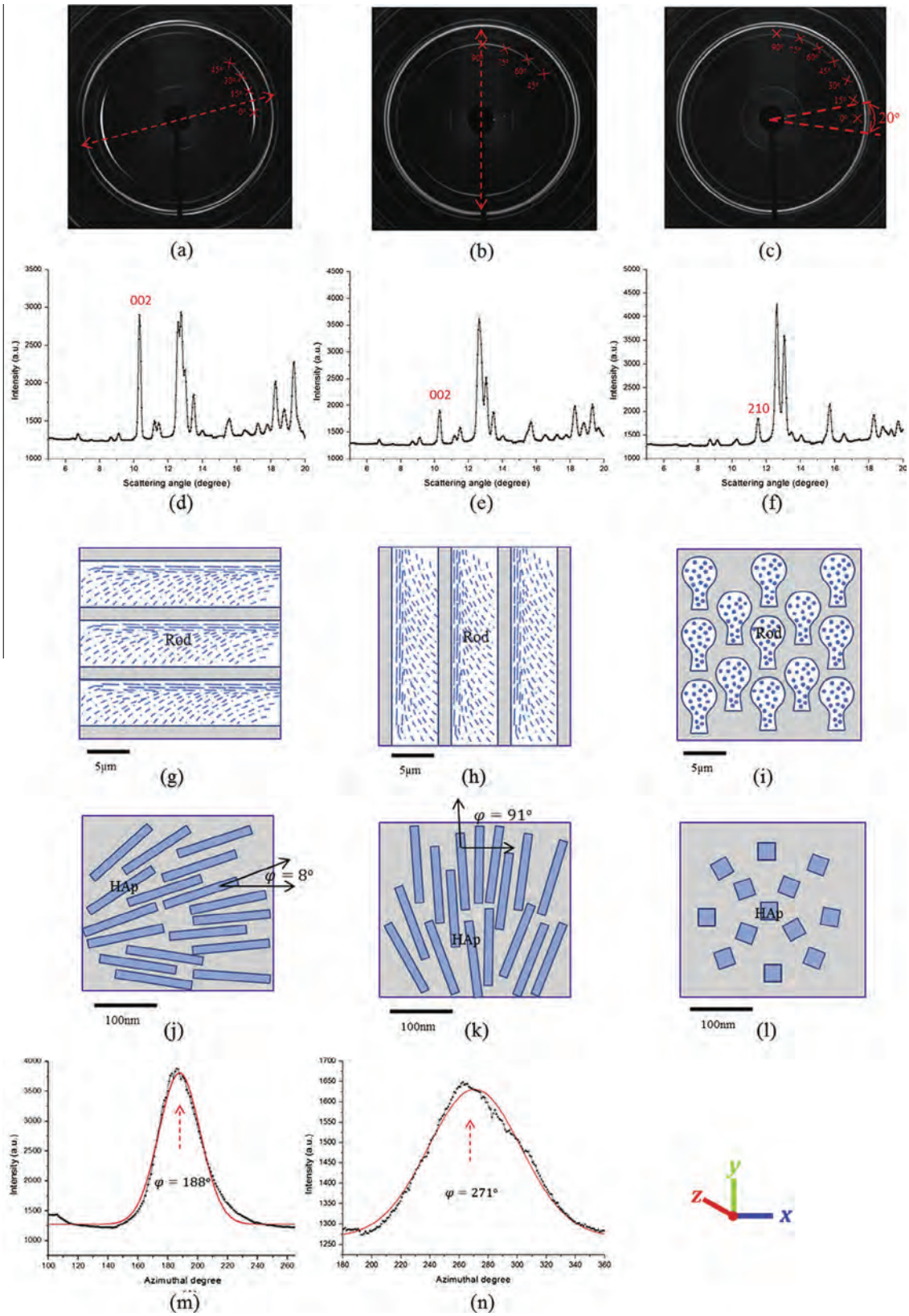

Fig. 2. (a)–(c) Representative WAXS patterns of Debye–Scherrer rings with differing intensities corresponding to each of the three samples (#6, #7 and #3, respectively). The dark region in the centre of the pattern is the beamstop. The direction with the red dashed double-arrow lines in (b) and (c) indicates the preferred orientation of HAp crystals. Multiple angles with respect to the x-axis were caked (within a 20° range) in order to examine the normal strain variation (red crosses). (d)–(f) The experimental diffraction pattern of integrated intensity vs. scattering angle 2θ of the three samples (#6, #7 and #3, respectively); the peaks of interested are marked in red. (g)–(i) Schematic illustration of the first-level geometric model of aligned rods with embedded HAp crystals in the three samples with respect to the laboratory coordinate system; the loading direction is into the page. (j–l) Schematic illustration of the second-level geometric model of HAp crystals with different crystalline distributions viewed in the *x*–*y* plane (#6: with the preferred orientation at 8°; #7: with the preferred orientation at 91°; #3: random). (m, n) The intensity variation with the Gaussian fit (red curve) corresponding to the orientation distribution of samples #6 and #7.

strain of HAp crystals was calculated from the changes in the interplanar spacing [26]:

$$\varepsilon = \frac{d_{hkl} - d^0_{hkl}}{d^0_{hkl}}, \quad (3)$$

where d_{hkl} is the deformed d-spacing of the lattice planes with the Miller index $\{hkl\}$, and d^0_{hkl} is the strain-free d-spacing value for the same set of planes.

The data analysis procedure involved pre-processing the 2-D diffraction using Fit2D [27]. Initially the peak of interest on each pattern was "caked" (a term used to refer to the selection of a sector in the radial-azimuthal coordinates of each pattern, and binning the data to obtain the equivalent 1-D radial pattern) within a range of 20°. The azimuthal angle is defined as the angle with respect to the x-axis in the x–y plane (perpendicular to the incident beam). For each specimen, a different azimuthal range was selected due to the preferred orientation of crystallites in the sample (for sample #6 between 0° and 45°, for sample #7 between 45° and 90°, and for sample #3 the available range was between 0° and 90°). This is indicated by the red crosses in Fig. 2a–c. The lattice spacing value deduced for the centre direction of each caked sector gives rise to the normal strain value for the corresponding orientation (see Fig. 2a–c). To determine the lattice spacing, the experimental diffraction pattern was converted to integrated 1-D plots of intensity vs. scattering angle. These plots for the three samples with peaks of interest are shown in Fig. 2d–f. The peaks of interest were fitted with a Gaussian function in order to obtain the peak centre. With increasing load, the peak centre position moved with respect to the strain-free reference value. Finally, the calculation of the HAp elastic lattice strain was performed using Eq. (3).

The orientation of the HAp crystals was also carried out using a similar "caking" approach. In this case, the 1-D intensity was plotted as a function of azimuthal angle $I_{WAXS}(\varphi) \sim \varphi_{WAXS}$ (Fig. 2m and n). Gaussian fitting of the azimuthal centre position of these peaks of plots can then be used to define an associated orientation [8].

3. Modelling

3.1. Finite-element analysis

The finite-element package ABAQUS® v. 6.9 was used to simulate the stress distributions and to obtain the associated photoelastic patterns. Direct comparison of photoelastic patterns between model and experiment provides a way of simultaneously verifying the correctness of the macroscopic properties (of epoxy and enamel) as well as the mechanical model of the stress distribution within the epoxy disk around the enamel samples. In order to visualize the photoelastic fringe patterns the "Tresca equivalent stress" σ_{Tresca} was selected as the output parameter. Initially a simulation of the solid photoelastic epoxy disk (the calibration specimen) was developed using a model of 12 mm diameter and 2 mm thickness. The elastic constants of the epoxy were identified by comparing σ_{Tresca} contour plot with the fringe patterns observed at different loads.

In order to model the enamel sample (2 mm × 2 mm × 2 mm), a cubic inclusion was introduced and embedded in the centre of the epoxy disk with the isotropic elastic constants obtained from the calibration. The experimentally applied loads were introduced on the edge of the epoxy model and the stress distribution around the sample (in the x–y plane in global coordinates) was recorded. The tractions present at the boundary of the enamel inclusion obtained from this model were then used for the externally applied stress values in the Eshelby model.

3.2. Geometrical assumptions

The geometrical assumptions used in the enamel model have been justified in our previous studies. An outline of these assumptions at this stage is given here [19]. At the first structural level, the geometric model of human enamel involves aligned rods with a keyhole-shaped cross-section. The second-level structural consists of the bundles of HAp needle-shaped crystallites found within each rod. These bundles are roughly aligned with the longitudinal direction of the rods with some minor misorientations. The degree of misorientation can be determined from careful WAXS data interpretation. This analysis assumes that the peak intensity at a given azimuthal angle is proportional to the number of HAp crystals of this orientation [28].

The orientation distributions of the rods in the enamel samples were derived from the analysis of experimental data and are illustrated in Fig. 2g–i. Furthermore, the predicted distributions of needle-shaped HAp crystals (in the measured cross-section, perpendicular to the beam direction) are shown in Fig. 2j–l in which the misorientation distribution is based on the intensity plots in Fig. 2m and n. The principal orientation of sample #3 is aligned so that orientation component is observed perpendicular to the beam, and therefore no equivalent plot is produced.

In the multiscale Eshelby model, both structural levels are considered as non-dilute systems consisting of a number of inhomogeneous inclusions (rods at the first level and HAp crystals at the second level). For simplicity, both rods and HAp crystals are assumed to be of cylindrical shape. Therefore, the classical solution for inclusion in the form of a cylinder is used to simulate both the needle-shaped rods and the individual HAp crystals. In the Eshelby approach, the cylinder is approximated by a prolate spheroid described by the three dimensions, a_1, a_2 and a_3, where $a_1 = a_2 \ll a_3$, i.e. the cross-section of the ellipsoid perpendicular to its longest axis is a circle [29]. The crystal c-axis (corresponding to the (002) peak) of the needle-shaped HAp crystals is normal to this cross-section of the cylinder, i.e. is aligned with the a_3 direction [28]. In the next section a detailed derivation and discussion of the model formulation and implementation is introduced.

3.3. Multiscale Eshelby model

Based on the hierarchical structure of enamel, a two-level Eshelby inclusion model can be used to demonstrate how the HAp crystals respond to external macroscopic loading. The original Eshelby solution gives the analytical expressions for the elastic fields around an ellipsoidal inclusion embedded in an infinite isotropic matrix that has the same elastic properties as the inclusion, but there is a misfit or mismatch strain (eigenstrain) between the inclusion and the matrix [30].

Eshelby introduced a tensor S that only depends on the inclusion shape and the Poisson's ratio of the matrix. For an inhomogeneity with a different stiffness from the matrix, the elastic field can be found using an equivalent inclusion method. This formulation regards the inhomogeneity as equivalent to an inclusion with an appropriate virtual misfit strain which needs to be determined. The function of the virtual misfit strain is to satisfy the equivalence where the elastic field of the inhomogeneity is identical to that of the equivalent inclusion. In this way the classical Eshelby theory can be used to determine the elastic field of any kind of inhomogeneity. This formulation has greater generality and includes the case of rods or HAp needle-like crystals (long cylinders) embedded in the isotropic protein matrix. In the next section, the multiscale model for enamel is briefly introduced, while a detailed derivation of the basic theory is given in the Appendix.

3.3.1. First-level model: multiple aligned rod inclusions within the enamel sample

The purpose of the first-level model for human enamel, which describes multiple aligned rod inclusions within enamel, is to establish the elastic relationship between the externally applied stress σ^{A} and the stress in the rod-like inclusions $\sigma^{\text{inclusion}} = \sigma^{\text{rod}}$.

According to the Eshelby model derivation [30], the stress in the rods at the first structural level of consideration can be written as:

$$\sigma^{\text{inclusion}} = \Big\{T - (1-f_1)C_{\text{matrix}}(S_1 - I)\{(C_{\text{matrix}} - C_{\text{rod}})[S_1 - f_1(S_1 - I)] - C_{\text{matrix}}\}^{-1}(C_{\text{matrix}} - C_{\text{rod}})T^{-T}C_{\text{matrix}}^{-1}\Big\}\sigma^{A}$$

or, expressed more simply:

$$\sigma^{\text{inclusion}} = H\sigma^{A}, \tag{4}$$

where f_1 is the volume fraction of rods, S_1 is the Eshelby tensor for the long cylinder simulating the rod shape, C_{matrix} and C_{rod} are the stiffnesses of the protein matrix and the rod, and T is the tensor transformation (rotation) matrix. T encapsulates the effect of the three Euler angles that define the orientation of the rods with respect to the fixed laboratory coordinate system. The stiffness of the rod in the simulation is initially unknown and is determined from the second-level model.

3.3.2. Second-level model: partially aligned HAp inclusions within each individual rod

In the second-level model, the relationship between the average strain in the partially aligned HAp crystals (averaged within the considered gauge volume) and the external stress (the rod stress from the first-level model) can be established as follows:

$$\langle\varepsilon\rangle_{\text{aligned}}^{\text{HAp}} = \Big\{\{(I - C_{\text{matrix}}^{-1}\langle C\rangle_{\text{HAp}})^{-1}[\langle S_2\rangle - f_2(\langle S_2\rangle - I)]^{-1} - I\}^{-1}T^{-T} + T^{-T}\Big\} \times C_{\text{matrix}}^{-1}\sigma^{\text{inclusion}}$$

or, expressed more simply:

$$\sigma^{\text{inclusion}} = K_{\text{aligned}}\langle\varepsilon\rangle_{\text{aligned}}^{\text{HAp}}, \tag{5}$$

where $\langle C\rangle_{\text{HAp}}$ and $\langle S_2\rangle$ are the average elastic stiffness tensor and the Eshelby tensor for HAp crystals within the gauge volume, respectively, and f_2 is the volume fraction of the HAp crystals with a certain orientation T_{HAp} within the rods. The stiffness of a single HAp has been reported to be transversely isotropic [31]. In Eq. (5), different orientation angles (different T_{HAp}) would lead to different values of $\langle\varepsilon\rangle_{\text{aligned}}^{\text{HAp}}$.

In order to evaluate the multidirectional normal strain components, each azimuthal angle was taken to correspond to a group of perfectly aligned HAp crystals, as illustrated by Eq. (5), with a certain volume fraction f_2 and orientation T_{HAp}, where f_2 is determined from the WAXS intensity plot (Fig. 2m and n). In other words, the bundled HAp crystals consist of a distribution of multiple groups with different orientations and different volume fractions. Meanwhile, for each group, all the crystals are perfectly aligned, thus $\langle C\rangle_{\text{HAp}}$ and $\langle S_2\rangle$ can be represented by the single-crystal values $\langle C\rangle_{\text{HAp}} = \langle C\rangle_{\text{HAp}}$, $\langle S_2\rangle = S_2$. Note that a single HAp crystal in the second level can be regarded as a single inhomogeneity with needle-like shape, thus the Eshelby tensor for a single HAp should be the same as the rod inclusion ($S_2 = S_1$).

Further, the stiffness of rod is obtained from the following equation:

$$C_{\text{rod}} = \Big\{C_{\text{matrix}}^{-1} - f_2\{(\tilde{C}_{\text{HAp}} - C_{\text{matrix}})[\tilde{S}_2 - f_2(\tilde{S}_2 - I)] + C_{\text{matrix}}\}^{-1} \times (\tilde{C}_{\text{HAp}} - C_{\text{matrix}})C_{\text{matrix}}^{-1}\Big\}^{-1}, \tag{6}$$

where $\tilde{S}_2 = T_{\text{HAp}}^{T}S_2T_{\text{HAp}}^{-T}$ is the transformed Eshelby tensor and $\tilde{C}_{\text{HAp}} = T_{\text{HAp}}^{-1}C_{\text{HAp}}T_{\text{HAp}}^{-T}$ is the transformed stiffness of aligned transversely isotropic HAp crystals. Finally, the relationship between the HAp strain and the overall external loading can be established by the combination of Eqs. 4 and 5 and simplified Eq. (6) to give:

$$\sigma^{A} = H^{-1}\sigma^{\text{rod}} = H^{-1}K_{\text{aligned}}\langle\varepsilon\rangle^{\text{HAp}} = K\langle\varepsilon\rangle^{\text{HAp}}. \tag{7}$$

4. Experimental results and modelling evaluation

4.1. Finite-element modelling of photoelastic patterns

The photoelastic fringe patterns of solid epoxy disks and epoxy with enamel embedded at the disk centre are shown in Fig. 3. The results for Tresca stress distribution simulated in ABAQUS are shown in Fig. 4. The stress variation along the edge of the samples simulated in ABAQUS was not constant, but was concentrated especially at the two corners. Direct comparison and matching of the model to the photoelastic patterns for solid epoxy disks lead to the isotropic elastic constants of epoxy disk being estimated to be $E_{\text{epoxy}} = 1.2 \pm 0.015$ GPa, $\upsilon_{\text{epoxy}} = 0.35$ [32]. These parameters were used for the samples with embedded enamel to calculate the predicted normal stress distribution around the enamel inclusion illustrated in Fig. 5a that corresponds to the maximum external load of 400 N. At this applied load, the stress values were

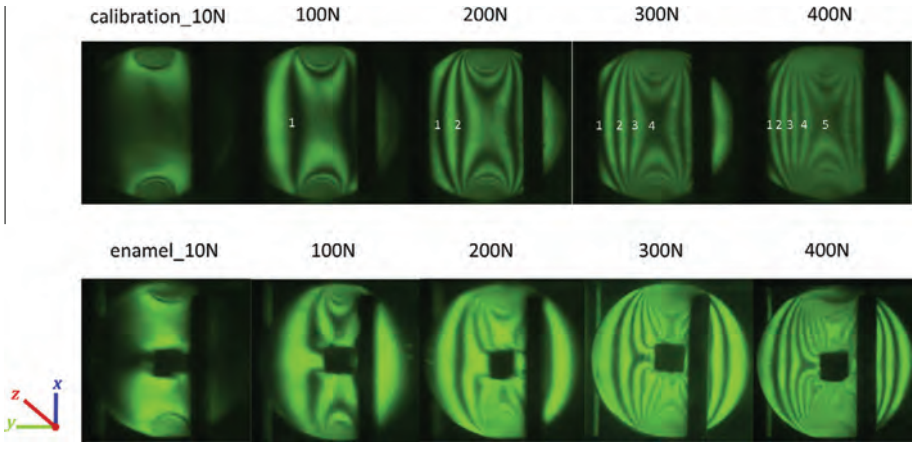

Fig. 3. Photoelastic images of epoxy disks without (first row) and with embedded enamel (second row) under a series of loading conditions. The number of fringes can be seen to increase with load. The patterns on the first row of solid epoxy disks were used as calibration in order to determine epoxy properties. The patterns on the second row of epoxy with enamel sample were further used for the determination of the stress distribution around the cubic enamel inclusion. The fringe number is marked.

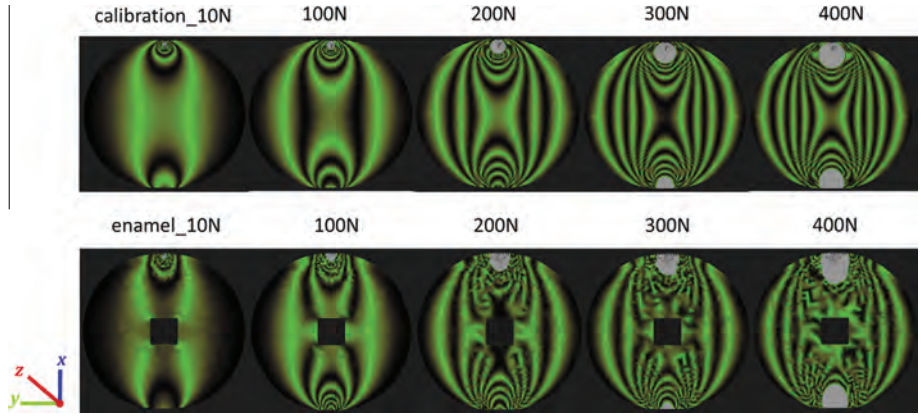

Fig. 4. ABAQUS simulation images of Tresca stress distribution of the epoxy disks without (first row) and with embedded enamel (second row) under a series of loading conditions. The isotropic elastic constants of the epoxy together with the normal stress distribution around the enamel sample were determined by matching the ABAQUS images with the photoelastic images in Fig. 3. The greyed regions represent the high stress concentration areas and were neglected in the images.

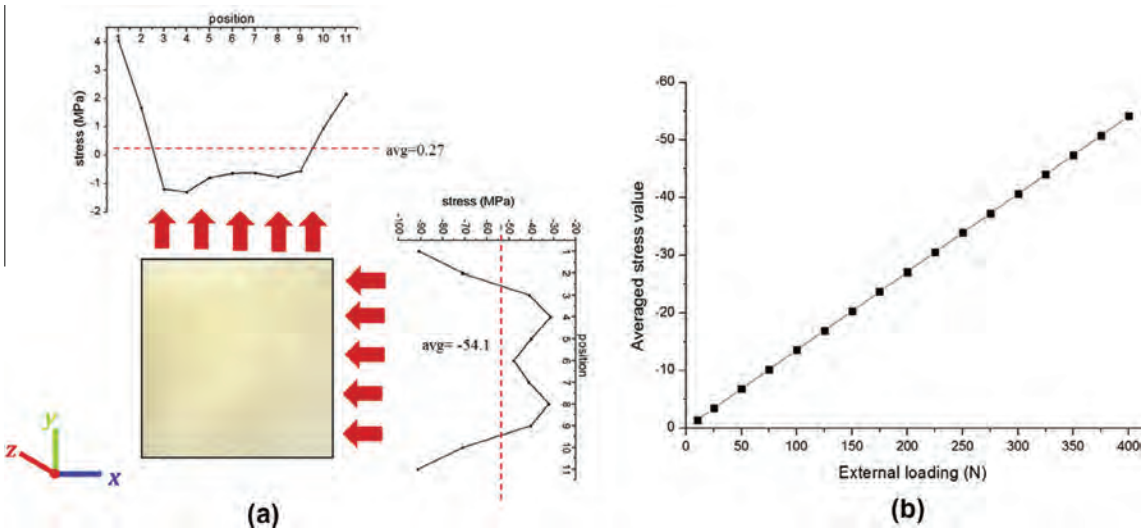

Fig. 5. (a) Normal stress distribution around the cubic enamel samples in the x- and y-directions (x–y plane is the measurement plane) at the maximum external loading of 400 N. The averaged value of the stress distribution was extracted as −54.1 MPa along the x-direction (loading direction) and 0.27 MPa in the y-direction (transverse direction). (b) The external load vs. the averaged stress value applied to the sample in the y-direction.

averaged over all the boundary nodes of each enamel cube sample edge. This uniform traction was applied in order to eliminate the effect of the singular points or stress oscillations at corners, with the result of −54.1 MPa in the x-direction and 0.27 MPa in the y-direction. Therefore the sample loading condition was found to be close to uniaxial. As expected, the average stress value applied to the sample was also found to be linearly proportional to the value of the externally applied load, as shown in Fig. 5b.

4.2. Nanoscale HAp distribution and mechanical response of enamel

Fig. 2a–c respectively represent the typical WAXS patterns of samples #6, #7 and #3, which consist of series of Debye–Scherrer rings (peaks). The textured nature of enamel meant that only limited azimuthal ranges within the rings could be captured in samples #6 and #7. In contrast, in sample #3 the crystals were approximately randomly distributed in the x–y plane, so that complete rings were observed. Fig. 2m and n show the azimuthal intensity variation within the available azimuthal ranges in the measurement plane (x–y plane) in samples #6 and #7, respectively. This provides information about the crystal orientation distribution, as described in Section 3.3. The preferred orientation direction of the basal plane in HAp crystals in samples #6 and #7 is approximately perpendicular to the central bisector of the arc of the peak of interest (see Fig. 2b and c). The precise values are determined from the Gaussian fit in Fig. 2m and n (red line). Since the deformation considered is elastic, the assumption was made that the crystal orientation remains unchanged, i.e. the peak centres found from the plots shown in Fig. 2m and n remain the same at all applied loads.

In order to obtain the variation of the average normal elastic lattice strain component of HAp crystals with applied load, the peak shifts at different azimuthal angles were obtained from the WAXS data through caking each pattern into 20° sectors. The available range for each sample was different, as shown by the red marks in Fig. 2a–c: in sample #6 between 0° and 45°, in sample #7 between 45° and 90°, and in sample #3 between 0° and 90°. For each of the samples, the elastic lattice strain as a function of applied stress is plotted as the argument against the applied stress for different azimuthal angles in Fig. 6 (in which 0° represents the loading direction). The experimental results indicate that, as expected, there is an approximately linear relationship in each direction and

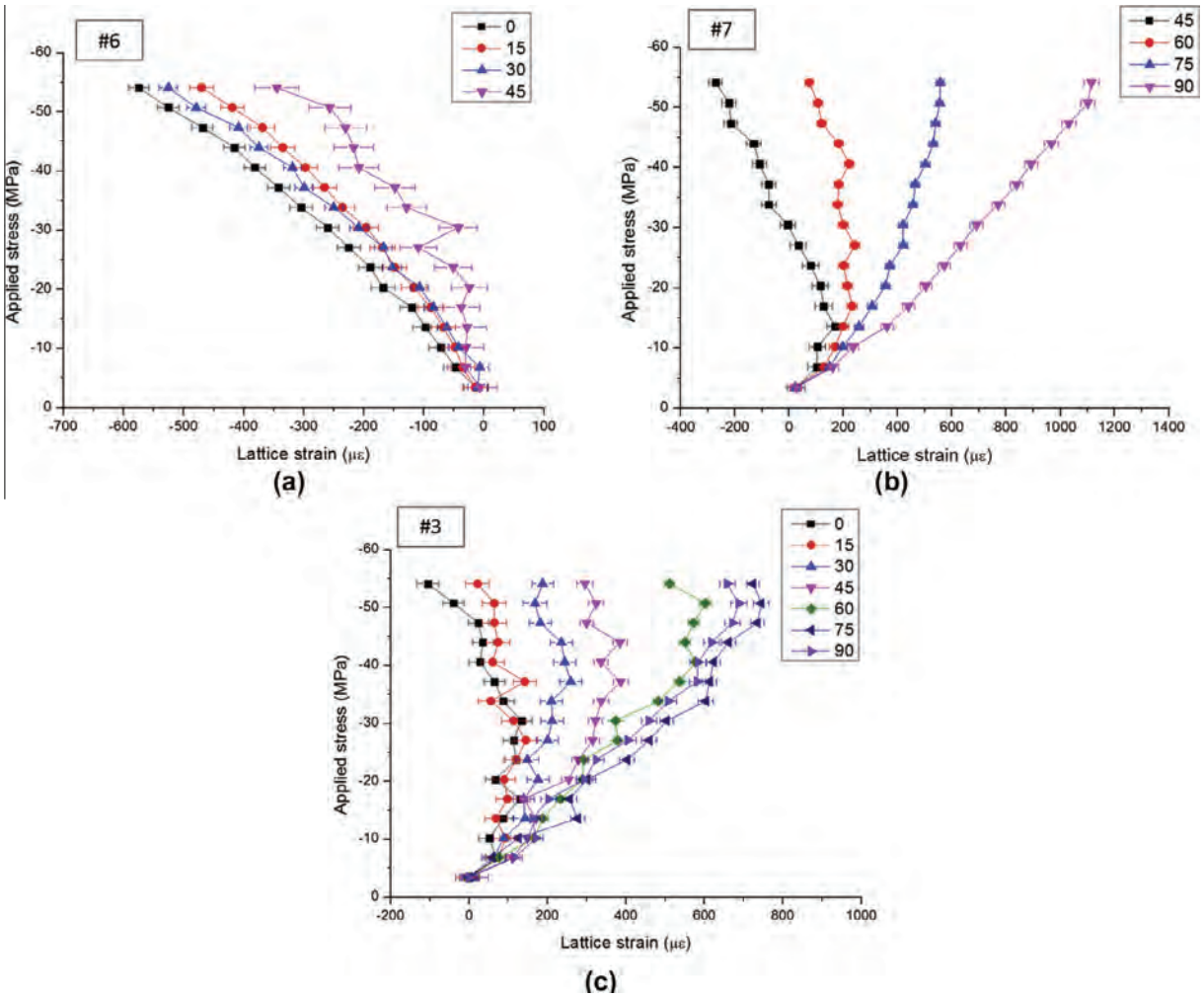

Fig. 6. The experimental results of applied compressive stress vs. elastic lattice strain of HAp crystals for the three samples at different azimuthal angles (every 15°) with respect to the loading direction. (a) Sample #6; due to symmetry, only the available angles from the (002) ring from 0° to 45° are selected. (b) Sample #7; due to symmetry, only the available angles from the (002) ring from 45° to 90° are selected. (c) Sample #3; due to the symmetry, only the available angles from the (210) ring from 0° to 90° are selected.

Table 1
Preferred orientation and refined structural parameters of the enamel used in the two-level Eshelby model (values reported in the literature are also presented).

Parameter	#6	#7	#3	Reference values
Preferred orientation	8°	91°	–	
$f_1 = f_2$	93%	90%	95%	95% [11]
$C_{matix\_1} = C_{matix\_2}$	E_m = 1 GPa, υ_m = 0.3			$E_{protein}$ = 1 GPa, $\upsilon_{protein}$ = 0.3 [34]
C_{HAp}	E_{xx} = 132.1 ± 9 GPa,			E_{xx} = 138.4 GPa,
	$G_{xy} = G_{xz}$ = 39.6 GPa			$G_{xy} = G_{xz}$ = 39.6 GPa
	$\upsilon_{xy} = \upsilon_{xz}$ = 0.33 ± 0.07,			$\upsilon_{xy} = \upsilon_{xz}$ = 0.30,
	υ_{yz} = 0.31 ± 0.08			υ_{yz} = 0.2
	$E_{yy} = E_{zz}$ = 114.3 ± 6.5 GPa			$E_{yy} = E_{zz}$ = 114.3 GPa [31]
$S_{cylinder\_1} = S_{cylinder\_2}$	a_1/a_2 = 1			[6]

that each azimuthal angle corresponds to a different slope. This ratio between the applied uniaxial external stress and the average HAp lattice strain gives the apparent modulus along different directions [33]. At this stage it is also relevant to mention that the initial residual strain in the samples was found to be negligible.

4.3. Evaluation of the multiscale Eshelby model

In setting up the multiscale Eshelby model, the average external stress derived from the ABAQUS model was used as the input external stress. The material properties and other parameters were taken from the literature [11,31,34,35], and refined by fitting with the experimental data of HAp crystal lattice strain. The initial volume fraction of HAp crystals was taken from the previous analysis of the self-similar hierarchical two-level model of enamel, i.e. approximately 95% at both the microscale and nanoscale levels [11]. The needle-like HAp crystals in the enamel were also assumed to have a transversely isotropic stiffness with five independent elastic constants [31]. To describe the geometry of rod and HAp crystals, the cylinder Eshelby tensor was used and the length of elliptical axes a_1 and a_2 within the transverse cross-section were expected to be equal to each other, i.e. $a_1/a_2 = 1$. In addition,

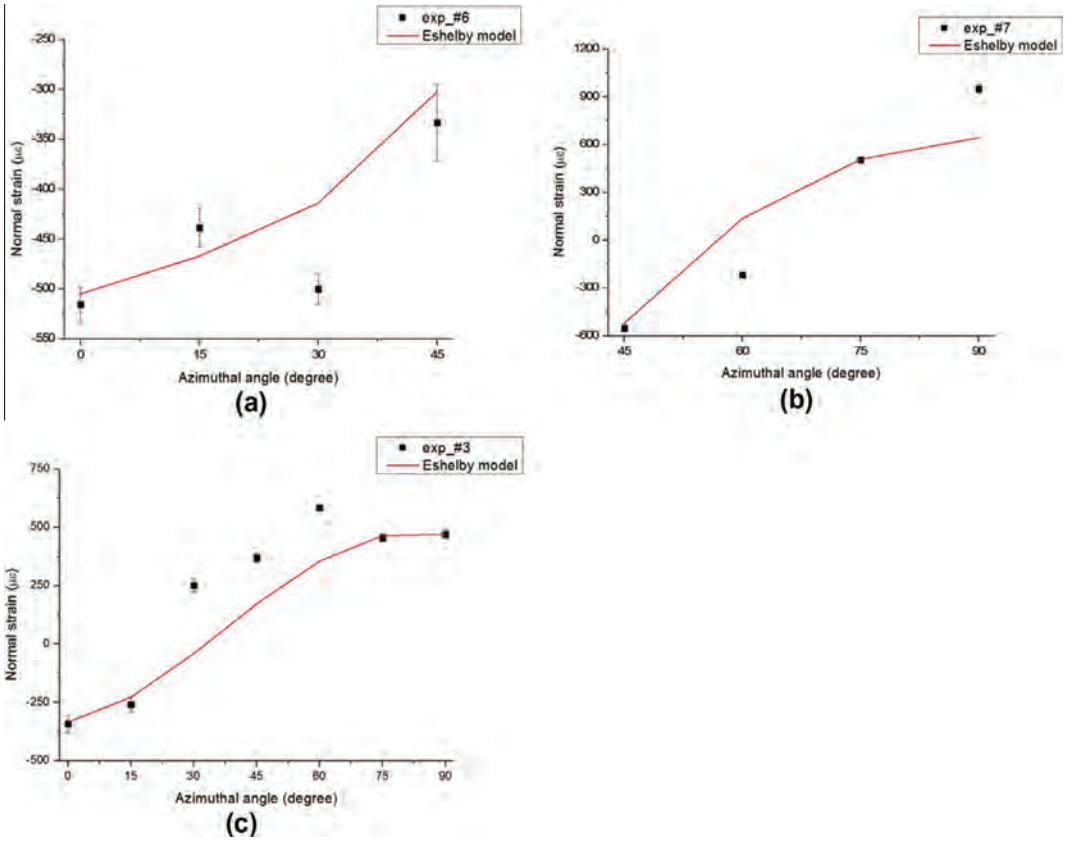

Fig. 7. Comparison of experimental data (black markers) and modelling results (solid black lines) for the variation of normal strain component with orientation distribution (azimuthal angle) at the maximum externally applied load of 400 N. (a) sample #6, from 0° to 45°; (b) sample #7, from 45° to 90°; (c) sample #3, from 0° to 90°.

Young's modulus of protein was set to 1 GPa (this does not take into account any effects from viscoelasticity or viscoplasticity [34,35]). The final refined parameters and reference values are summarized in Table 1.

In Fig. 7, the comparison between the model prediction and experimental data of the normal strain variation in the three samples under the maximum external load of 400 N is shown as a plot against the azimuthal angle.

5. Discussion

The hierarchical nanostructure of human enamel may vary significantly between patients due to personal history, diet, ethnic origin, etc. However, due to ethical legislation in the UK, it is not possible to obtain or publish any further information on the medical history of the patients.

This study was conducted using the penetrating power of synchrotron X-rays to provide a bulk probe for structure and strain analysis. Unlike the vast majority of studies that rely on the surface characterization (scanning electron microscope, atom force microscopy, nanoindentation, Raman, etc., and also the reflection mode of X-ray diffraction), this WAXS study required less preparation effort in terms of cutting and storage and surface conditioning. The use of much thicker samples and gauge volumes (~2 mm) than those for other methods (~0.05 mm) ensured that the bulk response investigated was not affected by minor surface changes. The combination of the data obtained using penetrating radiation (synchrotron X-ray) with model refinement offers the possibility of identifying the nanoscale parameters of bulk enamel. The parameter refinement and validation strategy employed in the model adopted in the present study is particularly helpful in the identification of nanoscale parameters that may be hard to determine in the other experiments. The relationship between the nanoscale structure and the macroscopic mechanical behaviour established in our study improves the understanding of the nanoparticle distribution effects that was lacking in the earlier studies [8,16,20].

5.1. Finite-element simulation

The high level of correlation seen between the finite-element analysis result (illustrated in Fig. 4) and the photoelastic patterns (shown in Fig. 3) suggests that the stress values extracted from the finite-element model are a good representation of the tractions applied to the enamel samples. In Fig. 4 the stress concentration region has been shaded grey. As this region is far enough away from the enamel inclusion, it can be neglected. Only the patterns and stress distribution close to the enamel need to be considered. The plot of the normal stress distribution in Fig. 5 is likely to originate from the frictional contact condition established between the enamel sample and epoxy in ABAQUS. However, the use of the averaged value of the stress distribution will minimize the effect of this oscillation. In short, the finite-element results suggest an accurate estimation of the input stress for the two-level Eshelby model.

5.2. Refined parameters of the two-level Eshelby model

The input from reference data on material parameters (HAp stiffness, etc.) are only used as the starting guess for the optimization of the elastic constants in order to obtain the best fit to our experimental data. The final parameters used in the multiscale Eshelby model are outlined in Table 1 and were refined iteratively, starting from the values reported in the literature. Of the refinable

parameters, the key ones were the volume fraction of inhomogeneities at each level and the elastic constants of a single HAp crystal. Among these parameters, the elastic constants, and the modulus in particular, exert the most profound influence on the result. The three samples studied were cut from the same tooth. Therefore their properties, such as the degree of mineralisation, size of particles, etc., can be assumed to be close and consistent, with the exception of the orientation distribution of nano-HAp crystals which is known to vary with location within the tooth. Model fitting was carried out so as to find the parameters that give the best agreement for all three samples. The single-crystal elastic constants of HAp were assumed to be the same. In the model matching (optimization) process, within each specimen, the volume fraction of the rods in enamel and the HAp crystals in rod were assumed to be the same. After the refinement of the elastic constants (within the range reported in the literature) the volume fraction was further refined. At this stage, further adjustments of other parameters were also attempted and it was found that this only had a minor effect. In order to estimate the error in our evaluation of parameters, we carried out a careful study of error propagation in our model-fitting procedure following the error analysis methods in Ref. [36]. The 95% confidence interval in the fitting results was propagated back into elastic modulus uncertainty. The final result with description has been added to Table 1 Note that since the results of our test are not sensitive to the shear modulus, the uncertainty of the shear modulus was not assessed.

The authors note that environmental and developmental factors may influence the mechanical behaviour of enamel [37]. Following tooth eruption, the interaction of the enamel surface with ions in saliva leads to enamel maturation. This post-eruptive maturation may affect the mechanical behaviour of enamel surface. For example, the incorporation of fluoride into enamel and the formation of fluoroapatite may exert an influence on the superficial layer of dental enamel. However, the transmission X-ray setup we employed ensured that the bulk rather than the surface was characterized for the samples obtained from freshly extracted teeth with no apparent damage, caries or evidence of dental treatments.

5.3. Residual strain

During the preparation process, a low-speed diamond saw and polishing papers were used to minimize the effect of induced residual strain. The other origin of residual strain may be the natural growth of teeth. At low load values, there is a transition region in the transversely loading samples (#7 and #3), which might result from the residual tensile strain in the transverse direction. However, as also shown in Fig. 6b and c, the residual strain in the enamel was found to be very small in magnitude and was relieved subsequently at higher loading values. Since the elastic response has been experimentally observed to be dominating after the transition (reflected in the linearity of the experimental stress–strain curve), the presence of this initial residual strain only amounts to an initial offset. This means that there has been no impact from residual strain on the prediction of the elastic properties and that this offset can be neglected in the present analysis.

5.4. Normal strain components variation

In this experiment, the main difference between the three different samples was the orientation of the rods with respect to the external loading direction. For sample #6 in Fig. 6b, in which the load was applied along the rod longitudinal direction, the crystal lattice strain at a given stress was larger at 0° (i.e. along the loading direction) than at any other angles (which is a direct result of the Poisson effect). However, for the other two samples (#3 and #7), in which the rod orientation was perpendicular to the loading direction, the lattice strain was found to be larger at 90° than at other angles. These plots also demonstrate that loading along the transverse direction of the rod induces higher levels in stress or strain in the HAp crystals. In addition, the deviation from linearity was found in the three samples (45° for samples #6 and #7, and all the orientation angles for sample #3). Such relatively large experimental errors may result from the relatively weak intensity at the edge of the rings for samples #6 and #7, while for sample #3, the whole ring demonstrates a relatively weak intensity.

The plots of applied stress against lattice strain also have a common trend, in that the linear relationship starts only after a certain applied stress has been reached, especially in samples #3 and #7 (shown in Fig. 6a and c). This initial trend may demonstrate that the HAp crystals in the samples were initially subjected to a hydrostatic stress condition. In any case, this effect appears to have only minor influence on the further response.

5.5. The elastic anisotropy of the HAp crystals

The different mechanical responses of HAp crystals with respect to the loading direction shown in Fig. 6 and 7 originate not only

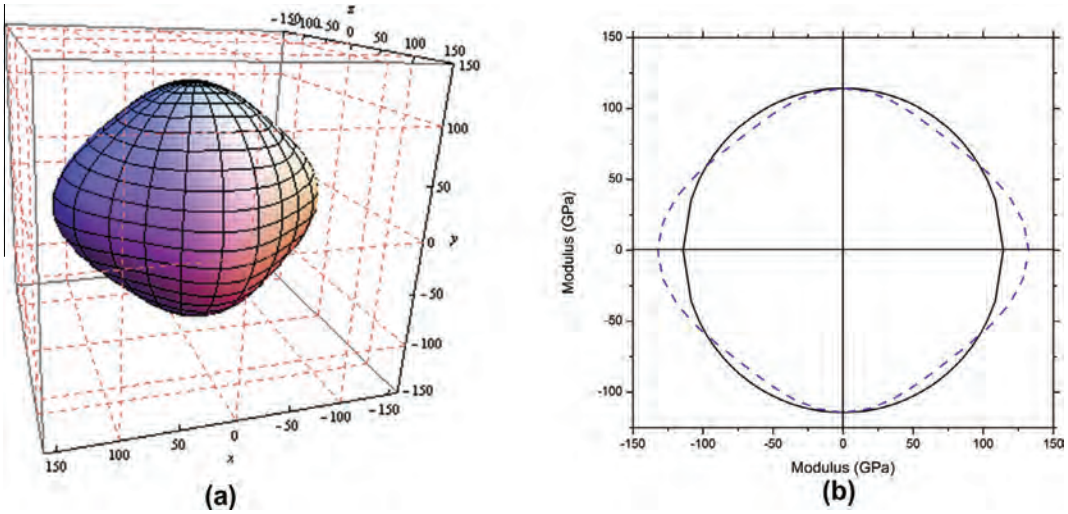

Fig. 8. Transversely isotropic elastic modulus of HAp. (a) 3-D representation of directional dependency of HAp elastic modulus (unit: GPa). (b) The projections of directionally dependent modulus on the x–y plane (blue dashed line) and y–z plane (solid black line).

from the different rod directions, but also in the strong anisotropic stiffness of HAp crystals. The 3-D directional modulus of a single HAp crystal was calculated by transforming the transversely isotropic stiffness matrix of a single crystal with different rotation matrices. The result is shown in Fig. 8a. The non-spherical shape corresponds to the elastic anisotropy of the HAp crystal. In Fig. 8a, the *x*-axis represents the longitudinal direction of the needle-shaped HAp crystal. Fig. 8b demonstrates the projections of the resulting modulus on the *x*–*y* plane and *y*–*z* plane. The projection on the *x*–*y* plane is similar to the cases of samples #6 and #7, and the circular projection on the *y*-*z* plane is similar to the case of sample #3 in which an isotropic modulus is observed. The orientation with the largest stiffness is found to be along the *x*-axis, as expected (longitudinal direction of the HAp crystal). However, the most compliant orientation observed in Fig. 8b is not at 90°, but rather around 60° due to the transverse isotropic stiffness of HAp crystals.

6. Conclusions

In this study, the lattice strain variation related to the nanoscale HAp distribution of human enamel was measured during in situ elastic compression by the combination of synchrotron WAXS and photoelasticity techniques. This study of the nanoscale phenomena and their effect on the macroscopic and microscopic mechanical behaviour provided access to information on both the structural and mechanical aspects of the sample, and allowed progress to be made in understanding the structure–property relationships in the hierarchical biomaterial of human enamel. In addition, as an improvement to an earlier proposed composite model [38,39], a multiscale Eshelby inclusion model was established and modified by introducing the misorientation distribution of HAp crystals at the nanoscale level. This second-level effect cannot be ignored since the mechanical behaviour shows strong dependence on the crystallite orientation distribution. The models were validated by the good agreement observed between the measured and calculated normal lattice strain component variation in different azimuthal directions.

This systematic experimental and modelling approach reported here is able to capture the complete picture of the multiscale structure of human enamel and its evolution under loading. The parameter refinement and validation in the modelling adopted in the present simulation offers the potential identification of nanoscale parameters, which may be hard to determine otherwise. By combining the results with previous studies of human dentine and enamel [12,19], an improved and comprehensive understanding of the multiscale structural-mechanical properties within human dental tissue can be achieved. Such information is essential for developing better prosthetic materials and dental fillings and has the potential to shed light on the mechanical evolution associated with the multiscale structural changes induced in human teeth by disease and treatment. Finally, this approach also enables the characterization of the structure–property relationship of other hard hierarchical biomaterials.

Acknowledgements

A.M.K. acknowledges the support of EPSRC through grants EP/I020691 "Multi-disciplinary Centre for In-situ Processing Studies (CIPS)", EP/G004676 "Micromechanical Modelling and Experimentation", and EP/H003215 "New Dimensions of Engineering Science at Large Facilities". Diamond Light Source is acknowledged for providing the beam time.

Appendix A.

A short overview of the Eshelby general inclusion theory is introduced, leading to the derivation of the constitutive law for a number of non-dilute HAp crystals (inhomogeneities) embedded in a finite protein matrix.

A.1. Dilute system

The general geometric structure for a dilute system is an ellipsoidal inclusion embedded in an infinite matrix. "Dilute" means that the volume fraction of the inclusion can be neglected. If there is a mismatch between the inclusion and the matrix, i.e. a uniform misfit strain ε^{t^*} in the inclusion, the Eshelby model shows that the total strain in the inclusion ε^i is related to ε^{t^*} by an Eshelby tensor S that only depends on the inclusion shape and the Poisson's ratio of the matrix:

$$\varepsilon^i = S\varepsilon^{t^*}. \tag{A1}$$

As a consequence, with the known stiffness tensor C_M (the same as the surrounding matrix) of the inclusion, the inclusion stress σ_I can be calculated based on Hooke's law:

$$\sigma_I = C_M(\varepsilon^i - \varepsilon^{t^*}) = C_M(S - I)\varepsilon^{t^*}. \tag{A2}$$

For an inhomogeneous inclusion (or an inhomogeneity) with a different stiffness C_I, its elastic field is shown to be identical to an equivalent inclusion with an appropriate misfit strain ε^t, which is to be determined from the equivalence relation:

$$\sigma_I = C_I(\varepsilon^i - \varepsilon^{t^*}) = C_M(\varepsilon^i - \varepsilon^t). \tag{A3}$$

Finally the external load σ^A that results in the overall composite strain ε^A can be added to Eq. (A3):

$$\sigma_I + \sigma^A = C_I(\varepsilon^i - \varepsilon^{t^*} + \varepsilon^A) = C_M(\varepsilon^i - \varepsilon^t + \varepsilon^A), \tag{A4}$$

where σ_I here is the stress caused by the mismatch between the inhomogeneity and the matrix.

A.2. Non-dilute system

A non-dilute system represents the condition that multiple inhomogeneities are embedded in the matrix in which their volume fraction cannot be neglected. To satisfy the boundary conditions at the external boundaries of the finite composite, Eshelby introduced the concept of a mean "image" stress, $\langle\sigma\rangle_M = C_M\langle\varepsilon\rangle_M$ as an average of the stresses within each individual phase. Then the equivalence relation Eq. (A4) becomes:

$$\langle C\rangle_I(\langle\varepsilon\rangle^i + \langle\varepsilon\rangle_M + \varepsilon^A - \langle\varepsilon\rangle^{t^*}) = C_M(\langle\varepsilon\rangle^i + \langle\varepsilon\rangle_M + \varepsilon^A - \langle\varepsilon\rangle^t), \tag{A5}$$

where "$\langle\cdot\rangle$" means the mean value, $\langle\varepsilon\rangle_M$ is the mean image strain in all the phases and $\langle C\rangle_I$ is the average stiffness of the multiple inhomogeneities. In a non-dilute system, the mean image stress $\langle\sigma\rangle_M$ and the mean stress in the equivalent inclusions $\langle\sigma\rangle_I$ due to the misfit strain can be expressed by [30,40]:

$$\langle\sigma\rangle_M = C_M\langle\varepsilon\rangle_M = -fC_M(\langle S\rangle - I)\langle\varepsilon\rangle^t \tag{A6}$$

$$\langle\sigma\rangle_I = (1-f)C_M(\langle S\rangle - I)\langle\varepsilon\rangle^t, \tag{A7}$$

where $\langle S\rangle$ is the average Eshelby tensor and f is the volume fraction of inclusions. Thus $\langle\varepsilon\rangle^t$ can be obtained as a function of the applied stress:

$$\langle\varepsilon\rangle^t = -\left\{(C_M - \langle C\rangle_I)[\langle S\rangle - f(\langle S\rangle - I)] - C_M\right\}^{-1}(C_M - \langle C\rangle_I)C_M^{-1}\sigma^A. \tag{A8}$$

A.3. Enamel first-level model

The first-level model considers multiple aligned rods as the inhomogeneous inclusion and the protein as the surrounding matrix. In an elastic problem, no misfit strain exists in the inhomogeneity. Thus according to Eq. (A5):

$$C_{\mathrm{rod}}\left(\langle\varepsilon\rangle^{i}+\langle\varepsilon\rangle_{\mathrm{matrix}}+\varepsilon^{A}\right)=C_{\mathrm{matrix}}\left(\langle\varepsilon\rangle^{i}+\langle\varepsilon\rangle_{\mathrm{matrix}}+\varepsilon^{A}-\langle\varepsilon\rangle^{t}\right), \tag{A9}$$

where C_{rod} is the stiffness of the rods. Further, in terms of Eqs. (A6)–(A8), the rod stress can be determined as shown in Eq. 4, consisting of two parts, namely the contribution from the elastic anisotropy and that from the applied stress.

A.4. Enamel second-level model

The second-level model considers each rod as a composite and the HAp crystals are multiply aligned inhomogeneous inclusions. The obtained rod stress serves as the external load in the second level. Similar to Eq. (A9):

$$\langle C\rangle_{\mathrm{HAp}}\left(\langle\varepsilon\rangle^{i}+\langle\varepsilon\rangle_{\mathrm{matrix}}+\varepsilon^{A}\right)=C_{\mathrm{matrix}}\left(\langle\varepsilon\rangle^{i}+\langle\varepsilon\rangle_{\mathrm{matrix}}+\varepsilon^{A}-\langle\varepsilon\rangle^{t}\right), \tag{A10}$$

where $\langle C\rangle_{\mathrm{HAp}}$ is the average stiffness of the aligned HAp crystals. The average lattice strain in HAp crystals consists of three parts:

$$\langle\varepsilon\rangle^{\mathrm{HAp}}_{\mathrm{aligned}}=\langle\varepsilon\rangle^{i}+\langle\varepsilon\rangle_{\mathrm{matrix}}+\varepsilon^{A}, \tag{A11}$$

where $\langle\varepsilon\rangle^{i}$ is the contribution from the elastic anisotropy, $\langle\varepsilon\rangle_{matrix}$ is due to the finite matrix effect and ε^{A} is the contribution from the applied load. The final expression in Eq. (5) is based on Eqs. (A6)–(A8), and Eqs. (A10) and (A11).

Appendix B. Figures with essential colour discrimination

Certain figures in this article, particularly Figs. 1–8 are difficult to interpret in black and white. The full colour images can be found in the on-line version, at doi: http://dx.doi.org/10.1016/j.actbio.2013.09.043

References

[1] Zarone F, Russo S, Sorrentino R. From porcelain-fused-to-metal to zirconia: clinical and experimental considerations. Dent Mater 2011;27:83–96.
[2] Macho GA, Jiang Y, Spears IR. Enamel microstructure—a truly three-dimensional structure. J Hum Evol 2003;45:81–90.
[3] Gao HJ, Ji BH, Jager IL, Arzt E, Fratzl P. Materials become insensitive to flaws at nanoscale: lessons from nature. Proc Natl Acad Sci U S A 2003;100:5597–600.
[4] Ten Cate AR, Dale AC. Oral histology: development, structure, and function. St. Louis, MO: Mosby; 1980.
[5] Ang SF, Saadatmand M, Swain MV, Klocke A, Schneider GA. Comparison of mechanical behaviors of enamel rod and interrod regions in enamel. J Mater Res 2012;27:448–56.
[6] He LH. Mechanical behavior of human enamel and the relationship to its structural and compositional characteristics. PhD thesis; 2008.
[7] Kerebel B, Daculsi G, Kerebel LM. Ultrastructural studies of enamel crystallites. J Dent Res 1979;58:844–51.
[8] Al-Jawad M, Steuwer A, Kilcoyne SH, Shore RC, Cywinski R, Wood DJ. 2D mapping of texture and lattice parameters of dental enamel. Biomaterials 2007;28:2908–14.
[9] Poole DFG, Brooks AW. The arrangement of crystallites in enamel prisms. Arch Oral Biol 1961;5:14.
[10] Nakamura T, Lu C, Korach CS. Mechanical properties of tooth enamel: microstructural modeling and characterization. Conf Proc Soc Exp Mech Ser 2011;9999:171–9.
[11] Bechtle S, Ozcoban H, Lilleodden ET, Huber N, Schreyer A, Swain MV, et al. Hierarchical flexural strength of enamel: transition from brittle to damage-tolerant behaviour. J R Soc Interface 2012;9:1265–74.
[12] Sui T, Sandholzer MA, Baimpas N, Dolbnya IP, Walmsley AD, Lumley PJ, et al. Multi-scale modelling and diffraction-based characterization of elastic behaviour of human dentine. Acta Biomater 2013;9:7937–47.
[13] Young ML, DeFouw J, Almer JD, Dunand DC. Load partitioning during compressive loading of a Mg/MgB2 composite. Acta Mater 2007;55:3467–78.
[14] Deymier-Black AC, Almer JD, Stock SR, Haeffner DR, Dunand DC. Synchrotron X-ray diffraction study of load partitioning during elastic deformation of bovine dentin. Acta Biomater 2010;6:2172–80.
[15] Giri B, Almer JD, Dong XN, Wang XD. In situ mechanical behavior of mineral crystals in human cortical bone under compressive load using synchrotron X-ray scattering techniques. J Mech Behav Biomed 2012;14:101–12.
[16] Almer JD, Stock SR. High energy X-ray scattering quantification of in situ-loading-related strain gradients spanning the dentinoenamel junction (DEJ) in bovine tooth specimens. J Biomech 2010;43:2294–300.
[17] Singhal A, Almer JD, Dunand DC. Variability in the nanoscale deformation of hydroxyapatite during compressive loading in bovine bone. Acta Biomater 2012;8:2747–58.
[18] Almer JD, Stock SR. Internal strains and stresses measured in cortical bone via high-energy X-ray diffraction. J Struct Biol 2005;152:14–27.
[19] Sui T, Sandholzer MA, Baimpas N, Dolbnya IP, Landini G, Korsunsky AM. Hierarchical modelling of elastic behaviour of human enamel based on synchrotron diffraction characterisation. J Struct Biol 2013; in press.
[20] Fujisaki K, Todoh M, Niida A, Shibuya R, Kitami S, Tadano S. Orientation and deformation of mineral crystals in tooth surfaces. J Mech Behav Biomed 2012;10:176–82.
[21] Nogueira BCL, Fernandes PM, Santana LNS, Lima RR. Ultrastructural characterization of bovine and buffalo enamel through scanning electron microscopy. In: XXIII Congress of the Brazilian Society of Microscopy and Microanalysis; 2011.
[22] Dally JW, Riley WF. Experimental stress analysis. 3rd ed. New York: McGraw-Hill; 1991.
[23] Xie ZH, Swain MV, Swadener G, Munroe P, Hoffman M. Effect of microstructure upon elastic behaviour of human tooth enamel. J Biomech 2009;42:1075–80.
[24] Berger MJ, Hubbell JH, Seltzer SM, Coursey JS, Zucker DS. XCOM: Photon Cross Section Database 1.2; 1999. Available from: http://physics.nist.gov/xcom.
[25] Young ML, Almer JD, Daymond MR, Haeffner DR, Dunand DC. Load partitioning between ferrite and cementite during elasto-plastic deformation of an ultrahigh-carbon steel. Acta Mater 2007;55:1999–2011.
[26] Korsunsky AM, Baimpas N, Song X, Belnoue J, Hofmann F, Abbey B, et al. Strain tomography of polycrystalline zirconia dental prostheses by synchrotron X-ray diffraction. Acta Mater 2011;59:2501–13.
[27] Hammersley AP. FIT2D: an introduction and overview. ESRF Internal Report; 1997.
[28] Huang Z, Newcomb CJ, Bringas P, Stupp SI, Snead ML. Biological synthesis of tooth enamel instructed by an artificial matrix. Biomaterials 2010;31:9202–11.
[29] Mura T. Micromechanics of defects in solids. 2nd rev. ed. Dordrecht: Martinus Nijhoff/Kluwer; 1987.
[30] Clyne TW, Withers PJ. An introduction to metal matrix composites. Cambridge: Cambridge University Press; 1993.
[31] Ochsner A, Ahmed W. Biomechanics of hard tissues. New York: John Wiley & Sons; 2011.
[32] McCrum NG, Buckley CP, Bucknall CB. Principles of polymer engineering. 2nd ed. Oxford: Oxford University Press; 1997.
[33] Powers JM, Farah JW. Apparent modulus of elasticity of dental amalgams. J Dent Res 1975;54:902.
[34] Qin Q-H, Swain MV. A micro-mechanics model of dentin mechanical properties. Biomaterials 2004;25:5081–90.
[35] Huo B. An inhomogeneous and anisotropic constitutive model of human dentin. J Biomech 2005;38:587–94.
[36] Taylor JR. An introduction to error analysis: the study of uncertainties in physical measurements. 2nd ed. Sausalito, CA: University Science Books; 1997.
[37] Takagi S, Liao H, Chow LC. Effect of tooth-bound fluoride on enamel demineralization/remineralization in vitro. Caries Res 2000;34:281–8.
[38] Bar-On B, Wagner HD. Elastic modulus of hard tissues. J Biomech 2012;45:672–8.
[39] Jones RM. Mechanics of composite materials. 2nd edn. Philadelphia, PA, London: Taylor & Francis; 1999.
[40] Withers PJ, Stobbs WM, Pedersen OB. The application of the Eshelby method of internal-stress determination to short fiber metal matrix composites. Acta Metall Mater 1989;37:3061–84.

Journal of Structural Biology 184 (2013) 136–146

Contents lists available at ScienceDirect

Journal of Structural Biology

journal homepage: www.elsevier.com/locate/yjsbi

Hierarchical modelling of elastic behaviour of human enamel based on synchrotron diffraction characterisation

Tan Sui [a,*], Michael A. Sandholzer [b], Nikolaos Baimpas [a], Igor P. Dolbnya [c], Gabriel Landini [b], Alexander M. Korsunsky [a]

[a] Department of Engineering Science, University of Oxford, Parks Road, Oxford OX1 3PJ, United Kingdom
[b] School of Dentistry, College of Medical and Dental Sciences, University of Birmingham, St Chad's Queensway, Birmingham B4 6NN, United Kingdom
[c] Beamline B16, Diamond Light Source, Harwell Oxford Campus, Didcot OX11 0DE, United Kingdom

ARTICLE INFO

Article history:
Received 3 August 2013
Received in revised form 20 September 2013
Accepted 26 September 2013
Available online 7 October 2013

Keywords:
Enamel
WAXS/SAXS
Eshelby
Mechanical properties

ABSTRACT

Human enamel is a hierarchical mineralized tissue with a two-level composite structure. Few studies have focused on the structure–mechanical property relationship and its link to the multi-scale architecture of human enamel, whereby the response to mechanical loading is affected not only by the rod distribution at micro-scale, but also strongly influenced by the mineral crystallite shape, and spatial arrangement and orientation. In this study, two complementary synchrotron X-ray diffraction techniques, wide and small angle X-ray scattering (WAXS/SAXS) were used to obtain multi-scale quantitative information about the structure and deformation response of human enamel to *in situ* uniaxial compressive loading. The apparent modulus was determined linking the external load and the internal strain in hydroxyapatite (HAp) crystallites. An improved multi-scale Eshelby model is proposed taking into account the two-level hierarchical structure of enamel. This framework has been used to analyse the experimental data for the elastic lattice strain evolution within the HAp crystals. The achieved agreement between the model prediction and experiment along the loading direction validates the model and suggests that the new multi-scale approach reasonably captures the structure–property relationship for the human enamel. The ability of the model to predict multi-directional strain components is also evaluated by comparison with the measurements. The results are useful for understanding the intricate relationship between the hierarchical structure and the mechanical properties of enamel, and for making predictions of the effect of structural alterations that may occur due to the disease or treatment on the performance of dental tissues and their artificial replacements.

1. Introduction

Enamel, a highly mineralized substance, is a hard and brittle outer layer above the amelo-dentinal junction (ADJ) that covers the crown portion of the tooth, serving as an important stiff and wear-resistant part of teeth. It is a biological composite with a complex hierarchical structure, mainly composed of high content of inorganic biological hydroxyapatite (HAp) crystals (approximately 25–30 nm of thickness). Enamel consists of 80–90% inorganic material by volume (around 96% by weight) (Bechtle et al., 2012) and relatively low content of organic globular protein (Ang et al., 2012; He, 2008). At the macro-scale level, the enamel can be seen as a continuum, while at the micro-scale some notable features are present, in particular, aligned long prisms (or rods) with a specific "keyhole" shape, with the top oriented toward the crown of the tooth (Macho et al., 2003). On the nano-scale level, enamel is modelled as a composite with ribbon-like HAp particles organized and bundled together by globular protein (Kerebel et al., 1979).

Understanding the effect of microstructural alterations of enamel on the performance of teeth requires the knowledge of how the mechanical properties are related to the complex hierarchical structure. Over half a century, research has been carried out on the mechanical properties of enamel, and on its macro- and micro-structure (He, 2008; Nakamura et al., 2011). However, few studies have focused on the influence of the nano-scale structure (Bechtle et al., 2012; Habelitz et al., 2001), where the macroscopic mechanical response can be considered to be a function of crystal shape and orientation of the mineral phase (Sui et al., 2013). Investigations at the nano-scale require the use of advanced techniques and systematic models to establish a firm basis for understanding the hierarchical structure–property relationships.

One suitable technique for the study of nano-structure is small angle X-ray scattering (SAXS), an advanced non-destructive

* Corresponding author. Fax: +44 18652 73010.
E-mail address: tan.sui@eng.ox.ac.uk (T. Sui).

1047-8477/$ - see front matter © 2013 Elsevier Inc. All rights reserved.
http://dx.doi.org/10.1016/j.jsb.2013.09.023

technique widely used to reveal quantitative information about the orientation and degree of alignment in crystalline and amorphous materials (Fratzl et al., 1996). Another X-ray technique, wide angle X-ray scattering (WAXS), is widely used to quantify the internal strain in crystal lattices, including in response to external loading, e.g. *in situ* compression or tension (Young et al., 2007a,b). SAXS/WAXS have been applied only recently to the study of mineralized biological composites, such as bones and bovine teeth (Almer and Stock, 2005, 2010; Deymier-Black et al., 2010; Singhal et al., 2012). Deymier-Black et al. (Deymier-Black et al., 2010) determined the longitudinal apparent modulus of hydroxyapatite (HAp) in bovine dentine using synchrotron based WAXS, while strain distribution across the ADJ in bovine teeth was investigated by Almer and Stock (Almer and Stock, 2010). None of these studies were performed on human enamel, in which different particularities of its morphology are expected to result in differences in the mechanical properties (Nogueira et al., 2011). Moreover, very few studies devoted to human enamel have been published (Fujisaki et al., 2012), and early studies did not take into account the nanoparticle shape, size and orientation distribution (Bechtle et al., 2012). Therefore, a deep understanding of the relationship between the nano-scale structure and the macroscopic mechanical behaviour of human enamel is still lacking.

Many models of composite mechanical behaviour have been proposed, notably the Voigt and Reuss bounds, as well as the Jones (Jones, 1999) and BW models (staggered microstructural model) (Bar-On and Wagner, 2012). Besides these, an improved multi-level model, based on the original Eshelby inclusion model (Takao and Taya, 1987; Withers et al., 1989) has been established and successfully applied in the evaluation of the mechanical response of human dentine by capturing the relationship between the nano-scale structure and macroscopic loading (Sui et al., 2013).

In this study, the *in situ* synchrotron technique, simultaneous SAXS/WAXS, was used to measure the elastic crystallite strain (WAXS), the alterations in crystal orientation and the degree of alignment of nano-scale HAp crystals (SAXS) in human enamel subjected to an externally applied uniaxial compressive loading along the approximately longitudinal direction with respect to the preferential rod orientation. The multi-scale Eshelby model was modified and extended to capture the hierarchical structure and properties of the human enamel. The model predictions were verified by comparison with experimental data. The ability of the model to capture the observed response is discussed.

2. Materials and method

2.1. Sample preparation

A freshly extracted normal human third molar (ethical approval obtained from the National Research Ethics Committee; NHS-REC reference 09.H0405.33/Consortium R&D No. 1465) was washed and cleaned in distilled water to eliminate residues so that the possibility of contamination or other chemical effect was excluded. The samples were kept for a maximum of 7 days in distilled water in a commercial fridge at 4 °C until the experiment was performed, implying relatively low diffusion rates that impede or exclude any possible superficial demineralization effect of water. It is also important to highlight that the technique we employed (X-ray diffraction in transmission) is a bulk, not a surface technique. As a consequence, even if small superficial changes were to arise, their contribution to the overall scattered signal would be negligible. Thus, the composition of the inorganic phase in the dental tissue was well-represented by pure organically-derived HAp. The crown was cut off below the ADJ using a low speed diamond saw (Isomet Buehler Ltd., Lake Bluff, Illinois, USA) and further cut into smaller cubes, and a series of polishing papers were used to produce the final $2 \times 2 \times 2$ mm cube of enamel. Regarding the rod direction of the enamel sample, the cut in the prepared sample was close to the region perpendicular to the occlusion surface. Therefore, the predominant rod direction was assumed to be in the longitudinal direction of the sample.

2.2. Micro-CT protocol and data processing

To determine the measuring positions and loading cross-section for the SAXS/WAXS experiments, a micro-CT scan was carried out at 1.9 μm resolution using 40 kV voltage, 120 μA current and a 0.5 mm Aluminium filter (SkyScan 1172, Bruker microCT, Kontich, Belgium). The resulting slices were reconstructed using the SkyScan NRECON software package, and subsequent 3-D planning models were created using Fiji imaging software (Eliceiri et al., 2012).

2.3. In situ scattering measurements

The experiment was performed on the B16 beamline at Diamond Light Source (DLS, Oxford, UK). A schematic diagram of the experimental set-up is shown in Fig. 1a. The sample of human enamel was slowly deformed in compression along the *x*-direction in the laboratory coordinates (Fig. 1a) at the displacement rate of 0.2 mm/min until failure, using a remotely operated and monitored compression rig (Deben, Suffolk, UK), with a 5kN calibrated load cell. The rig was equipped with custom-made jaws, allowing a high-energy transmission X-ray setup to be used.

The monochromatic X-ray beam at the photon energy of 17.99 keV was used and collimated to the spot size of 0.5×0.5 mm. The beam was incident at the sample in the direction perpendicular to its loading direction. Two separate WAXS and SAXS detectors were alternately setup to collect the patterns at consecutive loading increments downstream of the beam. The global *Z*-axis is along the beam direction; global *X*-axis corresponds to the horizontal (loading) direction, Y to the vertical. The *X*–*Y* plane is parallel to the detector plane. WAXS diffraction patterns were recorded using a Photonic Science Image Star 9000 detector (Photonic Science Ltd., UK) placed at a sample-to-camera distance of 128.72 mm. Further downstream, a Pilatus 300 K detector (Dectris, Baden, Switzerland) was positioned at a distance of 4358.47 mm to collect the SAXS patterns. In order to record both the WAXS and SAXS patterns at each scanning location, the WAXS detector was translated laterally to expose the SAXS detector after each WAXS exposure. A lightly compacted disk of standard silicon powder and a dry chicken collagen sample inserted close to the sample position were used as calibration standards and to determine the sample-to-detector distance with the required precision (Calibration, 2013).

2.4. Scattering data analysis

2.4.1. WAXS data analysis

WAXS data can be interpreted in terms of the shift of the diffraction peak obtained from a cluster of HAp crystals, so that the average micro-strain (lattice strain) in the crystals can be deduced (Young et al., 2007a,b). The typical WAXS pattern of HAp is shown in Fig. 2a (only the (002) peak is selected for interpretation). At each compressive load step, the beam was scanned between the loading platens, and only the results from the middle were selected for WAXS interpretation to guarantee that the same location was studied during compressive deformation. The elastic lattice strain of the HAp phase was computed by calculating the changes in the inter-planar spacing between the crystal planes (Korsunsky et al., 2011):

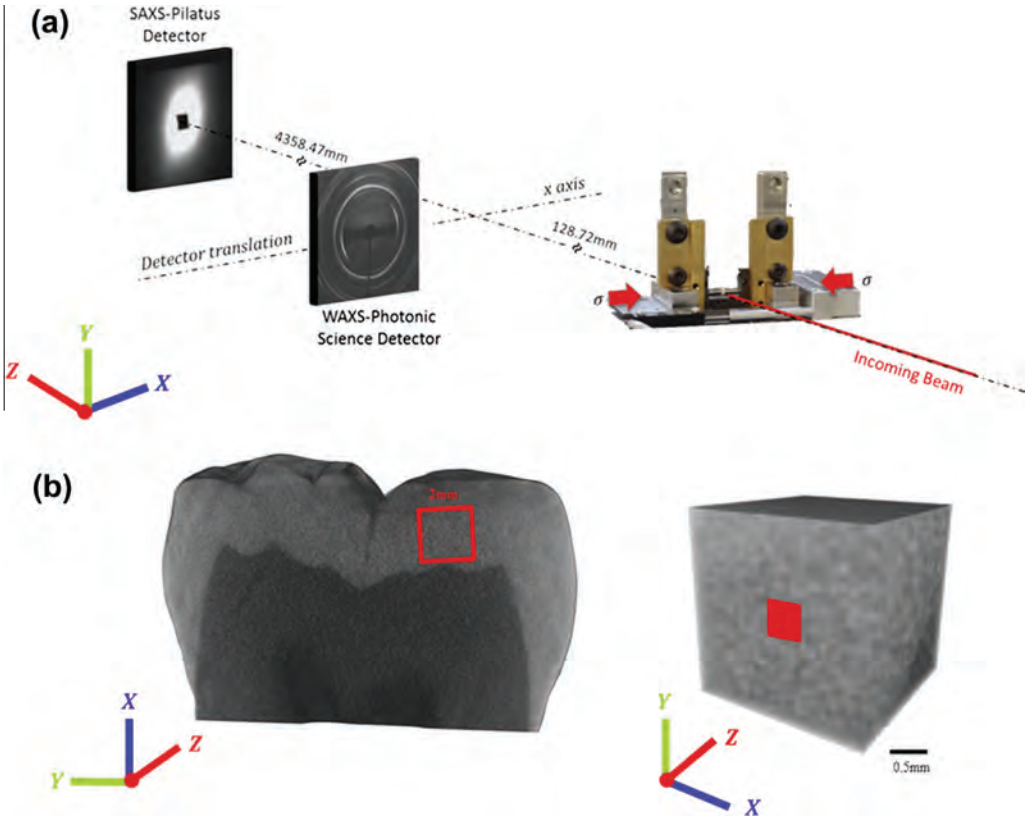

Fig.1. Schematic diagram of experimental setup and sample preparation; (a) the sample was under uniaxial compressive loading on the compression stage. The monochromatic X-ray beam was directed perpendicular to the sample surface and the loading direction. WAXS and SAXS diffraction patterns were recorded at each loading step at three locations on the sample. The WAXS detector was translated laterally out of the beam to expose the SAXS detector after each collection of WAXS and (b) micro-CT based models of the two preparation stages. (1) Cross-section of reconstructed human dental model with region to be cut marked by red square and (2) the final $2 \times 2 \times 2$ mm cubes of enamel. The red square in the middle indicates the central position of the X-ray beam. (For interpretation of the references to colour in this figure legend, the reader is referred to the web version of this article.)

$$\varepsilon = \frac{d_{002} - d^0_{002}}{d^0_{002}} \tag{1}$$

where d_{002} is the deformed d-spacing and d^0_{002} is the reference strain-free value. In detail, 2D diffraction images were firstly pre-processed using Fit2D (Hammersley, 1997). The (002) peak of interest from each pattern was "caked" (a professional jargon term used to refer to the selection of a sector in the radial–azimuthal coordinates of each pattern, and binning the data to obtain the equivalent 1D radial pattern) within the range of 20° around the loading direction (Fig. 2a). The strain measurement needs high quality of peaks in order to determine the shift of the peak centre by Gaussian fitting. The smaller the angular width of the bin is, the lower (or noisier) the integrated (averaged) intensity will be. Since the crystalline perfection in biomaterials is not as good as that in the pure crystal, the binning angle of 20° is often used in order to guarantee the pronounced peak to fit. Furthermore, each pattern was "caked" with the same width of 20° in the direction of −15°, 0°, 15°, 30° and 45° of the (002) peak (see Fig. 2a). The normal strain component along the centre direction of each "cake slice" represents the strain component in the corresponding orientation. Subsequently the 1D radial plot of each individual (002) peak within each sector was fitted with a Gaussian function to obtain the peak centre position. The sample under strain-free condition (without any load) was characterised by WAXS and used as the reference state for strain measurement. As the load increased, the shift of the peak centre position with respect to the strain-free reference point allowed the calculation of the HAp elastic lattice strain. In addition, the structural orientation angle was determined from the strain-free sample by azimuthal–radial "caking" of the (002) peak over the range of available peak (−30° ∼ 60°), and fitting the azimuthal centre position of the pronounced peaks of $I_{WAXS}(\varphi)$∼$\varphi_{\_WAXS}$ plot (Fig. 2c) (Al-Jawad et al., 2007).

2.4.2. SAXS data analysis

For SAXS data analysis, the pattern from the strain-free enamel sample was taken as a reference. Due to the dense packing of crystals in enamel, it is the electron density change occurring in the gaps between crystalline particles that gives rise to the scattering signal (Tanaka et al., 2010). It is also understood that the orientation of the gaps between rods roughly coincides with the orientation of the crystals within the rod (Tanaka et al., 2010). Thus, the information from gap scattering can be used to deduce the orientation and degree of alignment (percentage of aligned particles) of HAp crystals. To quantify it, the 2D SAXS patterns were processed by integrating over the entire relevant range of scattering vector q, resulting in a function $I_{SAXS}(\varphi)$ of the azimuthal angle $\varphi_{\_SAXS}$ (Fig. 2d) (Tesch et al., 2001, 2003). The predominant orientation ϕ_{0_SAXS} of the mineral crystals is determined by the position of the two peaks in the plot of $I_{SAXS}(\varphi)$ (e.g. ϕ_{0_SAXS} in Fig. 2d), which is corresponding to the short axis of SAXS pattern. Further, the degree of alignment ρ with respect to the predominant orientation of HAp can be calculated by the ratio of the two areas under the curve of $I_{SAXS}(\varphi)$:

$$\rho = \frac{A_{oriented}}{A_{oriented} + A_{unoriented}} \tag{2}$$

where $A_{unoriented}$ is the area of constant background level accounting for the scattering from unoriented particles and $A_{oriented}$ depicts the total area below the curve of $I_{SAXS}(\varphi)$∼$\varphi_{\_SAXS}$ subtracting $A_{unoriented}$.

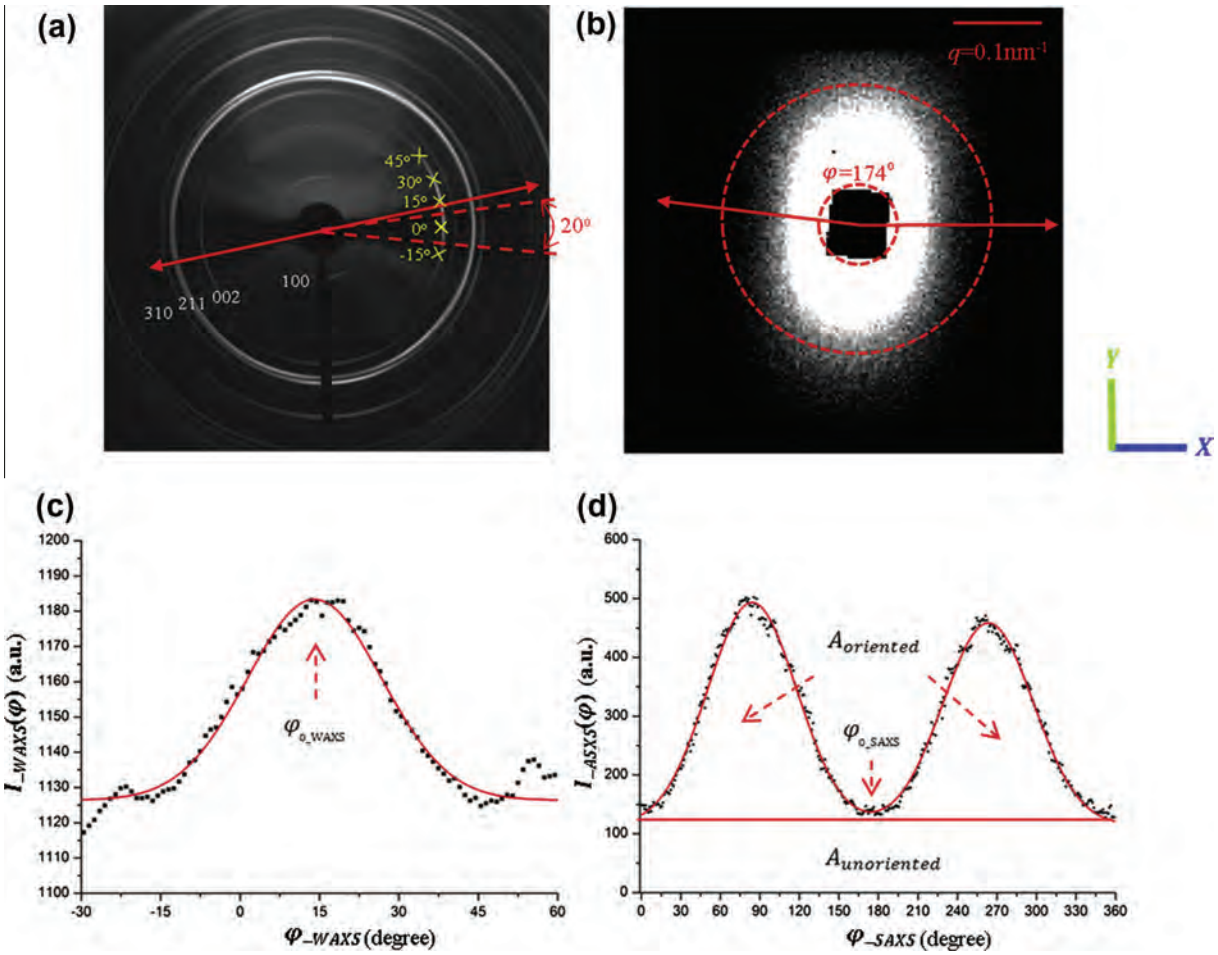

Fig.2. (a) A representative enamel WAXS pattern of Debye–Scherrer rings with different intensities. The dark region in the centre is the beamstop. The (002) peak is marked with a small red arrow. Peak shifts at different positions on the (002) ring represent the average strains of (002) along different directions. Multiple angles with respect to the global *X*-axis were caked (within a 20° range) in order to examine the strain variation (five angles are shown as examples −15°, 0°, 15°, 30°, 45°). The direction with the double-arrow line indicates the orientation interpreted from WAXS, (b) a representative enamel SAXS pattern. The direction of the short axis of the ellipse pattern indicates the predominant orientation of the HAp crystals. The integration over q was performed from the beamstop radius to the outer radius of the pattern as marked with red dash, (c) a plot of $I_{WAXS}(\varphi)\sim\varphi_{\_WAXS}$ without any external load (black dots, Gaussian fit indicated in red). The predominant orientation $\varphi_{0\_WAXS} = 14°$ is given by the position of the pronounced peak centre and (d) a plot of $I_{SAXS}(\varphi)\sim\varphi_{\_SAXS}$ without any external load (black dots, Gaussian fit shown in red). The predominant orientation $\phi_{0\_SAXS} = 174°$ is the average position of the two peaks. The ratio $A_{oriented}/(A_{oriented} + A_{unoriented})$ gives the degree of alignment. (For interpretation of the references to colour in this figure legend, the reader is referred to the web version of this article.)

Thus, the value of ρ ranges from 0 to 1, with $\rho = 0$ indicating no predominant orientation within the plane of the section, while $\rho = 1$ indicates a perfect alignment of all the crystals (Tesch et al., 2001, 2003).

3. Model formulation

3.1. Geometrical assumptions

Human enamel has a hierarchical two-level composite structure, where the first level is represented by a rod with a keyhole-like section and the second level by the organized and bundled HAp crystallites within each rod (Nanci and Ten Cate, 2003). Fig. 3a shows the keyhole-like microstructure of enamel, modified from Habelitz (Habelitz et al., 2001) and the distribution of the HAp crystals within the rod in 3D. Fig. 3b–d provides schematic illustration of the geometric model derived from the enamel structure, where the first-level regards the whole enamel sample as composed of aligned rods bundled by the joining medium of globular protein phase (Fig. 3b), and the second level considers the rod as a composite in detail, consisting of partially aligned HAp crystals and globular proteins.

In theoretical model, especially in describing complex systems, some reasonable simplifications need to be made in order to capture the basic mechanism. Thus the direction of rods in the first level is assumed to be uniform to minimize the number of variables. Based on the objective of this study, which is the nano-scale particle distribution effect on macro-scale elastic behaviour, WAXS and SAXS could capture the orientation distribution (i.e. texture) of HAp crystals in the second level, which in turn can be used to reflect the orientation inside actual rod in the gauge volume since the rod is composed by HAp crystallites. The partially aligned distribution of HAp crystals is based on the observation using scanning transmission electron microscopy (STEM), where a high percentage of HAp crystals have a perfect alignment while the other crystals are more randomly distributed (Huang et al., 2010). Both levels are non-dilute systems consisting of a number of inhomogeneous inclusions. For simplicity, both rod and HAp crystals are assumed to be of ribbon-like shape (Fig. 3b–d).

In a previous study of dentine, the penny-shape inclusion was used to simulate the platelet-like structure of HAp crystals in human dentine (Sui et al., 2013). As for the ribbon-like shaped HAp crystals in human enamel, a ribbon-shaped inclusion is used to simulate an individual HAp crystal. In the Eshelby approach, the cylinder is approximated by a prolate spheroid described by the

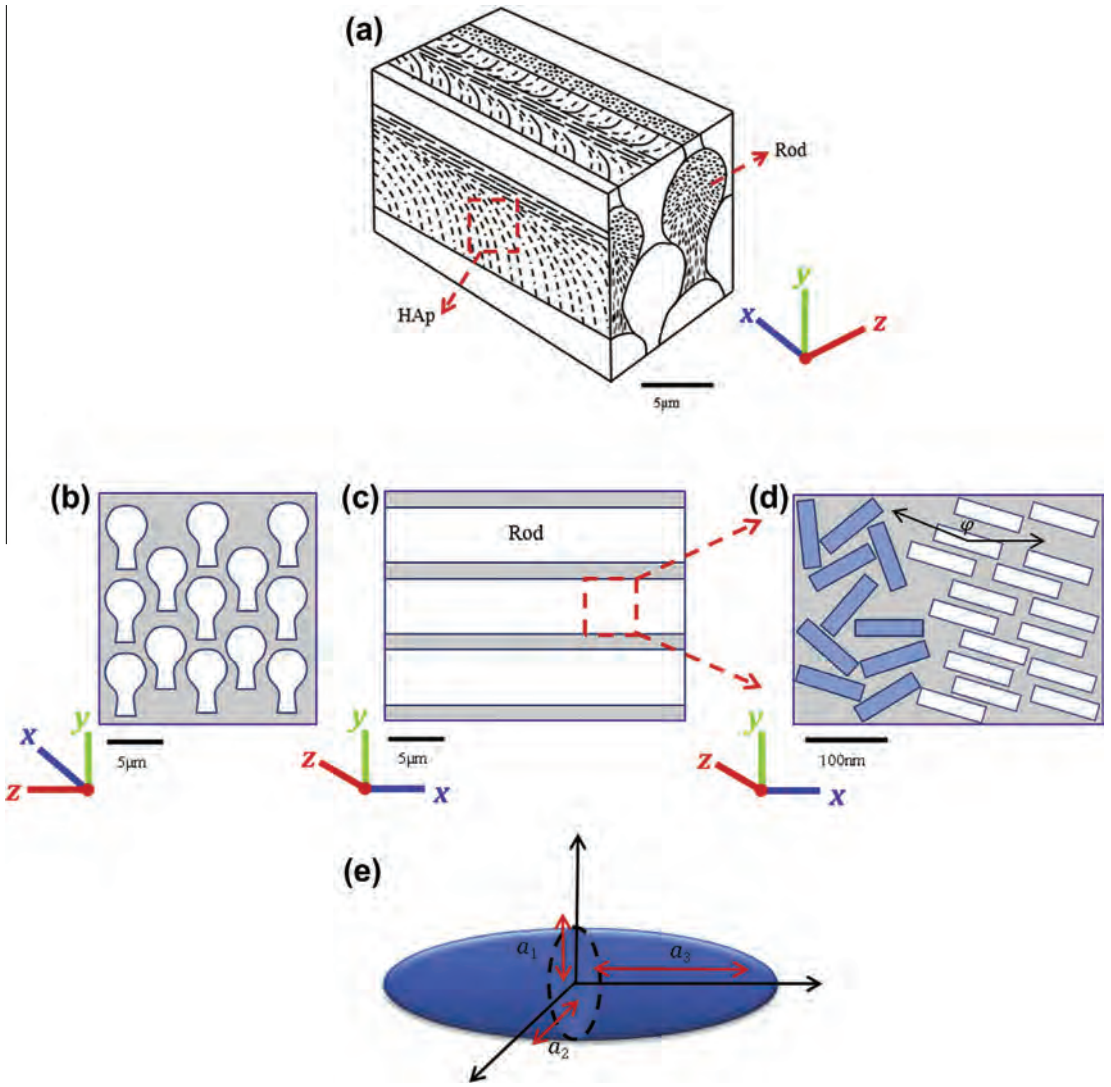

Fig.3. (a) A schematic 3D structure of enamel, showing keyhole-like rods aligned in parallel (modified from Habelitz (2001). The rods contain organized and bundled HAp crystals, (b) rods viewed along their longitudinal direction, (c) rods viewed along their transverse direction, (d) the structure of partial aligned ribbon-like HAp crystals viewed from the cross-section parallel to the rods direction. The alignment angle φ with respect to the global X-axis is also shown and (e) a typical prolate spheroid inclusion model with principal half axis a_1, a_2 and a_3.

three dimensions, a_1, a_2 and a_3 in Fig. 3e. Normally $a_1 = a_2 \ll a_3$, i.e. the cross section is a circle (Mura, 1987). The crystal c-axis (corresponding to the (002) peak) of ribbon-like shaped HAp crystals is normal to the cross section of the cylinder, i.e. along a_3 direction (Huang et al., 2010). In the next section, the model is briefly introduced, while a detailed derivation is shown in Appendix.

3.2. First-level model: multiple aligned rod inclusions within enamel sample

The purpose of the first-level model for human enamel, which describes multiple aligned rod inclusions within enamel, is to establish the elastic relationship between the externally applied stress σ^A and the stress in the rod-like inclusions $\sigma^{inclusion} = \sigma^{rod}$. According to the Eshelby model derivation (Clyne and Withers, 1995), the stress in the rod can be expressed as

$$\sigma^{rod} = \{T - (1 - f_1)C_{matrix}(S_1 - I)\{(C_{matrix} - C_{rod})[S_1 - f_1(S_1 - I)] - C_{matrix}\}^{-1}(C_{matrix} - C_{rod})T^{-T}C_{matrix}^{-1}\}\sigma^A$$

$$\text{or, written more simply,} \quad \sigma^{rod} = H\sigma^A \tag{3}$$

In the above expression, f_1 is the volume fraction of rods in the enamel, S_1 is the Eshelby tensor for a cylinder that approximates the rod shape, C_{matrix}, C_{rod} are the stiffness tensors of the globular protein and rod respectively, and T is the tensor transformation (rotation) matrix that depends on the Euler angles (see Appendix) giving the orientation of an individual rod with respect to the laboratory coordinate system. In the present model, the laboratory coordinates were fixed, and it was assumed that the rods were all aligned along the loading direction, thus T was constant. The rod stiffness remains to be determined from the second level model.

3.3. Second-level model: partially aligned HAp inclusions within each individual rod

The purpose of the second-level model of enamel, which describes partially aligned HAp inclusions within one rod, is to establish the relationship between the rod inclusion stress and the average strain in the HAp crystals in rod $\langle\varepsilon\rangle^{HAp}$ ($\sigma^{rod} = K_1\langle\varepsilon\rangle^{HAp}$). The measured crystal strain corresponds to the mean strain value for all the crystals within the considered gauge volume (Chou et al., 2012). Due to the partial alignment of HAp crystals within

the rod, the real apparent stiffness K_1 is to be given by the values bounded by the two extreme cases, namely that of fully random distribution and that of perfect alignment.

3.3.1. Multiple perfectly aligned HAp crystals

Supposing all the crystals are perfectly aligned and the alignment direction is described by the transformation matrix T, the relationship between the average HAp strain and the rod inclusion stress obtained from the first-level model can be established as follows:

$$\langle\varepsilon\rangle^{HAp}_{aligned} = \left\{\left\{\left(I - C^{-1}_{matrix}\langle C\rangle_{HAp}\right)^{-1}[\langle S_2\rangle - f_2(\langle S_2\rangle - I)]^{-1} - I\right\}^{-1} T^{-T} + T^{-T}\right\} C^{-1}_{matrix}\sigma^{rod} \quad \text{or expressed more simply} \quad \sigma^{rod} = K_{aligned}\langle\varepsilon\rangle^{HAp}_{aligned} \tag{4}$$

where $\langle C\rangle_{HAp}$ and $\langle S_2\rangle$ are the average stiffness and Eshelby tensor. Since all the crystals are perfectly aligned, $\langle C\rangle_{HAp}$ and $\langle S_2\rangle$ can be represented by the single crystal values $\langle C\rangle_{HAp} = C_{HAp}$, $\langle S_2\rangle = S_2$. Note that a single HAp crystal in the second level can be regarded as a single inhomogeneity with ribbon-like shape, thus the Eshelby tensor for a single HAp should be the same as the rod inclusion ($S_2 = S_1$) and the stiffness of a single HAp has been reported to be transversely isotropic (Ochsner and Ahmed, 2011). In Eq. (4), different orientation angles (different T) would lead to different values of $\langle\varepsilon\rangle^{HAp}_{aligned}$.

3.3.2. Multiple randomly distributed HAp crystals

Supposing all the crystals are randomly distributed the relationship between average HAp crystal strains and rod stress is independent of the transformation matrix in Eq. (4). Thus the relationship becomes

$$\langle\varepsilon\rangle^{HAp}_{random} = \left\{\left\{\left(I - C^{-1}_{matrix}\langle C\rangle_{HAp}\right)^{-1}[\langle S_2\rangle - f_2(\langle S_2\rangle - I)]^{-1} - I\right\}^{-1} + I\right\} C^{-1}_{matrix}\sigma^{rod} \quad \text{or expressed more simply} \quad \sigma^{rod} = K_{random}\langle\varepsilon\rangle^{HAp}_{random} \tag{5}$$

Different from perfectly aligned crystals, the average value of $\langle S_2\rangle$ can no longer be the value of a single crystal, but should be obtained by the volume average value of all the crystals. However, as an alternative, the averaging effect can be captured by using the single crystal relationship as Eq. (4) and averaging over all the values with different Euler angles (see Appendix, averaging the results obtained from each single crystal relationship as Eq. (4) over all possible orientations).

3.3.3. The combination of random and aligned HAp inclusions

In order to model the observed preferred orientation of HAp inclusions (Fig. 3d), we represent it as the combination of a random distribution with a volume fraction $f_{aligned}$ of perfectly aligned particles. In this case the overall apparent stiffness $K^{HAp}_{partial\_aligned}$ is given by the rule of mixture between K_{random} and $K_{aligned}$:

$$K^{HAp}_{partial\_aligned} = (1 - f_{aligned})K_{random} + f_{aligned}K_{aligned} \tag{6}$$

where $(1 - f_{aligned})$ now represents the volume fraction of the randomly distributed, and $f_{aligned}$ corresponds to the degree of alignment of crystals revealed by SAXS. Thus, the relationship between rod inclusion stress and average internal HAp lattice strain becomes

$$\sigma^{rod} = K^{HAp}_{partial\_aligned}\langle\varepsilon\rangle^{HAp} \tag{7}$$

3.4. Determination of the rod stiffness

In Eq. (3), the stiffness of the rod C_{rod} still remains to be determined. Since the rod is regarded as a composite consisting of globular protein and mineral HAp crystals, C_{rod} can also be determined using the Eshelby inclusion model, taking into account the volume fraction (f_2), average Eshelby tensor ($\langle S_2\rangle$) and average stiffness ($\langle C_{HAp}\rangle$) of HAp crystals in the second level. To simplify the determination, it is assumed that all HAp crystals in the rods are aligned with an angle with respect to the longitudinal direction of rod (thus $\langle C\rangle_{HAp} = C_{HAp}$, $\langle S_2\rangle = S_2$). Such orientation is the preferred orientation revealed by SAXS/WAXS and is reflected in the model by a unique transformation matrix T_{HAp}. The expression of the stiffness of rod is given here without detailed derivation

$$C_{rod} = \left\{C^{-1}_{matrix} - f_2\left\{(\tilde{C}_{HAp} - C_{matrix})\left[\tilde{S}_2 - f_2(\tilde{S}_2 - I)\right] + C_{matrix}\right\}^{-1} (\tilde{C}_{HAp} - C_{matrix})C^{-1}_{matrix}\right\}^{-1} \tag{8}$$

where $\tilde{S}_2 = T^{T}_{HAp}S_2T^{-T}_{HAp}$ is the transformed Eshelby tensor and $\tilde{C}_{HAp} = T^{-1}_{HAp}C_{HAp}T^{-T}_{HAp}$ is the transformed stiffness of aligned transversely isotropic HAp crystals. Further, the overall relationship between the average HAp strain and the externally applied stress can be established by combining Eqs. (3) and (7).

$$\sigma^{A} = H^{-1}\sigma^{rod} = H^{-1}K^{HAp}_{partial\_aligned}\langle\varepsilon\rangle^{HAp} = K\langle\varepsilon\rangle^{HAp} \tag{9}$$

4. Experiment result and model evaluation

4.1. Nano-scale HAp distribution and mechanical response of enamel

The loading areas of the samples were accurately determined by micro-CT measurement, which is 3.55 mm^2. Fig. 2a shows a WAXS pattern of enamel consisting of a system of Debye–Scherrer rings (peaks). Since the enamel is textured, only limited range of rings can be captured. The apparent radial shifts of the (002) peak in the WAXS pattern were measured under uniaxial compressive loading applied in longitudinal direction with respect to the rod direction. The preferential orientation of HAp crystals obtained by WAXS pattern is shown to be roughly perpendicular to the arc of (002) peak and the detailed value is determined from the stress-free plot of $I_{WAXS}(\varphi)\sim\varphi$ (Fig. 2c) with the Gaussian fit (red line).

The SAXS pattern as shown in Fig. 2b contains the information of orientation and degree of alignment of the gaps between the HAp crystals. As mentioned above, the information about HAp crystallites orientation distribution can be deduced by gap scattering. The preferential orientation shown in Fig. 2b is roughly along the short axis of the elliptical pattern and the detailed value is also determined from the stress-free plot of $I_{SAXS}(\varphi)/\varphi$ (Fig. 2d) with the Gaussian fit (red line). The detailed values of the orientation and degree of alignment obtained by WAXS and SAXS patterns are listed in Table 1, from which these parameters were used in the Eshelby model evaluation.

The shifts of (002) peak from WAXS along x-direction were used to obtain the elastic lattice strain values. Fig. 4 shows the experimental results of the applied stress vs. HAp lattice strain of sample along the loading direction, indicating a linear increase as expected. Two results are given respectively using the preferred orientation angles obtained by SAXS and WAXS but keeping the other parameters the same. The ratio of the uniaxial stress and the average HAp lattice strain gives the apparent modulus (Powers and Farah, 1975), which is listed in Table 1. Meanwhile, the residual (initial) strain was found to be quite small and can therefore be neglected. The shifts of (002) peak along other directions were also measured, e.g. by caking each pattern with the width of 20° along the directions of −15°, 0°, 15°, 30° and 45° to determine the azimuthal variation of the normal strain component. The result is shown as an azimuthal plot in Fig. 5a and b, where 0° represents the loading direction. Note that the normal strain component undergoes a transition from negative and to positive at around 25°.

Table 1
Experimental results from SAXS/WAXS, and the refined structural parameters of the enamel used in the multi-scale Eshelby model (values reported in literature are also presented).

Parameter	Enamel	Reference values
Orientation (from SAXS)	174°	N/A
Orientation (from WAXS)	14°	N/A
Degree of alignment	0.6	N/A
K_exp.	124.3 GPa	N/A
$f_1 = f_2$	95%	95% (Bechtle et al., 2012)
$C_{matix-1}$	E_m = 1 GPa, υ_m = 0.3	$E_{protein}$ = 1 GPa, $\upsilon_{protein}$ = 0.3 (Qin and Swain, 2004)
$C_{matix-2}$	E_m = 1 GPa, υ_m = 0.3	$E_{protein}$ = 1 GPa, $\upsilon_{protein}$ = 0.3 (Qin and Swain, 2004)
C_{HAp}	E_{xx} = 148.42 GPa, G_{xy}= G_{xz}=39.6 GPa $\upsilon_{xy} = \upsilon_{xz}$ = 0.34, υ_{yz} = 0.21 $E_{yy} = E_{zz}$ = 114.26 GPa	E_{xx} = 140 GPa, G_{xy} = G_{xz}=39.6 GPa $\upsilon_{xy} = \upsilon_{xz}$ = 0.3, υ_{yz} = 0.2 $E_{yy} = E_{zz}$ = 114.26 GPa (Ochsner and Ahmed, 2011)
$S_{cylinder_1} = S_{cylinder_2}$	a_1/a_2 = 1	(He, 2008)
K_model (from SAXS)	122.9 GPa	N/A
K_model (from WAXS)	120.4 GPa	N/A

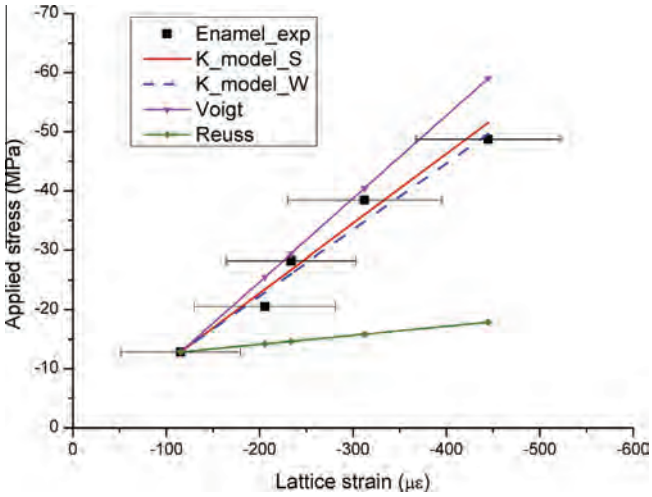

Fig.4. Comparison of experimental data and modelling results of the applied compressive stress vs. elastic lattice strain for HAp crystals. Experimental data (black points) and modelling results (orientation distributions determined by SAXS is in red line and WAXS in blue dash) with the compressive stress along longitudinal direction with respect to the rod direction. The prediction results from models of Voigt (upper line) and Reuss (lower line) are also shown. The stress at failure was 53.5 MPa. (For interpretation of the references to colour in this figure legend, the reader is referred to the web version of this article.)

4.2. Evaluation and testing of multi-scale Eshelby model

In the model, the material properties and other parameters used were taken from the literature, and refined by fitting with the experimental data. The average mineral concentration (HAp volume fraction) has been reported to be ~95% at each level of enamel (Bechtle et al., 2012). In detail, at the first level, 95% represents the volume fraction of rods within the globular proteins, while at the second level, 95% represents the volume fraction of mineral within each rod. This means that the overall volume fraction of mineral in the enamel is 95% × 95% ~90%. In general, Young's modulus of 1 GPa for globular protein is found in the literature, without taking into account the viscoelasticity or viscoplasticity (Huo, 2005; Qin and Swain, 2004). Polycrystalline HAp is considered to be transversely isotropic with five independent elastic constants (Ochsner and Ahmed, 2011). To represent the shape of the rod and of the HAp crystallites for each level, the Eshelby tensor for the cylinder (prolate spheroid) was used. The elliptical semi-axes a_1 and a_2 within the transverse cross-section were assumed to be the same, (a_1/a_2 = 1), but different from a_3. The apparent modulus K was calculated based on the different preferred orientation angles of the HAp crystals obtained by both SAXS and WAXS. All the parameters refined to obtain the best fit are listed in Table 1, as well as the reference values from literature. A comparison of the stress/strain curve along the loading direction between the model prediction and the experiment is plotted in Fig. 4, where the Voigt and Reuss bounds are also indicated. As expected, it is found that the modified Eshelby model prediction lies between the two bounds and gives a satisfactory agreement with the experimental data. Meanwhile, the comparison of normal strain variation with the azimuthal angle is presented in Fig. 5a and b. Fig. 5a gives the model prediction results using different preferred orientation angles of HAp crystals obtained by both SAXS and WAXS. It is apparent that the model prediction of the transverse tensile strain that arises under compression (the Poisson effect) falls short of the observed strain. A satisfactory agreement can be achieved by adding a tensile transverse strain component (along the global Y-axis in Fig. 1) perpendicular to the rod and loading direction (the global X-axis in Fig. 1). The updated result is illustrated in Fig. 5b. This remarkable effect deserves further detailed analysis and discussion.

5. Discussion

The Eshelby model can be constructed to simulate the hierarchical structure. It has the strong physical significance in that it captures the interaction between two different phases (inhomogeneity and matrix), compared with other simple models, like Voigt and Reuss. For the interface, the Eshelby model assumes fully coherent interface, in line with the prevailing view in the literature. The main shortcoming of the shear-lag model (Ji and Gao, 2004) is that it does not consider the influence of the nanoparticle distribution within the enamel. This is the key aspect that Eshelby model allows deeper understanding of the relationship between the nano-scale structure and mechanical behaviour, even though the uniform Eshelby tensor is used to describe the monodisperse distribution of crystal size for the simplifications when developing a theoretical model. Furthermore, the key aspect of interest in this study lies in the apparent modulus of enamel, i.e. the relationship between the strain in the nano-crystallites and the macroscopic material loading. The composite effect cannot be ignored. The woven structure (Palmer et al., 2008) of blocking effect is expected to be effective only during tensile loading rather than the uniaxial

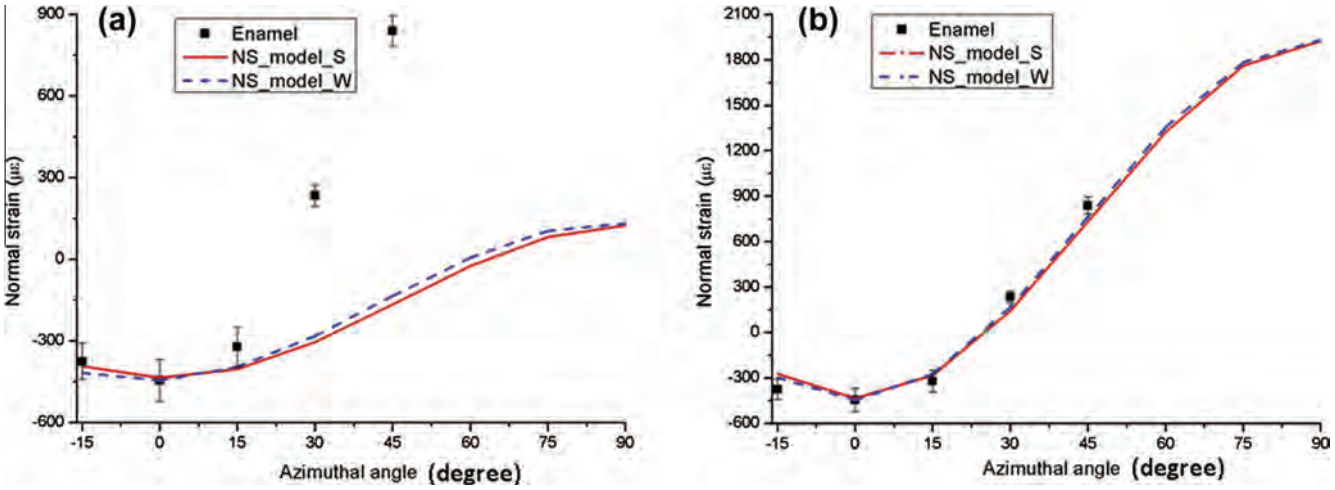

Fig.5. Comparison of experimental data (black markers) and modelling results for the variation of normal strain (NS) with orientation (azimuthal angle). (a) Zero pre-strain model predictions using the orientation distributions determined respectively by SAXS (red curve) and WAXS (blue dash) and (b) modified predictions by the model incorporating tensile pre-strain using the orientation distributions determined respectively by SAXS (red curve) and WAXS (blue dash). (For interpretation of the references to colour in this figure legend, the reader is referred to the web version of this article.)

compressive loading. It is considered particularly when investigating the fracture mechanism of enamel rather than the elastic deformation.

5.1. Refined parameters by Eshelby model

The refined parameters of the multi-scale Eshelby model are listed in Table 1. Most of the values reported in the literature were found to give satisfactory results. The key parameters varied in the analysis were the volume fraction (the volume fraction of rods in the enamel and of HAp crystallites within rods were assumed to be the same) and the elastic constants of the HAp crystal. Among these parameters, the elastic constants have the most significant influence on the result. In the optimization process, the volume fraction was first fixed at the reported value (95%), and the elastic constants, especially the Young's modulus, were refined. Subsequently, other parameters (e.g. the globular protein modulus) were refined as well, although it was found that they have a minor effect on the apparent result. This leads to the conclusion that the elastic modulus of soft globular protein phase, whether it be taken as isotropic or anisotropic, does not exert a large effect on the validation within the scope of model-experiment matching considered here. In addition, the refinement process also helps in the identification of nano-scale parameters, which may be hard to determine directly from the experiments. In addition, the model can be applied to diseased tissues as well, in which case, the model needs to be adjusted correspondingly, given different initial parameters to be refined.

5.2. Residual strain

During the preparation process using a low speed diamond saw and polishing papers, as even during the natural growth, a thin layer of residual strain may be induced at the sample surface. However, as shown in Fig. 4, the pre-existing residual strain is very small. Since only the linear elastic response of enamel is considered in the experiment (reflected in the linearity of the experimental stress–strain curve), the presence of initial residual strain only amounts to an offset that does not affect the parameters like the apparent modulus. Hence, the low level residual strain was neglected in the present analysis.

5.3. Gap scattering of SAXS

The good agreement between the apparent modulus K results calculated using different HAp preferential orientations determined by SAXS and WAXS provides strong evidence and validates the argument that the SAXS pattern arising from gap scattering (Tanaka et al., 2010) can be used to deduce the HAp crystallite orientation distribution, i.e. the gaps are almost parallel to HAp crystals inside the rod. Therefore, we report direct confirmation that SAXS data provides beneficial complimentary information for determining the crystal orientation distribution in enamel and other mineralized tissues.

5.4. Normal strain components variation

The normal strain components variation of the HAp crystals with respect to different azimuthal angles (0–90°) is shown in

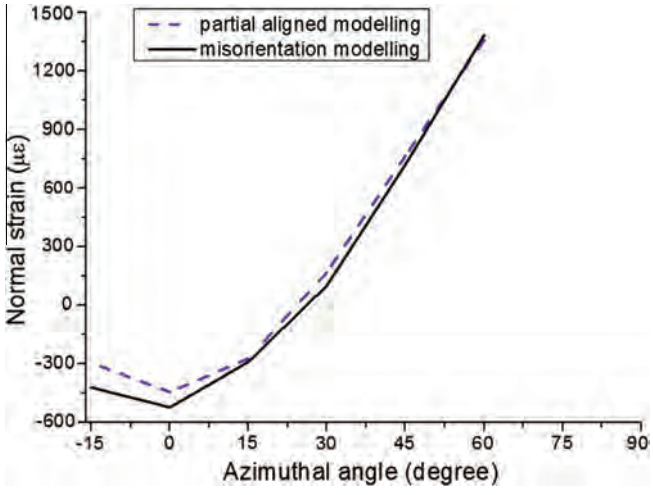

Fig.6. Comparison between the predictions for normal strain variation with the azimuthal angle obtained using the combination of random and perfectly aligned distributions (blue dashed curve) and using continuous orientation distribution modelling (solid black curve). (For interpretation of the references to colour in this figure legend, the reader is referred to the web version of this article.)

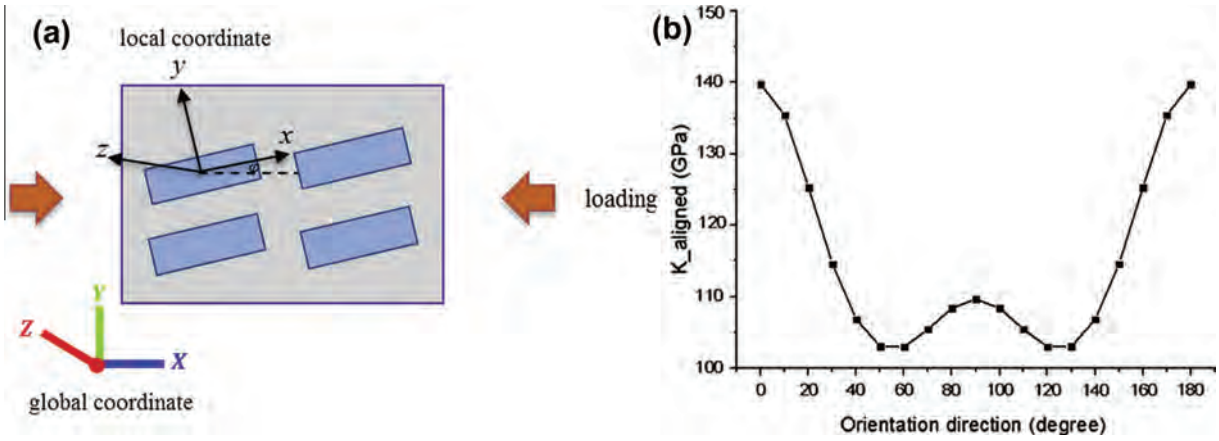

Fig.7. (a) A simplified visualization of the alignment of HAp crystals. The beam direction is along the global *Z*-axis and the alignment here represents the angle between the local *x*-axis and global *X*-axis (initially the aligned angle $\varphi = 0°$, i.e. the local *x*-axis of a ribbon-like shape is initially along the global *X*-axis) and (b) by changing the alignment angle (0–180°), the average strain of the crystals along the loading direction can be obtained by the multi-scale Eshelby model, which then indicates that $K_{aligned}$ varies with respect to the preferential alignment angle.

Fig. 5a. The excellent agreement in the azimuthal plot (shown in Fig. 5b between the experimental data and the modified model incorporating transverse strain) indicates that the deformation state in the sample is likely to be multi-axial, with an additional tensile strain component existing along the transverse direction. An explanation for this observation must lie in the fact that a disproportionately large transverse tensile strain is developed within the sample due to the interaction between the material structure and the loading arrangement. One possible mechanism to explain this is the barrelling effect (mid-section expansion) in the enamel sample: the external uniaxial compression causes local locking of the enamel to the platen surface accompanied by the expansion of the sample perpendicular to the loading direction in the mid-section (where the measurements were performed). In addition, micro-cracks smaller than 2 μm (below the resolution of the micro-CT scan) pre-existing in the enamel may result in the debonding between rods (Bajaj and Arola, 2009), and thus modify the transverse strain. Such mechanisms are not captured by the multi-scale Eshelby model and need to be introduced externally. The validation of the precise mechanism needs direct observation using advanced ultra-high resolution (sub-micron) imaging and analysis techniques, e.g. digital volume correlation.

5.5. HAp crystals orientation distribution effects

The combination of random and perfectly aligned HAp inclusions (that can be referred to as "partially aligned") was described in the previous section (Fig. 5). We note that this is an approximation, since in practice the orientation distribution of HAp crystals is a continuous function of the angle between the *c*-axis of HAp crystals and a chosen direction (the global *X*-axis) in the laboratory coordinate system. The WAXS intensity variation with the azimuthal angle plotted in Fig. 2c allows us to extract the volume fraction of HAp crystals with different orientations. Based on this, continuous orientation distribution model can be carried out based on the probability density function of finding crystals of given orientation. The result obtained using this approach is shown in Fig. 6. The comparison between this result and that obtained earlier using the combination of random and perfectly aligned crystallites indicates that the difference between the two approaches is negligible in terms of the prediction of the apparent modulus. Thus, the angle of the preferred orientation has a dominant effect on the mechanical response.

5.6. The effects of preferred orientation of HAp crystals

The effect of the nano-scale structure (the HAp crystallite distribution) on the macroscopic mechanical response was further investigated by changing the preferential crystal orientations (changing the transformation matrix in Eq. (5)). A 3D model of perfectly aligned crystals inside a rod is established (Fig. 7a) with the angle φ describing the rotation of the alignment direction around the global *Z*-axis. The local coordinate system with respect to the apatite has been designated *x*,*y*,*z* in Fig. 7a. When all HAp crystals are aligned along the global *X*-axis, φ equals to 0°. By changing the relative alignment direction, the variation of $K_{aligned}$ with respect to the loading direction can be calculated (Fig. 7b). From Fig. 7b, the corresponding results using the real orientation angles found in the experiment (174° from SAXS and 14° from WAXS) are found to be $Kaligned\_SAXS = 138.1$ GPa and $Kaligned\_WAXS = 131.8$ GPa, i.e. closely similar values. Meanwhile, due to the high degree of alignment of HAp crystals in the enamel, the value of the overall apparent modulus $K^{HAp}_{partialaligned}$ lies closer to $K_{aligned}$ rather than K_{random}. The enamel displays strong microscopic elastic anisotropy. It is interesting to note that the orientation with the largest stiffness is found, as expected, around 0° with respect to the loading direction. However, the most compliant orientation observed is not at 90° (perpendicular to the loading direction), but rather around 50° or 130°. This is due to the transversely isotropic stiffness of HAp crystals.

6. Conclusions

In this study, the longitudinal apparent modulus of human enamel was measured during *in situ* elastic compression by the combination of synchrotron WAXS and SAXS. This is the first combined SAXS/WAXS study on the nano-scale structure and its influence on the macroscopic mechanical behaviour of human enamel. The coherent results obtained for both WAXS and SAXS indicates that the SAXS pattern arising from the inter-mineral gaps can be used to reflect the HAp crystal orientation. This provided access to the information on both the structural and mechanical aspects of the sample and allowed us to make further progress compared with the previous studies which only used WAXS (Almer and Stock, 2005; Fujisaki et al., 2012). As an improvement of the earlier proposed composite model (Bar-On and Wagner, 2012; Jones, 1999), a multi-scale Eshelby inclusion model was established to estimate the elastic properties of enamel, considering it as a two-level

composite. Good agreement between the measured and calculated lattice strains along the loading direction validates the model. With respect to the normal strain component in a general azimuthal direction, the underestimation of the tensile strain by the model required the introduction of additional transverse internal strain. The modified model result demonstrates that the deformation state in the enamel sample may not have been fully uniaxial and may have been caused by the barrelling effect or crystal debonding.

This systematic experimental and modelling approach reported here is able to capture the complete picture of the multi-scale structure, material elastic properties and its evolution under loading. The parameter refinement and validation approach adopted in the present study offers an important alternative route to the identification of nano-scale parameters. Other established experimental characterisation techniques, such as nanoindentation and microscopy, are confined to the sample surface, making overall bulk parameter identification difficult. Combining the present results on enamel with previously published data on human dentine, an improved and comprehensive understanding of the multi-scale structural–mechanical properties within human dental tissues can be given. Besides the implications for the characterisation of the structure–property relationship of other hierarchical biomaterials, this knowledge is essential for developing better prosthetic materials and dental fillings, and could also shed light on the mechanical property evolution associated with the multi-scale structural changes within human teeth due to disease and treatment.

Acknowledgements

Acknowledgments

AMK acknowledges the support of EPSRC through grants EP/I020691 "Multi-disciplinary Centre for In situ Processing Studies (CIPS)", EP/G004676 "Micromechanical Modelling and Experimentation", and EP/H003215 "New Dimensions of Engineering Science at Large Facilities". Diamond Light Source is acknowledged for providing the beam time.

Appendix A.

A short overview of the Eshelby inclusion theory is given in (Sui et al., 2013), which leads to the detailed model derivation for a non-dilute system of human dentine composite, with a population of HAp crystals organised and bundled in a finite globular protein phase. The modified Eshelby model for the similar two-level composite of human enamel is given here.

1. Enamel first-level model

The equivalent inclusion method for multiple inhomogeneities with the averaged stiffness $\langle C\rangle_I$ in a non-dilute system during elastic deformation is

$$C_M\left(\langle\varepsilon\rangle^i+\langle\varepsilon\rangle_M+\langle\varepsilon\rangle^A-\langle\varepsilon\rangle^t\right)=\langle C\rangle_I\left(\langle\varepsilon\rangle^i+\langle\varepsilon\rangle_M+\langle\varepsilon\rangle^A\right) \tag{A1}$$

where C_M is the isotropic stiffness of the globular protein, $\langle\varepsilon\rangle^i$ the averaged total strain in the multiple inhomogeneities, $\langle\varepsilon\rangle_M$ the mean image strain in the whole material due to the non-dilute system, $\langle\varepsilon\rangle^A$ the external strain caused by the applied stress and $\langle\varepsilon\rangle^t$ is the average transformation strain for the equivalent inclusions to be determined. In a non-dilute system, the mean image stress $\langle\sigma\rangle_M$ and the mean stress in the equivalent inclusions $\langle\sigma\rangle_I$ due to the transformation strain can be expressed by (Clyne and Withers, 1995; Withers et al., 1989)

$$\langle\sigma\rangle_M=C_M\langle\varepsilon\rangle_M=-fC_M(\langle S\rangle-I)\langle\varepsilon\rangle^t \tag{A2}$$

$$\langle\sigma\rangle_I=(1-f)C_M(\langle S\rangle-I)\langle\varepsilon\rangle^t \tag{A3}$$

where $\langle S\rangle$ is the average Eshelby tensor and f is the volume fraction of inclusions. Thus $\langle\varepsilon\rangle^t$ can be obtained as a function of the applied stress

$$\langle\varepsilon\rangle^t=-\left\{(C_M-\langle C\rangle_I)[\langle S\rangle-f(\langle S\rangle-I)]-C_M\right\}^{-1}(C_M-\langle C\rangle_I)C_M^{-1}\sigma^A \tag{A4}$$

Therefore, in the first-level model of enamel, if C_M and $\langle C\rangle_I$ are respectively the stiffness of globular protein and rod, f the volume fraction of rods ($f=f_1$) and $\langle S\rangle$ is the average cylinder-like Eshelby tensor for rods ($\langle S\rangle=\langle S_1\rangle$), with Eqs. (A3) and (A4), the total stress in rods can be obtained as the sum of $\langle\sigma\rangle_I$ and σ^A.

2. Enamel second-level model

The second-level model considers the rods of the first-level model to be a composite consisting of partially aligned HAp crystals and globular protein. In Eq. (A1), if we consider $\langle\varepsilon\rangle^A$ as the average strain in the globular protein in the second level, f the volume fraction of HAp crystals in rods ($f=f_2$), and $\langle S\rangle$ and $\langle C\rangle_I$ are the average Eshelby tensor and average stiffness of HAp crystals in rods ($\langle S\rangle=\langle S_2\rangle$, $\langle C\rangle_I=\langle C_{HAp}\rangle$), the similar method as that in Appendix Section 1 can be used to determine the average strain and stress in HAp crystals. Here we focus on the average strain. The relationship between the strain in a single HAp crystallite and the rod stress can be established initially based on Eqs. (A1)–(A4)

$$\varepsilon_{single}^{HAp}=T^T\left\{\left\{\left(I-C_M^{-1}C_{HAp}\right)^{-1}[S_2-f_2(S_2-I)]^{-1}-I\right\}^{-1}T^{-T}+T^{-T}\right\}C_M^{-1}\sigma^{rod}=K\sigma^{rod} \tag{A5}$$

where T is the orientation matrix described by three Euler angles (θ,φ,ψ). The partial alignment is understood to be a combination of perfect alignment and random distribution. The expression for the average strain in multiple perfectly aligned HAp crystals is similar to Eq. (A5), as shown in Eq. (4), while that for the average strain in multiple randomly distributed HAp crystals needs to be obtained by the volume average method, which is introduced here. The purpose of using volume average method is to avoid the complex calculation of average Eshelby tensor and average stiffness of randomly distributed HAp crystals.

In a random distribution, each crystal follows the relationship of Eq. (A5) by an individual transformation matrix T. Crystals can have any possible orientation in the space, thus the volume average method is to calculate the mean strain value over all the crystals in the rod by averaging over all possible orientations based on Eq. (A5).

$$\left\langle\varepsilon_{random}^{HAp}\right\rangle=\frac{1}{V}\int_V\varepsilon_{single}^{HAp}dV=\frac{\int_0^{2\pi}\int_0^{\pi}\int_0^{2\pi}Ksin\theta d\phi d\theta d\psi}{\int_0^{2\pi}\int_0^{\pi}\int_0^{2\pi}sin\theta d\phi d\theta d\psi}\sigma^{rod}=\frac{\sigma^{rod}}{2\pi^2}\int_0^{2\pi}\int_0^{\pi}\int_0^{2\pi}Ksin\theta d\phi d\theta d\psi=\langle K\rangle\sigma^{rod} \tag{A6}$$

References

Al-Jawad, M., Steuwer, A., Kilcoyne, S.H., Shore, R.C., Cywinski, R., Wood, D.J., 2007. 2D mapping of texture and lattice parameters of dental enamel. Biomaterials 28, 2908–2914.

Almer, J.D., Stock, S.R., 2005. Internal strains and stresses measured in cortical bone via high-energy X-ray diffraction. J. Struct. Biol. 152, 14–27.

Almer, J.D., Stock, S.R., 2010. High energy X-ray scattering quantification of in situ-loading-related strain gradients spanning the dentinoenamel junction (DEJ) in bovine tooth specimens. J. Biomech. 43, 2294–2300.

Ang, S.F., Saadatmand, M., Swain, M.V., Klocke, A., Schneider, G.A., 2012. Comparison of mechanical behaviors of enamel rod and interrod regions in enamel. J. Mater. Res. 27, 448–456.
Bajaj, D., Arola, D., 2009. Role of prism decussation on fatigue crack growth and fracture of human enamel. Acta Biomater. 5, 3045–3056.
Bar-On, B., Wagner, H.D., 2012. Elastic modulus of hard tissues. J. Biomech. 45, 672–678.
Bechtle, S., Ozcoban, H., Lilleodden, E.T., Huber, N., Schreyer, A., Swain, M.V., Schneider, G.A., 2012. Hierarchical flexural strength of enamel: transition from brittle to damage-tolerant behaviour. J. R. Soc. Interface 9, 1265–1274.
Calibration, D.L.S., 2013. Diamond Light Source Calibration.
Chou, T.W., Sun, C.T., 2012. Nanocomposites, In M. Hyer, W, (ed.). DEStech Inc.
Clyne, T.W., Withers, P.J., 1995. An introduction to metal matrix composites. First paperback edition. Cambridge University Press, Cambridge.
Deymier-Black, A.C., Almer, J.D., Stock, S.R., Haeffner, D.R., Dunand, D.C., 2010. Synchrotron X-ray diffraction study of load partitioning during elastic deformation of bovine dentin. Acta Biomater 6, 2172–2180.
Eliceiri, K.W., Berthold, M.R., Goldberg, I.G., Ibanez, L., Manjunath, B.S., Martone, M.E., Murphy, R.F., Peng, H., Plant, A.L., Roysam, B., Stuurmann, N., Swedlow, J.R., Tomancak, P., Carpenter, A.E., 2012. Biological imaging software tools. Nat. Methods 9, 697–710.
Fratzl, P., Schreiber, S., Klaushofer, K., 1996. Bone mineralization as studied by small-angle X-ray scattering. Connect Tissue Res. 35, 9–16.
Fujisaki, K., Todoh, M., Niida, A., Shibuya, R., Kitami, S., Tadano, S., 2012. Orientation and deformation of mineral crystals in tooth surfaces. J. Mech. Behav. Biomed. 10, 176–182.
Habelitz, S., Marshall, S.J., Marshall, G.W., Balooch, M., 2001. Mechanical properties of human dental enamel on the nanometre scale. Arch. Oral Biol. 46, 173–183.
Hammersley, A.P. 1997. FIT2D: An Introduction and Overview ESRF Internal Report.
He, L.H., 2008. Mechanical behavior of human enamel and the relationship to its structural and compositional characteristics. PhD thesis.
Huang, Z., Newcomb, C.J., Bringas, P., Stupp, S.I., Snead, M.L., 2010. Biological synthesis of tooth enamel instructed by an artificial matrix. Biomaterials 31, 9202–9211.
Huo, B., 2005. An inhomogeneous and anisotropic constitutive model of human dentin. J. Biomech. 38, 587–594.
Ji, B.H., Gao, H.J., 2004. Mechanical properties of nanostructure of biological materials. J. Mech. Phys. Solids 52, 1963–1990.
Jones, R.M., 1999. Mechanics of Composite Materials, second ed. Taylor & Francis, Philadelphia, Pa.; London.
Kerebel, B., Daculsi, G., Kerebel, L.M., 1979. Ultrastructural studies of enamel crystallites. J Dental Res. 58, 844–851.
Korsunsky, A.M., Baimpas, N., Song, X., Belnoue, J., Hofmann, F., Abbey, B., Xie, M.Y., Andrieux, J., Buslaps, T., Neo, T.K., 2011. Strain tomography of polycrystalline zirconia dental prostheses by synchrotron X-ray diffraction. Acta Mater. 59, 2501–2513.
Macho, G.A., Jiang, Y., Spears, I.R., 2003. Enamel microstructure – a truly three-dimensional structure. J. Hum. Evol. 45, 81–90.
Mura, T., 1987. Micromechanics of Defects in Solids. In: second rev. ed. M. Nijhoff; Distributors the U.S. and Canada, Kluwer Boston.
Nakamura, T., Lu, C., Korach, C.S., 2011. Mechanical Properties of Tooth Enamel: Microstructural Modeling and Characterization. In: Conference Proceedings of the Society for Experimental Mechanics Series 9999, 171–179.
Nanci, A., Ten Cate, A.R., 2003. Ten Cate's Oral Histology: Development, Structure, and Function, sixth ed. Mosby, St. Louis, Mo, London.
Nogueira, B.C.L., Fernandes, P.M., Santana, L.N.S., Lima, R.R., 2011. Ultrastructural Characterization of Bovine and Buffalo Enamel Through Scanning Electron Microscopy. XXIII Congr. Brazilian Soc. Microsc. Microanal..
Ochsner, A., Ahmed, W., 2011. Biomechanics of hard tissues. John Wiley & Sons.
Palmer, L.C., Newcomb, C.J., Kaltz, S.R., Spoerke, E.D., Stupp, S.I., 2008. Biomimetic systems for hydroxyapatite mineralization inspired by bone and enamel. Chem. Rev. 108, 4754–4783.
Powers, J.M., Farah, J.W., 1975. Apparent modulus of elasticity of dental amalgams. J. Dental Res. 54, 902.
Qin, Q.-H., Swain, M.V., 2004. A micro-mechanics model of dentin mechanical properties. Biomaterials 25, 5081–5090.
Singhal, A., Almer, J.D., Dunand, D.C., 2012. Variability in the nanoscale deformation of hydroxyapatite during compressive loading in bovine bone. Acta Biomater. 8, 2747–2758.
Sui, T., Sandholzer, M.A., Baimpas, N., Dolbnya, I.P., Walmsley, A.D., Lumley, P.J., Landini, G., Korsunsky, A.M., 2013. Multi-scale modelling and diffraction-based characterization of elastic behaviour of human dentine. Acta Biomater. 9, 7937–7947.
Takao, Y., Taya, M., 1987. The effect of variable fiber aspect ratio on the stiffness and thermal-expansion coefficients of a short fiber composite. J. Compos. Mater. 21, 140–156.
Tanaka, T., Yagi, N., Ohta, T., Matsuo, Y., Terada, H., Kamasaka, K., To-o, K., Kometani, T., Kuriki, T., 2010. Evaluation of the distribution and orientation of remineralized enamel crystallites in subsurface lesions by X-ray diffraction. Caries Res. 44, 253–259.
Tesch, W., Eidelman, N., Roschger, P., Goldenberg, F., Klaushofer, K., Fratzl, P., 2001. Graded microstructure and mechanical properties of human crown dentin. Calcified Tissue Int. 69, 147–157.
Tesch, W., Vandenbos, T., Roschgr, P., Fratzl-Zelman, N., Klaushofer, K., Beertsen, W., Fratzl, P., 2003. Orientation of mineral crystallites and mineral density during skeletal development in mice deficient in tissue nonspecific alkaline phosphatase. J. Bone. Miner. Res. 18, 117–125.
Withers, P.J., Stobbs, W.M., Pedersen, O.B., 1989. The application of the Eshelby method of internal-stress determination to short fiber metal matrix composites. Acta Metall Mater. 37, 3061–3084.
Young, M.L., DeFouw, J., Almer, J.D., Dunand, D.C., 2007a. Load partitioning during compressive loading of a Mg/MgB2 composite. Acta Mater. 55, 3467–3478.
Young, M.L., Almer, J.D., Daymond, M.R., Haeffner, D.R., Dunand, D.C., 2007b. Load partitioning between ferrite and cementite during elasto-plastic deformation of an ultrahigh-carbon steel. Acta Mater. 55, 1999–2011.

Acta Biomaterialia 9 (2013) 7937–7947

Contents lists available at SciVerse ScienceDirect

Acta Biomaterialia

journal homepage: www.elsevier.com/locate/actabiomat

Multiscale modelling and diffraction-based characterization of elastic behaviour of human dentine

Tan Sui [a,*], Michael A. Sandholzer [b], Nikolaos Baimpas [a], Igor P. Dolbnya [c], Anthony Damien Walmsley [b], Philip J. Lumley [b], Gabriel Landini [b], Alexander M. Korsunsky [a]

[a] Department of Engineering Science, University of Oxford, Parks Road, Oxford OX1 3PJ, UK
[b] School of Dentistry, College of Medical and Dental Sciences, University of Birmingham, St. Chad's Queensway, Birmingham B4 6NN, UK
[c] Beamline B16, Diamond Light Source, Harwell Oxford Campus, Didcot OX11 0DE, UK

ARTICLE INFO

Article history:
Received 23 November 2012
Received in revised form 10 April 2013
Accepted 11 April 2013
Available online 18 April 2013

Keywords:
Dentine
WAXS/SAXS
Eshelby model
Mechanical properties

ABSTRACT

Human dentine is a hierarchical mineralized tissue with a two-level composite structure, with tubules being the prominent structural feature at a microlevel, and collagen fibres decorated with hydroxyapatite (HAp) crystallite platelets dominating the nanoscale. Few studies have focused on this two-level structure of human dentine, where the response to mechanical loading is thought to be affected not only by the tubule volume fraction at the microscale, but also by the shape and orientation distribution of mineral crystallites, and their nanoscale spatial arrangement and alignment. In this paper, in situ elastic strain evolution within HAp in dentine subjected to uniaxial compressive loading along both longitudinal and transverse directions was characterized simultaneously by two synchrotron X-ray scattering techniques: small- and wide-angle X-ray scattering (SAXS and WAXS, respectively). WAXS allows the evaluation of the apparent modulus linking the external load to the internal HAp crystallite strain, while the nanoscale HAp distribution and arrangement can be quantified by SAXS. We proposed an improved multiscale Eshelby inclusion model that takes into account the two-level hierarchical structure, and validated it with a multidirectional experimental strain evaluation. The agreement between the simulation and measurement indicates that the multiscale hierarchical model developed here accurately reflects the structural arrangement and mechanical response of human dentine. This study benefits the comprehensive understanding of the mechanical behaviour of hierarchical biomaterials. The knowledge of the mechanical properties related to the hierarchical structure is essential for the understanding and predicting the effects of structural alterations that may occur due to disease or treatment on the performance of dental tissues and their artificial replacements.

1. Introduction

Dentine is a hydrated biological mineral composite tissue with a hierarchical structure and versatile mechanical properties [1]. At the microscopic level, dentine has a well-oriented structure with an arrangement of dentinal tubules that extend throughout the entire dentine thickness, from the amelo-dentinal junction (ADJ) to the pulp [1–3]. At the nanoscale, dentine is a composite of plate-like hydroxyapatite crystals (HAp) that have the shape of elongated pancakes (~2–4 nm thick, ~30 nm wide and up to 100 nm long) randomly embedded in a collagen matrix [4,5]. Characterizing the mechanical properties of the tissue according to its complex hierarchical structure benefits the understanding of the internal architecture and hierarchical properties of materials.

Previously, most research in this area has concentrated on the mechanical properties of dentine at the macro- and microscale, i.e. Young's modulus, Poisson's ratio, hardness and fracture properties, using a variety of measurement methods [6]. However, few studies have focused on the nanoscale, where mechanical alterations can be considered to be a function of crystal shape and orientation of the mineral phase [7,8]. During elastic loading, stresses are expected to be transferred to the stiff HAp platelets from the surrounding collagen matrix [7]. To investigate this, it is required to use techniques that allow in situ quantification of the mechanical response of nanoscale HAp phases to loading.

Synchrotron-based X-ray diffraction, and small- and wide-angle X-ray scattering (SAXS and WAXS, respectively), are advanced non-destructive techniques that enable characterization of the nanoscale and subnanoscale structure of materials, and have been widely used to study load transfer between two phases in matrix composites [9–11]. In situ compression testing, in combination with the WAXS technique, has been used to quantify the internal strains of

* Corresponding author. Tel.: +44 18652 83447; fax: +44 18652 73010.
E-mail address: tan.sui@eng.ox.ac.uk (T. Sui).

1742-7061/$ - see front matter © 2013 Acta Materialia Inc. Published by Elsevier Ltd. All rights reserved.
http://dx.doi.org/10.1016/j.actbio.2013.04.020

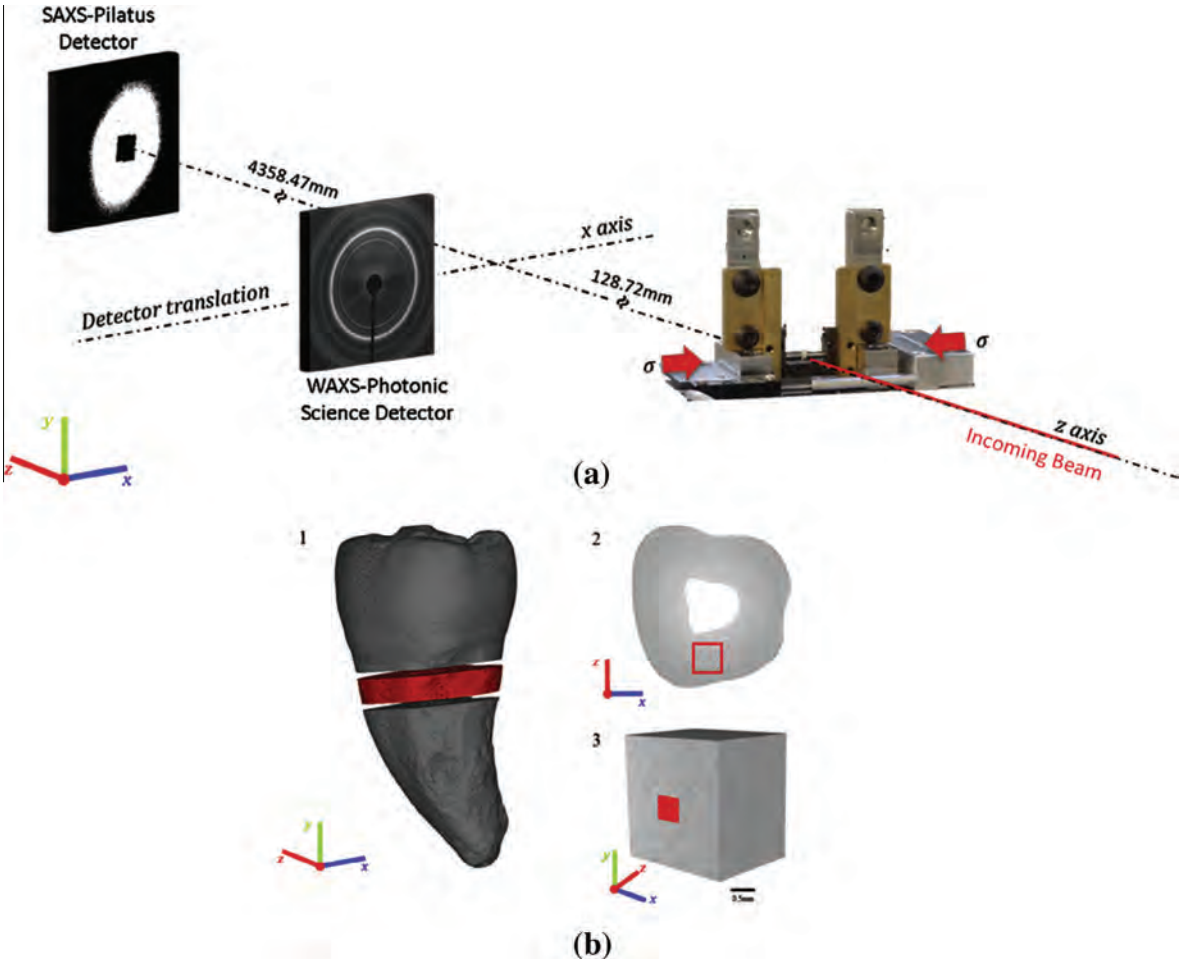

Fig. 1. Schematic diagram of experimental setup and sample preparation. (a) Sample under uniaxial compressive loading on the compression stage. The monochromatic X-ray beam was directed perpendicular to the sample surface and the loading direction. WAXS and SAXS diffraction patterns were recorded at each loading step at three locations on the sample. The WAXS detector was translated laterally out of the beam to expose the SAXS detector after each collection of WAXS. (b) Micro-CT-based models of the three preparation stages. (1) 2 mm thick dentine disk (coloured red) cut below the enamel–cement line and (2) further cut and polished to produce (3) the final 2 mm × 2 mm × 2 mm cubes of dentine. The red square indicates the central position of the X-ray beam.

the phase [9–11]. In addition, for mineralized tissues, SAXS is able to reveal quantitative nanoscale information about the structure, orientation and degree of alignment of crystals [12]. Those parameters have been identified as critical for the mechanical properties and stability of the materials [13–15]. It is only recently that this technique has been applied to the study of mechanical behaviour in mineralized biological composites such as bone [16–19] and teeth [7,8,20]. Deymier-Black et al. [7] determined the longitudinal apparent modulus of HAp in bovine dentine using synchrotron-based WAXS, while strain distribution across the ADJ in bovine teeth was investigated by Almer and Stock [20]. A deep understanding of the relationship between the nanoscale structure and macroscopic mechanical behaviour is lacking. Earlier studies do not take into account the nanoparticle distribution [7,20], which can be derived from SAXS data. In addition, all these studies were carried on non-human samples, in which different particularities of the tubule structure and morphology are expected to result in differences in the mechanical properties [21].

In parallel, various analytical models of composites have been proposed to describe the interaction of different mineral phases and model the elastic properties of hard tissues (e.g. [22–24]). Besides these, one widely accepted model is the Eshelby inclusion model [25,26]. Recently, the Eshelby model has also been applied in dental research based on nanoindentation and finite-element model data [27–30] to explain and predict the elastic response of dentine on the microscopic level. However, the models used in previous simulations were limited, in which no consideration was given to the nanoscale structure, and this led to discrepancies of overestimation between the predictions and experimental results [7].

In order to improve the understanding of the influence of the nanoscale structure variation of the two-level composite of human dentine on its mechanical response, in this study, the in situ synchrotron X-ray techniques (simultaneous SAXS/WAXS) were used to measure the elastic strain (WAXS), alterations in crystal orientation and degree of alignment of HAp phases (SAXS) in human dentine under externally uniaxial compressive loading along two directions, longitudinal as well as transverse with respect to the preferential tubule direction. Meanwhile, an extended multiscale Eshelby model for a two-level composite was established. The capability of the model in capturing the relationship between the nanoscale structure and macroscopic loading was evaluated.

2. Materials and methods

2.1. Sample preparation

Two freshly extracted sound human third molars (ethical approval obtained from the National Research Ethics Committee; NHS-REC reference 09.H0405.33/Consortium R&D No. 1465) were

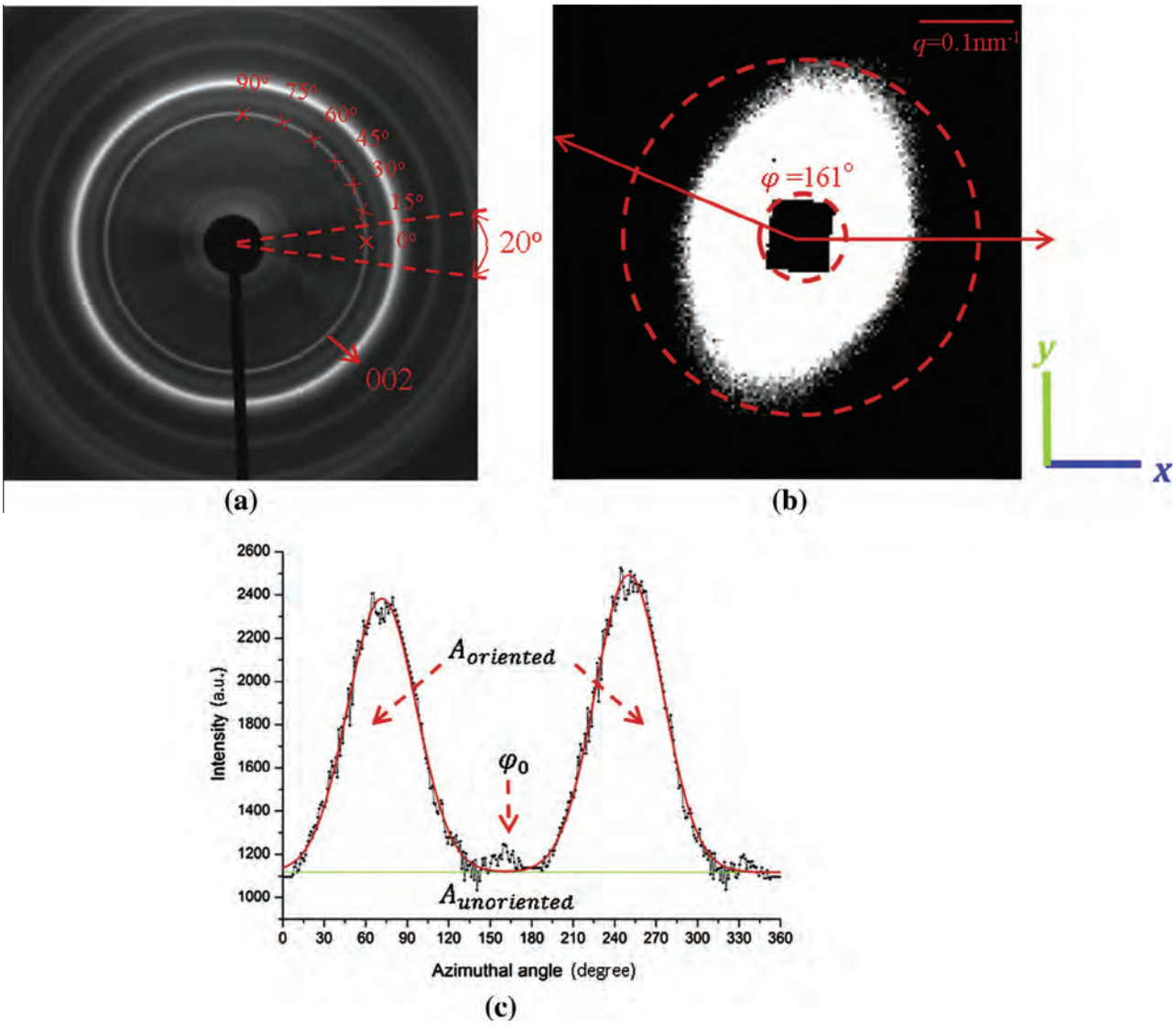

Fig. 2. (a) A representative dentine WAXS pattern of Debye–Scherrer rings with different intensities. The dark region in the centre is the beam stop. The (002) peak is marked with a red arrow. Peak shifts at different positions on the (002) ring represent the average strains of (002) along different directions. Multiple angles with respect to the x-axis were caked in order to examine the strain variation (seven angles are shown as an example: 0°, 15°, 30°, 45°, 60°, 75°, 90°). Each cake was with a 20° range. (b) A representative dentine SAXS pattern of the HD2 sample. The q scale in the SAXS pattern is in reciprocal space, which is the inverse of d dimension in the real space. The relation is $q = 2\pi/d$. If all the HAp platelets are oriented in the φ direction parallel to their long dimension in the real space, q would be the smallest in the elliptical pattern of the SAXS. Thus the direction of the short axis of the ellipse pattern indicates the predominant orientation of the crystals. (c) A plot of $I(\varphi)$ of the HD2 sample without any external load (black points). The Gauss fit is also shown in the figure (red line). The predominant orientation $\varphi_0 = 161^\circ$ is the average position of the two peaks. The ratio $A_{oriented}/(A_{oriented} + A_{unoriented})$ gives the degree of alignment.

washed and cleaned in distilled water to eliminate residues and kept in a −20 °C freezer for a maximum of 14 days before the experiment. The samples were rehydrated using distilled water and 2 mm thick dentine disks were cut just below the enamel–cement line using a low-speed diamond saw (Isomet Buehler Ltd., Lake Bluff, IL, USA). The disks were further cut into smaller bars and a series of polishing papers was used to produce the final 2 mm × 2 mm × 2 mm cubes of dentine (Fig. 1b). The samples were kept for a maximum of 7 days in distilled water in a commercial fridge at 4 °C until the experiment was performed.

2.2. In situ scattering measurements

2.2.1. Mechanical loading setup

Uniaxial compressive loading was carried out on two dentine samples in the form of small 2 mm × 2 mm × 2 mm cubes. The samples were designated HD2, for which the loading was applied in the transverse direction, and HD3, for which the loading was applied in the longitudinal direction with respect to the tubules, respectively. Loading was carried out using a remotely operated and monitored compression rig (Deben, Suffolk, UK), with a 5 kN calibrated load cell. The rig was equipped with custom-made jaws, allowing a high-energy transmission X-ray setup to be used, as illustrated in Fig. 1a. The samples were deformed at a displacement rate of 0.2 mm min^{-1} up to 400 N (corresponding to ~100 MPa for the samples) along the x-direction. After each constant loading increments (HD2 50 N, HD3 100 N), the load was maintained and the WAXS and SAXS patterns were collected.

2.2.2. Beamline diffraction setup

The experiment was carried out on B16 experimental beamline at Diamond Light Source, Oxford Harwell Campus, Didcot, UK. A

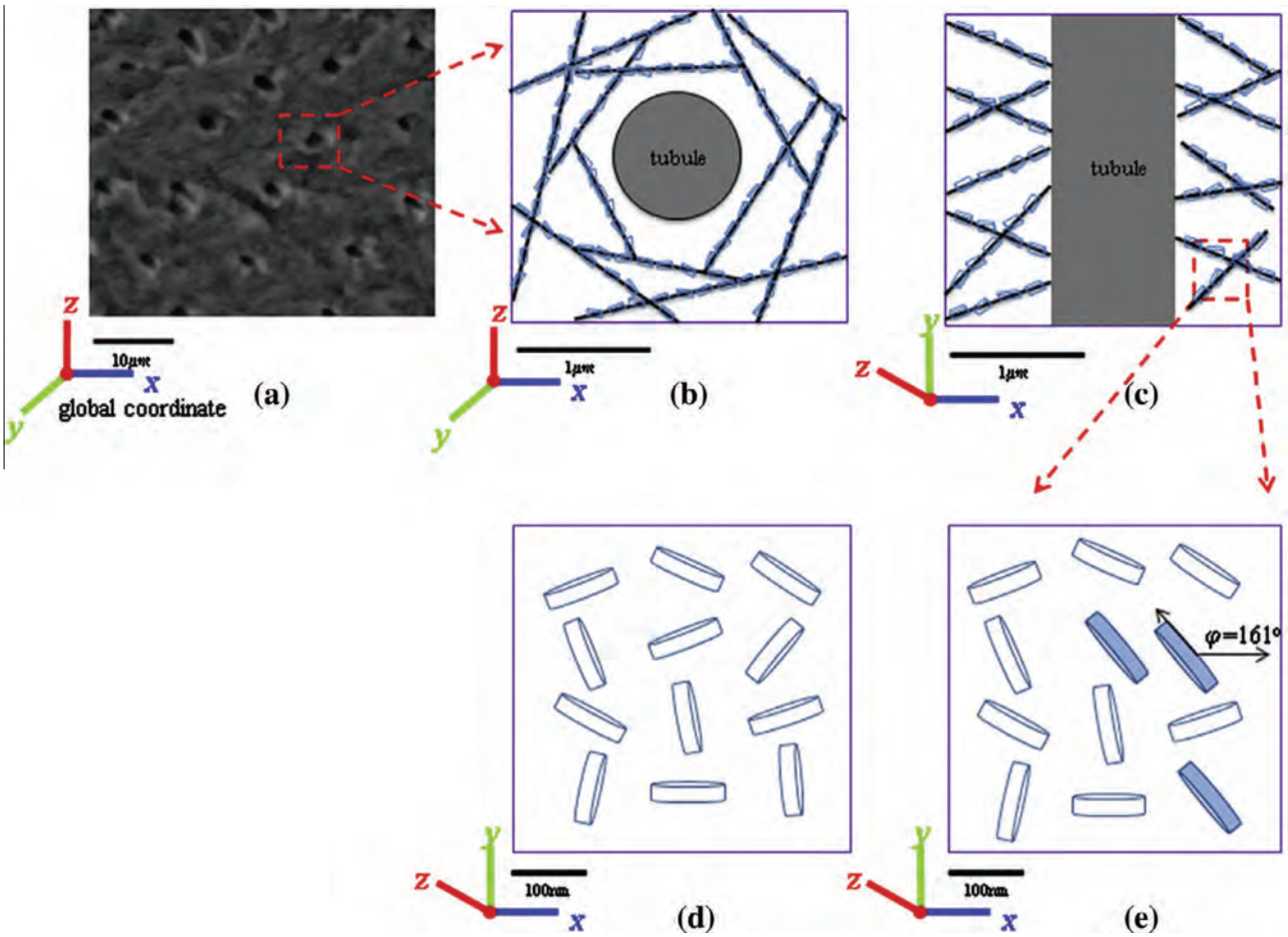

Fig. 3. (a) SEM observation of the first-level tubule structure of human dentine. (b) A schematic structure of the random distribution of collagen fibrils (black lines) beside the tubules, viewed along the longitudinal direction of tubules. (c) Same as (b), viewed along the transverse direction of tubules. (d) The structure of the random distribution of HAp crystals viewed from the cross-section parallel to the tubule direction. (e) The real structure of partial alignment, where the pennies having an alignment angle 161° (showing the example of HD2) with respect to the global x-axis are shown in blue.

monochromatic X-ray beam was used to illuminate the sample as illustrated schematically in Fig. 1a. The incident beam was monochromated to the photon energy of 17.99 keV, and collimated to the spot size of 0.5 mm × 0.5 mm on the sample. WAXS and SAXS patterns were alternately collected at three locations across the sample. A silicon powder was used for the WAXS data calibration and dry chicken collagen was used for the SAXS data calibration [31].

WAXS diffraction patterns were recorded using a Photonic Science Image Star 9000 detector (Photonic Science Ltd., UK) placed at a sample-to-camera distance of 128.72 mm (Fig. 1a). Further downstream of the beam a Pilatus 300K detector (Dectris, Baden, Switzerland) was positioned at a distance of 4358.47 mm to collect the SAXS patterns (Fig. 1a). In order to record both the WAXS and SAXS patterns at each scanning location, the WAXS detector was translated laterally to expose the SAXS detector after each WAXS collection.

2.3. Micro-CT protocol and data processing

For the purpose of planning the measuring positions and determination of the precise loading cross-sectional area of the dentine cubes, a commercial micro-computed tomography (micro-CT) system was used to scan the samples with a SkyScan 1172 scanner (SkyScan, Kontich, Belgium) at 1.9 μm isotropic resolution using 40 kV voltage, 120 μA current and a 0.5 mm Al filter. The resulting slices were reconstructed with the SkyScan NRECON package and subsequent 3-D planning models were created with Fiji imaging software [32].

2.4. Scattering data analysis

2.4.1. WAXS data analysis

The data analysis was done in accordance with previous studies [9–11]. The WAXS data interpretation was limited to the (002) peak of Debye–Scherrer rings of the middle scanning location (see Fig. 2a), guaranteeing that the same position could be detected during the compressive deformation of the dentine. Changes in the d-spacing between the lattice planes in the HAp were used to determine the elastic strain in the mineral HAp phase [33]. The apparent lattice elastic strain ε was computed from the definition:

$$\varepsilon = \frac{d_{002} - d^0_{002}}{d^0_{002}}, \tag{1}$$

where d_{002} is the apparent strained d-spacing and d^0_{002} is the reference strain-free value of the d-spacing.

To determine the strain from the mineral HAp phase, 2-D diffraction images were pre-processed into a 1-D intensity plot using Fit2D [34] by "caking" (a professional jargon term used to refer to the selection of a sector in the radial–azimuthal coordinates of each pattern) each pattern with a step of 20° in the range of 0°–360° of the (002) peak under laboratory coordinates (Fig. 2a, only

Table 1
Experimental results from SAXS/WAXS and refined parameters in the Eshelby model of the two dentine samples.

Parameters	HD2_value	HD3_value	Reference values
Orientation (degree)	161	78	
Degree of alignment	0.289	0.168	
K_exp. (GPa)	22.129	24.156	
f_1	10%	10%	3.6 – 10.2% [45]
f_2	40%	38%	30.5%, 44.4% [46]
$C_{M1} = C_{M2}$	E_m = 1.1 GPa, υ_m = 0.3	E_m = 0.8 GPa, υ_m = 0.27	$E_{collagen}$ = 1 GPa, $\upsilon_{collagen}$ = 0.30 [27]
C_{HAp}	E_{HAp} = 90 GPa, υ_{HAp} = 0.32	E_{HAp} = 90 GPa, υ_{HAp} = 0.32	E_{HAp} = 40–117 GPa, υ_{HAp} = 0.27 [47]
a_1/a_3	31	31	$(2–4) \times 30 \times 100$ nm^3[4,5]
K_model (GPa)	22.870	24.189	

0°–90° is shown). The normal strain component along the centre direction of each cake represents the strain distribution at the corresponding orientation. Subsequently, the 1-D intensity plot of each cake (covering 20°) was obtained by the integration, with respect to the azimuthal angle, of the converted 2-D images. Afterwards, the 1-D profiles of each individual (002) peak was fitted with Gaussian curves to determine the centre position after the subtraction of the linearly fitted background. To calculate the HAp lattice strain, the WAXS pattern of the unloaded condition was used as a strain-free reference point.

2.4.2. SAXS data analysis

For the SAXS data analysis, a reference pattern representing the strain-free sample was used to determine the orientation and degree of alignment (ρ) of HAp crystalline particles, which describes the percentage of aligned particles. Fig. 2b is an example reference SAXS pattern of HD2. In order to quantify the orientation and degree of alignment, the SAXS patterns were integrated along all the possible scattering vectors q to account for the main scattering effect (with the range selected from the outline of beamstop to the outline of the pattern as marked with red dashes in Fig. 2b), which results in a function $I(\varphi)$ with the azimuthal angle φ [35–37] (Fig. 2c). The predominant orientation is determined by the average position of two peaks in the plot of $I(\varphi)$ (e.g. φ_0 in Fig. 2c), while the degree of alignment with respect to the predominant orientation of HAp is defined as the ratio of peak area and the overall area under the curve of $I(\varphi)$:

$$\rho = \frac{A_{oriented}}{A_{oriented} + A_{unoriented}}, \tag{2}$$

where $A_{unoriented}$ is the area of the constant background level and $A_{oriented}$ depicts the total area subtracting the background. The value of degree of alignment ranges from 0 to 1, where $\rho = 0$ indicates no predominant orientation within the plane of the section and $\rho = 1$ indicates a perfect alignment of all crystals [35,37].

3. Model formulation

3.1. Geometrical assumptions

Human dentine has a hierarchical two-level composite structure, where the first level is represented by the dentinal tubules and the second level by the HAp crystals within a fibrous collagen matrix. Fig. 3a–c are images of the first-level dentine structure, where Fig. 3a is obtained by scanning electron microscopy (SEM) and Fig. 3b,c show the random distribution of collagen fibril viewed respectively along longitudinal and transverse direction of tubules as proposed by Bozec [38]. Fig. 3d,e are images of the second-level dentine structure, where a randomly distributed structure of HAp crystals shown in Fig. 3d is to be combined with a fully aligned structure to determine the real structure of partial alignment (Fig. 3e for HD2), given the detailed information of degree of alignment by SAXS interpretation. Both levels are non-dilute systems consisting of a number of inhomogeneous inclusions. The multiscale Eshelby model for a non-dilute system is established and is used here to model the two-level composite of dentine [39] (for details see Appendix). The first-level model regards the whole dentine sample as composed of aligned tubules within a matrix phase, while the second-level model considers the matrix of the first level as a composite in detail, consisting of HAp crystals and a collagen matrix.

The shape of the HAp crystalline platelets in dentine is thought to correspond to elongated flagstone. In classical Eshelby modelling, a very good approximation is to use a penny-shape inclusion to simulate an individual platelet, as the integrals can be readily written. The Eshelby penny-shaped tensor has two parameters, where a_1 is the radius while a_3 is half of the thickness of the penny-shaped inclusion [40]. The thickness of the penny-shape is taken to be equal to the thickness of the dentine crystal platelet (2–4 nm). The diameter of the penny-shape is the average of the length (100 nm) and width (30 nm) of HAp to guarantee the identical cross-sectional area. The size of crystal platelet and the parameters of penny-shape tensor are listed in Table 1. The crystal c-axis (corresponding to the (002) peak) of the HAp crystallites is thought to be parallel to the long dimension of the platelet [41,42]. Therefore, in the model, the c-axis lies along the radial direction within the penny and is in the x–y plane shown in Fig. 3e.

3.2. First-level model: multiple aligned tubule inclusions within dentine matrix

The purpose of the first-level model for human dentine is to establish the elastic relationship between the external stress σ^A and dentine matrix stress σ_{M1}, which will serve as the external stress in the second level. Without any transformation strain in tubules, the Eshelby model for a non-dilute system (Appendix Eqs. (B1), (B2), (B3), (B4), (B5)) indicates that the mechanical response of the tubules can be related to an equivalent inclusion with the same property as the matrix:

$$\langle C\rangle_{tubule}(\langle\varepsilon\rangle^i + \langle\varepsilon\rangle_{M1} + \varepsilon^A) = C_{M1}(\langle\varepsilon\rangle^i + \langle\varepsilon\rangle_{M1} + \varepsilon^A - \langle\varepsilon\rangle^t), \tag{3}$$

where "*M1*" means the first-level matrix, $\langle\varepsilon\rangle^i$ the average total strain in tubules, $\langle C\rangle_{tubule}$ the average stiffness matrix of tubules, $\varepsilon^A = C_{M1}\sigma^A$ the external strain, $C_{M1}\langle\varepsilon\rangle_{M1} = \langle\sigma\rangle_{M1}$ the "image" stress defined to satisfy the boundary conditions at the external surface of a finite composite [25,39] and $\langle\varepsilon\rangle^t$ is the average transformation strain in the equivalent inclusion to be determined. Considering that the average stiffness of tubules is null $\langle C\rangle_{tubule} = 0$, the average stress in the dentine first-level matrix can be expressed merely in terms of the volume fraction of tubules f_1 (for further details see Appendix, Eqs. ((B7), (B8), (B9), (B10)), [25,39]):

$$\sigma_{M1} = \sigma^A + \langle\sigma\rangle_{M1} = \frac{1}{1-f_1}\sigma^A. \tag{4}$$

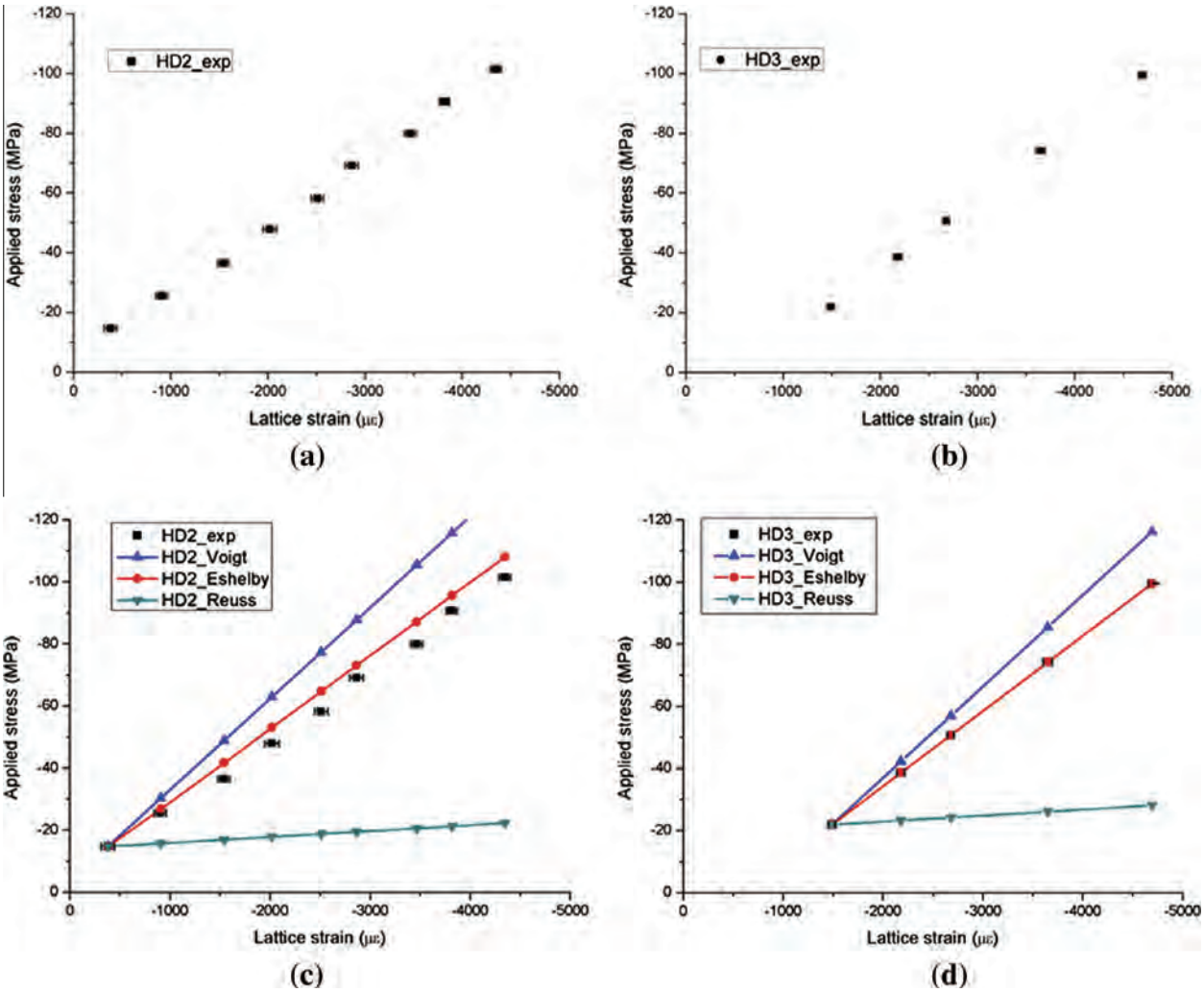

Fig. 4. Comparison of experimental data and modelling results of applied compressive stress vs. elastic lattice strain for HAp. (a) HD2 experimental data (error bar: 1 SD); (b) HD3 experimental data (error bar: 1 SD). (c) HD2 data (black points) and modelling results (red line: multiscale Eshelby model; blue line: Voigt bound; dark grey: Reuss bound) with the compressive stress along transverse direction with respect to the tubules. (d) HD3 data (black points) and modelling results (red line: multiscale Eshelby model; blue line: Voigt bound; dark grey: Reuss bound) with the compressive stress along longitudinal direction with respect to the tubules. The compressive stresses of HD2 and HD3 were uniformly selected under 100 MPa.

3.3. Second-level model: HAp inclusion of collagen matrix

The dispersion of multiple HAp crystals within the matrix of collagen forms the second hierarchical level model for dentine. The purpose of the second level model is to establish a relationship between the first-level dentine matrix stress and the average strain in the HAp crystals $\langle\varepsilon\rangle^{HAp}$, and thereby to determine the apparent modulus [43] between the global external load and local HAp crystal strain.

3.3.1. Multiple perfectly aligned HAp crystals

If all HAp crystals are perfectly aligned described by an orientation matrix T, the relationship between the average Hap crystal strain and the external load (here the first-level dentine matrix stress) can be expressed as [39] (Appendix Eq. (B11)):

$$\langle\varepsilon\rangle^{HAp}_{aligned} = \{\{(I - C_{M2}^{-1}\langle C\rangle_{HAp})^{-1}[\langle S\rangle - f_2(\langle S\rangle - I)]^{-1} - I\}^{-1}T^{-T} + T^{-T}\}C_{M2}^{-1}\sigma_{M1}$$

or, expressed more simply

$$\sigma_{M1} = K_{aligned}\langle\varepsilon\rangle^{HAp}_{aligned}, \quad (5)$$

where $\langle C\rangle_{HAp}$ and $\langle S\rangle$ are the average stiffness and Eshelby tensor of HAp crystals in the gauge volume [44], C_{M2} is the collagen stiffness, and f_2 is the volume fraction of HAp with respect to the whole second-level structure. For perfectly aligned crystals, $\langle C\rangle_{HAp}$ and $\langle S\rangle$ can be represented by the value of a single crystal $\langle C\rangle_{HAp} = C_{HAp}$, $\langle S\rangle = S$. Note that different orientations (different transformation matrices) may result in different results of $\langle\varepsilon\rangle^{HAp}_{aligned}$. The variation of $K_{aligned}$ with different alignment angles of particles with respect to the loading direction can be calculated by changing the transformation matrix in Eq. (5).

3.3.2. Multiple randomly distributed HAp crystals

If HAp crystals have a random distribution, this group of crystals will have an isotropic stiffness, as well as an isotropic Eshelby tensor, and thus the relationship between the average local Hap crystal strain and external load is independent on the orientation matrix in Eq. (5):

$$\langle\varepsilon\rangle^{HAp}_{random} = \{\{(I - C_{M2}^{-1}\langle C\rangle_{HAp})^{-1}[\langle S\rangle - f_2(\langle S\rangle - I)]^{-1} - I\}^{-1} + I\}C_{M2}^{-1}\sigma_{M1}$$

or, expressed more simply

$$\sigma_{M1} = K_{random}\langle\varepsilon\rangle^{HAp}_{random}. \quad (6)$$

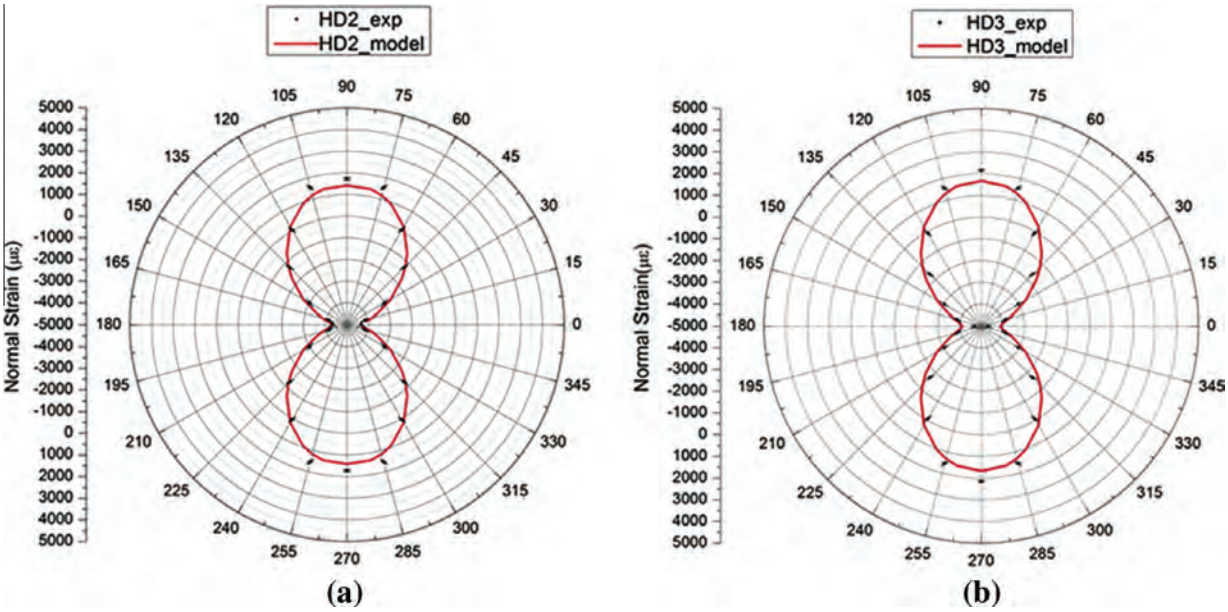

Fig. 5. Comparison of experimental data and modelling results of normal strain component variation with orientation distribution (0°–360°) under polar coordinates. (a) HD2 data (black points) and model fitting (red curve), with the compressive stress along transverse direction with respect to the tubules. (b) HD3 data (black points) and model fitting (red curve), with the compressive stress along the longitudinal direction with respect to the tubules.

In contrast to perfectly aligned crystals, $\langle S \rangle$ and $\langle C \rangle_{HAp}$ values were not those of the single crystal, but were obtained from the volume average of all the randomly distributed crystals (see Appendix, averaging the results obtained from each single-crystal relationship as Eq. (5) over all possible orientations).

3.3.3. Multiple HAp inclusions with partial alignment

In general, HAp crystals are partially aligned, thus $K^{HAp}_{partial\_aligned}$ is expected to be between K_{random} and $K_{aligned}$:

$$K^{HAp}_{partial\_aligned} = (1 - f_{aligned})K_{random} + f_{aligned}K_{aligned}, \quad (7)$$

where $f_{aligned}$ is the volume fraction of aligned crystals with respect to all HAp crystals, i.e. the degree of alignment of crystals revealed by SAXS measurements.

4. Experimental results and model validation

4.1. Nanoscale HAp distribution and mechanical response of dentine

The loading areas of the samples were accurately determined by micro-CT measurement. The loading areas were 4.466 mm^2 (HD2) and 4.413 mm^2 (HD3), respectively. Fig. 2a shows a WAXS pattern of dentine consisting of a system of Debye–Scherrer rings (peaks). The apparent radial shifts of the (002) peak in the WAXS pattern were measured under uniaxial compressive loading applied on both longitudinal and transverse directions with respect to the preferential tubule direction. Values of the shifts along the x-direction were used to obtain the elastic lattice strain variation along loading direction. Fig. 4a,b show the experimental results of the applied stress vs. HAp lattice strain of samples HD2 and HD3, indicating a linear increasing tendency as expected. The maximum load used in the model of the two samples was limited to ~100 MPa in the elastic region. The ratio of the uniaxial stress and the average HAp lattice strain gives the apparent modulus, which is listed in Table 1. From Fig. 4, it is observed that the dentine sample loaded along the longitudinal axis (HD3) has a slightly higher apparent modulus than the one loaded transversally (HD2). The residual (initial) strains were found to be quite small, namely, 205 $\mu\varepsilon$ (HD2) and −578.6 $\mu\varepsilon$ (HD3).

The (002) peak shifts along other directions were also measured by caking each pattern with a step of 20° (in the range of 0°–360°, Fig. 2a) to determine the normal strain component variation. The result is shown in polar coordinate as an azimuthal plot in Fig. 5a,b for HD2 and HD3, respectively, where 0° or 180° represents the loading direction and 90° or 360° represents that perpendicular to the loading direction. Being symmetrical, the results in the typical range of 0°–90° display a positive normal strain from 60°–90° and a negative normal strain from 0°–60°.

Fig. 2b is one of the SAXS patterns of the HD2 sample. The preferential orientation of HAp crystals is shown in the figure to be roughly along the short axis of the elliptical pattern. Fig. 2c is the plot of $I(\varphi)$ of the HD2 sample without any external load. The Gauss fit is also shown in the figure (red line). The detailed values of the orientation and degree of alignment were obtained by examining the plot of $I(\varphi)$ and are listed in Table 1. The degree of alignment values for both samples are relatively small, indicating that, as expected, the distribution of HAp crystals in human dentine is close to random, but nevertheless not entirely random.

4.2. Evaluation and testing of the multiscale Eshelby model

In the model, the material properties and other parameters were derived from the literature and were refined by fitting with the experimental data. It should be noted that a precise determination of the volume fraction of tubules in the first level is not available with commercial micro-CT systems, due to the polychromatic nature of the X-ray source and the limited resolution. Thus, the reported volume fraction of tubules between 3.6 and 10.2% was used [45]. The average mineral concentration (HAp volume fraction) has been reported to be between 30.5% and 44.4% in human third molars, with a decreasing gradient towards the pulp [46]. In general, a Young's modulus of 1 GPa and Poisson's ratio is 0.30 for collagen is given in the literature, without taking into account the viscoelasticity and viscoplasticity for human dentine [27,28]. Polycrystalline HAp has a high Young's modulus (40–117 GPa), whereas the Poisson's ratio is 0.27 [47]. However, these values of the HAp Young's modulus were all from a single perfect crystal. In biological mineralized composites such as dentine, imperfectly shaped

crystals are likely to exist, thus the high Young's modulus may induce an error by overestimation [7]. In accordance with Qin and Swain, 40 GPa was chosen here as a combination of the intertubular modulus (35.8 GPa) and peritubular modulus (66.76 GPa) in the respective volume fractions [27]. For the penny-shaped Eshelby tensor, only the ratio of radius and thickness (a_1/a_3) of the penny is needed [4,5]. All the parameters refined to obtain a best fitting are listed in Table 1, also with the reported values from the literature.

4.2.1. First-level model

The dentine matrix stress for the first level is only dependent on the volume fraction of tubules (see Eq. (4)). The same volume fraction of tubules was used for both samples, thus they have the same value of matrix stress, $\sigma_{M1} = 1.09\sigma^A$.

4.2.2. Second-level model

Based on the SAXS measurement of degree of alignment (Table 1), the apparent moduli for each sample can be obtained from Eq. (7) with the values listed in Table 1. A comparison of the stress–strain curve along the loading direction between the experiment and model evaluation is shown in Fig. 4c,d, where the Voigt and Reuss bound predictions are also given. It is found that the Eshelby model prediction lies between the two bound results and is closer to the experimental data, which also reflects the overestimation of the apparent modulus in previous investigation using the Voigt bound [7]. Meanwhile, the comparison of normal strain variation in the azimuthal plot is presented in Fig. 5a,b. Good agreement was also observed.

5. Discussion

This is the first time that the combined SAXS/WAXS technique has been used to capture the nanoscale structure and its influence on the macroscopic mechanical behaviour of human dentine. Moreover, it is important to emphasize that the study was conducted using penetrating radiation (synchrotron X-rays), i.e. a probe for bulk structure and strain analysis. Unlike the vast majority of studies that rely on surface characterisation (SEM, atomic force microscopy, nanoindentation, Raman, etc.), this ensures that the effects of sample preparation (e.g. cutting and storage) are minimal, since they typically affect depths not exceeding ~0.05 mm out of the total sample thickness of 2 mm.

5.1. Refined parameters by the Eshelby model

The parameters refined by the multiscale Eshelby model, listed in Table 1, lie within the range of the values reported in literature. This indicates that the model can be used to predict the nanoscale parameters which are hard to obtain by experiment. Of the five refined parameters, the three key parameters are two volume fractions and the Young's modulus of the HAp crystal. Among these three parameters, the Young's modulus exerts the most significant influence on the result. In the optimization process, the two volume fractions were initially fixed at approximate values, and the Young's modulus was refined within the range reported in the literature. The samples of dental tissue in this case were taken from teeth extracted from young patients. Consequently, the volume fraction of tubules was expected to be high, and was assumed to be 10% for both samples. For the same reasons, HAp crystals were assumed to have a low volume fraction (~40%). Other reasons for the small volume fraction of HAp crystals may include that the cubes were cut from a position near the pulp chamber where the volume fraction is relatively small [46], and the possible superficial demineralization effect of water storage [48]. Based on the above assumption about the two volume fractions, the refined Young's modulus of HAp crystal was found to be approximately 90 GPa. At this stage, other parameters were refined as well, although it was found that they only had a minor effect on the apparent modulus result. The influence of the thickness variation on the apparent modulus is found to be small. For a crystal thickness of 2 nm, the K_model is respectively 22.87 GPa (HD2) and 24.189 GPa (HD3), while the K_model is 23.15 GPa (HD2) and 24.62 GPa (HD3) at for a thickness of 4 nm. In order to get best fitting both along loading direction and for normal strain variation, 2 nm is the best refined parameter.

5.2. Residual strain

Indeed, a thin layer of initial residual strain may be induced at the sample surface during cutting using a low-speed diamond saw. However, as clarified above, the effect of this step on the overall measurement will not exceed 5% overall. Initial strain may also be associated with the natural growth process of the tooth. In any case, as shown in Section 4.1, the initial existing residual strain is quite small. Furthermore, our experiment only considered the elastic response. (This is reflected in the linearity of the experimental stress–strain curve, and is an underlying assumption for the Eshelby model.) The presence of initial strain amounts to an offset that does not affect such parameters as the apparent modulus. In conclusion, the low-level residual strain can be ignored in the present analysis, as it does not influence the elastic mechanical behaviour of the crystals.

5.3. Normal strain components variation

To characterize and validate the model of the strain components in different directions, the normal strain variation of the HAp crystals with respect to different azimuthal angles (0°–90°) is shown in Fig. 5. The ratio of the normal strain component at 90° to that at 0° (absolute value) for each sample is almost the Poisson's ratio of the HAp crystals, which is reasonable. Meanwhile, it should be noted that HAp crystals oriented at around 60° azimuthal angle exhibit no normal strain, i.e. no peak shift, which demonstrates that the HAp crystals at this corresponding position are subjected to pure shear stress. From the model, since the first-level dentine matrix stresses are the same for the two samples, the difference in the modulus as well as the normal strain component variation may result from different orientations and degrees of alignment of HAp crystals (observed and measured by SAXS).

5.4. HAp crystal distribution effects

The extended multiscale Eshelby model established in the present analysis is able to capture the relationship between the function of human dentine and its multiscale structure. Moreover, it is also capable of evaluating the effect of the nanoscale structure (e.g. HAp crystal distribution) on the macroscopic mechanical response, which was not included in earlier studies [7,20]. To demonstrate the detailed effect of crystal distribution on the apparent modulus, a schematic diagram of a 3-D model of perfectly aligned crystals is selected (Fig. 6a) with only one angle freedom φ around the z-axis. All aligned HAp crystals are initially oriented at a 90° angle to the platelet surface along the global y-direction, which represents the position of $\varphi = 0^{\circ}$. The variation of $K_{aligned}$ along the loading direction was calculated and visualized in Fig. 6b (only the result of HD2 is shown since both samples have similar results). The larger the value of $K_{aligned}$, the smaller the average lattice strain of HAp crystals will be under a certain value of external load, i.e. the stiffer the HAp crystals will be. It is found that the value of

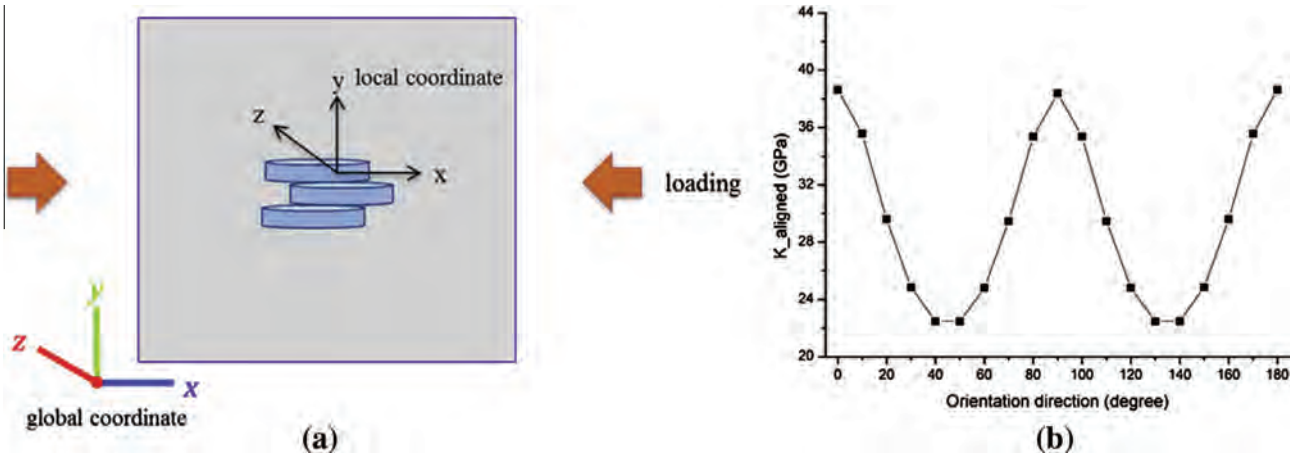

Fig. 6. (a) A simplified example of the alignment of HAp crystals. The beam direction is along the global z-axis and the alignment here represents the angle between the local x-axis and global x-axis (initially aligned angle $\varphi = 0^{\circ}$, i.e. the local x axis of a penny is initially along global x-axis). (b) By changing the alignment angle (0°–180°), the average strain of the crystals along loading direction can be obtained by the multiscale Eshelby model, which then indicates that $K_{aligned}$ varies with respect to the preferential alignment angle.

$K_{aligned}$ along the loading direction is strongly dependent on the crystal orientation direction. The orientations of HD2 and HD3 in our in situ loading experiments were 161° and 78°, respectively. Hence, from Fig. 6b, $K_{aligned\_HD3} > K_{aligned\_HD2}$. However, sample HD3 had a lower degree of alignment overall, so that overall the $K^{HAp}_{partial\_aligned\_HD3}$ value lies closer to K_{random}, which is the reason for the similar results of the apparent moduli of the two samples (Table 1).

6. Conclusions

In this study, the relationship between the nanoscale crystal distribution and macroscopic mechanical elastic response of human dentine was investigated for the first time using a combined in situ synchrotron SAXS/WAXS technique. This provided access to the information on both the structural and mechanical aspects of the sample that thus allowed us to make further progress compared to previous studies that only used WAXS [49]. Moreover, an extended multiscale Eshelby inclusion model was established to estimate and evaluate the elastic material properties of dentine as a two-level composite in terms of its constituents, showing good agreement with the experimental data both on lattice strain along loading direction and normal strain component in a general azimuthal plot, improving the Voigt composite model proposed earlier for bovine dentine [7]. The difference in the mechanical behaviour observed in the experimental results can be attributed to the second-level model effects, i.e. the degree of alignment and orientation angles.

Through this systematic experiment and modelling work, we are capable of observing the nanoscale structure, which is used to validate the model linking the nanoparticle arrangement and deformation behaviour to the macroscopic loading response. In addition, the parameter refinement and validation in the model adopted in the present study offers a possibility to identify the nanoscale parameters. The usual limitations of experimental characterization techniques such as nanoindentation or microscopy, e.g. confinement to the sample surface, make parameter identification difficult. We therefore argue that our approach enables the general characterization of the structure–property relationship in hierarchical biomaterials. An improved understanding of the multiscale structural–mechanical properties within human dentine is important for developing better prosthetic materials and dental fillings. It may also shed light on the mechanical property evolution due to multiscale structural changes within dentine because of disease and treatment.

Acknowledgements

A.M.K. acknowledges the support of EPSRC through grants EP/I020691 "Multi-disciplinary Centre for In-situ Processing Studies (CIPS)", EP/G004676 "Micromechanical Modelling and Experimentation", and EP/H003215 "New Dimensions of Engineering Science at Large Facilities". Diamond Light Source is acknowledged for providing the beam time.

Appendix A. Figures with essential colour discrimination

Certain figures in this article, particularly Figs. 1–6, are difficult to interpret in black and white. The full colour images can be found in the on-line version, at http://dx.doi.org/10.1016/j.actbio.2013.04.020

Appendix B. Appendix

A short overview of the Eshelby inclusion theory is given, leading to the derivation of the constitutive law for a non-dilute population of inhomogeneities (HAp crystals) embedded in a finite matrix.

B.1. Eshelby general theory

B.1.1. Dilute system

If a uniform transformation strain ε^{t*} exists in an ellipsoidal inclusion embedded in an infinite matrix, the Eshelby model shows that the total strain in the inclusion ε^{i} is related to ε^{t*} by the Eshelby tensor S that depends on the inclusion shape and Poisson's ratio:

$$\varepsilon^{i} = S\varepsilon^{t*}. \tag{B1}$$

Consequently, Hooke's law can be used to calculate the inclusion stress σ_I in terms of the elastic strain and the inclusion stiffness tensor C_M (which is the same as the surrounding isotropic matrix):

$$\sigma_I = C_M(\varepsilon^{i} - \varepsilon^{t*}) = C_M(S - I)\varepsilon^{t*}. \tag{B2}$$

If an inhomogeneity with a different stiffness tensor C_I is present, then the equivalent inclusion method can be used by considering the inhomogeneity as equivalent to an inclusion with an appropriate transformation strain ε^{t}, to be determined from the equivalence relation:

$$\sigma_I = C_I(\varepsilon^i - \varepsilon^{t*}) = C_M(\varepsilon^i - \varepsilon^t). \tag{B3}$$

If the material is subjected to an external load σ^A that results in the overall composite strain ε^A, then using Eq. (B3) the inclusion stress can be written as:

$$\sigma_I + \sigma^A = C_I(\varepsilon^i - \varepsilon^{t*} + \varepsilon^A) = C_M(\varepsilon^i - \varepsilon^t + \varepsilon^A). \tag{B4}$$

B.1.2. Non-dilute system

If multiple inhomogeneities are embedded in a finite matrix so that their volume fraction is not small, the composite is considered to be a non-dilute system. To satisfy the boundary conditions at the external boundaries of the finite composite, Eshelby introduced the concept of a mean "image" stress, $\langle\sigma\rangle_M = C_M\langle\varepsilon\rangle_M$ as an average of the stresses within individual phases, in order to maintain the balance of stress. The application of averaging to the linear Eq. (B4) gives:

$$C_M(\langle\varepsilon\rangle^i + \langle\varepsilon\rangle_M + \langle\varepsilon\rangle^A - \langle\varepsilon\rangle^t) = \langle C\rangle_I(\langle\varepsilon\rangle^i + \langle\varepsilon\rangle_M + \langle\varepsilon\rangle^A - \langle\varepsilon\rangle^{t*}), \tag{B5}$$

where $\langle C\rangle_I$ is the average stiffness of the inhomogeneities.

B.2. Dentine first-level model

The first-level model considers dentine as a composite consisting of aligned tubules within a finite matrix phase. According to Eq. (B5):

$$C_{M1}(\langle\varepsilon\rangle^i + \langle\varepsilon\rangle_{M1} + \varepsilon^A - \langle\varepsilon\rangle^t) = \langle C\rangle_{tubule}(\langle\varepsilon\rangle^i + \langle\varepsilon\rangle_{M1} + \varepsilon^A - \langle\varepsilon\rangle^{t*}), \tag{B6}$$

where $\langle C\rangle_{tubule}$ is the average stiffness of the tubules, and C_{M1} is the stiffness of the isotropic matrix or the equivalent inclusion ("*M1*" means the first-level matrix). Note that $\langle C\rangle_{tubule} = 0$ and $\langle\varepsilon\rangle^i = \langle S\rangle\langle\varepsilon\rangle^t$, thus:

$$\langle\varepsilon\rangle^t = (I - \langle S\rangle)^{-1}(\varepsilon^A + \langle\varepsilon\rangle_{M1}). \tag{B7}$$

In a non-dilute system, the mean image stress is related to the transformation strain [39] by:

$$\langle\sigma\rangle_{M1} = -f_1 C_{M1}(\langle S\rangle - I)\langle\varepsilon\rangle^t, \tag{B8}$$

where f_1 is the volume fraction of tubules with respect to the whole dentine. From Eq. (B7), considering that ($\langle\sigma\rangle_{M1} = C_{M1}\langle\varepsilon\rangle_{M1}$),

$$\langle\varepsilon\rangle_{M1} = \frac{f_1}{1 - f_1}\varepsilon^A. \tag{B9}$$

Therefore, the stress in the matrix is the sum of the applied stress and the image stress:

$$\sigma_{M1} = \sigma^A + \langle\sigma\rangle_{M1} = \frac{1}{1 - f_1}\sigma^A. \tag{B10}$$

Eq. (B10) indicates that the stress in the first-level matrix is independent on the direction and detailed shape (Eshelby tensor) of tubules.

B.3. Dentine second-level model

The second-level model considers the matrix of the first-level model to be a composite consisting of partially aligned HAp crystals and a collagen matrix. The volume-average method is introduced to determine the relationship between the external applied stress and the local averaged total strain in multiple HAp crystals.

The relationship between the strain in a single crystallite and the external stress can be established initially based on Eqs. (B1), (B2), (B3), (B4), (B5):

$$\begin{aligned}\varepsilon^{single} &= \{\{(I - C_{M2}^{-1}C_I)^{-1}[S - f_2(S - I)]^{-1} - I\}^{-1}T^{-T} \\ &\quad + T^{-T}\}C_{M2}^{-1}\sigma^A \\ &= K\sigma^A,\end{aligned} \tag{B11}$$

where "*M2*" means the second-level collagen matrix. C_I, S are the stiffness matrix and the Eshelby tensor for a single crystal, f_2 the volume fraction of HAp crystals with respect to the second-level composite and T is the orientation matrix described by three Euler angles (θ, ϕ, ψ). For a group of perfectly aligned HAp crystals, the relationship between the strain of the group and the external stress is the same as Eq. (B11), with the averaged stiffness and Eshelby tensor $\langle C\rangle_{HAp} = C_{HAp}, \langle S\rangle = S$. As for a group of randomly distributed HAp crystals, $\langle C\rangle_{HAp}, \langle S\rangle$ are isotropic and the way is to average the results of each single crystal (Eq. (B11)) within the group over all possible orientations:

$$\begin{aligned}\langle\varepsilon^{single}\rangle &= \frac{\int_0^{2\pi}\int_0^{\pi}\int_0^{2\pi} K\sin\theta\, d\phi\, d\theta\, d\psi}{\int_0^{2\pi}\int_0^{\pi}\int_0^{2\pi}\sin\theta\, d\phi\, d\theta\, d\psi}\sigma^A \\ &= \frac{\sigma^A}{2\pi^2}\int_0^{2\pi}\int_0^{\pi}\int_0^{2\pi} K\sin\theta\, d\phi\, d\theta\, d\psi = \langle K\rangle\sigma^A.\end{aligned} \tag{B12}$$

References

[1] Ten Cate AR, Dale AC. Oral histology: development, structure, and function. St. Louis, MO: Mosby; 1980.
[2] Petrovic LM, Spasic DT, Atanackovic TM. On a mathematical model of a human root dentin. Dent Mater 2005;21:125–8.
[3] Pashley DH, Ciucchi B, Sano H, Carvalho RM, Russell CM. Bond strength versus dentine structure: a modelling approach. Arch Oral Biol 1995;40:1109–18.
[4] Johansen E, Parks HF. Electron microscopic observations on the 3-dimensional morphology of apatite crystallites of human dentine and bone. J Biophys Biochem Cytol 1960;7:743–6.
[5] Voegel JC, Frank RM. Ultrastructural-study of apatite crystal dissolution in human dentin and bone. J Biol Buccale 1977;5:181–94.
[6] Kinney JH, Marshall SJ, Marshall GW. The mechanical properties of human dentin: a critical review and re-evaluation of the dental literature. Crit Rev Oral Biol Med 2003;14:13–29.
[7] Deymier-Black AC, Almer JD, Stock SR, Haeffner DR, Dunand DC. Synchrotron X-ray diffraction study of load partitioning during elastic deformation of bovine dentin. Acta Biomater 2010;6:2172–80.
[8] Deymier-Black AC, Almer JD, Stock SR, Dunand DC. Variability in the elastic properties of bovine dentin at multiple length scales. J Mech Behav Biomed Mater 2012;5:71–81.
[9] Young ML, Almer JD, Daymond MR, Haeffner DR, Dunand DC. Load partitioning between ferrite and cementite during elasto-plastic deformation of an ultrahigh-carbon steel. Acta Mater 2007;55:1999–2011.
[10] Mueller R, Rossoll A, Weber L, Bourke MAM, Dunand DC, Mortensen A. Tensile flow stress of ceramic particle-reinforced metal in the presence of particle cracking. Acta Mater 2008;56:4402–16.
[11] Young ML, DeFouw J, Almer JD, Dunand DC. Load partitioning during compressive loading of a Mg/MgB_2 composite. Acta Mater 2007;55:3467–78.
[12] Fratzl P, Schreiber S, Klaushofer K. Bone mineralization as studied by small-angle X-ray scattering. Connect Tissue Res 1996;35:9–16.
[13] Wagner HD, Weiner S. On the relationship between the microstructure of bone and its mechanical stiffness. J Biomech 1992;25:1311–20.
[14] Currey JD. The relationship between the stiffness and the mineral content of bone. J Biomech 1969;2:477–80.
[15] Bonfield W, Grynpas MD. Anisotropy of Youngs modulus of bone. Nature 1977;270:453–4.
[16] Deymier-Black AC, Yuan F, Singhal A, Almer JD, Brinson LC, Dunand DC. Evolution of load transfer between hydroxyapatite and collagen during creep deformation of bone. Acta Biomater 2012;8:253–61.
[17] Singhal A, Almer JD, Dunand DC. Variability in the nanoscale deformation of hydroxyapatite during compressive loading in bovine bone. Acta Biomater 2012;8:2747–58.
[18] Almer JD, Stock SR. Internal strains and stresses measured in cortical bone via high-energy X-ray diffraction. J Struct Biol 2005;152:14–27.
[19] Almer JD, Stock SR. Micromechanical response of mineral and collagen phases in bone. J Struct Biol 2007;157:365–70.
[20] Almer JD, Stock SR. High energy X-ray scattering quantification of in situ-loading-related strain gradients spanning the dentinoenamel junction (DEJ) in bovine tooth specimens. J Biomech 2010;43:2294–300.
[21] Lopes MB, Sinhoreti MA, Gonini Junior A, Consani S, McCabe JF. Comparative study of tubular diameter and quantity for human and bovine dentin at different depths. Braz Dent J 2009;20:279–83.
[22] Katz JL. Hard tissue as a composite material. 1. Bounds on elastic behavior. J Biomech 1971;93:455–73.

[23] Hashin Z. Analysis of composite-materials—a survey. J Appl Mech T Asme 1983;50:481–505.
[24] Gottesman T, Hashin Z. Analysis of viscoelastic behavior of bones on the basis of microstructure. J Biomech 1980;13:89–96.
[25] Withers PJ, Stobbs WM, Pedersen OB. The application of the Eshelby method of internal-stress determination to short fiber metal matrix composites. Acta Metall Mater 1989;37:3061–84.
[26] Takao Y, Taya M. The effect of variable fiber aspect ratio on the stiffness and thermal-expansion coefficients of a short fiber composite. J Compos Mater 1987;21:140–56.
[27] Qin Q-H, Swain MV. A micro-mechanics model of dentin mechanical properties. Biomaterials 2004;25:5081–90.
[28] Huo B. An inhomogeneous and anisotropic constitutive model of human dentin. J Biomech 2005;38:587–94.
[29] Wang YN, Qin QH. A generalized self consistent model for effective elastic moduli of human dentine. Compos Sci Technol 2007;67:1553–60.
[30] Huo B, Zheng QS. Effect of dentin tubules on the mechanical properties of dentin. Part I Stress–strain relations and strength criterion. Acta Mech Sin 1999;15:355–65.
[31] Diamond Light Source Calibration. 2013.
[32] Eliceiri KW, Berthold MR, Goldberg IG, Ibanez L, Manjunath BS, Martone ME, et al. Biological imaging software tools. Nat Methods 2012;9:697–710.
[33] Korsunsky AM, Baimpas N, Song X, Belnoue J, Hofmann F, Abbey B, et al. Strain tomography of polycrystalline zirconia dental prostheses by synchrotron X-ray diffraction. Acta Mater 2011;59:2501–13.
[34] Hammersley AP. FIT2D: an introduction and overview. ESRF Internal Report, 1997.
[35] Rinnerthaler S, Roschger P, Jakob HF, Nader A, Klaushofer K, Fratzl P. Scanning small angle X-ray scattering analysis of human bone sections. Calcified Tissue Int 1999;64:422–9.
[36] Tesch W, Vandenbos T, Roschgr P, Fratzl-Zelman N, Klaushofer K, Beertsen W, et al. Orientation of mineral crystallites and mineral density during skeletal development in mice deficient in tissue nonspecific alkaline phosphatase. J Bone Miner Res 2003;18:117–25.
[37] Tesch W, Eidelman N, Roschger P, Goldenberg F, Klaushofer K, Fratzl P. Graded microstructure and mechanical properties of human crown dentin. Calcified Tissue Int 2001;69:147–57.
[38] Bozec L, de Groot J, Odlyha M, Nicholls B, Nesbitt S, Flanagan A, et al. Atomic force microscopy of collagen structure in bone and dentine revealed by osteoclastic resorption. Ultramicroscopy 2005;105:79–89.
[39] Clyne TW, Withers PJ. An introduction to metal matrix composites. 1st pbk ed. Cambridge: Cambridge University Press; 1995.
[40] Mura T. Micromechanics of defects in solids. 2nd rev. ed. Dordrecht: Martinus Nijhoff; 1987.
[41] Stock SR, Veis A, Telser A, Cai Z. Near tubule and intertubular bovine dentin mapped at the 250 nm level. J Struct Biol 2011;176:203–11.
[42] Wenk HR, Heidelbach F. Crystal alignment of carbonated apatite in bone and calcified tendon: results from quantitative texture analysis. Bone 1999;24:361–9.
[43] Powers JM, Farah JW. Apparent modulus of elasticity of dental amalgams. J Dent Res 1975;54:902.
[44] Chou TW, Sun CT. In: Hyer MW, editor. Nanocomposites. DEStech Inc.; 2012.
[45] Dourda AO, Moule AJ, Young WG. A morphometric analysis of the cross-sectional area of dentine occupied by dentinal tubules in human third molar teeth. Int Endod J 1994;27:184–9.
[46] Kinney JH, Habelitz S, Marshall SJ, Marshall GW. The importance of intrafibrillar mineralization of collagen on the mechanical properties of dentin. J Dent Res 2003;82:957–61.
[47] Marten A, Fratzl P, Paris O, Zaslansky P. On the mineral in collagen of human crown dentine. Biomaterials 2010;31:5479–90.
[48] Habelitz S, Marshall Jr GW, Balooch M, Marshall SJ. Nanoindentation and storage of teeth. J Biomech 2002;35:995–8.
[49] Daniels JE, Pontoni D, Hoo RP, Honkimaki V. Simultaneous small- and wide-angle scattering at high X-ray energies. J Synchrotron Radiat 2010;17:473–8.